PERFORMANCE AND EFFECTIVENESS OF A THIN PAVEMENT SECTION USING GEOGRIDS AND DRAINAGE GEOCOMPOSITES IN A COLD REGION

Christopher L. Helstrom, Dana N. Humphrey,
and Jeremy M. Labbe

August, 2007

NETCR60 NETC Project No. 00-8

Prepared for
New England Transportation Consortium

Prepared by:
Department of Civil and Environmental Engineering
University of Maine
Orono, Maine

ACKNOWLEDGEMENTS

The following are the members of the Technical Committee that developed the scope of work for the project and provided technical oversight throughout the course of the research:

Scott Hayden, Maine Department of Transportation, Chairperson
David Hoyne, Vermont Agency of Transportation
David Kilpatrick, Connecticut Department of Transportation
Richard Nolan, Rhode Island Department of Transportation
Alan Perkins, New Hampshire Department of Transportation
Matt Turo, Massachusetts Highway Department
Gerald Varney, Federal Highway Administration – Maine Division

Technical Report Documentation Page

1. Report No.	2. Government Accession No.	3. Recipient's Catalog No.
NETCR60	N/A	N/A

4. Title and Subtitle	5. Report Date
Performance and Effectiveness of a Thin Pavement Section Using Geogrids and Geocomposites in a Cold Region	January 20, 2006
	6. Performing Organization Code: N/A

7. Author(s)	8. Performing Organization Report No.
Christopher L. Helstrom, Dana N. Humphrey, & Jeremy M. Labbe	N/A

9. Performing Organization Name and Address	10. Work Unit No. (TRAIS)
Department of Civil and Environmental Engineering University of Maine 5711 Boardman Hall Orono, ME 04469-5711	N/A
	11. Contract or Grant No.: N/A

12. Sponsoring Agency Name and Address	13. Type of Report and Period Covered
New England Transportation Consortium c/o Adv. Technology & Manufacturing Center University of Massachusetts Dartmouth 151 Martine Street Fall River, MA 02723	FINAL
	14. Sponsoring Agency Code: N/A

15. Supplementary Notes

N/A

16. Abstract: Test sections were constructed in two portions of Maine Route 9 to investigate the use of geosynthetics for reinforcement and drainage for subbase courses that were 300 mm (12 in.) and 600 mm (24 in.) thick with 150 mm (6-in.) of flexible pavement. Four types of test sections were constructed: geogrid reinforcement, drainage geocomposite, drainage geocomposite with geogrid reinforcement, and control. Test sections using reinforcement geogrid have strain gages attached to the geogrid to measure induced forces. Some of the reinforcement sections have geogrid on subgrade whereas some have geogrid in the center of the subbase to evaluate the effects of geogrid location. Drainage geocomposite and control sections have vibrating wire piezometers to monitor porewater pressure in the subgrade and subbase course. Thermocouples were used to measure the depth of frost penetration. The results of falling weight deflectometer tests were used to backcalculate the effective structural number for each section. Reinforcement geogrid and drainage geocomposite increased the effective structural number by between 5% and 17% for sections with 300 mm (12 in.) subbase. However, they had no apparent effect for sections with 600 mm (24 in.) of subbase. The increase in backcalculated effective structural number that was produced by geogrid and/or drainage geocomposite in the 300-mm (12-in.) subbase sections could also be obtained by adding between 25 and 75 mm (1 and 3 in.) of subbase aggregate to an unreinforced section.

17. Key Words	18. Distribution Statement
geogrid, drainage geocomposite, reinforcement, drainage, subbase, subgrade, structural number	No restrictions. This document is available to the public through the National Technical Information Service Springfield, Virginia 22161

19. Security Classif. (of this report)	20. Security Classif. (of this page)	21. No. of Pages	22. Price
Unclassified	Unclassified	265	N/A

Form DOT F 1700.7 (8-72) Reproduction of completed page authorized

SI* (MODERN METRIC) CONVERSION FACTORS

APPROXIMATE CONVERSIONS TO SI UNITS

Symbol	When You Know	Multiply By	To Find	Symbol
		LENGTH		
in	inches	25.4	millimetres	mm
ft	feet	0.305	metres	m
yd	yards	0.914	metres	m
mi	miles	1.61	kilometres	km
		AREA		
in^2	square inches	645.2	millimetres squared	mm^2
ft^2	square feet	0.093	metres squared	m^2
yd^2	square yards	0.836	metres squared	m^2
ac	acres	0.405	hectares	ha
mi^2	square miles	2.59	kilometres squared	km^2
		VOLUME		
fl oz	fluid ounces	29.57	mililitres	mL
gal	gallons	3.785	Litres	L
ft^3	cubic feet	0.028	metres cubed	m^3
yd^3	cubic yards	0.765	metres cubed	m^3

NOTE: Volumes greater than 1000 L shall be shown in m^3

		MASS		
oz	ounces	28.35	grams	g
lb	pounds	0.454	kilograms	kg
T	short tons (2000 lb)	0.907	megagrams	Mg
		TEMPERATURE (exact)		
°F	Fahrenheit temperature	5(F-32)/9	Celcius temperature	°C

* SI is the symbol for the International System of Measurement

APPROXIMATE CONVERSIONS TO SI UNITS

Symbol	When You Know	Multiply By	To Find	Symbol
		LENGTH		
mm	millimetres	0.039	inches	in
m	metres	3.28	feet	ft
m	metres	1.09	yards	yd
km	kilometres	0.621	miles	mi
		AREA		
mm^2	millimetres squared	0.0016	square inches	in^2
m^2	metres squared	10.764	square feet	ft^2
ha	hectares	2.47	acres	ac
km^2	kilometres squared	0.386	square miles	mi^2
		VOLUME		
mL	millilitres	0.034	fluid ounces	fl oz
L	litres	0.264	gallons	gal
m^3	metres cubed	35.315	cubic feet	ft^3
m^3	metres cubed	1.308	cubic yards	yd^3
		MASS		
g	grams	0.035	ounces	oz
kg	kilograms	2.205	pounds	lb
Mg	megagrams	1.102	short tons (2000 lb)	T
		TEMPERATURE (exact)		
°C	Celcius temperature	1.8C+32	Fahrenheit temperature	°F

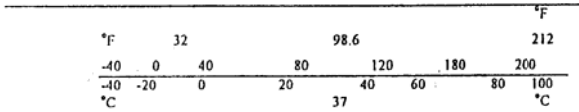

TABLE OF CONTENTS

TABLE OF CONTENTS ..... **v**

LIST OF TABLES ..... **ix**

LIST OF FIGURES ..... **xii**

LIST OF SYMBOLS ..... **xix**

LIST OF ACRONYMS ..... **xx**

EXECUTIVE SUMMARY **1**

CHAPTER 1 INTRODUCTION **11**

1.1. BACKGROUND 11

1.2. SCOPE OF STUDY 14

1.3. ORGANIZATION OF REPORT 14

CHAPTER 2 LITERATURE REVIEW **17**

2.1. INTRODUCTION 17

2.2. PERFORMANCE IMPROVEMENT FUNCTIONS 18
2.2.1. Reinforcement 18
2.2.1.1. Lateral Subbase Restraint 18
2.2.1.2. Tensioned Membrane Effect 20
2.2.2. Separation 21
2.2.3. Filtration 21
2.2.4. Drainage 22

2.3. LABORATORY STUDIES OF UNPAVED ROADS 22

2.4. RESEARCH OF GEOSYNTHETICS IN PAVED ROADS 25
2.4.1. Laboratory Studies 25
2.4.1.1. Ruddock, Potter, and McAvoy 25
2.4.1.2. Barksdale, Brown, and Chan 26
2.4.1.3. University of Waterloo 27
2.4.1.4. Virginia Polytechnic Institute 28
2.4.1.5. University of Alaska Fairbanks 30
2.4.1.6. Montana Department of Transportation 32
2.4.2. Field Studies of Paved Roads 33
2.4.2.1. Ontario Field Study 33

2.4.2.2. Perkins and Lapeyre 34
2.4.2.3. Terracon Inc. Investigation in Dallas 35
2.4.2.4. Study of Reinforced Pavements for Light Aircraft 36
2.4.2.5. Fetten and Humphrey 36

2.5. NUMERIC MODELING 38
2.5.1. Modeling For Unpaved Roads 38
2.5.2. Modeling For Paved Roads 41

2.6. DESIGN METHODS 45
2.6.1. Reinforcement Design Methods for Unpaved Roads 45
2.6.2 Design Methods for Paved Permanent Roads 48
2.6.2.1. Penner, Haas, and Walls 48
2.6.2.2. Vischer 50

2.7. SUMMARY 52

CHAPTER 3 PROJECT DESCRIPTION 55

3.1. INTRODUCTION 55

3.1. TEST SECTION LAYOUT 56
3.2.1. Test Section 1 - Reinforcement 58
3.2.2. Test Section 2 - Reinforcement 58
3.2.3. Test Section 3 - Control 58
3.2.4. Test Section 4 – Drainage/Reinforcement 58
3.2.5. Test Section 5 - Drainage 59
3.2.6. Test Section 6 - Reinforcement 59
3.2.7. Test Section 7 - Reinforcement 59
3.2.8. Test Section 8 - Control 60
3.2.9. Test Section 9 - Drainage 60
3.2.10. Test Section 10 – Drainage/Reinforcement 60
3.2.11. Test Section 11 - Drainage 61
3.2.12. Test Section 12 - Control 61

3.3. GEOSYNTHETIC PROPERTIES 61
3.3.1. Reinforcement Geogrid Properties 61
3.3.2. Drainage Geocomposite Properties 63

3.4. SUBGRADE AND SUBBASE COURSE PROPERTIES 64
3.4.1. In-Situ Subgrade Properties 64
3.4.2. Subbase Course Properties 68

3.5. CONSTRUCTION PROCEDURES 69
3.5.1. Reinforcement Geogrid Installation 70
3.5.2. Drainage Geocomposite Installation 74

3.6. SUMMARY 77

CHAPTER 4 INSTRUMENTATION AND FIELD MEASUREMENTS 79

4.1. INTRODUCTION 79

4.2. STRAIN GAGES ON GEOGRIDS 80
4.2.1. Strain Gage Characteristics 80
4.2.2. Strain Gage Attachment to Geogrid 82
4.2.3. Strain Gage Locations 86
4.2.4. Field Installation 86
4.2.5. Strain Gage Calibration 89

4.3. VIBRATING WIRE PIEZOMETERS 91
4.3.1. Vibrating Wire Piezometer Characteristics 91
4.3.2. Vibrating Wire Piezometer Locations 93
4.3.3. Field Installation 93

4.4. FLOW METERS 96
4.4.1. Flow Meter Characteristics 96
4.4.2. Flow Meter Locations 97
4.4.3. Field Installation 98
4.4.3.1 Automated Flow Meter Installation 98
4.4.3.2 Manual Flow Meter Installation 100

4.5. THERMOCOUPLE STRINGS 100
4.5.1. Thermocouple Characteristics 100
4.5.2. Thermocouple String Locations 102
4.5.3. Field Installation 103

4.6. DATA ACQUISITION SYSTEMS 104

4.7. SUMMARY 106

CHAPTER 5 RESULTS 109

5.1. INTRODUCTION 109

5.2. STRAIN GAGE RESULTS 109
5.2.1. Strain Gages Perpendicular to Centerline 111
5.2.1.1. Construction Forces 118
5.2.1.2. Long Term Forces 125
5.2.1.3. Summary of Forces 140
5.2.1.4. Statistical Comparisons of Forces Perpendicular to Centerline 142
5.2.2. Strain Gages Parallel to Centerline 151
5.2.2.1. 300-mm Subbase Sections 155
5.2.2.2. 600-mm Subbase Sections 156
5.2.3. Thermal Strain Gages 158

5.2.4. Mobilization of geogrid strength 159
5.2.5. Creep Test Results 159

5.3. VIBRATING WIRE PIEZOMETER RESULTS 166
5.3.1. Reconstructed Section Results 166
5.3.2. Reclaimed Section Results 172

5.4. FLOW METER RESULTS 178
5.4.1. Automated Flow Results 178
5.4.2. Manual Flow Results 182
5.4.3. Discussion 182

5.5. FROST PENETRATION RESULTS 184

5.6. FALLING WEIGHT DEFLECTOMETER RESULTS 197

5.7. SUMMARY 201

CHAPTER 6 SUMMARY, CONCLUSIONS, AND RECOMMENDATIONS 207

6.1. SUMMARY 207
6.1.1. Literature Review 208
6.1.2. Construction and Instrumentation of Test Sections 211
6.1.3. Results 212
6.1.3.1. Strain Gages 212
6.1.3.2. Piezometers 215
6.1.3.3. Flow Meters 216
6.1.3.4. Thermocouples 216
6.1.3.5. Falling Weight Deflectometer 217

6.2. CONCLUSIONS 217

6.3. RECOMMENDATIONS FOR FUTURE RESEARCH 220

REFERENCES 221

APPENDIX A - LABORATORY CALIBRATION TESTS 225

APPENDIX B - FALLING WEIGHT DEFLECTOMETER RESULTS 243

LIST OF TABLES

Table 2.1 Subgrade stresses measured in laboratory test (Lai and Robnett, 1982)..... 23

Table 2.2 Summary of subbase layer moduli backcalculated from FWD results (Anderson and Killeavy, 1989 34

Table 3.1 Reinforcement geogrid properties. 62

Table 3.2 Drainage geocomposite properties. 63

Table 3.3 Subgrade sample properties. 65

Table 3.4 MaineDOT subbase grain size specifications. 68

Table 3.5 Critical project dates. 69

Table 4.1 Summary of gage offsets and orientations. 85

Table 4.2 Strain gage locations. 86

Table 4.3 Summary of best fit slopes from geogrid calibration tests. 92

Table 4.4 Piezometer locations. 93

Table 4.5 Flow meter characteristics. 97

Table 4.6 Flow meter locations. 98

Table 4.7 Thermocouple string locations. 103

Table 5.1 Geogrid strain gage pair survivability 110

Table 5.2 Actual force in geogrid after subbase compaction in test sections constructed with 300-mm (12-in.) subbase. 119

Table 5.3 Actual force in geogrid immediately following paving in test sections constructed with 300-mm (12-in.) subbase. 120

Table 5.4 Change in geogrid force between subbase compaction and paving in test sections constructed with 300-mm (12-in.) subbase..... 121

Table5.5 Actual force in geogrid after subbase compaction in test sections constructed with 600-mm (24-in.) subbase. 123

Table 5.6 Change in geogrid force between subbase compaction and paving in test sections constructed with 600-mm (24-in.) subbase..... 124

Table 5.7 Actual force in geogrid immediately following paving in test sections constructed with 600-mm (24-in.) subbase. 125

Table 5.8 Change in geogrid force between paving and 12 months after installation in test sections constructed with 300-mm (12-in.) subbase.... 127

Table 5.9 Actual force in geogrid 12 months after installation in test sections constructed with 300-mm (12-in.) subbase. 128

Table 5.10 Change in geogrid force between 12 and 24 months after installation in test sections constructed with 300-mm (12-in.) subbase. 129

Table 5.11 Actual force in geogrid 24 months after installation in test sections constructed with 300-mm (12-in.) subbase. 130

Table 5.12 Change in geogrid force between 24 and 35 months after installation in test sections constructed with 300-mm (12-in.) subbase. 131

Table 5.13 Actual force in geogrid 35 months after installation in test sections constructed with 300-mm (12-in.) subbase. 132

Table 5.14 Change in geogrid force between paving and 12 months after installation in test sections constructed with 600-mm (24-in.) subbase.... 133

Table 5.15 Actual force in geogrid 12 months after installation in test sections constructed with 600-mm (24-in.) subbase. 134

Table 5.16 Change in geogrid force between 12 and 24 months after installation in test sections constructed with 600-mm (24-in.) subbase. 135

Table 5.17 Actual force in geogrid 24 months after installation in test sections constructed with 600-mm (24-in.) subbase. 136

Table 5.18 Change in geogrid force between 24 and 35 months after installation in test sections constructed with 600-mm (24-in.) subbase. 137

Table 5.19 Actual force in geogrid 35 months after installation in test sections constructed with 600-mm (24-in.) subbase. 138

Table 5.20 Change in geogrid force between 35 and 45 months after installation in test sections constructed with 600-mm (24-in.) subbase. 139

Table 5.21 Actual force in geogrid 45 months after installation in test sections constructed with 600-mm (24-in.) subbase. 140

Table 5.22 Summary of average actual force in geogrid, all test sections 141

Table 5.23 Effect of geogrid location for 300 mm subbase sections analyzed using statistical z-test. 144

Table 5.24 Effect of geogrid location for 600 mm subbase sections analyzed using statistical z-test. 145

Table 5.25 Effect of subbase thickness for sections with geogrid located on subgrade analyzed using statistical z-test. 145

Table 5.26 Effect of subbase thickness for sections with geogrid located at center of subbase analyzed using statistical z-test. 146

Table 5.27 Elapsed time effects in 300-mm subbase sections, analyzed using the statistical t-test. 149

Table 5.28 Elapsed time effects in 600-mm subbase sections, analyzed using the statistical t-test. 150

Table 5.29 Force in geogrid ribs oriented parallel to centerline in test sections constructed with 300-mm (12-in.) subbase. 156

Table 5.30 Force in geogrid ribs oriented parallel to centerline in test sections constructed with 600-mm (24-in.) subbase. 157

Table 5.31 Collector pipe lengths. 178

Table 5.32 Manual flow meter results. 182

Table 5.33 Frost penetration in test sections 4, 6, 10, 11, and 12. 194

Table 5.34 Frost penetration in test sections 4, 6, 10, 11, and 12. 197

LIST OF FIGURES

Figure 2.1 Tensioned membrane effect (Bender and Barenberg, 1978)..... 20

Figure 2.2 Permanent displacement profile at 800 cycles (Al-Qadi, et al., 1994)..... 30

Figure 2.3 Cross section and plan view of University of AK Fairbanks test facility (Kinney, et al., 1998). 31

Figure 2.4 Increased confinement-effect model (Thompson and Raad, 1981). 40

Figure 2.5 Comparison of bounding surface model and experimental results for..... 44

Figure 2.6 Comparison of bounding surface model and experimental results for cyclic loading (Ling, et al., 2001). 45

Figure 2.7 Subbase aggregate load distribution for the unreinforced (a) and reinforced (b) case (Giroud and Noiray, 1981). 47

Figure 3.1 Test section layout. 57

Figure 3.2 Photo of reinforcement geogrid..... 62

Figure 3.3 Photo of internal structure of drainage geocomposite and external filter fabric. 64

Figure 3.4 Subgrade sieve and hydrometer analysis for test sections 1 through 4. 66

Figure 3.5 Subgrade sieve and hydrometer analysis for test sections 6 and 7..... 66

Figure 3.6 Subgrade sieve and hydrometer analysis for test sections 8 through 10. 67

Figure 3.7 Subgrade sieve and hydrometer analysis for test section 11. 67

Figure 3.8 Subbase course aggregate sieve analysis. 68

Figure 3.9 Geogrid unrolled on subgrade. 72

Figure 3.10 Subbase material bladed onto geogrid..... 72

Figure 3.11 Wave of geogrid ahead of subbase placement. 73

Figure 3.12 Butt joint detail. 75

Figure 3.13 Centerline overlap joint detail. 75

Figure 3.14 Collector pipe detail. 76

Figure 3.15 Drainage geocomposite and collector pipe. 76

Figure 4.1 Wheatstone bridge configuration (Texas Measurements, 2001). 81

Figure 4.2 Photo of epoxy coated strain gages. 83

Figure 4.3 Photo of 4-in. PVC electrical junction box. 84

Figure 4.4 Photo of strain gages. 85

Figure 4.5 Photo of manual readout station and PVC conduit in the backslope. 87

Figure 4.6 Manual readout station. 88

Figure 4.7 Wide-width tensile test specimen. 90

Figure 4.8 Sample wide-width tensile test calibration plot. 91

Figure 4.9 Photo of automated flow meter installation. 99

Figure 4.10 Test section six thermocouple diagram. 102

Figure 4.11 Photo of data acquisition system enclosure. 106

Figure 5.1 Force perpendicular to centerline in geogrid located on subgrade with 300-mm (12-in.) subbase in test section 1 station 1+540 m. 112

Figure 5.2 Force perpendicular to centerline in geogrid located on subgrade with 300-mm (12-in.) subbase in test section 1 station 1+560 m. 112

Figure 5.3 Force perpendicular to centerline in geogrid located in 300-mm (12-in.) subbase in test section 2 station 1+600 m. 113

Figure 5.4 Force perpendicular to centerline in geogrid located in 300-mm (12-in.) subbase in test section 2 station 1+620 m. 113

Figure 5.5 Force perpendicular to centerline in geogrid located in 300-mm (12-in.) subbase in test section 4 station 1+720 m. 114

Figure 5.6 Force perpendicular to centerline in geogrid located in 300-mm (12-in.) subbase in test section 4 station 1+740 m. 114

Figure 5.7 Force perpendicular to centerline in geogrid located on subgrade with 600-mm (24-in.) subbase in test section 6 station 3+950 m. 115

Figure 5.8 Force perpendicular to centerline in geogrid located on subgrade with 600-mm (24-in.) subbase in test section 6 station 3+970 m. 115

Figure 5.9 Force perpendicular to centerline in geogrid located in 600-mm (24-in.) subbase in test section 7 station 3+990 m. 116

Figure 5.10 Force perpendicular to centerline in geogrid located in 600-mm (24-in.) subbase in test section 7 station 4+010 m. 116

Figure 5.11 Force perpendicular to centerline in geogrid located in 600-mm (24-in.) subbase in test section 10 station 4+110 m. 117

Figure 5.12 Force perpendicular to centerline in geogrid located in 600-mm (24-in.) subbase in test section 10 station 4+130 m. 117

Figure 5.13 Summary of average force in geogrid. 142

Figure 5.14 Force parallel to centerline in geogrid located on subgrade with 300-mm (12-in.) subbase in test section 1 station 1+540 m. 151

Figure 5.15 Force parallel to centerline in geogrid located on subgrade with 300-mm (12-in.) subbase in test section 1 station 1+560 m. 152

Figure 5.16 Force parallel to centerline in geogrid located on subgrade with 600-mm (24-in.) subbase in test section 6 station 3+970 m. 152

Figure 5.17 Force parallel to centerline in geogrid located in 600-mm (24-in) subbase in test section 7 station 3+990 m. 153

Figure 5.18 Force parallel to centerline in geogrid located in 600-mm (24-in.) subbase in test section 7 station 4+010 m. 153

Figure 5.19 Force parallel to centerline in geogrid located in 600-mm (24-in.) subbase in test section 10 station 4+110 m. 154

Figure 5.20 Force parallel to centerline in geogrid located in 600-mm (24-in.) subbase in test section 10 station 4+130 m. 154

Figure 5.21 Creep test results plotted with linear time scale. 160

Figure 5.22 Creep test results plotted with logarithmic time scale. 160

Figure 5.23 Average strain measured by strain gage pair 1-2 in test section 1 station 1+560 versus elapsed time. 162

Figure 5.24 Average strain measured by strain gage pair 1-2 in test section 1 station 1+560 versus log elapsed time. 162

Figure 5.25 Average strain measured by strain gage pair 1-2 in test section 2 station 1+600 versus elapsed time. 163

Figure 5.26 Average strain measured by strain gage pair 1-2 in test section 2 station 1+600 versus log elapsed time..... 163

Figure 5.27 Average strain measured by strain gage pair 9-10 in test section 6 station 3+970 versus elapsed time..... 164

Figure 5.28 Average strain measured by strain gage pair 9-10 in test section 6 station 3+970 versus log elapsed time..... 164

Figure 5.29 Average strain measured by strain gage pair 1-2 in test section 10 station 4+110 versus elapsed time..... 165

Figure 5.30 Average strain measured by strain gage pair 1-2 in test section 10 station 4+110 versus log elapsed time..... 165

Figure 5.31 Porewater pressures in test section 3 (control)..... 168

Figure 5.32 Porewater pressures in test section 4 (drainage). 169

Figure 5.33 Porewater pressures in test section 8 (control)..... 169

Figure 5.34 Porewater pressures in test section 9 (drainage). 170

Figure 5.35 Porewater pressures in test section 10 (drainage). 170

Figure 5.36 Subbase porewater pressures in test sections 3, 4, 8, 9, and 10. 171

Figure 5.37 Subgrade porewater pressures in test sections 3, 4, 8, 9, and 10..... 172

Figure 5.38 Porewater pressures in test section 11 (drainage). 174

Figure 5.39 Porewater pressures in test section 12 (control)..... 175

Figure 5.40 Subbase porewater pressures in reclaim sections..... 176

Figure 5.41 Subgrade porewater pressures in reclaim sections..... 177

Figure 5.42 Flow from collector pipe in test section 4 station 1+760 RT..... 179

Figure 5.43 Flow from collector pipe in test section 4 station 1+760 LT. 179

Figure 5.44 Flow from collector pipe in test section 5 station 1+820 RT..... 180

Figure 5.45 Flow from collector pipe in test section 5 station 1+820 LT 180

Figure 5.46 Flow from collector pipe in test section 9 station 4+100 RT..... 181

Figure 5.47 Flow from collector pipe in test section 10 station 4+140 RT..... 181

Figure 5.48 Flow and rainfall in test section 9 station 4+100 RT. 184

Figure 5.49 Frost penetration in test section 1 station 1+550 winter of 02-03. 185

Figure 5.50 Frost penetration in test section 1 station 1+550 winter of 03-04. 185

Figure 5.51 Frost penetration in test section 1 station 1+550 winter of 04-05. 186

Figure 5.52 Frost penetration in test section 2 station 1+612 winter of 02-03. 186

Figure 5.53 Frost penetration in test section 2 station 1+612 winter of 03-04. 187

Figure 5.54 Frost penetration in test section 2 station 1+612 winter of 04-05. 187

Figure 5.55 Frost penetration in test section 3 station 1+670 winter of 02-03. 188

Figure 5.56 Frost penetration in test section 3 station 1+670 winter of 03-04. 188

Figure 5.57 Frost penetration in test section 3 station 1+670 winter of 04-05. 189

Figure 5.58 Frost penetration in test section 7 station 4+000 winter of 02-03. 189

Figure 5.59 Frost penetration in test section 7 station 4+000 winter of 03-04. 190

Figure 5.60 Frost penetration in test section 7 station 4+000 winter of 04-05. 190

Figure 5.61 Frost penetration in test section 8 station 4+040 winter of 02-03. 191

Figure 5.62 Frost penetration in test section 8 station 4+040 winter of 03-04. 191

Figure 5.63 Frost penetration in test section 8 station 4+040 winter of 04-05. 192

Figure 5.64 Frost penetration in test section 9 station 4+080 winter of 02-03. 192

Figure 5.65 Frost penetration in test section 9 station 4+080 winter of 03-04. 193

Figure 5.66 Frost penetration in test section 9 station 4+080 winter of 04-05. 193

Figure 5.67 Cumulative degree-days for freezing season of 2001-02. 195

Figure 5.68 Cumulative degree-days for freezing season of 2002-03. 195

Figure 5.69 Cumulative degree-days for freezing season of 2003-04. 196

Figure 5.70 Cumulative degree-days for freezing season of 2004-05. 196

Figure 5.71 Effective structural number for sections with 300 mm (12 in.) subbase aggregate. 198

Figure 5.72 Effective structural number for sections with 600 mm (24 in.) subbase aggregate. 199

Figure 5.73 Effective structural number for reclaim sections. 201

Figure A-1 Wide width tensile test calibration curve, specimen 1, test 1, gage 1. 226

Figure A-2 Wide width tensile test calibration curve, specimen 1, test 1, gage 2. 226

Figure A-3 Wide width tensile test calibration curve, specimen 1, test 1, gage 3. 227

Figure A-4 Wide width tensile test calibration curve, specimen 1, test 1, gage 4. 227

Figure A-5 Wide width tensile test calibration curve, specimen 1, test 2, gage 1. 228

Figure A-6 Wide width tensile test calibration curve, specimen 1, test 2, gage 2. 228

Figure A-7 Wide width tensile test calibration curve, specimen 1, test 2, gage 3. 229

Figure A-8 Wide width tensile test calibration curve, specimen 1, test 2, gage 4. 229

Figure A-9 Wide width tensile test calibration curve, specimen 2, test 1, gage 1. 230

Figure A-10 Wide width tensile test calibration curve, specimen 2, test 1, gage 2. 230

Figure A-11 Wide width tensile test calibration curve, specimen 2, test 1, gage 3. 231

Figure A-12 Wide width tensile test calibration curve, specimen 2, test 1, gage 4. 231

Figure A-13 Wide width tensile test calibration curve, specimen 2, test 2, gage 1. 232

Figure A-14 Wide width tensile test calibration curve, specimen 2, test 2, gage 2. 232

Figure A-15 Wide width tensile test calibration curve, specimen 2, test 2, gage 3. 233

Figure A-16 Wide width tensile test calibration curve, specimen 2, test 2, gage 4. 233

Figure A-17 Wide width tensile test calibration curve, specimen 2, test 3, gage 1. 234

Figure A-18 Wide width tensile test calibration curve, specimen 2, test 3, gage 2. 234

Figure A-19 Wide width tensile test calibration curve, specimen 2, test 3, gage 3. 235

Figure A-20 Wide width tensile test calibration curve, specimen 2, test 3, gage 4. 235

Figure A-21 Wide width tensile test calibration curve, specimen 2, test 4, gage 1. 236

Figure A-22 Wide width tensile test calibration curve, specimen 2, test 4, gage 2. 236

Figure A-23 Wide width tensile test calibration curve, specimen 2, test 4, gage 3. 237

Figure A-24 Wide width tensile test calibration curve, specimen 2, test 4, gage 4. 237
Figure A-25 Wide width tensile test calibration curve, specimen 3, test 1, gage 1. 238
Figure A-26 Wide width tensile test calibration curve, specimen 3, test 1, gage 2. 238
Figure A-27 Wide width tensile test calibration curve, specimen 3, test 1, gage 3. 239
Figure A-28 Wide width tensile test calibration curve, specimen 3, test 1, gage 4. 239
Figure A-29 Wide width tensile test calibration curve, specimen 3, test 2, gage 1. 240
Figure A-30 Wide width tensile test calibration curve, specimen 3, test 2, gage 2. 240
Figure A-31 Wide width tensile test calibration curve, specimen 3, test 2, gage 3. 241
Figure A-32 Wide width tensile test calibration curve, specimen 3, test 2, gage 4. 241

List of Symbols

a_n =	layer coefficient for n^{th} layer
A_r/A_u =	effect of geogrid reinforcement of structural capacity of subbase
D =	the average difference between matched samples
d_n =	layer thickness for n^{th} layer
d_r =	thickness of reinforced subbase
d_u =	thickness of ureinforced subbase
E =	excitation voltage
e =	output voltage
h =	thickness of granular layer
K =	strain gage factor
K_o =	coefficient of earth pressure at rest
K_s =	modulus of subgrade reaction
n =	the number of matched samples
n_1 =	number of values in sample 1
n_2 =	number of values in sample 2
P_o =	applied surface pressure
r =	radius of loaded area
R =	$R_1 - R_4$
R_1 =	gage resistance
R_2,R_3,R_4 =	resistance of fixed resistors
s(D) =	the standard deviation of the population difference
s(Y – X) =	standard deviation of the sampling distribution
s_1 =	standard deviation of sample 1
s_2 =	standard deviation of sample 2
sD =	the standard deviation of the matched sample differences
SN =	structural number
SN_{gr} =	structural number of granular base
$(SN_{gr})_r$ =	structural number of reinforced granular base
$(SN_{gr})_u$ =	structural number of unreinforced granular base
T =	statistical variable based on the confidence interval and n
t* =	statistical t-score
Y – X =	difference between sample means
z* =	statistical z-score
ε =	strain
μ_1 =	mean of population 1
μ_2 =	mean of population 2
σ_v =	applied vertical stress
Δ_p =	permanent deformation
Δ_r =	resilient deformation
$\Delta\sigma/\sigma$ =	increase in confinement at interface due to fabric deformation, expressed in terms of the confinement before the fabric deforms, σ
$\Delta\mu\varepsilon$ =	change in microstrain
ΔR =	$\Delta(R_1 - R_4)$

List of Acronyms

AASHTO	American Association of State Highway and Transportation Officials
ASTM	American Society for Testing and Materials
AWG	American wire gauge
CBR	California bearing ratio
ESAL	Equivalent single axle load
FHWD	Federal Highway Administration
FWD	Falling weight deflectometer
LT	Left of centerline
LVDT	Linear variable differential transformer
MaineDOT	Maine Department of Transportation
MD	Machine direction
NA	Not applicable
NEMA	National Electrical Manufactures Association
NETC	New England Transportation Consortium
NOAA	National Oceanic & Atmospheric Administration
NF	Not functioning
PVC	Polyvinylchloride
RT	Right of centerline
XD	Cross machine direction

PERFORMANCE AND EFFECTIVENESS OF A THIN PAVEMENT SECTION USING GEOGRIDS AND DRAINAGE GEOCOMPOSITES IN A COLD REGION
NETC Project No. 00-8

EXECUTIVE SUMMARY

By: Christopher L. Helstrom, Dana N. Humphrey, and Jeremy M. Labbe
Department of Civil & Environmental Engineering, University of Maine, Orono, Maine

Test sections were constructed in two portions of Route 9 in the towns of Monmouth, Litchfield, and West Gardiner, Maine to investigate the use of geosynthetics for reinforcement and drainage for subbase courses that were 300 mm (12 in.) and 600 mm (24 in.) thick. Previous research on geosynthetic reinforcement in flexible pavement systems generally focused on subbases 50 to 365 mm (2 to 14 in.) thick, which are thinner than used by most New England state transportation agencies. An earlier study by the Maine Department of Transportation (MaineDOT) investigated geogrid and geotextile reinforcement with subbases 584 mm (23 in.) and 640 mm (25 in.) thick. The use of drainage geocomposites was also investigated in this study. The present study expands upon the MaineDOT work by examining the use of drainage geocomposites and geogrid reinforced flexible pavement systems with subbase courses 300 mm (12 in.) and 600 mm (24 in.) thick, and 150-mm (6-in.) thick pavement. These thicknesses are typical of those used by New England DOT's.

The objective of this study was to evaluate the reinforcement and drainage capabilities of geosynthetics in roadways in cold regions constructed on soft subgrade soils with the thick subbases typical of roads built by New England DOT's. The following tasks were completed:

- Literature review of laboratory tests, field trials, computer analyses, and design methods for geosynthetic reinforcement in both unsurfaced and paved roads was conducted.
- Portions of Route 9 in the towns of Monmouth, Litchfield, and West Gardiner, Maine, were instrumented with strain gages, piezometers, flow meters, and thermocouples to evaluate the performance of the geosynthetics.
- The instruments were monitored from September, 2001 until June, 2005. Force in the geogrid, porewater pressures in the drainage sections, flow from the drainage sections, and frost penetration were examined. Falling weight deflectometer tests were conducted on the completed pavement.
- The performance of the test sections was evaluated by comparing results from sections constructed with geosynthetics with those from previous studies as well as control sections from this study.

Literature Review

Geosynthetics have been in use since the mid-1970's. Early research focused on applications in temporary haul roads and unpaved roads. Their beneficial reinforcing effects in unsurfaced roads have since been documented. As wheel ruts develop the resulting movement of subbase particles allows for shear interaction with the geosynthetic. The tensile loads developed at the bottom of the subbase are transmitted to the geosynthetic, effectively providing the subbase with tensile strength (Bender and Barenberg, 1978). Some work suggests that geogrid is superior to geotextile for lateral subbase restraint due to the interlock between the geogrid and subbase (Haas, et al., 1985; Barksdale, et al., 1989). Development of wheel ruts also deforms the subgrade and geosynthetic. The tensile forces in the deformed geosynthetic provide an upward resultant force just outside the wheel path that reduces the vertical stress applied to the subgrade. In addition, the tensile forces in the geosynthetic also provide a downward resultant force that helps to confine the subgrade on either side of the wheel path and increase its bearing capacity (Bender and Barenberg, 1978). These mechanisms have been shown to increase performance in unpaved roads where wheel ruts can readily develop. However, the effects of these mechanisms may be limited in roads paved with flexible pavements which cannot tolerate large permanent deflections.

Several full-scale laboratory experiments of the reinforcement mechanisms of geosynthetics beneath flexible pavements showed some improvement (Kennepohl, et al., 1985; Penner, et al., 1985; Haas, et al., 1988; Barksdale, et al.,1989; Al-Qadi, et al., 1994; Cancelli, et al.,1996; Perkins, et al.,1996; Montanelli, et al., 1997),. However, only one study examined the reinforcing benefit of geosynthetics in cold regions with subbase and pavement layers as thick as those constructed by New England DOT's (Fetten and Humphrey, 1997). A computer analysis showed that geogrid reinforcement was not expected to improve performance for roadway sections with pavement layers greater than 65 to 90 mm (2.5 to 3.5 in.) thick, even when constructed on weak subgrades. Moreover, the beneficial effects of geosynthetic reinforcement in terms of stress, strain, and deflection were relatively small for reinforced sections designed to support more than approximately 200,000 equivalent 80-kN (18-kip) single axle loads (Barksdale, et al., 1989). For comparison, the pavement section at the test site for the present study was designed to carry 500,000 equivalent 80-kN (18-kip) single axle loads.

A limited number of design procedures are available for reinforcement beneath flexible pavements. One method uses a layer coefficient ratio or equivalence factor applied to the reinforced layer to reflect the structural improvement to the subbase. Comparisons of this ratio to the behavior of test sections indicated that subbase thickness and performance improvement were inversely proportional. It was projected that no improvement would occur for subbase thicknesses greater than 300 mm (12 in.) (Penner, et al., 1985).

The excess subgrade porewater pressure generated under cyclic traffic loads results in a pressure gradient between the subbase and subgrade. Geosynthetics intercept water flowing to the subbase and redirect it to pavement edge drains where it can be properly discharged, effectively increasing the rate of excess porewater pressure dissipation. Alobaidi and Hoare (1994, 1996) showed that geotextiles with high permeability provided greater rates of dissipation. Zhao and Banks (1997) concluded that

a high compressive strength, high flow rate drainage geocomposite on subgrade can provide a means of escape for water in the pavement system. When placed below subgrade the geocomposite can act as capillary barrier, which helps mitigate frost heaving (Henry, 1996). The performance of drainage geocomposite was previously investigated by MaineDOT (Hayden, et al., 1999). It was concluded that the drainage geocomposite below subgrade could improve the structural characteristics of the road. In addition, the drainage geocomposite helped remove water from the pavement system and was most beneficial in cut sections when located as far below the pavement as possible (Hayden, et al., 1999).

Construction and Instrumentation of Test Sections

Route 9 in the towns of Monmouth, Litchfield, and West Gardiner, Maine, is underlain by very poor subgrade soils. These soils are classified as AASHTO A-2-4, A-4, and A-6 and are highly frost susceptible. Several of the subgrade soil samples taken for this study had standard penetration field blow counts as low as 7 and natural water contents approaching the liquid limit. Historically, Route 9 has been plagued with local bearing capacity failures resulting in substantial pavement cracking. The low shear strengths of the subgrade soils combined with the inadequacy of the existing drainage made this a suitable site for testing geosynthetics for reinforcement and drainage applications.

Two portions of Route 9 were used to study the performance of Tensar BX1200 geogrid and Tenax Tendrain 100-2 drainage geocomposite. A total of twelve test sections were constructed. Test sections 1 through 5 were constructed with a 300 mm (12 in.) subbase whereas test sections 6 through 10 were constructed with a 600 mm (24 in.) subbase. This allowed the effects of reducing subbase thickness to be evaluated. Test sections 11 and 12 used 75 to 150 mm (3 to 6 in.) of pavement grindings as the subbase. These are referred to as reclaimed sections. All of the test sections were surfaced with approximately 150 mm (6 in.) of bituminous pavement.

Four types of test sections were constructed: reinforcement, drainage, drainage with reinforcement, and control. The sections with 300 mm (12 in.) and 600 mm (24 in.) of subbase had all four types of sections, where as the claimed sections had only drainage and control sections as shown in the figure on the following page. Test sections using reinforcement geogrid have strain gages attached to the geogrid to measure induced forces. Some of the reinforcement sections have geogrid on subgrade whereas some have geogrid in the center of the subbase to evaluate the effects of geogrid location within the pavement structure. Drainage sections were constructed with drainage geocomposite on subgrade and have vibrating wire piezometers to monitor porewater pressure in the subgrade and subbase course. The drainage sections use a 100-mm (4-in.) diameter underdrain pipe to collect water from the drainage geocomposite. The outlet of each collector pipe is equipped with a flow meter to measure the amount of water coming from the drainage geocomposite. Each of the test sections has a thermocouple string that is used to measure frost penetration.

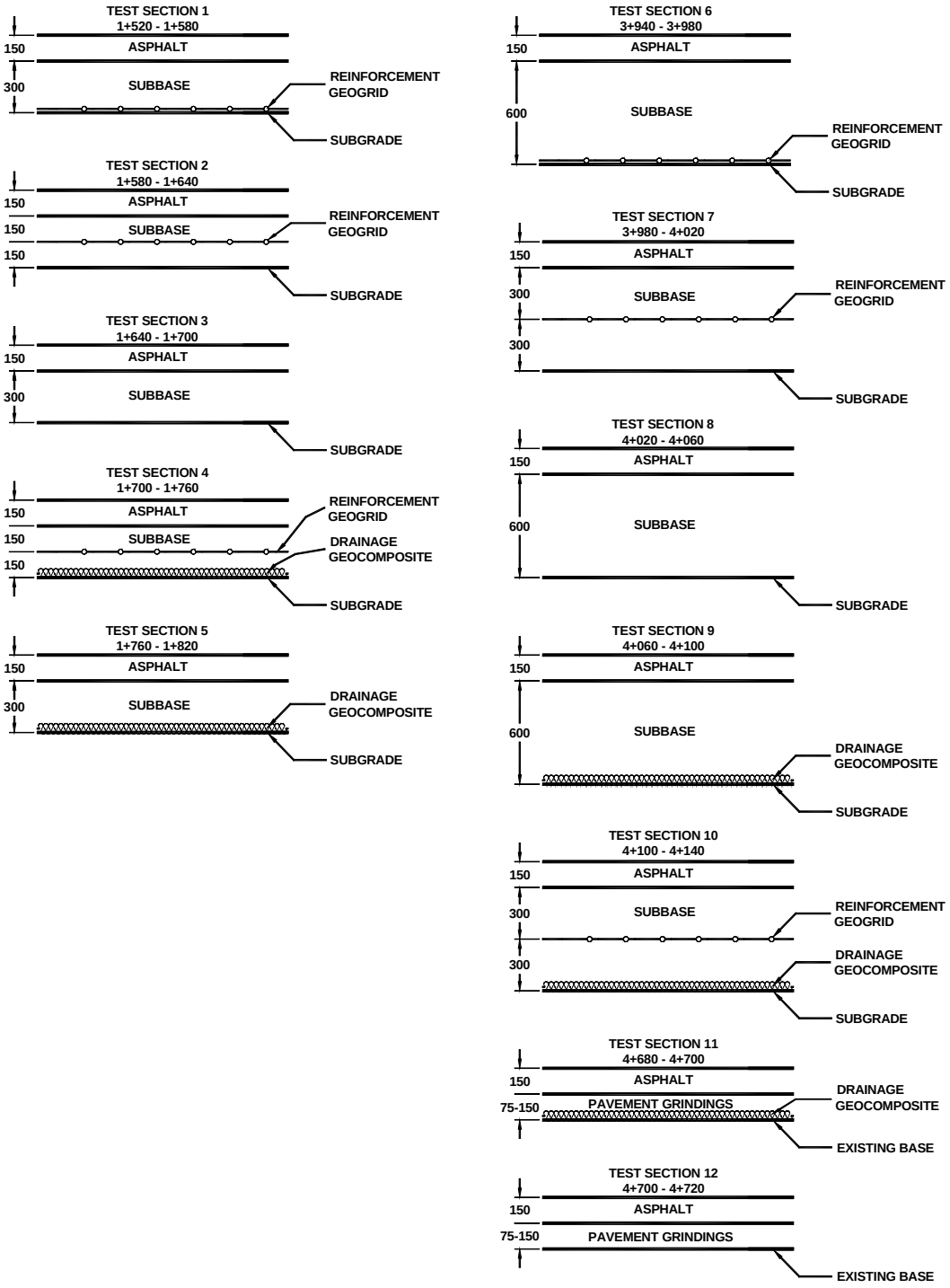

*All dimensions shown are in millimeters

Test section layout

Force in Geogrid

Each instrumented geogrid rib has a pair of strain gages. The data from each pair is averaged to remove the effects of bending from the results. The survival rate of strain gage pairs was 93% at the end of construction but this had decreased to 35% by May 2005. Failure was defined as malfunction of one strain gage in a pair. A technique was developed to obtain useable data for the situation where only one gage in a pair was still working.

Average geogrid forces were examined after compaction, immediately after paving, and at 12, 24, 35, and 45 months after paving. Readings immediately before and after paving were essentially the same. Average forces are summarized in the following table.

300 mm Subbase –Average Force in Geogrid kN/m (lb/ft)							
Test Section	Geogrid Placement	After Subbase Compaction	After Paving	At 12 Months	At 24 Months	At 35 Months	After 45 Months
Section 1	Geogrid on subgrade	0.53 (36)	1.62 (111)	2.19 (150)	2.78 (191)	2.90 (199)	NA
Sections 2 & 4	Geogrid in center of subbase	0.81 (55)	1.27 (87)	1.56 (107)	1.93 (132)	1.95 (134)	NA
600 mm Subbase – Actual Force in Geogrid kN/m (lb/ft)							
Section 6	Geogrid on subgrade	1.08 (74)	1.81 (124)	1.54 (106)	1.41 (97)	1.24 (85)	1.30 (89)
Sections 7 & 10	Geogrid in center of subbase	0.37 (25)	1.06 (72)	1.09 (75)	1.38 (95)	1.67 (114)	1.41 (97)

NA = Not Applicable – only 35 months of data available from installation through end of monitoring.

Placement and compaction of the overlying subbase course developed between 18% and 83% of the force measured at the end of monitoring, in May, 2005. This had increased to 65% to 139% of the May, 2005 force by the time the sections were paved. Thus, placement and compaction of the overlying subbase course, and the action of traffic and concomitant passage of time prior to paving, are both important to mobilization of the force in the geogrid. The average geogrid strain was between 0.5% and 0.7% for sections with 300 mm (12 in.) base and 0.3% to 0.4% for sections with 600 mm (24 in.) base. Perkins (1999) concluded that geogrid strains between 0.5 and 2.0% were adequate to mobilize the reinforcement and improve pavement performance. Thus, the sections with 300 mm (12 in.) base were at the lower bound of the range where

improvement would be expected and the sections with 600 mm (24 in.) base were below this range.

The geogrid forces in ribs oriented perpendicular to centerline were analyzed statistically to evaluate the effects of elapsed time, subbase thickness, and geogrid location in the pavement system on the force in the geogrid. The force in the geogrid located on subgrade and in the middle of the subbase was statistically equal for 300-mm (12 in.) subbase sections immediately after subbase compaction and after paving. However, for 12, 24, and 35 months after paving, geogrid located on the subgrade produced a statistically higher force than when located in the subbase. In the 600-mm (24-in.) subbase sections, the opposite trends occurred. Up to 12 months after paving geogrid located on subgrade produced a statistically higher force, but for 24 months to the end of the project monitoring period the forces were statistically equal. Taken in total, these results suggest that geogrid located on subgrade develops a force that is equal to or greater than when the geogrid is located within the subbase for both subbase thicknesses in this study.

The force in the geogrid immediately after paving in 300-mm (12 in.) subbase sections was statistically equal to that in the 600-mm (24 in.) subbase sections for both geogrid on subgrade and in the subbase. However, after 12, 24, and 35 months, the force in the geogrid in the 300-mm (12 in.) subbase sections was statistically greater that in the 600-mm (24 in.) subbase sections for geogrid on subgrade. The same was true for geogrid located in the subbase for 12 and 24 months after paving. This suggests that pavements with thinner pavement sections develop greater forces over time than thicker pavement sections.

The analysis indicated that the average force in the geogrid on subgrade and in the subbase in the 300-mm (12 in.) subbase sections increased between subbase compaction and paving, paving to 12 months, and 12 to 24 months after installation. However, the forces in the subgrade geogrid sections decreased or remained the same from 24 to 35 months, unlike the subbase geogrid sections which continued to increase. This suggests that reinforcement mechanisms continue to develop after paving in the sections with of 300 mm (12 in.) subbase. The geogrid on subgrade and in the subbase in the 600-mm (24 in.) subbase sections exhibited increases in force between subbase compaction and paving. However, these forces either decreased, or failed to exhibit appreciable increases from paving to 45 months. This indicates that reinforcement mechanisms did not continue to develop after paving in sections with 600-mm (24-in.) subbase sections.

The force in the geogrid parallel to centerline was also measured. Immediately after paving these forces were similar to that perpendicular to centerline for both the 300-mm (12-in.) and 600-mm (24-in.) subbase sections. At the end of the monitoring period (May, 2005) they were also similar for the 600-mm (24-in.) subbase sections. However, for the 300-mm (12-in.) subbase sections the forces perpendicular to centerline in May 2005 were higher than parallel to centerline.

Laboratory tests showed that the geogrid may experience creep, as reflected by increases in strain, when subjected to a constant load similar to those measured in the field. Considering that in this study the force per unit width in the geogrid was obtained from the change in strain in the instrumented ribs, strain due to creep would be

interpreted as an increase in force per unit width. Strain rates measured in the lab and long-term strain rates measured in the field were similar. Thus, the increases in force per unit width with time reported in this study could be due to creep rather than an actual increase in force carried by the geogrid.

Piezometer Measurements

Vibrating wire piezometers were used to measure porewater pressure in the subbase course and subgrade soils. Previous work showed that these types of piezometers indicate negative porewater pressures when the degree of saturation drops below about 50%. Low saturation indicates that the section is well drained.

Results from subbase piezometers showed that the sections with drainage geocomposite exhibited long periods of negative porewater pressure unlike the control sections, which exhibited mostly positive porewater pressures. This suggests that the drainage geocomposite assists with the removal of water from the subbase.

The subgrade piezometers also exhibit negative porewater pressures indicating significant periods of partial saturation. However, for the subgrade piezometers, there is no clear difference in behavior between sections with and without drainage geocomposite. This suggests that the drainage geocomposite had little effect on subgrade porewater pressures.

The subbase and subgrade piezometers in the reclaimed control section with no drainage geocomposite had lower porewater pressure than those in the reclaimed section with drainage geocomposite. This suggests that the drainage geocomposite's ability to remove water from the subbase and subgrade may be inhibited in sections utilizing reclaim construction techniques.

Geocomposite Collector Pipe Flow Measurements

The flowmeters used to measure the quantity of water discharging from the geocomposite collector pipes proved to be unreliable and were easily clogged by iron that precipitated from the water. Thus, reliable data was obtained only for the spring of 2003. The majority of the collector pipes experienced their maximum flow at the onset of the spring thaw between 3/27/03 and 4/3/03. Flow events following the spring thaw appear to correspond with rainfall events. In test sections 4, 9, and 10 the peak flow observations coincide with negative porewater pressure in the subbase. This indicates that water was being removed from the pavement system by the drainage geocomposite.

Frost Depth Measurements

Thermocouples were used to monitoring the depth of frost penetration. Minimum frost penetration over the monitoring period occurred during the winter of 2004-05 in test section 12, with a depth of 450 mm (18 in.). Maximum frost penetration over the monitoring period occurred during the winter of 2003-04 in test section 6, with a depth of 1720 mm (68 in.). The data obtained from the other instrumentation was evaluated in the context of the extent of frost penetration.

Effective Structural Number Measurements

The results from falling weight deflectometer tests performed on eight days in spring and early summer of 2004 were used to backcalculate the effective structural number for each of the test sections. Results are summarized in the following figures.

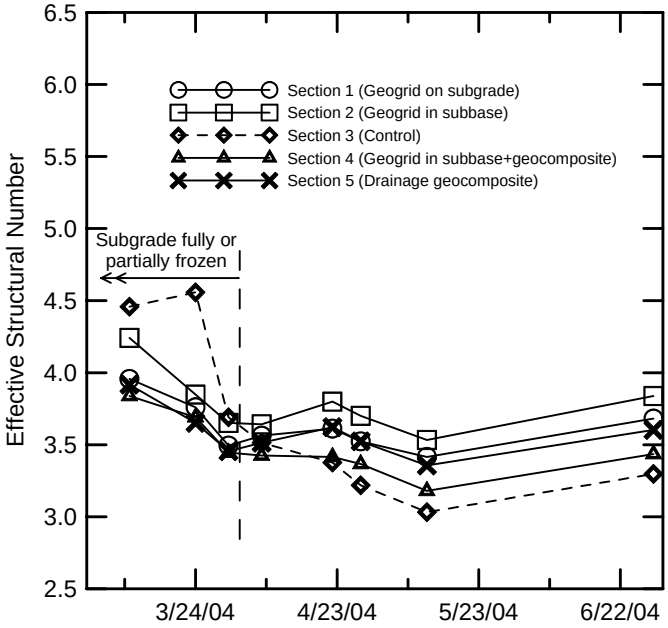

Effective structural number for sections with 300 mm (12 in.) subbase aggregate.

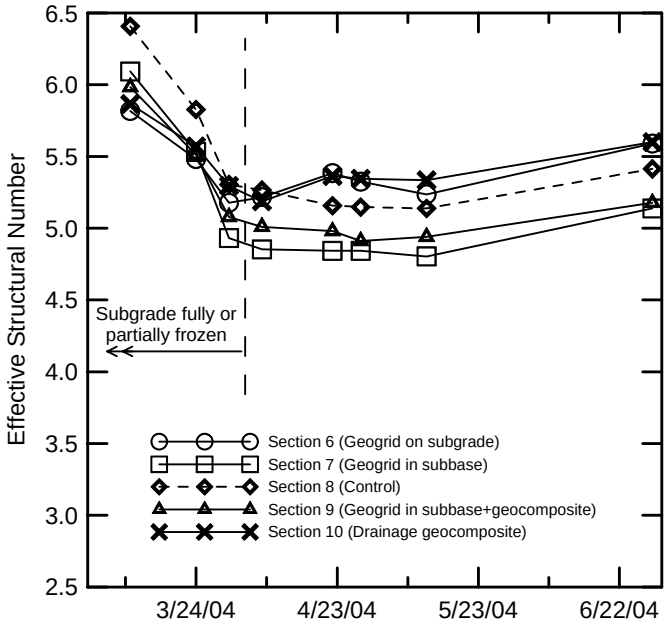

Effective structural number for sections with 600 mm (24 in.) subbase aggregate.

The results show that reinforcement geogrid and drainage geocomposite increased the effective structural number by between 5% and 17% for sections with 300 mm (12 in.) of subbase aggregate. However, they had no apparent effect for sections with 600 mm (24 in.) of subbase aggregate. The reclaim section without drainage geocomposite had about the same structural number as the reclaim section with drainage geocomposite. Comparing control sections with 300 mm (12 in.) and 600 mm (24 in.) of subbase aggregate showed that doubling the subbase thickness increased the effective structural number by 70%. The results suggest that the increase in backcalculated effective structural number that was produced by geogrid and/or drainage geocomposite in the 300-mm (12-in.) subbase sections could also be obtained by adding between 25 mm (1 in.) and 75 mm (3 in.) of subbase aggregate to an unreinforced section.

The results of this study are in general agreement with previous work which indicates that little improvement from geosynthetics reinforcement is expected in flexible pavement systems designed to carry more than 200,000 equivalent 80-kN (18-kip) single axle loads or constructed with subbases thicker than 300 mm (12 in.).

(BLANK PAGE)

CHAPTER 1
INTRODUCTION

1.1. Background

Route 9 in the towns of Monmouth, Litchfield, and West Gardiner is underlain by areas of very poor subgrade soils. These soils are classified as AASHTO A-2-4, A-4, and A-6 and are highly frost susceptible. Several of the subgrade soil samples taken for the proposed reconstruction of Route 9 had standard penetration field blow counts as low as 7 and natural water contents approaching the liquid limit. Historically, Route 9 has been plagued with local bearing capacity failures resulting in substantial pavement cracking. The low shear strengths of the subgrade soils combined with the inadequacy of the existing drainage made this a suitable site for testing geosynthetics for reinforcement and drainage applications.

Geosynthetics have been in use since the mid-1970's. Early research focused on applications in temporary haul roads and unpaved roads. Their beneficial reinforcing effects in unsurfaced roads has since been studied and proven. The use of geosynthetics in roadway construction has increased significantly over the past few decades. Recent studies have examined both their reinforcing and drainage capabilities in permanent roads surfaced with flexible pavements. However, few have investigated their use in pavement structures with subbase and pavement layers as thick as those used in Maine.

Although New England state transportation agencies have been using geosynthetics since the 1980's, there has been only one previous research project using geosynthetics for reinforcement and drainage purposes. Fetten and Humphrey (1998)

explored the effects of geogrid, separation geotextile, and drainage geocomposite in a flexible pavement system on Route 1A in the towns of Frankfort and Winterport (project no. F-STP-026(109)).

In the current study, federal aid project no. STP-8471(00)X was used to evaluate the use of geosynthetics in Maine on two sections of Route 9 in the towns of Monmouth, Litchfield, and West Gardiner. Force in the geogrid, porewater pressure in the subbase and subgrade in the drainage sections, and discharge from drainage section collector pipes was measured. The results were compared with those from the Frankfort-Winterport project and previous studies from other states to evaluate the performance of the geosynthetics.

Geosynthetics have proven beneficial in temporary haul roads and unpaved roads. Beneath wheel loads, the roadway behaves much like a simply supported beam under a uniform load. The upper portion develops compression while the lower portion develops tension. Subbase aggregate has compressive strength but lacks tensile strength. In contrast, geosynthetics have tensile strength but lack compressive strength. As wheel ruts develop, the resulting movement of subbase particles allows for shear interaction with the geosynthetic. The tensile loads developed at the bottom of the subbase are transmitted to the geosynthetic, effectively providing the subbase with tensile strength. (Bender and Barenberg, 1978). Some authors believe that geogrid is superior to geotextile for lateral base course restraint due to the interlock between the geogrid and subbase aggregate (Haas, et al., 1985; Barksdale et al. 1989).

Several full-scale laboratory experiments have been performed to investigate the improvement mechanisms of geosynthetics beneath flexible pavements. Studies by

Kennepohl, et al. (1985), Penner, et al. (1985), Haas, et al. (1988), Barksdale, et al. (1989), Al-Qadi, et al. (1994), Cancelli, et al. (1996), Perkins, et al. (1996), and Montanelli, et al. (1997), showed some benefits of geosynthetic reinforcement beneath flexible pavements. However, the amount of wheel rutting required for the development of the reinforcement mechanisms may not occur when thick subbase and pavement sections such as those in Maine are used. The behavior of geosynthetics under these conditions requires further examination.

Placing a high compressive strength, high flow rate drainage geocomposite on subgrade can provide a means of escape for water in the pavement system (Zhao and Banks, 1997). When placed below subgrade the geocomposite can act as capillary barrier, which helps mitigate frost heaving (Henry, 1996). The performance of drainage geocomposite was previously investigated by Maine DOT in the towns of Frankfort and Winterport (Fetten and Humphrey, 1998). The present study continues to investigate the performance of drainage geocomposite at the subgrade-subbase interface for the type of field conditions encountered in Maine.

The purpose of this study is to provide a rational means of determining whether geosynthetic reinforcement and drainage geocomposite layers improve the performance of flexible highway pavements constructed over weak subgrades. Instruments installed in sections built with geogrid and drainage geocomposite will measure force in the geogrid and porewater pressure in the subbase and subgrade. These values will be compared to results from previous studies to evaluate the performance of the geogrid and drainage geocomposite.

1.2. Scope of Study

Two portions of Route 9 were used to study the performance of two different geosynthetics. A total of twelve test sections were constructed. These included reinforcement sections, drainage sections, and control sections. The test sections were instrumented to monitor the behavior of the geosynthetics. Strain gages were attached to the geogrid, piezometers measured porewater pressure, flow meters measured the amount of water removed from the pavement structure, and thermocouples measured the frost penetration in the test sections.

Although previous studies have investigated the performance of geosynthetics as reinforcement in flexible pavement systems, only Humphrey and Fetten (1998) investigated their performance with thick subbase and pavement layers. This project evaluated the reinforcement and drainage properties of geosynthetics in road sections up to 750 mm (30 in.) thick. The strain gages attached to the geogrid measured the force induced in the material. The piezometers measured porewater pressure to identify periods of saturation within the pavement structure. The results of this study will allow DOT's to decide if geosynthetics can provide a cost-effective means of performance improvement for thick flexible pavement systems.

1.3. Organization of Report

This report contains six chapters and one appendix. Chapter 2 is a literature review canvassing laboratory and field studies of geosynthetics in unsurfaced and paved roads, computer modeling and analysis of performance and potential benefits, and design methods for unsurfaced roads and flexible pavement systems.

Chapter 3 is a project description detailing the layout and construction procedures in each test section as well as the material properties of the subbase, subgrade and geosynthetics.

Chapter 4 discusses the procedures for the installation and field measurement of the strain gages attached to the geogrid, piezometers in the subbase and subgrade, flow meters, and thermocouples. The calibration procedure for the strain gages is also described.

Chapter 5 gives the results of the strain gage, piezometer, flow meter, and thermocouple, and falling weight deflectometer (FWD) measurements. The behavior of the test sections is compared using statistical tests.

Chapter 6 summarizes the findings and conclusions of the study. In addition, recommendations for future research are provided. The appendixes contain strain gage calibration and testing data, and FWD results.

(BLANK PAGE)

CHAPTER 2
LITERATURE REVIEW

2.1. Introduction

Geosynthetics have been in general use since the mid-1970's. Evaluation of geotextiles began first, as geogrids did not become readily available until the mid-1980's. During their infancy, transportation applications of geosynthetics were targeted primarily for temporary haul roads and unpaved roads. Since that time their beneficial reinforcing effects in unsurfaced roads has been studied and proven. The use of geosynthetics has increased significantly over the past few decades. Recently, studies have been performed to examine both their reinforcing and drainage capabilities in permanent roads surfaced with flexible pavements. This chapter focuses on previous research done on geosynthetics for subbase reinforcement and drainage.

Geosynthetics is a general term that includes geogrids, geotextiles, and geocomposites. The four major functions of geosynthetics in roads are reinforcement, separation of subbase and subgrade, filtration of suspended subgrade particles to prevent their being washed into the subbase, and drainage. The effectiveness of these improvement functions depends on the subgrade and roadway section properties, including the location of the geosynthetics within the section, aggregate size, subbase and pavement thickness, and stiffness of the geosynthetics.

Although many studies have been performed to examine the effectiveness of geosynthetics in unsurfaced roads, only a limited number have focused on reinforcement of permanent roads using flexible pavements. A few laboratory investigations as well as full-scale field tests have been performed to evaluate performance of geosynthetic

reinforcement with various roadway section properties. Subbase and subgrade drainage capabilities have also been examined. Computer modeling has been used to demonstrate possible effects of geosynthetic reinforcement on flexible pavement structures.

2.2. Performance Improvement Functions

Geosynthetics can improve roadway performance through the functions of reinforcement and separation (McGown and Ozelton, 1972; Barenberg, 1975) as well as filtration and drainage (Snaith and Bell, 1978; Bell, et al., 1982; Alobaidi and Hoare, 1994, 1996; Perkins and Brandon, 1998). Several researchers have examined these functions and their findings are described in the following sections.

2.2.1. Reinforcement

Geosynthetics can provide reinforcement to the roadway by carrying a portion of the loads from construction traffic as well as daily operating traffic. The two major reinforcement modes are lateral base course restraint and the tensioned membrane effect (Steward, et al., 1977; Bender and Barenberg, 1978). Typically these modes work together with other improvement functions to benefit roadway performance.

2.2.1.1. Lateral Subbase Restraint. As traffic loads are applied the subbase behaves much like a simply supported beam under a uniform load. The upper portion experiences compression and tension is developed at the bottom. As subbase aggregate has no inherent tensile strength, tensile strains are developed at the bottom the subbase. In unreinforced roads this causes lateral spreading of the subbase which results in vertical

strains and the development of wheel ruts. However, in reinforced roads movement of the subbase particles allows for shear interaction with the geosynthetic. The tensile load is effectively transmitted to the geosynthetic and further lateral spreading of the subbase is reduced. This reduces vertical strains and development of wheel ruts (Bender and Barenberg, 1978). Some authors believe that geogrid is superior to geotextile for lateral subbase restraint due to the interlock between the geogrid and subbase aggregate (Haas, et al., 1985; Barksdale et al. 1989).

Confinement of the subbase increases the normal stress in the aggregate particles, making the subbase stiffer. This apparent increase in elastic modulus results in reduced vertical strains in the subbase, which also limits further development of wheel ruts. In addition, increasing the elastic modulus of the subbase could reduce fatigue in the pavement by decreasing the magnitude of dynamic surface deformations (Kinney and Barenberg, 1982).

The increased stiffness of the subbase could also improve its ability to distribute traffic loads over the subgrade, helping to reduce the vertical stress in the subgrade beneath the wheel path. In addition, the shear interaction between the subbase and the geosynthetic results in less shear stress being transferred to the subgrade. The reduced state of stress in the subgrade could lead to less subgrade deformation (Kinney and Barenberg, 1982).

2.2.1.2. Tensioned Membrane Effect. As wheel loads are applied, the subgrade deforms downward directly beneath the wheel path. The shear failure of the subgrade causes an upward deformation to the right and left of the wheel path. This gives the geosynthetic at the interface of the subbase and subgrade the deformed shape shown in Figure 2.1. Under the wheel path the tensile forces in the deformed geosynthetic provide an upward resultant force that reduces the vertical stress applied to the subgrade. In addition, just outside the wheel path the tensile forces in the geosynthetic provide a downward resultant force that helps to confine the subgrade and increase its bearing capacity (Bender and Barenberg, 1978).

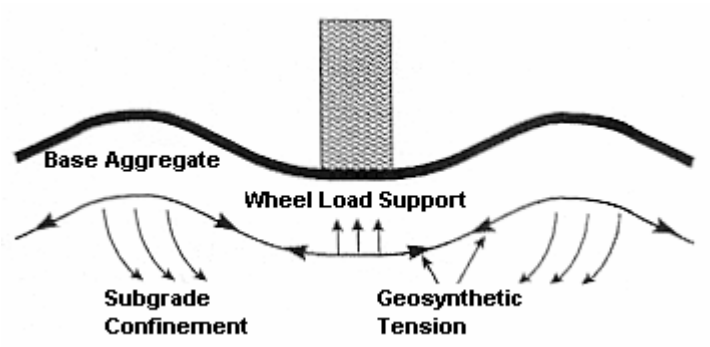

Figure 2.1 Tensioned membrane effect (Bender and Barenberg, 1978).

The tensioned membrane effect was also shown by Barksdale, et al. (1989) to increase the subgrade bearing capacity. Decreases in surficial rutting and more uniform rutting patterns in unsurfaced roads were observed by several authors (Bathurst and Raymond, 1987; Montanelli, et al., 1997).

2.2.2. Separation

It is possible for subbase aggregate to become contaminated with soft subgrade material. This can happen during construction or during the service life of the road. Subgrade material can be squeezed up into the subbase or aggregate particles can be pushed down into the subgrade. Contamination of the subbase with subgrade material reduces its strength, stiffness, and drainage capabilities. Geosynthetic separators themselves provide no structural support to the roadway. Rather, they prevent mixing of subbase and subgrade materials, preserving the strength and drainage characteristics of the roadway section (Brorsson and Eriksson, 1986; Richardson and Behr, 1990).

2.2.3. Filtration

Repetitive traffic loads can generate excess porewater pressure in the subgrade. This promotes flow of water to the subbase. Particles suspended in the porewater are filtered by the geosynthetic, preventing the subbase from becoming contaminated with fines. Henry (1996) examined the use of geotextiles as a capillary barrier, and concluded it is unlikely geotextiles act as a capillary barrier for long-term field conditions.

Snaith and Bell (1978) showed that the amount of fines passing into the subbase was dependent on the type of geotextile used. In a later study Bell, et al. (1982) found that opening size affected material passing through the geotextile. Larger opening sizes resulted in a greater degree of subbase contamination. Stress concentrations in the geotextile may promote further contamination. Hoare (1982) observed high degrees of contamination at points where large stones were in contact with the geosynthetic. Glynn and Cochrane (1987) found that depressions in the geotextile caused by subbase

aggregate particles allowed porewater to pond and form a slurry that could then be pumped into the subbase.

2.2.4. Drainage

The excess subgrade porewater pressure generated under cyclic traffic loads results in a pressure gradient between the subbase and subgrade. Geosynthetics intercept water flowing to the subbase and redirect it to pavement edge drains where it can be properly discharged, effectively increasing the rate of excess porewater pressure dissipation. Alobaidi and Hoare (1994, 1996) showed that geotextiles with high permeability provided greater rates of dissipation. However, increased rates of porewater pressure dissipation may come at the expense of filtration performance. It was found that higher dissipation rates corresponded to higher degrees of subbase contamination (Alobaidi and Hoare, 1994, 1996; Perkins and Brandon, 1998).

2.3. Laboratory Studies of Unpaved Roads

A laboratory study by the University of Illinois (Bender and Barenberg, 1978) indicated that unpaved roadway sections constructed using geotextile at the interface of the subgrade and subbase could withstand larger traffic volumes than sections constructed using no geosynthetics. The test used a strip footing and a circular plate to which static and cyclic loads were applied. The reinforced sections showed less rutting under simulated traffic loads (Bender and Barenberg, 1978). The authors attribute the improved performance of the sections constructed using geotextile to increased distribution of traffic loads over the subgrade, reduced mixing of the subbase and

subgrade particles, and limitation of free-flow of water from the subgrade into the subbase (Bender and Barenberg, 1978).

Lai and Robnett (1982) showed that vertical subgrade stresses decreased under a simulated wheel load when geotextile was installed at the interface of the subbase and subgrade. The laboratory testing apparatus used a 762-mm (30-in.) thick subgrade (CBR = 0.9) overlain by 381 mm (15 in.) of subbase aggregate. Pressure cells in the subgrade measured vertical stress at various depths beneath the centerline of the simulated wheel load and at radial distances between 304 and 457 mm (12 and 18 in.) from the wheel load centerline. The presence of geotextile reduced compressive stresses in the subgrade as much as 33 kPa (4.8 psi). The authors attributed the vertical stress reduction to increased load distribution capability of the confined aggregate and the tensioned membrane effect. Results from this study are summarized in Table 2.1.

Table 2.1 Subgrade stresses measured in laboratory test (Lai and Robnett, 1982).

All Pressure Cells Located in Subgrade		**Stress Normal to Pressure Cell – kPa (psi)**		
Depth From Surface (in.)	**Offset From Load Centerline (in.)**	**Reinforced with Typar 3401**	**No Reinforcement**	**Subgrade Stress Reduction (%)**
16	0	82.7 (12.0)	106.8 (15.5)	22
20	0	75.8 (11.0)	106.8 (15.5)	29
30	0	--	--	--
42	0	37.9 (5.5)	44.8 (6.5)	15
20	6	56.5 (8.2)	89.6 (13.0)	36.9
20	12	48.2 (7.0)	51.7 (7.5)	6.6
20	18	11.0 (1.6)	5.5 (0.8)	-50
16	18	23.4 (3.4)*	34.4 (5.0)*	32*
32	30	23.4 (3.4)*	23.4 (3.4)*	0*

*Radial stress; all other stresses are vertical

Leng and Gabr (2002) investigated the behavior of geogrid-reinforced aggregates over a soft subgrade. A cyclic load of 550 kPa (80 psi) was applied to aggregate subbase thicknesses of 152 mm (6 in.) and 254 mm (10 in.) using a 305-mm (12 in.) diameter loading plate attached to a hydraulic actuator. The subgrade material had a CBR of 3 and ranged in thickness from 75 to 90 mm (3.0 to 3.5 in.). Two biaxial geogrids, designated BX1 and BX2, were installed at the interface of the subbase and subgrade. The manufacturer of the geogrid was not specified. In general, the presence of geogrid reduced surface deformations, improved stress distribution to the subgrade, and inhibited degradation of the subbase (Leng and Gabr, 2002). The higher modulus BX2 geogrid performed better overall, showing less plastic surface deformation than in tests performed using geogrid BX1. The authors believe that the primary improvement mechanisms were lateral base course restraint due to aggregate interlock with the geogrid, and the tensioned membrane effect (Leng and Gabr, 2002).

Das (2000) performed rigid strip loading tests on granular material underlain by subgrade with undrained shear strength (determined with a laboratory vane) of 14 kN/m^2 (290 psf). The section was reinforced with geogrid at the interface of the two materials. Theoretical bearing capacities were calculated using procedures developed by Meyerhof and Hanna (1978). The geogrid provided an increase in ultimate bearing capacity compared to theoretical values when the ratio of the thickness of the aggregate layer to the width of the loaded area was 4/3, with the maximum increase occurring at a ratio of 2/3. These ratios could be applied to reinforcement of unpaved roads in terms of tire width and subbase thickness. According to these results, the subgrade bearing capacity would see the largest increase under a 203 mm (8 in.) wheel load if the thickness of the

reinforced subbase were 305 mm (12 in.). The minimum width of the geogrid layer for bearing capacity improvement was six times the width of the loaded area (Das, 2000).

Geosynthetic reinforcement of unpaved roads has been well studied since the mid-1970's and it is clear that both geotextiles and geogrids can provide performance improvement. The subgrade confinement and tensioned membrane subgrade improvement mechanisms originally investigated by Bender and Barenberg (1978) have also been shown to increase performance by Lai and Robnett (1982) and Leng and Gabr (2002).

2.4. Research of Geosynthetics in Paved Roads

2.4.1. Laboratory Studies

Several full-scale laboratory experiments have been performed to investigate the improvement mechanisms of geosynthetics beneath flexible pavements. Studies by Kennepohl, et al. (1985), Penner, et al. (1985), Haas, et al. (1988), Barksdale, et al. (1989), Al-Qadi, et al. (1994), Cancelli, et al. (1996), Perkins, et al. (1996), and Montanelli, et al. (1997), showed some benefits of geosynthetic reinforcement beneath flexible pavements. However, a study by Ruddock, et al. (1982) showed geotextile reinforcement over soft subgrade provided no structural improvement.

2.4.1.1. Ruddock, Potter, and McAvoy. Ruddock, et al. (1982) performed full-scale laboratory experiments and showed that a woven multi-filament polyester geotextile provided no structural improvement. A subgrade with CBR = 0.7 was overlain by the geotextile, 300 mm (12 in.) of crushed granite subbase, and 160 mm (6.3 in.) of

bituminous pavement. The system was loaded with a two-axle truck for 4600 repetitions and an additional 7700 repetitions with the axle load increased to 133 kN (30 kips). Measurements of surface deformation, dynamic stress and strain in the subgrade, permanent strain in the geotextile, and dynamic tensile strain at the base of the bituminous layer indicated no difference in structural performance between the reinforced and control sections (Ruddock, et al., 1982).

2.4.1.2. Barksdale, Brown, and Chan. Barksdale, et al. (1989) investigated geogrid reinforcement using full-scale pavement tests on sections constructed with a subbase thickness of 150 or 200 mm (6 or 8 in.) overlain by asphaltic pavement ranging in thickness from 25 to 38 mm (1.0 to 1.5 in.). Test tracks were used to simulate moving a wheel. In addition to the laboratory tests, an analytical study was performed using a linear elastic finite element model with cross-anisotropic subbase aggregate. The authors indicated that the effects of geogrid on stress, strain, and deflection were small for pavements designed to carry more than 200,000 equivalent 80-kN (18-kip) single axle loads. Moreover, they expected no improvement from geosynthetic reinforcement for pavement thicknesses greater than 65 to 90 mm (2.5 to 3.5 in.), even when the subbase aggregate is placed on soft subgrade. It was concluded that relatively little improvement is likely with structural numbers greater than 2.5 to 3.0 (Barksdale, et al., 1989).

2.4.1.3. University of Waterloo. Experiments conducted at the University of Waterloo by Penner, et al. (1985) used six test series each with four test sections to evaluate the effects of pavement thickness, subbase thickness, geosynthetic location in the subbase, and subgrade CBR.

The subgrade in series 1 through 3 was very fine graded beach sand (99% passing the #40 sieve, 32% passing the #100 sieve, 4% passing the #200 sieve). Series 4 through 6 used the same material mixed with peat to obtain a subgrade CBR of 1. Well graded subbase aggregate and hot mix asphalt was used in all test series. The asphalt thickness was 75 mm (3 in.) in all series except series 1 where 100 mm (4 in.) was used. The geogrid was Tensar SS1, a biaxial polypropylene material. A 40-kN (9-kip) load was applied to a 305-mm (12-in.) diameter plate at a frequency of 8 Hz to simulate cyclic traffic loads in each series.

Results from series 1, which used a 200 mm (8 in.) subbase, showed that geogrid placed on subgrade (CBR = 8) showed improved performance in comparison to control sections with no reinforcement. Sections with geogrid at the top of the subbase and unreinforced sections began deteriorating quickly after 10,000 cycles. However, sections with geogrid on subgrade or in the center of the 200 mm (8 in.) subbase did not show significant pavement deterioration until after more than 100,000 cycles.

Results from series 2 where subbase thickness ranged from 100 to 200 mm (6 to 8 in.) the sections reinforced with geogrid on subgrade (CBR = 4) carried three times the load cycles to failure as unreinforced sections. Reinforced sections in series 3 did not perform as well as those in series 1 and 2. The authors attributed this to the decreased subgrade strength (CBR < 4) and the decreased pavement thickness.

Results from series 4 showed that sections with geogrid located within the base course could carry three times the load cycles to failure as control sections with no reinforcement. In addition, reinforced sections using 25% less subbase thickness performed the same as control sections using no reinforcement. Series 5 examined the effects of pretensioning the geogrid, however no beneficial effects were observed.

Series 6 examined multi-layers of geogrid; one section had geogrid in the center of the subbase and also on subgrade. This test section carried the greatest number of load cycles and did not reach failure until 15,000 cycles. This was a 275% improvement over the control section.

In a later study at the University of Waterloo Haas, et al. (1988) indicated that geogrid could provide improvement in low-deformation systems if located properly. He suggested that the most effective location was the zone of tensile stress upon the first load application, and that the geogrid should remain in this tensile zone for the duration of the roadway's design life. The study concluded that for a subbase thickness of 100 to 203 mm (4 to 8 in.) the optimum position for the geogrid was on subgrade. For subbase thicknesses of 254 to 305 mm (10 to 12 in.) it is more beneficial for the geogrid to be placed at the mid point of the layer. It is noted that the maximum pavement thickness in this study was 38 mm (1.5 in.).

2.4.1.4. Virginia Polytechnic Institute. A secondary road in Virginia was simulated using four laboratory test sections; two sections reinforced with geotextiles, one section reinforced with geogrid, and a control section. The sections were constructed in a 3.1-m by 1.8-m by 2.1-m deep (10-ft by 6-ft by 7-ft deep) concrete pit. The

geotextiles were placed on a 1220 mm (48 in.) subgrade consisting of compacted silty sand and overlain by 150-mm (6 in.) of well graded subbase aggregate and 70 mm (2.75 in.) of hot mix asphalt. A 40-kN (9-kip) cyclic load was applied at a rate of 0.5 Hz until 25 mm (1 in.) of displacement had occurred beneath the 300-mm (12 in.) diameter loading plate. Relationships between the effects of loading cycles on displacement, pavement displacement after 800 cycles, and displacement beneath the center of the loading plate as a function of the number of applied cycles were used to evaluate pavement performance.

The study concluded that reinforced sections performed better than the unreinforced control section, as shown in the displacement profiles after 800 cycles shown in Figure 2.2. The authors concluded that geotextiles and geogrid can offer substantial improvement in pavement performance provided the section is constructed on a subgrade with a low CBR (Al-Qadi, et al., 1994). It is noted that the subbase thickness of 150 mm (6 in.) and pavement thickness of 70 mm (2.75 in.) are significantly smaller than sections typical of New England state highways.

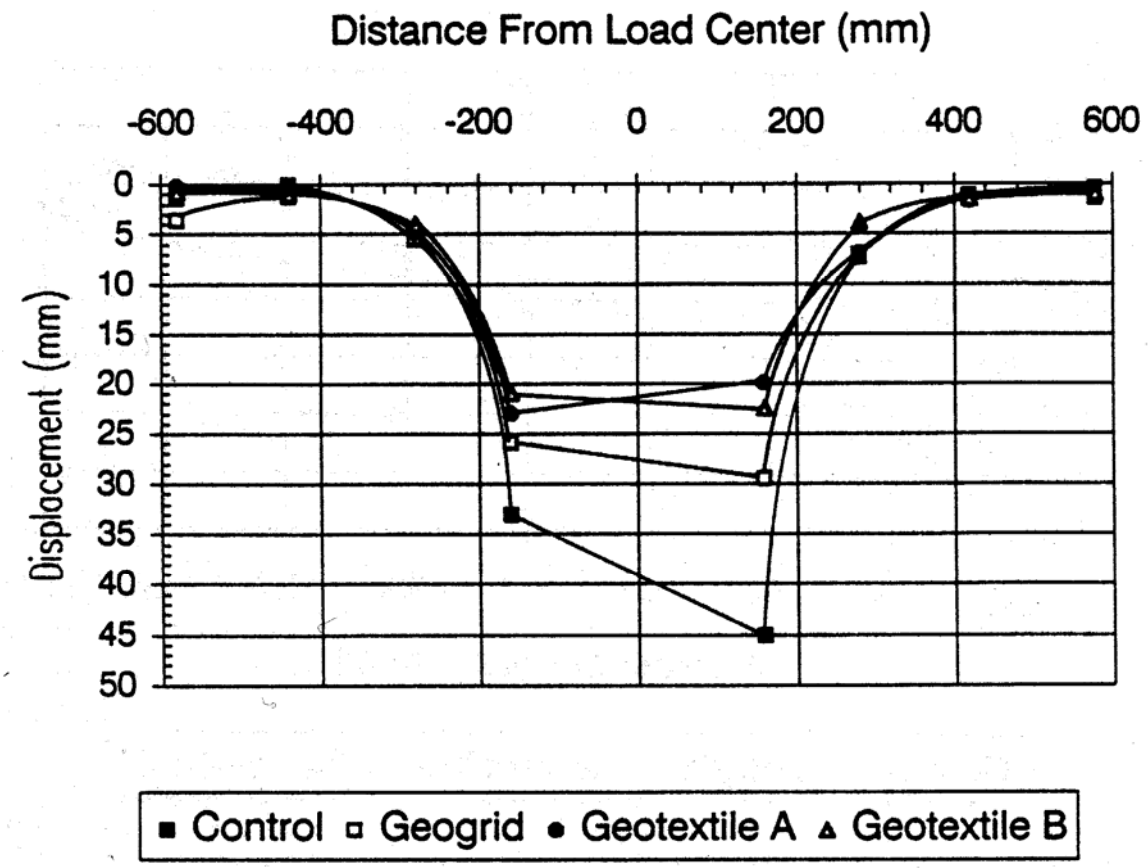

Figure 2.2 Permanent displacement profile at 800 cycles (Al-Qadi, et al., 1994).

2.4.1.5. University of Alaska Fairbanks. Three test sections were constructed in a steel-reinforced plywood box 18.1 m by 2.44 m by 1.22 m deep (60 ft by 8 ft by 4 ft deep). Pea gravel approximately 9 mm (0.35 in.) in diameter was placed in the bottom of the box to simulate a layer of stiff frozen soil 350 mm (1.1 ft) thick (Kinney, et al., 1998). The pea gravel was overlain by subgrade material consisting of a mixture of alluvial sand and silt with a CBR of approximately 1. Two of the sections had geogrid on subgrade, the other was constructed as an unreinforced control. Crushed rock subbase was placed on the subgrade and varied in thickness from 152 to 533 mm (6 to 21 in.) however because of edge effects of the test box, the study focused on subbase thicknesses of 203

to 365 mm (8 to 14 in.). The subbase was surfaced with 61 mm (2.4 in.) of hot mix asphalt. The test facility is shown in Figure 2.3.

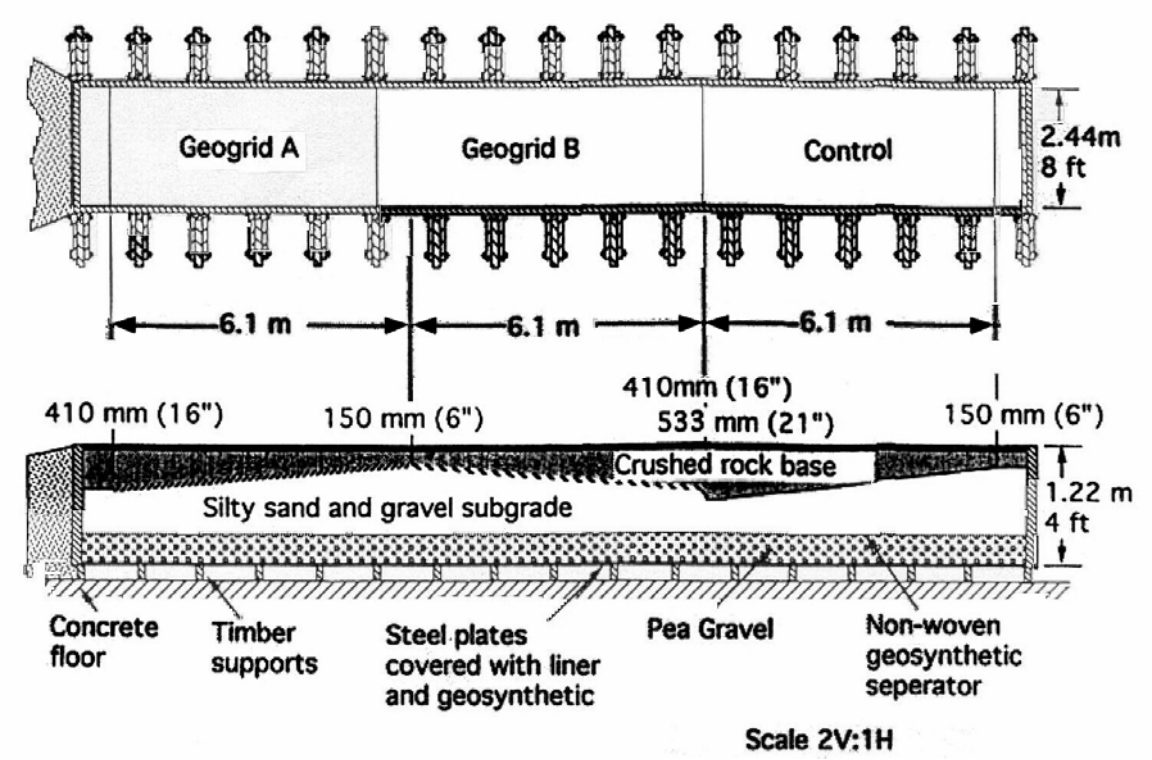

Figure 2.3 Cross section and plan view of University of AK Fairbanks test facility (Kinney, et al., 1998).

Two different geogrids were examined. Geogrid A is extruded polystyrene composite with vertical posts 6.4 mm (0.25 in.) high extending from every other rib. The modulus of geogrid A is 192 kN/m (13,500 lb/ft) in both the machine and cross-machine direction. Geogrid B is an extruded polystyrene product with an open area of 70% and modulus in the machine and cross-machine direction of 270 kN/m (18,500 lb/ft).

Truck loads were simulated using a pneumatically loaded cart. Load cycles in the western lane used a tire pressure of 276 kPa (40 psi) whereas the east lane used a tire pressure of 551 kPa (80 psi). The cart was loaded to 91 kN (2 kip) for each forward pass

and 18.2 kN (0.4 kip) for each reverse pass to simulate the direction of principal stresses during normal trafficking. However, the applied loads were significantly less than actual truck loadings. Deflections after approximately 2,000 cycles were measured and compared with subbase depth for the two reinforced sections and the control section. The performance improvement in terms of decreased rutting was a function of tire pressure, geogrid properties, and subbase thickness. Deformations in the control section were greater than in the reinforced sections for both tires pressures. In general, the higher modulus and open structure of geogrid B showed more improvement than the three dimensional structure of geogrid A, particularly between subbase thicknesses of 200 to 300 mm (8 to 12 in.). Deflections increased with increasing subbase thickness in a nearly linear fashion in the section reinforced with geogrid B. The authors concluded that there is a possibility that the three dimensional nature of geogrid A could keep subbase aggregate from packing tightly between the posts and could create a zone of soft subbase material approximately 6.4 mm (0.25 in.) thick just above the subgrade. This soft zone may limit the shear interaction between geogrid A and the subbase material. The beneficial effects of both geogrids when used with subbase thicknesses in excess of 406 mm (16 in.) were deemed negligible (Kinney, et al., 1998).

2.4.1.6. Montana Department of Transportation. Perkins (1999) studied geosynthetic reinforcement of flexible pavement systems at a laboratory facility in Bozeman, Montana. A concrete test box measuring 2 m (6.5 ft) square and 1.5 m (4.9 ft) deep was filled with 750 mm (2.5 ft) of clayey subgrade with a CBR of 1.5. The subgrade was overlain by 300 mm (1 ft) of aggregate subbase. 75 mm (3 in.) of

pavement was placed on the subbase. Experiments were performed with Tensar BX1200 geogrid at the interface of the subgrade and subbase as well as 100 mm (4 in.) above the interface. Loads were applied with a circular plate 300 mm (1 ft) in diameter attached to a pneumatic actuator (Perkins, 1999).

The geogrid was instrumented with strain gages to monitor its behavior during loading. Rut depths were measured using LVDT's at the pavement surface. A significant reduction in rut development was observed at geogrid strains ranging from 0.5 to 2.0%. It was also concluded that reinforcing mechanisms could be mobilized and performance benefit realized at rut depths as small as 5mm (0.2 in.).

2.4.2. Field Studies of Paved Roads

2.4.2.1. Ontario Field Study. Anderson and Killeavy (1989) studied geogrid reinforcement beneath flexible pavement at a trucking facility in southern Ontario. The road had a 15-year ESAL design of 1.8 million and geosynthetics were used in the design primarily to improve subgrade stability and uniformity. Three test sections were constructed. The control section had 450 mm (18 in.) of limestone subbase surfaced with 105 mm (4 in.) of asphalt. One reinforcement section used Tensar SS1 geogrid on subgrade with a 200-mm (8-in.) subbase and 105 mm (4 in.) of pavement. The other reinforcement section used geotextile on subgrade with 350 mm (14 in.) of limestone subbase and 90 mm (3.5 in.) of pavement. Pavement performance was evaluated by FWD (falling weight deflectometer) results and by observation of surface cracking and deformation. It was determined from FWD deflection basins and elastic layer analysis that the reinforcement had reduced strain in the asphalt and subgrade after approximately

1,100 ESAL's. FWD deflections were normalized to a load of 40 kN (9 kips) for the purpose of comparison between sections as the actual load applied varies with the pavement stiffness. The modulus of the granular layer in each test section was calculated and the results are shown in Table 2.2. The authors concluded that the locked-in stress necessary to effectively increase the modulus of the subbase was achieved after deformations in excess of 25 mm (1 in.) occurred in the subbase and subgrade as a result of high water contents during construction of the test sections (Anderson and Killeavy, 1989).

Table 2.2 Summary of subbase layer moduli backcalculated from FWD results (Anderson and Killeavy, 1989

Test Section	Mean	Standard Deviation	Range
Geogrid Reinforcement 200-mm (8-in.) Subbase	560 (81)	190 (27)	300 to 800 (43 to 116)
Geotextile Reinforcement 350-mm (14-in.) Subbase	400 (58)	120 (17)	280 to 590 (40 to 85)
Control 450-mm (18-in.) Subbase	170 (24)	70 (10)	160 to 270 (23 to 39)

All values are given in Mpa (ksi)

2.4.2.2. Perkins and Lapeyre. Perkins and Lapeyre (1997) instrumented geogrid with Kyowa foil strain gages (KFE-5-120-C1) to determine if the material deformed under traffic loads. The objective of the study was not to generate data for comparison between reinforced and unreinforced sections. Rather, the goal was to gain sufficient experience with instrumentation of geosynthetics to provide adequate instrument survivability, which would in turn allow further study of pavement performance improvements. It was determined that procedures for attaching and protecting the strain gages were critical to the success of the instrument. A single gage

was attached to each instrumented rib, sandwiched between sheets of butyl rubber and thin neoprene, and then encased with clear plastic and silicone. Over the course of the 3-month preliminary study an instrument survival rate of 90% was achieved. Results from the study indicated that very little strain was developed in the geogrid as a result of subbase placement without compaction. Strains in the instrumented ribs of between 0.3 and 0.4% were measured during initial compaction of the aggregate. Additional strains ranging from 0.05 to 0.15% were measured when the subbase was leveled and compacted a second time (Perkins and Lapeyre, 1997).

2.4.2.3. Terracon Inc. Investigation in Dallas. In a study for the Tenax Corporation, Terracon Inc., (1998) evaluated the performance of Dallas streets constructed with geogrid-reinforced subbase. Effective structural numbers for each section were backcalculated from FWD results. It was shown that for residential streets constructed with 127 to 140 mm (5.0 to 5.5 in.) of pavement and 127 to 229 mm (5 to 9 in.) of subbase with geogrid on subgrade, the reinforcement provided no significant increase in the effective structural numbers. Sections constructed with 127 to 280 mm (5 to 11 in.) of asphalt concrete underlain by 203 to 254 mm (8 to 10 in.) of subbase aggregate with geogrid on subgrade exhibited increases in the effective structural number ranging from 1.0 to 1.9 (Terracon Inc., 1998). These findings are in sharp contrast with those from previous studies. Improvement from geosynthetics reinforcement is not typically expected for pavement layers as thick as those used in the Dallas investigation.

2.4.2.4. Study of Reinforced Pavements for Light Aircraft. Webster (1992) investigated the performance of flexible pavements with reinforced subbase under simulated light aircraft traffic. Two test lanes were constructed. The average subgrade CBR for test lanes 1 and 2 were 7.1 and 2.5, respectively. Both test lanes used a 50-mm (2-in.) crushed stone subbase. Pavement thickness ranged from 56 to 66 mm (2.2 to 2.6 in.). Aircraft loads were simulated with a single wheel 133 kN (30 kip) cart. It was concluded that the performance improvement effects of geogrid reinforcement was a function of the depth of placement. For flexible pavements under typical lightweight aircraft traffic the minimum depth should be at least 152 mm (6 in.), consisting of a 101-mm (4-in.) subbase and 50-mm (2-in.) asphalt surface. For subgrade CBR's greater than 1.5, geogrid performs best when placed at the interface of the subbase and subgrade (Webster, 1992).

2.4.2.5. Fetten and Humphrey. The University of Maine (Humphrey and Fetten, 1998) investigated the effectiveness of geosynthetics as reinforcement, separation, and drainage layers in a cold region. This research went beyond the scope of previous studies by examining geosynthetic performance using subbase thicknesses between 580 and 640 mm (23 to 25 in.). Prior investigations used subbases up to 305 mm (12 in.) thick.

The test sections were constructed with different combinations of Tenax MS330 reinforcement geogrid, Mirafi 67809 reinforcement geotextile, Mirafi 180N non-woven geotextile used as a separator, and Tenax Tendrain 100-2 drainage geocomposite. Instrumentation was installed to evaluate the performance of the geosynthetics. The

majority of the force measured in the reinforcement geotextile and geogrid was induced during placement and compaction of the first lift of the overlying subbase course aggregate. This force did not vary for geogrid placed at depths ranging 250 to 640 mm (10 to 25 in.) in sections with 180 mm (7 in.) of asphalt. The maximum long-term force in the geogrid was less than 5% of its ultimate tensile strength. The reinforcement geotextile exhibited forces after construction ranging from 0 to 6 kN/m (0 to 411 lb/ft). It was determined that the force in the geotextile was influenced by local conditions such as initial slack in the geotextile, tensioning from construction traffic rutting, and subgrade strength.

The effective structural number was backcalculated from FWD test results. The structural number from each test section was compared to that in section C2, constructed with only separation geotextile on subgrade. The effective structural number in sections with reinforcement geogrid ranged from 74 to 101% of the value determined for a section with only separation geotextile. It was concluded that reinforcement did not increase the effective structural number and that the small magnitude of the forces induced in the geogrid and geotextile suggests little reinforcing benefit for the thick subbase used for this project. In addition, it was concluded that the drainage geocomposite could slightly improve the effective structural number when placed below subgrade and should be placed as far below the pavement as possible (Fetten and Humphrey, 1998).

2.5. Numeric Modeling

2.5.1. Modeling For Unpaved Roads

Several authors have used numeric modeling along with laboratory tests to investigate improvement mechanisms and achievable levels of improvement for geotextile reinforced roadway sections. Numeric behavior models ILLI-PAVE, LSTRN3, BISAR, and a simple confinement model were used in a study by Thompson and Raad (1981) to assess soil geotextile systems with deformations less than 38 mm (1.5 in.).

Results from LSTRN3, an elastic-based finite-element model, indicated that for transformed sections at least 12 times the thickness of the original fabric, lateral strains in the fabric, vertical subgrade stresses and strains, and surface deformations are not affected (Thompson and Raad, 1981). A transformed section was defined as a fabric reinforced section designed to have the same stiffness as an unreinforced section of subgrade and stone base.

Thompson and Raad (1981) also used ILLI-PAVE, a stress-dependent finite-element model, to investigate the effects of a fabric layer in unpaved roads. The parameters were a soft subgrade, a fabric that would not slip on the subgrade or overlying crushed stone, and a 203-mm (8-in.) thickness of crushed stone. Their analysis showed that the fabric had no effect on vertical stress distribution, failure zones in the granular base, and deflection pattern in the pavement section (Thompson and Raad, 1981). There was only 18 mm (0.70 in.) of surface deflection, which may not have been enough to mobilize the tensile reinforcement effect of the fabric.

Thompson and Raad (1981) developed a simple model to show that significant improvement in shear strength, stiffness, and permanent deformation behavior in the granular material can be correlated to small increases in confining pressure. The correlation is described by Equations 2.1 and 2.2. The model is shown in Figure 2.4. The results of the computer analysis showed that the benefits of fabric reinforcement are only realized when there is adequate geotextile deformation to develop confining pressures.

$$\Delta\sigma/\sigma = [P_o(r) / K_s K_o h(h+r)](1+\alpha) \qquad \text{Equation 2.1}$$

where:

$$\alpha = \Delta_p / \Delta_r \qquad \text{Equation 2.2}$$

$\Delta\sigma/\sigma$ = increase in confinement at interface due to fabric deformation, expressed in terms of the confinement before the fabric deforms, σ

P_o = applied surface pressure

r = radius of loaded area

K_s = modulus of subgrade reaction

K_o = coefficient of earth pressure at rest

h = thickness of granular layer

Δ_p = permanent deformation

Δ_r = resilient deformation

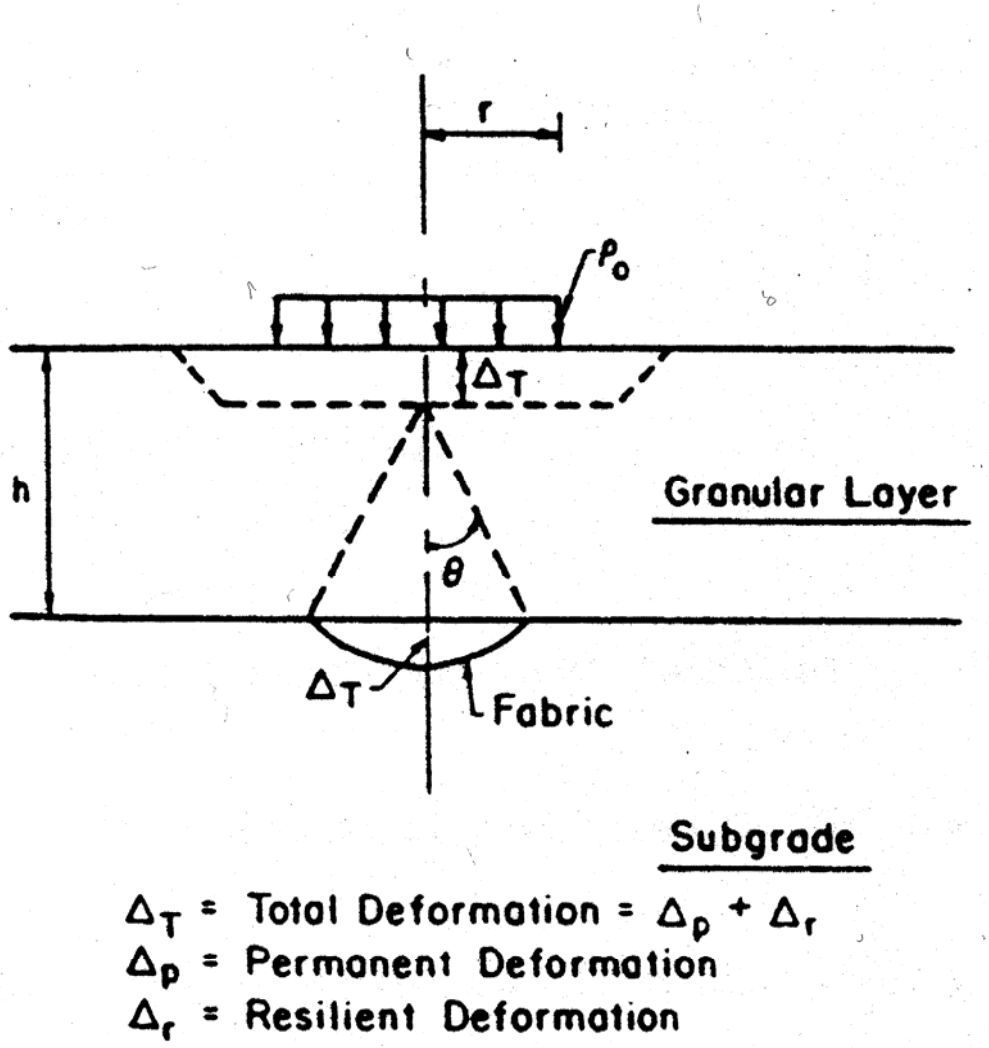

Figure 2.4 Increased confinement-effect model (Thompson and Raad, 1981).

The effect of fabric slippage at the interface between the subbase and subgrade was analyzed using BISAR, an elastic layered program. In a finite-element study by

Bender, et al. (1987) it was shown that the fabric provides reinforcement by restricting the horizontal strains in the subbase, which reduces critical horizontal strains at the interface between the subbase and subgrade. The results of this finite-element study were consistent with observed behavior.

2.5.2. Modeling For Paved Roads

The use of recycled subbase materials in conjunction with geosynthetic reinforcement was investigated by Lui, et al. (1999). In a finite element study, the program CAPA-2D was used to show that loss of pavement stiffness due to inferior stiffness properties of recycled subbase materials could be compensated for by installing geosynthetics at the interface of the subbase and subgrade. The presence of geosynthetic reinforcement not only rendered viable secondary subbase materials such as crushed concrete and masonry, but also significantly restricted the propagation of surficial pavement cracks (Lui, et al., 1999).

Parametric studies were performed by Ling and Liu (2003) using the finite element program PLAXIS. Soils were modeled as elastoplastic using Mohr-Coulomb failure criteria and geogrids were considered linear elastic. It was shown that load settlement relationships were a function of geogrid stiffness and that there was an upper limit to the stiffness that improved bearing capacity. Geogrid modeled with a stiffness of 1,000 kN/m (68,500 lb/ft) provided nearly the same increase in bearing capacity as geogrid modeled with a stiffness of 400 kN/m (27,400 lb/ft). The study also showed that the ideal pavement thickness was 40 mm (1.5 in.) and that for greater thicknesses the bearing capacity of the system was determined by the asphalt layer (Ling and Liu, 2003).

Parametric studies showed the reinforcement effects increased as strain level increased and subgrade strength decreased. Despite the fact that these findings are in good agreement with the authors' laboratory tests, they strongly believe that a linear elastic model of geogrid behavior is inappropriate and that PLAXIS should incorporate a non-linear model such as that proposed by Ling, et al. (1995, 2000).

Models have been developed that deal strictly with the behavior of geosynthetics, rather than that of roadways they are installed in. Perkins (1999) developed a constitutive model to simulate direction-dependent elastic, plastic, and time-dependent creep properties. Results from the model were compared with laboratory uniaxial tension tests on an AMOCO polypropylene biaxial geogrid. The anisotropic elastic-plastic responses of the geosynthetics as was well as creep effects under sustained loads were reasonably well predicted (Perkins, 1999).

Perkins, et al. (2000) developed a 3-D finite element model using ABAQUS to predict the behavior of reinforced roadway sections after repeated traffic loading. Shear interactions between the subbase and geosynthetics were simulated using a Coulomb-type frictional model. An isotropic elastic-plastic model was used for the geosynthetics as well as subbase, subgrade, and asphaltic concrete materials. Nominal thicknesses of 75 mm (3 in.) and 300 mm (12 in.) were used for the pavement and subbase, respectively. The model subgrade had a CBR of 1.5. Three models were created using generic properties for the asphalt, subbase, reinforcement, and subgrade layers: a typical unreinforced section, a geosynthetic reinforced section, and a perfectly reinforced section where the nodes at the interface of the subbase and subgrade were restricted from horizontal movement to simulate perfect lateral base course restraint. Under a cyclic load

of 550 kpa (11,500 psf) the model simulated the improvement mechanisms associated with geosynthetics. The model predictions qualitatively agree with results from previous large-scale experimental work on pavement test sections (Perkins and Ismeik, 1997; Perkins, 1999). Reduced pavement deflections, reduced shear stress in the subgrade, and increased horizontal stress in the subbase were all well represented (Perkins, et al., 2000).

Ling, et al. (2001) modeled the highly non-linear behavior and hysteresis of geogrids under cyclic loads using a 1-D bounding surface model. The model used non-parallel bounding lines to simulate the non-compressional behavior of geogrids. Experimental results from two geogrids under varying amplitudes of cyclic loading were well simulated (Ling, et al., 2001). Comparisons between model predictions and experimental results for monotonic loading and cyclic loading are shown in Figures 2.5 and 2.6. The results show that the 1-D bounding surface model is an adequate means of predicting the non-linear responses of cyclically loaded geogrids.

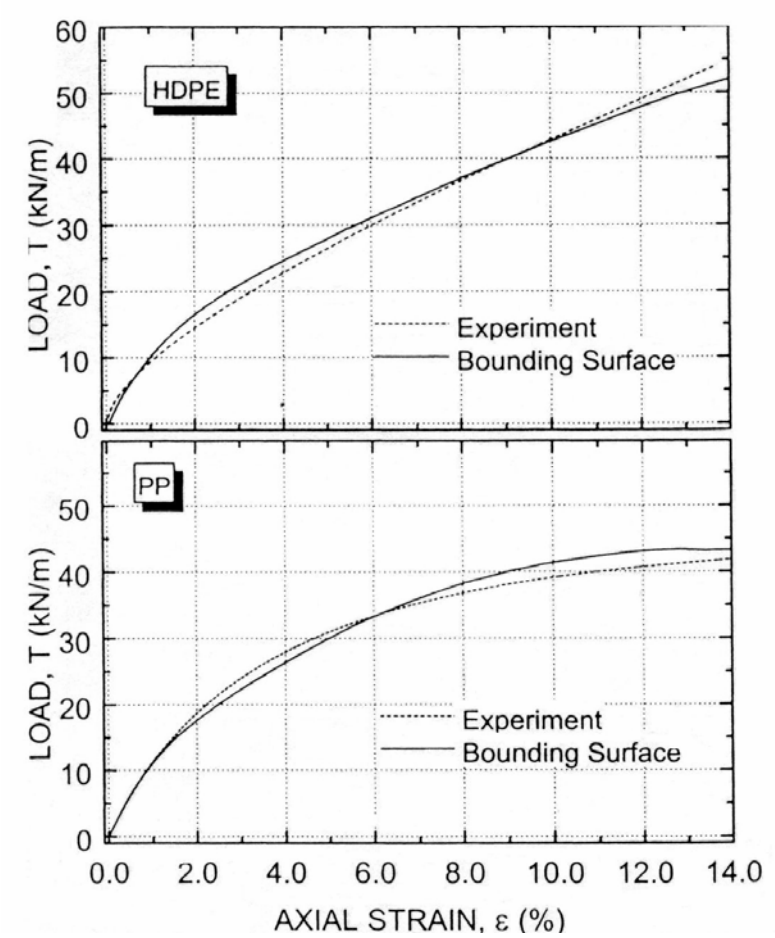

Figure 2.5 Comparison of bounding surface model and experimental results for monotonic loading (Ling, et al., 2001).

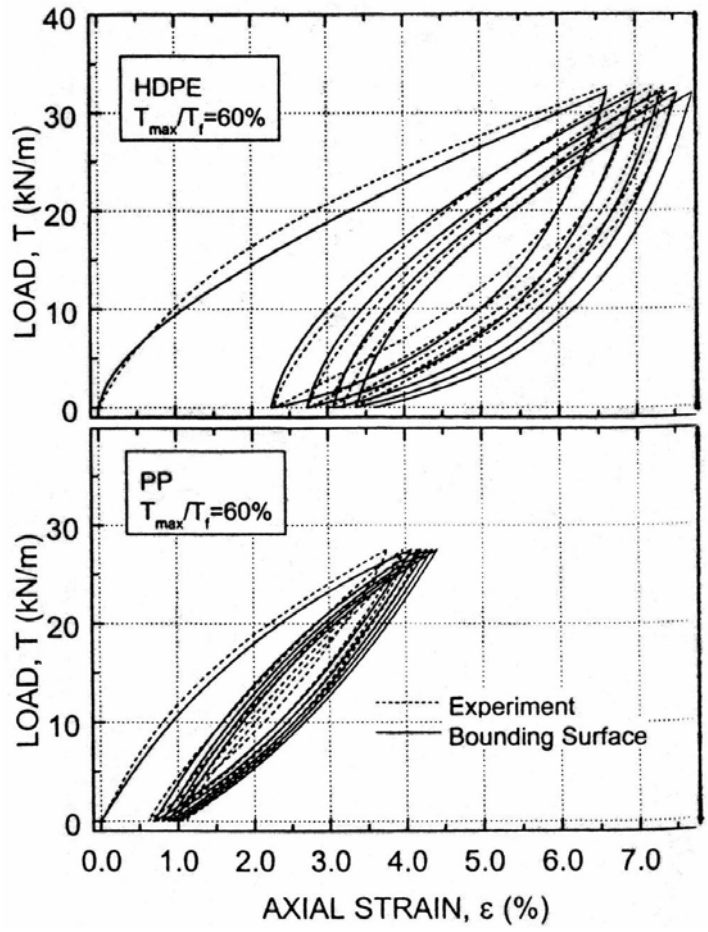

Figure 2.6 Comparison of bounding surface model and experimental results for cyclic loading (Ling, et al., 2001).

2.6. Design Methods

A limited number of design methods for reinforced roadways are available. In addition, techniques available for unpaved reinforced roads are presented and provide insight into paved reinforced road design.

2.6.1. Reinforcement Design Methods for Unpaved Roads

Bender and Barenberg (1978) examined the behavior of a test road and determined relationships between the stress applied to the subgrade, the development of

ruts, and the presence of reinforcement in the system. It was concluded that rutting significantly increased after 100 load cycles if the stress applied to the subgrade in an unreinforced system exceeded 3.3 times the subgrade's undrained shear strength (c_u). However, rutting after 100 load cycles did not increase in the reinforced system until the applied subgrade stress exceeded $6c_u$. It was concluded that the presence of reinforcement geotextile in the system changed the failure mechanism from local shear to general shear, and that a reinforced subgrade could support a stress 1.8 times greater than an unreinforced subgrade. This allowed for a thinner subbase aggregate layer to be used. Design charts indicating required subbase thickness over the geotextile were developed in terms of subgrade undrained shear strength and fabric modulus based on the assumption of low traffic volumes (less than 100 passes) and an acceptable rut depth of 101 mm (4 in.) (Kinney and Barenberg, 1980, 1982).

Steward, et al. (1977) examined the performance of a test road constructed with geotextile. The fabric had low strength and modulus and was used primarily for separation of the subbase and subgrade. A design table was developed that recommends values for the bearing capacity factor N_c, based on traffic level, acceptable rutting, and the presence of geotextile. This method was also recommended by Holtz, et al. (1994) and is also accepted by FHWA (Holtz, et al., 1998).

Giroud and Noiray (1981) developed a widely used method for design of geotextile reinforced unpaved roads. The method assumes the tire pressure is applied to a rectangular area at the surface and is distributed over progressively larger areas with increasing depth. These areas are defined by lines sloping down and away from the corners of the surface load. The slope of these lines from vertical is termed the stress

distribution angle. The load distribution by the aggregate layer is shown in Figure 2.7 for the reinforced and unreinforced case.

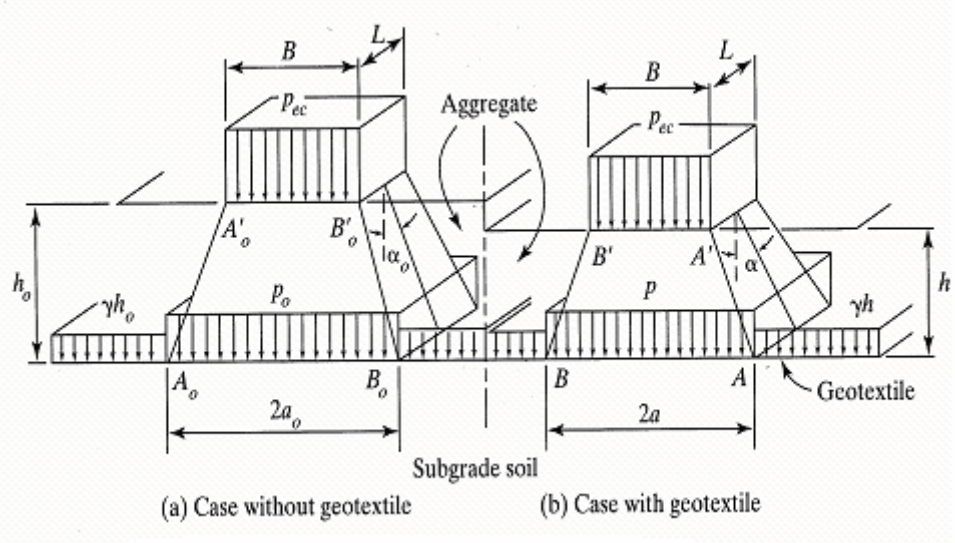

Figure 2.7 Subbase aggregate load distribution for the unreinforced (a) and reinforced (b) case (Giroud and Noiray, 1981).

Wheel load, tire pressure, and subgrade shear strength are considered in the computations and the method assumes that the presence of geotextile effectively increases the subgrade bearing capacity by changing the shear failure mechanism from local to general. The method determines the subbase thickness above the geosynthetic required to reduce the applied subgrade stress to a value equal to its estimated bearing capacity (Giroud and Noiray, 1981).

Giroud and Han (2001) modified the original Giroud and Noiray (1981) method based on results from several large-scale plate load tests using Tensar BX1100 and BX1200 geogrid reinforcement conducted at North Carolina State University (Gabr, 2001). The laboratory data was used to quantify effects of base course thickness and reinforcement on the initial stress distribution angle as well as changes in the angle from

continued load applications. Through incorporation of the strength and modulus of the subbase aggregate, stiffness of the geosynthetic, and fluctuations in the load distribution angle, the method provides better performance predictions and more efficient use of materials, equipment, and time (Giroud and Han, 2001).

The design methods for reinforced unpaved roads generally agree that the change in subgrade failure mode from local to general associated with geosynthetic reinforcement is a key improvement mechanism. The procedures described can be of use for the construction of paved roads, particularly when designing for loads associated with the construction process prior to the placement of an asphalt surface. Furthermore, for pavement sections less than 1.5 in. (38 mm) thick where the asphalt thickness is not the controlling variable in the bearing capacity of the system, the methods developed for unpaved roads could be used for reinforcement design (Ling and Liu, 2003).

2.6.2 Design Methods for Paved Permanent Roads

2.6.2.1. Penner, Haas, and Walls. There are a limited number of design procedures available for reinforcement beneath flexible pavements. Penner, et al. (1985) developed a method that used a layer coefficient ratio or equivalence factor applied to the reinforced layer to reflect the structural improvement to the subbase. Design relationships for geogrid-reinforced subbase layers were developed based on methods outlined in the AASHTO Interim Guide. The AASHTO method allows comparison between the structural strengths of pavement sections using the structural number as defined by equations 2.3 and 2.4.

The structural number of the entire system is defined by:

$SN = a_1d_1 + a_2d_2 + \ldots a_nd_n$ Equation 2.3

The structural number of the granular subbase is the structural number of the entire system less the structural number of the asphalt pavement:

$SN_{gr} = SN - a_1d_1$ Equation 2.4

where:

a_1 = layer coefficient for asphalt concrete (typically 0.4)

d_1 = thickness of the asphalt concrete layer (in.)

The ratio relating unreinforced to reinforced subbase layer coefficients was determined through laboratory tests at the University of Waterloo (see section 2.4.1.3) and is defined by:

$A_r / A_u = (SN_{gr})_r * d_u / (SN_{gr})_u * d_r$ Equation 2.5

where:

$(SN_{gr})_r$ = structural number of reinforced granular subbase

$(SN_{gr})_u$ = structural number of unreinforced granular subbase

d_r = thickness of reinforced subbase

d_u = thickness of unreinforced subbase

A_r / A_u = effect of geogrid reinforcement on structural capacity of subbase

This ratio expresses the amount of improvement in subbase structural capacity that the geogrid can provide. Comparisons of this ratio to the behavior of test sections

indicated that subbase thickness and performance improvement were inversely proportional. The ratio Ar / Au becomes 1 at a subbase thickness of approximately 270 mm (11 in.). Although no test sections were constructed with a subbase thickness greater than 300 mm (12 in.), no improvement was expected for thicker subbase sections (Penner, et al., 1985).

2.6.2.2. Vischer. In a recent reconstruction project by the U.S. Forest Service and North Dakota Department of Transportation, design methods for flexible pavements with geogrid-reinforced subbase were reviewed by Vischer (2003). Separate design analyses were used for bearing capacity under construction traffic and flexible pavement support of long-term light recreation traffic.

Two approaches were examined for the construction traffic bearing capacity analysis: the TTN:BR5 method developed by Tensar, Inc. and the computer program SpectraPave 2 produced by Jensen Earth Technologies. The TTN:BR5 method is based on static loading conditions. The SpectraPave 2 program is based on the Giroud-Noiray method. Both analyses assumed a dual axle wheel load of 80 kN (18 kips). For the SpectraPave 2 calculations, a 76-mm (3-in.) rut depth and 1,000 ESAL's were assumed. The SpectraPave 2 (Giroud-Noiray) method proved more conservative than the Tensar method, recommending thicker sections for both unreinforced and reinforced base.

Empirical methods were used to determine reinforced subbase thickness beneath a 51-mm (2-in.) flexible asphalt pavement section required to support the long-term recreational traffic expected. The techniques investigated were the Tensar Earth Technologies base course reinforcement method and the Perkins-Michigan Department

of Transportation method, both of which use the basic inputs and methodology outlined by the AASHTO 1993 Design Guide. The Tensar Earth Technologies method uses the SpectraPave program and incorporates the type of geogrid used and an assumed traffic benefit ratio. The Perkins-Michigan DOT method includes inputs for reinforcement characteristics and is considered more comprehensive because finite element modeling, parametric studies, and regression analysis supported its development. In addition, the method provides an estimate of the effective reinforced subbase modulus, which can then be used in a mechanistic approach (Vischer, 2003).

The mechanistic approach was based on multilayered elastic analysis using the computer programs EVERSTRESS and KENLAYER. The required inputs for this approach are the design wheel load as well as the modulus and Poisson's ratio of each layer in the flexible pavement system. The subbase was entered as two separate layers, with the lower portion having a higher modulus to simulate the effects of lateral base course restraint from the reinforcing. Through the elastic analyses the computer programs calculate pavement deflections as a function of section property inputs.

It was concluded that the SpectraPave program produced the more conservative results in the flexible pavement analysis, suggesting larger subbase sections beneath the 51-mm (2 in.) asphalt surface than all of the other methods examined. Perkins trial 1 yielded results similar to the SpectraPave program at lower subgrade moduli. Perkins trail 2 and the mechanistic approach proved the least conservative and at low subgrade moduli suggested subbase thicknesses not feasible for this project, even with reduced construction loads. The results of the flexible pavement analyses are shown in Figure 2.15. The author feels that the mechanistic approach provides the designer with the most

rational analysis and supports a better understanding of the material behaviors within the pavement structure. However, (Vischer, 2003) recommends that several design analyses be used to generate a range of results upon which the final design should be based.

2.7. Summary

Research on the performance of geosynthetics in roadway construction began in the 1970's. There are four major improvement functions that geosynthetics provide in roadways: separation of subbase and subgrade materials, subbase reinforcement, filtration of suspended particles migrating from the subgrade into the subbase, and drainage of the subgrade.

Studies have shown that use of geosynthetics in unpaved roads can be beneficial. Geosynthetic reinforcement can reduce the subbase thickness required to sustain traffic loads or increase the life of the road when a typical subbase thickness is used (Bender, et al., 1978; Thompson and Raad, 1981; Robnett and Lai, 1982). Leng and Gabr (2002) showed that geogrid reinforcement reduced surface deformations, improved stress distribution on the subgrade, and inhibited subbase degradation. It was concluded that the level of improvement attained was a function of geogrid stiffness and the authors attributed the enhanced performance of reinforced subbase material to the tensioned membrane effect and lateral base course restraint due to aggregate-geogrid interlock (Leng and Gabr, 2002).

Studies by Kennepohl, et al. (1985), Penner, et al. (1985), Haas, et al. (1988), Barksdale, et al. (1989), Al-Qadi, et al. (1994), Cancelli, et al. (1996), Perkins, et al. (1996), and Montanelli, et al. (1997), showed some benefits of geosynthetic

reinforcement beneath flexible pavements. Performance improvement is dependent on loading conditions, subgrade and roadway section properties, and the characteristics of the geosynthetic. In general, as subgrade strength decreases the level of improvement increases. Laboratory investigations concluded that reinforcement increased the number of load cycles the pavement system could carry or allowed for the system to be constructed using a reduced subbase thickness (Penner, et al., 1985; Haas, et al., 1988; Perkins, et al., 1997). Additional findings indicate that, under the proper circumstances, geosynthetic reinforcement can reduce the rate of permanent deformation (rutting) and increase pavement life (Haas, et al., 1988). It was concluded that for a subbase thickness of 100 to 203 mm (4 to 8 in.) the optimum position for the geogrid was on subgrade. For subbase thicknesses of 254 to 305 mm (10 to 12 in.) it is more beneficial for the geogrid to be placed at the mid point of the layer. It is noted that the maximum pavement thickness in this study was 38 mm (1.5 in.) (Haas, et al., 1988).

Despite the beneficial performance reported by several researchers, some studies have shown that geosynthetic reinforcement provided negligible performance improvement. Ruddock, et al. (1982) evaluated the performance of a 160-mm (6.3 in.) pavement section underlain by 300 mm (12 in.) of crushed granite subbase with geotextile on subgrade. Measurements of surface deformation, dynamic stress and strain in the subgrade, and permanent strain in the geotextile under simulated truck loads indicated no difference in structural performance between the reinforced and control sections (Ruddock, et al., 1982).

Barksdale, et al. (1989) investigated the performance of geosynthetics using full-scale pavement tests on sections constructed with a subbase thickness of 150 or 200 mm

(6 or 8 in.) overlain by asphaltic pavement ranging in thickness from 25 to 38 mm (1.0 to 1.5 in.). The authors indicated that the effects of geosynthetics on stress, strain, and deflection were small for pavements designed to carry more than 200,000 equivalent 80-kN (18-kip) single axle loads. Moreover, they expected no improvement from geosynthetic reinforcement for pavement thicknesses greater than 65 to 90 mm (2.5 to 3.5 in.), even when the subbase aggregate is placed on soft subgrade (Barksdale, et al., 1989).

Laboratory studies conducted at the University of Waterloo, Virginia Polytechnic Institute, Montana State University, and the University of Alaska-Fairbanks have evaluated the use of geosynthetics in flexible pavement design. However, very few studies have investigated reinforcement with asphalt thicknesses greater than 101 mm (4 in.) or subbase thicknesses greater than 300 mm (12 in.). Humphrey and Fetten (1998) may have been the first to examine geotextile and geogrid reinforcement with larger material sections, using subbase thicknesses of 580 and 640 mm (22 and 25 in.) and a pavement thickness of 180 mm (7 in.). The geosynthetic reinforcement did not increase the structural number backcalculated from FWD results. Consequently the reinforcing benefits to the thick subbase used in the study were deemed negligible.

CHAPTER 3
PROJECT DESCRIPTION

3.1. Introduction

Reconstruction of Route 9 in the towns of Monmouth, Litchfield, and West Gardiner took place over the course of two work seasons. During the reconstruction a total of twelve test sections were built in the town of Litchfield. The east end of the test area is located approximately 10 km (6.2 mi) west of the I-95/Route 9 interchange. Test sections 6 through 12 were constructed first, starting in September, 2001 at station 3+940 m (129+26 ft). Operations proceeded until mid-October when the work season concluded. Work on test sections 1 through 5 began in June, 2002 at station 1+520 m (49+87 ft) and concluded in late July.

All of the test sections have poor subgrade soils. These soils are classified as AASHTO A-2-4, A-4, and A-6 and are highly frost susceptible. Prior to reconstruction, the road had many local bearing capacity failures resulting in substantial pavement cracking. Several of the subgrade soil samples had natural water contents approaching the liquid limit. The low shear strengths of the subgrade soils combined with the inadequacy of the existing drainage made this a suitable site for testing geosynthetics for reinforcement and drainage applications.

The reconstructed roadway pavement section was designed to carry 500,000 equivalent 80-kN (18-kip) single axle loads. Reinforcement geogrid and drainage geocomposite were installed to evaluate their performance and effectiveness on soft subgrade soils in cold regions. This was done by comparing field data from test sections

using the geosynthetics with control sections, as well as by making comparisons with previous field studies.

3.1. Test Section Layout

A total of twelve test sections were constructed. Test sections 1 through 5 were constructed with a 300 mm (12 in.) subbase whereas test sections 6 through 10 were constructed with a 600 mm (24 in.) subbase. This allowed the effects of reducing subbase thickness to be evaluated. In test sections 11 and 12, a 75 to 150 mm (3 to 6 in.) thickness of pavement grindings was used as the subbase. These are referred to as reclaimed sections. All of the test sections were surfaced with 150 mm (6 in.) of bituminous pavement.

Twelve test sections were constructed to examine the effects of the following variables: subbase thickness and material type; reinforcement including the effect of location within the pavement structure; drainage; and drainage combined with reinforcement. Test sections using reinforcement geogrid are equipped with strain gages that are used to deduce tensile loads. Drainage test sections have vibrating wire piezometers to monitor porewater pressure in the subgrade and subbase course. The drainage sections use a 100-mm (4-in.) diameter underdrain pipe to collect water from the drainage geocomposite. The outlet of each underdrain pipe is equipped with a flow meter to measure the amount of water coming from the drainage geocomposite. Each of the test sections has a thermocouple string that is used to measure frost penetration. A profile of each test section is shown in Figure 3.1. The test sections are described in detail in the following sections. Chapter 4 contains the instrumentation details and the field measurements taken.

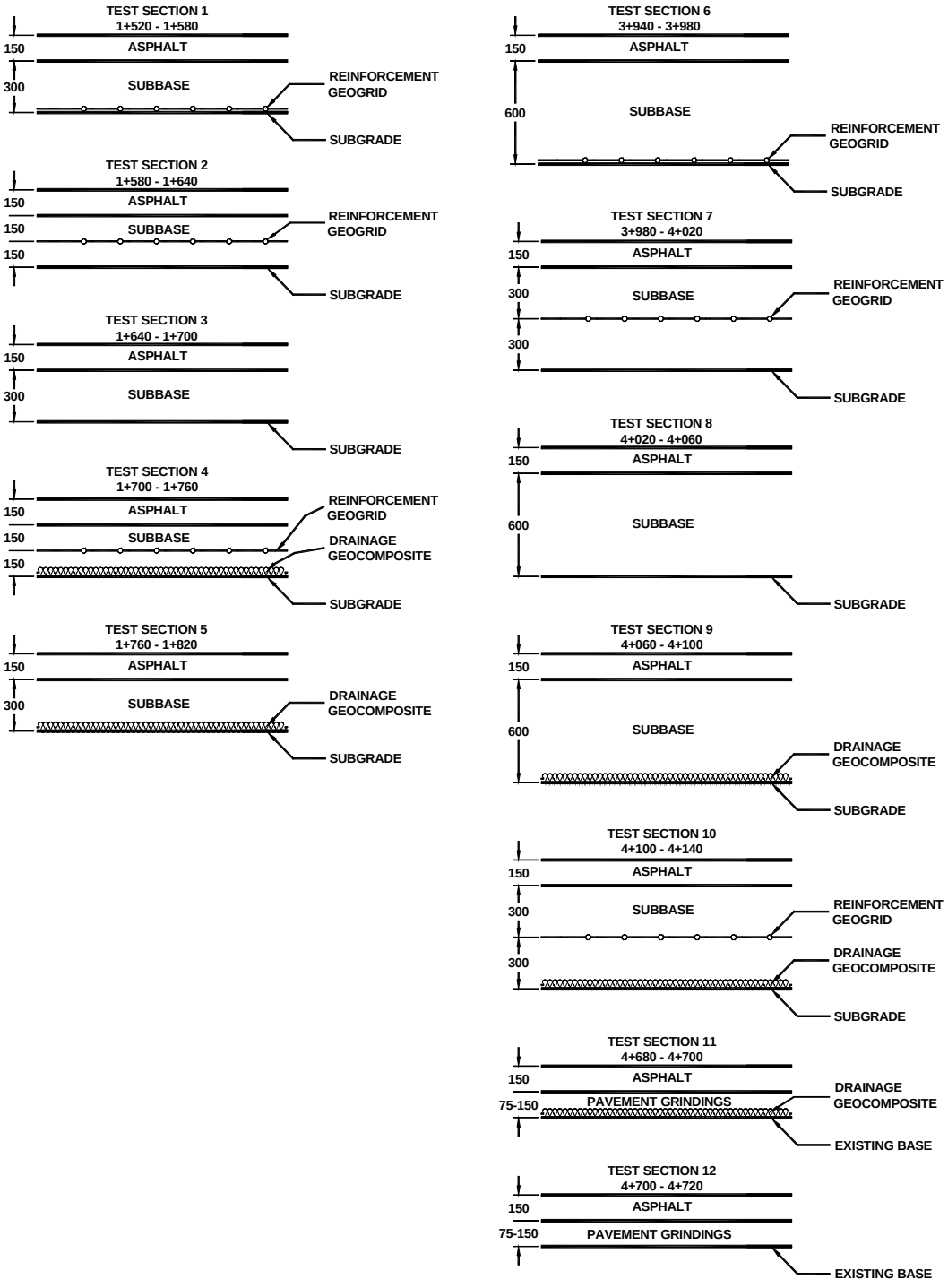

*All dimensions shown are in millimeters

Figure 3.1 Test section layout.

3.2.1. Test Section 1 - Reinforcement

Test section 1 uses a single layer of reinforcement geogrid located on subgrade with 300 mm (12 in.) of subbase cover. The geogrid is equipped with five pairs of strain gages at both stations 1+540 m (5+052 ft) and 1+560 m (5+118 ft). A thermocouple string was installed at station 1+550 m (5+085 ft).

3.2.2. Test Section 2 - Reinforcement

Test section 2 uses a single layer of reinforcement geogrid located in the center of the 300-mm (12-in.) thick subbase course. The geogrid is equipped with five pairs of strain gages at both stations 1+600 m (5+249 ft) and 1+620 m (5+315 ft). A thermocouple string was installed at station 1+612 m (5+289 ft).

3.2.3. Test Section 3 - Control

Test section 3 is a control section that was constructed using a 300-mm (12-in.) thick subbase course with no geosynthetics. A pair of vibrating wire piezometers was installed at station 1+673 m (5+489 ft). A thermocouple string was installed at station 1+670 m (5+479 ft).

3.2.4. Test Section 4 – Drainage/Reinforcement

Test section 4 uses both drainage geocomposite and reinforcement geogrid. The drainage geocomposite was placed on subgrade. The reinforcement geogrid is located in the center of the 300-mm (12-in.) thick subbase course. The geogrid is equipped with five pairs of strain gages at both stations 1+720 m (5+643 ft) and 1+740 m (5+709 ft). A

pair of vibrating wire piezometers was installed at station 1+732 m (5+682 ft). A thermocouple string was installed at station 1+730 m (5+676 ft). Flow meters were installed at collector pipe outlets at station 1+760 m (5+774 ft) on both the right and left shoulders.

3.2.5. Test Section 5 - Drainage

Test section 5 uses drainage geocomposite on subgrade overlain with a 300-mm (12-in.) thick subbase course. A pair of vibrating wire piezometers was installed at station 1+793 m (5+883 ft). Flow meters were installed at collector pipe outlets at station 1+820 m (5+971 ft) on both the right and left shoulders.

3.2.6. Test Section 6 - Reinforcement

Test section 6 uses a single layer of reinforcement geogrid located on subgrade with 600 mm (24 in.) of subbase cover. The geogrid is equipped with five pairs of strain gages at stations 3+950 m (12+959 ft) and 3+970 m (13+025 ft). A thermocouple string was installed at station 3+965 m (13+008 ft).

3.2.7. Test Section 7 - Reinforcement

Test section 7 uses a single layer of reinforcement geogrid located at the center of a 600-mm (24-in.) thick subbase course. The geogrid is equipped with five pairs of strain gages at stations 3+990 m (13+090 ft) and 4+010 m (13+156 ft). A thermocouple string was installed at station 4+000 m (13+123 ft).

3.2.8. Test Section 8 - Control

Test section 8 was constructed using a 600-mm (24-in.) thick subbase course with no geosynthetics. A pair of vibrating wire piezometers was installed at station 4+042 m (13+261 ft). A thermocouple string was installed at station 4+040 m (13+255 ft).

3.2.9. Test Section 9 - Drainage

Test section 9 was uses drainage geocomposite on subgrade overlain with a 600-mm (24-in.) thick subbase course. A pair of vibrating wire piezometers was installed at station 4+082 m (13+392 ft). A thermocouple string was installed at station 4+080 m (13+386 ft). Flow meters were installed at the collector pipe outlets at station 4+110 m (13+484 ft) on the both right and left shoulders.

3.2.10. Test Section 10 – Drainage/Reinforcement

Test section 10 uses both drainage geocomposite and reinforcement geogrid. The drainage geocomposite was placed on subgrade. The reinforcement geogrid is located in the center of the 600-mm (24-in.) subbase course. The geogrid is equipped with five pairs of strain gages at stations 4+110 m (13+484 ft) and 4+130 m (13+550 ft). A pair of vibrating wire piezometers was installed at station 4+122 m (13+524 ft). A thermocouple string was installed at station 4+120 m (13+517 ft). Flow meters were installed at the collector pipe outlets at station 4+160 m (13+648 ft) on both the right and left shoulders.

3.2.11. Test Section 11 - Drainage

Test Section 11 uses drainage geocomposite placed on the existing base covered with 75 to 150 mm (3 to 6 in.) of pavement grindings. A pair of vibrating wire piezometers was installed at station 4+692 m (15+394 ft). A thermocouple string was installed at station 4+690 m (15+387 ft). Flow meters were installed at the collector pipe outlets at station 4+677 m (15+344 ft) on both the right and left shoulders.

3.2.12. Test Section 12 - Control

Test section 12 was constructed using 75 to 150 mm (3 to 6 in.) of pavement grindings with no geosynthetics. A pair of vibrating wire piezometers was installed at station 4+712 m (15+459 ft). A thermocouple string was installed at station 4+710 m (15+453 ft).

3.3. Geosynthetic Properties

Two types of geosynthetics were used on this project: reinforcement geogrid and drainage geocomposite. The manufacturers donated both types of the geosynthetics. The properties of each type are described in the following sections.

3.3.1. Reinforcement Geogrid Properties

The reinforcement geogrid was Tensar BX1200. This is a polypropylene plastic with openings approximately 25 mm by 33 mm (1.0 in. by 1.3 in.) and a rib thickness of about 1.27 mm (0.05 in.). It was delivered in rolls 4 m (13.1 ft) wide and 50 m (164 ft) long. The material properties published by the manufacturer as well as the minimum

requirements specified by MaineDOT are summarized in Table 3.1. A photo of the geogrid is shown in Figure 3.2.

Table 3.1 Reinforcement geogrid properties.

Geogrid Property	Test Method	Values Required by Project Specifications	Properties Reported by Manufacturer*
Modulus @ 5% Strain (MD)	ASTM D4595	≥175 kN/m (≥12,000 lb/ft)	236 kN/m (16,200 lb/ft)
Modulus @ 5% Strain (XD)	ASTM D4595	≥350 kN/m (≥24,000 lb/ft)	397 kN/m (27,200 lb/ft)
Ultimate Tensile Strength	ASTM D4595	MD & XD: ≥17.5 kN/m (≥1,200 lb/ft)	MD: 19 kN/m (1300 lb/ft) XD: 29 kN/m (1985 lb/ft)
Aperture Openings		19 to 76 mm (0.75 to 3.0 in.)	25 (MD) x 33 mm (XD) (1.0 x 1.3 in.)
Percent Open Area		≥50%	70%

MD = Machine Direction (longitudinal to the roll)
XD = Cross Direction (across roll width)
*Tensar BX1200 product information

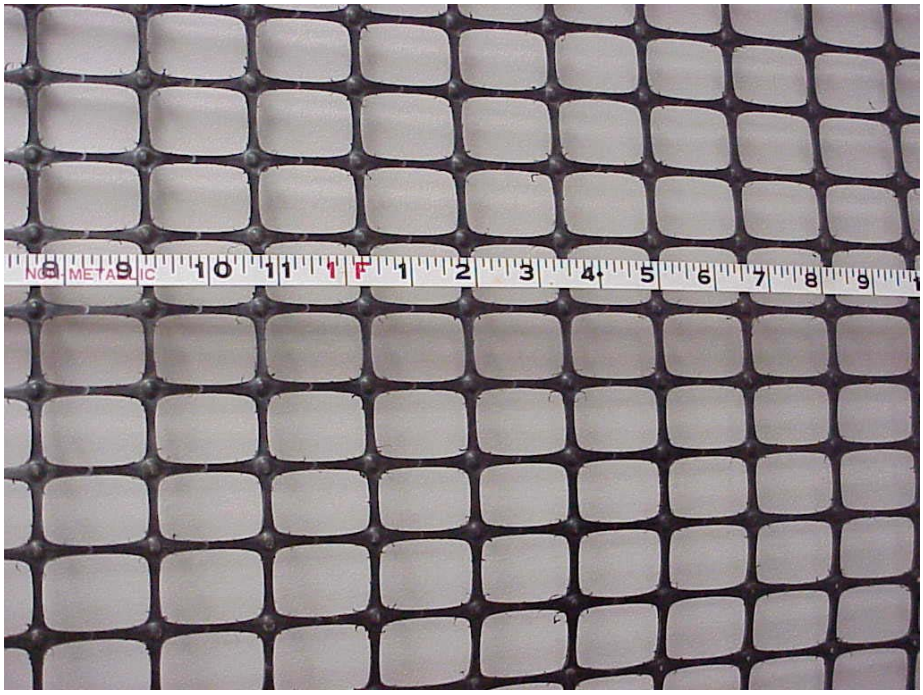

Figure 3.2 Photo of reinforcement geogrid.

3.3.2. Drainage Geocomposite Properties

The drainage geocomposite was Tendrain 100-2. The internal drainage structure consists of a thick central support rib with diagonal top and bottom ribs constructed of high-density polyethylene. Sheets of non-woven polypropylene geotextile are thermally laminated on both sides of the internal drainage structure to prevent intrusion of fine-grained soil. Panels of this composite material 4 m (13 ft) wide and 30 m (100 ft) long were folded and delivered on wooden pallets. The material properties published by the manufacturer are given in Table 3.2. The non-woven geotextile as well as the internal drainage structure of the drainage geocomposite is shown in Figure 3.3.

Table 3.2 Drainage geocomposite properties.

Internal Drainage Structure Properties	**Test Method**	**Typical Value**
Tensile Strength	ISO 10319	25.0 kN/m (1,713 lb/ft)
Elongation at Peak	ISO 10319	60%
Thickness at 20 kPa (418 lb/ft^2)	ISO 9863	7.0 mm (0.27 in)
Thickness at 200 kPa (4,177 lb/ft^2)	ISO 9863	6.5 mm (0.25 in.)
Hydraulic Flow Rate (gradient = 1)		
σ_v = 20 kPa (418 lb/ft^2)	ISO 12958	84 l/m/min (6.72 gal/ft/min)
σ_v = 100 kPa (2,089 lb/ft^2)	ISO 12958	72 l/m/min (5.76 gal/ft/min)
σ_v = 200 kPa (4,177 lb/ft^2)	ISO 12958	66 l/m/min (5.34 gal/ft/min)
σ_v = 500 kPa (10,443 lb/ft^2)	ISO 12958	48 l/m/min (3.84 gal/ft/min)
Non-woven Geotextile Properties		
Mass Per Unit Area	ISO 9864	120 to 140 g/m^2 (0.025 to 0.029 lb/ft^2)
Opening Size	ISO 12956	0.07 mm (0.0027 in.)

σ_v = vertical stress

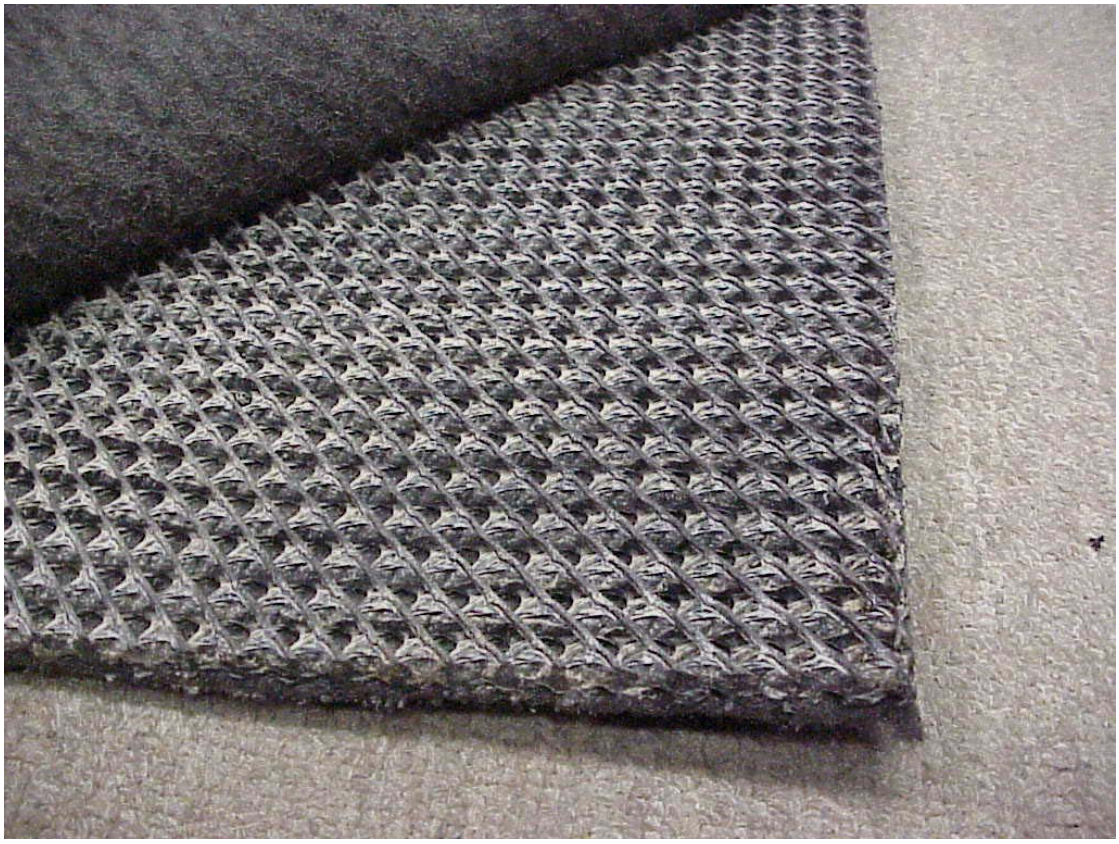

Figure 3.3 Photo of internal structure of drainage geocomposite and external filter fabric.

3.4. Subgrade and Subbase Course Properties

3.4.1. In-Situ Subgrade Properties

The soils beneath this section of Route 9 are known for their poor performance as highway subgrade. Prior to reconstruction, this portion of Route 9 had suffered several local bearing capacity failures, resulting in substantial rutting and pavement cracking.

A subsurface investigation reported poor subgrade soils throughout the length of the project (Fogg, 2002). Moist clay soils were encountered in every boring. These soils are known as the Presumpscot Formation, a marine clay deposited during the retreat of

the glacier that had covered the state of Maine during the Wisconsin glaciation 11,000 to 14,000 years ago. These soils were moist and plastic with standard penetration blow counts as low as 10. The water content, liquid limit, plasticity index, and classification of the subgrade samples taken during the subsurface investigation are summarized in Table 3.3. Grain size distributions of the subgrade samples are shown in Figures 3.4 through 3.7.

Table 3.3 Subgrade sample properties.

Boring and Sample ID	Test Section	Station (m)	Offset (m)	Depth (m)	WC	LL	PI	Classification	
								Unified	AASHTO
HB-MONM 101/TS1-1	1	1+550	RT	Subgrade	12.8	--	--	SM	A-4
HB-MONM 101/TS1-2	1	1+550	RT	Subgrade	13.1	--	--	SM	A-4
HB-MONM 102/TS2-1	2	1+610	RT	Subgrade	15.7	--	--	SM	A-2-4
HB-MONM 102/TS2-2	2	1+610	RT	Subgrade	16.8	--	--	SM	A-4
HB-MONM 103/TS3-1	3	1+670	RT	Subgrade	14.0	--	--	CL-ML	A-4
HB-MONM 103/TS3-2	3	1+670	RT	Subgrade	21.1	27	10	CL	A-4
HB-MONM 104/TS4-1	4	1+730	RT	Subgrade	17.1	--	--	CL-ML	A-4
6-4	6	3+965	0.88 RT	2.29-3.0	23.4	21	5	CL-ML	A-4
7-4	7	4+000	0.88 RT	1.52-2.0	26.1	27	9	CL	A-4
8-2	7	4+040	0.88 RT	0.52-1.52	38.6	NP		CL-ML	A-4
8-3	8	4+040	0.88 RT	1.52-1.83	23.3	NP		CL-ML	A-4
8-4	8	4+040	0.88 RT	1.83-3.0	27.3	24	6	CL-ML	A-4
9-2	9	4+080	0.88 RT	0.61-1.22	29.5	26	6	CL-ML	A-4
10-2	10	4+120	0.88 RT	0.76-3.0	16.6	20	3	ML	A-4
11-1	11	4+690	0.88 RT	0.30-0.88	15.2	--	--	CL-ML	A-4
11-2	11	4+690	0.88 RT	0.88-1.34	55.9	40	7	ML	A-4
11-3	11	4+690	0.88 RT	1.34-2.44	30.7	31	14	CL	A-6
12-2	12	4+710	0.88 RT	2.44-3.0	--	--	--	--	--

*Data Provided by MaineDOT
*NP = Non-plastic

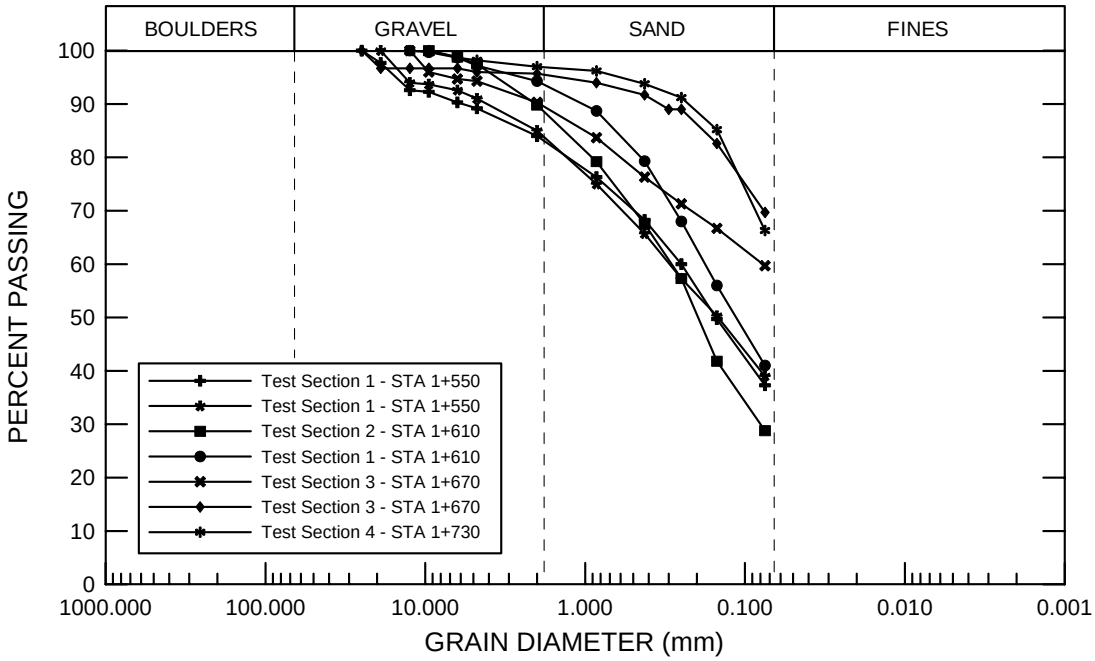

Figure 3.4 Subgrade sieve and hydrometer analysis for test sections 1 through 4.

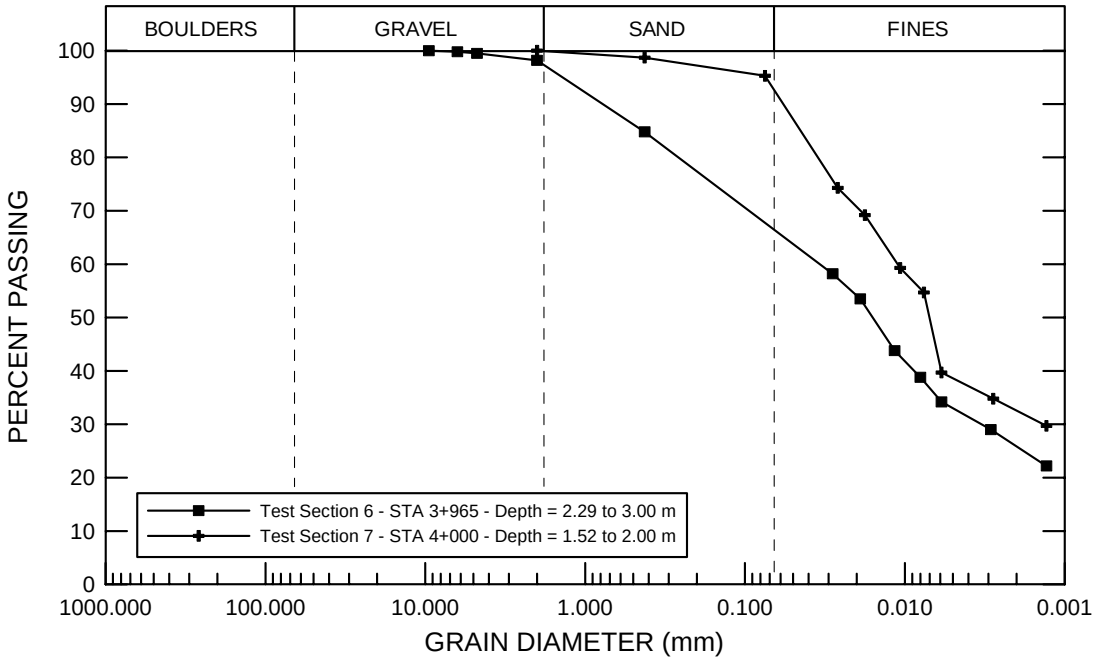

Figure 3.5 Subgrade sieve and hydrometer analysis for test sections 6 and 7.

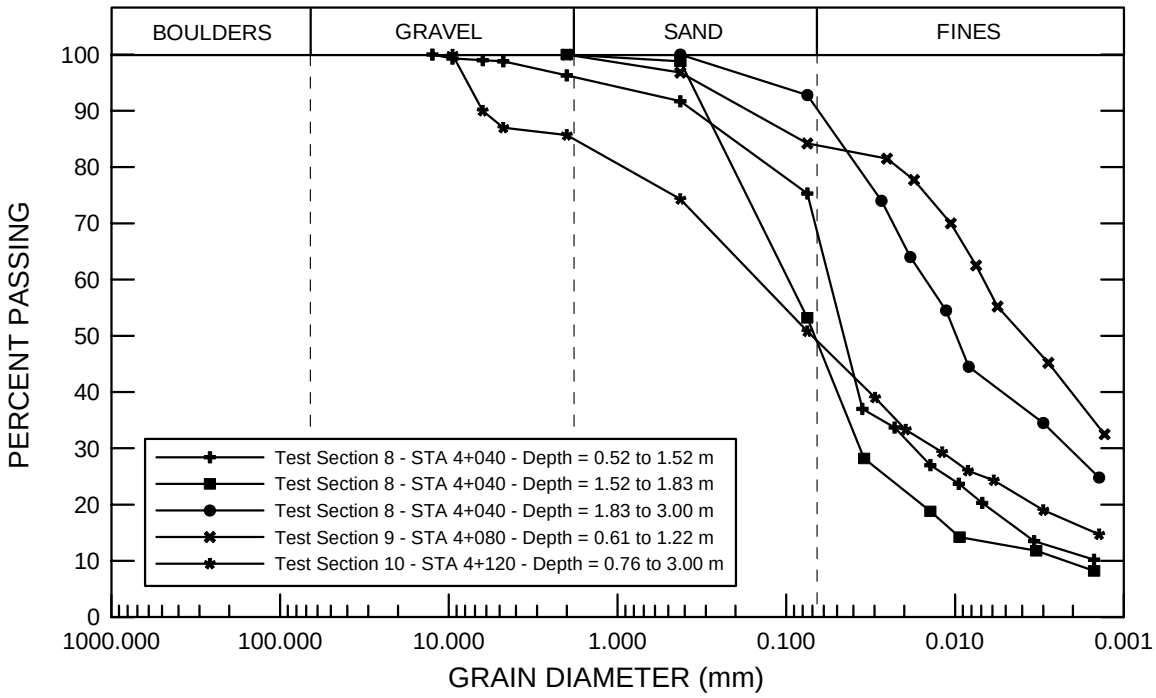

Figure 3.6 Subgrade sieve and hydrometer analysis for test sections 8 through 10.

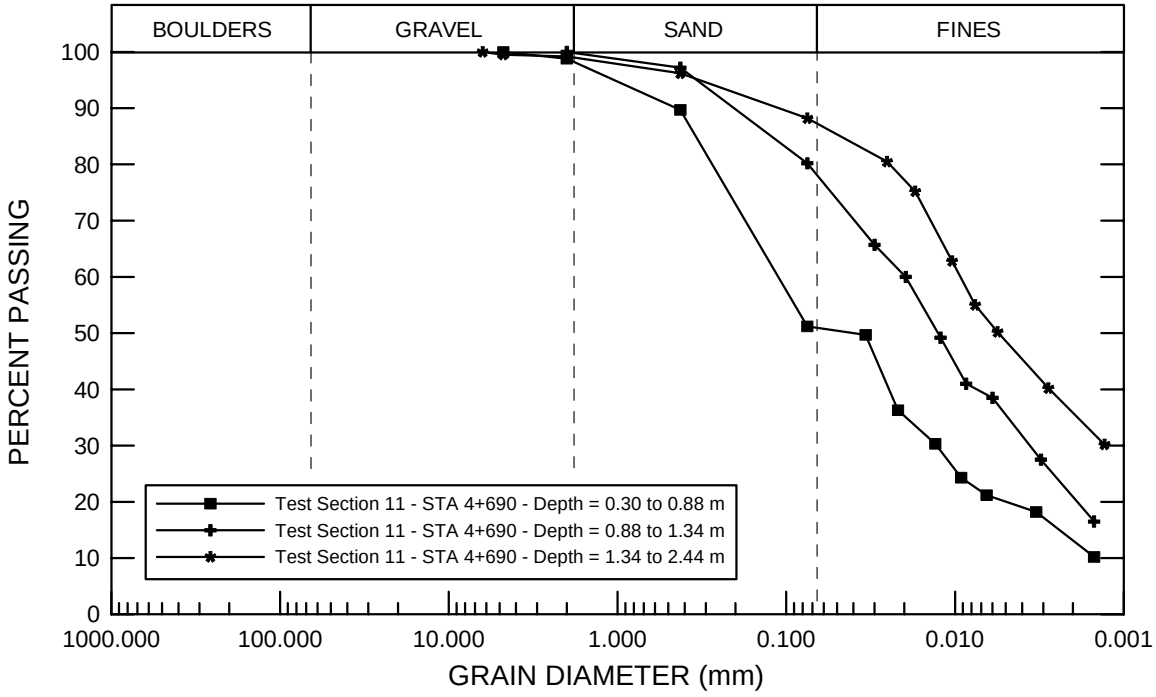

Figure 3.7 Subgrade sieve and hydrometer analysis for test section 11.

3.4.2. Subbase Course Properties

The subbase course aggregate used in the reconstruction of Route 9 in Litchfield was well-graded sandy gravel. It is classified as AASHTO A-1-a. MaineDOT specified Type D subbase as shown in Table 3.4. The grain size distributions of three samples of this material as well as the specified gradation are shown in Figure 3.8.

Table 3.4 MaineDOT subbase grain size specifications.

Sieve Size	Specified Percent Passing
150-mm (6-in.)	100%
6.3-mm (0.25-in.)	25 to 70%
0.425-mm (No. 40)	0 to 30%
0.075-mm (No. 200)	0 to 7%

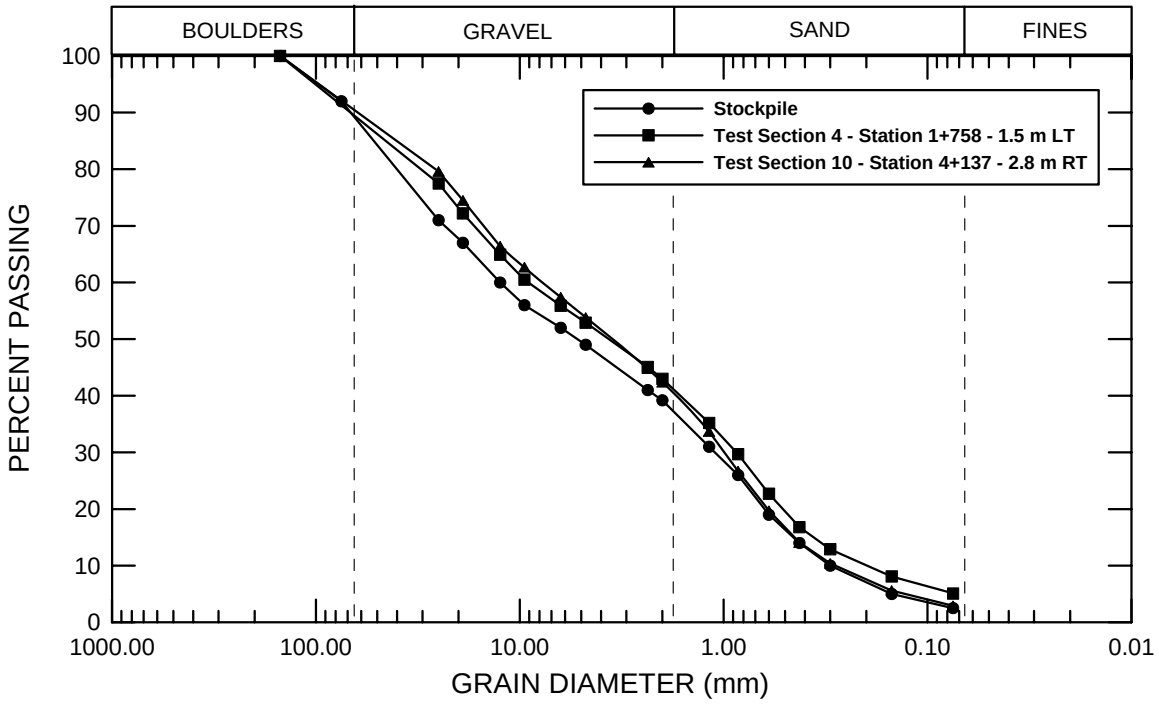

Figure 3.8 Subbase course aggregate sieve analysis.

3.5. Construction Procedures

The prime contractor during the first work season was Farrin Brothers. Construction of test sections 6 through 12 began on September 11, 2001 and continued until mid-October when the test sections were paved. M&H Logging was the prime contractor during the second work season. Construction of test sections 1 through 5 began on June 24, 2002 and continued until July 17 when paving began.

Typical construction procedures were used. In test sections 1 through 5 the existing roadway was excavated to subgrade. The new subbase was installed in two 150 mm (6 in.) lifts and compacted to 95% of modified proctor maximum dry density. In test sections 6 through 10 the new subbase was installed in two 300 mm (12 in.) lifts. Test sections 11 and 12 were reclaimed to a depth of 75 mm (3 in.). The reclaiming did not extend into the underlying subbase, so the material consisted only of pavement grindings. The resulting compacted subbase ranged from 75 to 150 mm (3 to 6 in.) thick.

Critical project dates are summarized in Table 3.5. The installation of the reinforcement geogrid and drainage geocomposite is described in the following sections.

Table 3.5 Critical project dates.

Date	Task
9/11/01 through 10/4/01	Test sections 6 through 12 constructed and instrumented.
10/11/02 through 10/23/02	Test sections 6 through 12 paved.
11/17/01	Subbase course piezometers in test sections 8 through 10 stop working.
12/4/01	Inoperable subbase course piezometers replaced.
2/16/02	Instruments in test sections 6 through 10 connected to data acquisition system.
6/24/02 through 7/1/02	Test sections 1 through 5 constructed and instrumented.
7/15/02	Instruments in test sections 1 through 5 connected to data acquisition system.
7/17/02	Test sections 1 through 5 paved.
3/6/03	Flow meters installed*

*Installation delayed due to difficulties in calibrating suitable instrumentation.

Upon excavation to subgrade near the western end of the project between stations 1+460 m (4+790 ft) and 1+520 m (4+987 ft) very soft subgrade soils were encountered. Rather than utilize this area to evaluate the performance of an instrumented section of reinforcement geogrid as originally planned, MaineDOT opted to construct the 60-m (197-ft) section using 600 mm (24 in.) of subbase course gravel. Although no test sections were constructed in this area, contractors placed geogrid on subgrade between stations 1+460 m (4+790 ft) and 1+520 m (4+987 ft) to facilitate reconstruction. Test sections 1 through 5 were moved forward 60 meters. Under the revised work plan test section one began at station 1+520 m (4+987 ft). The locations of test sections four and five were switched under the revised work plan to allow for the installation of a section of instrumented reinforcement geogrid on particularly wet subgrade soils.

3.5.1. Reinforcement Geogrid Installation

Construction procedures developed for the placement of the reinforcement geogrid are based on recommendations of Dr. Barry Christopher, a geotechnical consultant in the geosynthetics industry. They are generally the same as those recommended by the manufacturer. The contractors adhered to the procedures listed below.

The reinforcement geogrid was unrolled and laid down at the proper elevation and alignment as shown on MaineDOT construction plans. The geogrid was oriented such that the roll length was parallel to the roadway centerline. Consecutive rolls were overlapped a minimum of 300 mm (12 in.). Rolls adjacent at the centerline were

overlapped a minimum of 450 mm (18 in.). All seams were tied with plastic ties spaced 2000 to 3000 mm (80 to 120 in.). Granular subbase course aggregate was dumped from trucks riding on reinforced fill and bladed onto the geogrid with a dozer, keeping the fill ahead of the blade by gradually raising the blade while moving forward. No construction equipment was allowed to travel over the geogrid without a minimum of 150 mm (6 in.) of subbase course aggregate cover. Initial compaction was done with a dozer and then a smooth drum vibratory roller was used to compact the subbase course aggregate. Ruts that formed during construction were filled with additional material rather than blading material from high areas between the ruts. This procedure is necessary to prevent damage to the geogrid in high areas between the ruts. In areas where the geogrid is placed within the subbase course rather than on subgrade, the aggregate was uniformly graded to a tolerance of plus or minus 25 mm (1 in.) of the desired elevation.

The geogrid installation is shown in Figures 3.9 and 3.10. The most common problem encountered during the installation was a wave that developed in the geogrid just ahead of advancing fill, as shown in the photo in Figure 3.11.

Figure 3.9 Geogrid unrolled on subgrade.

Figure 3.10 Subbase material bladed onto geogrid.

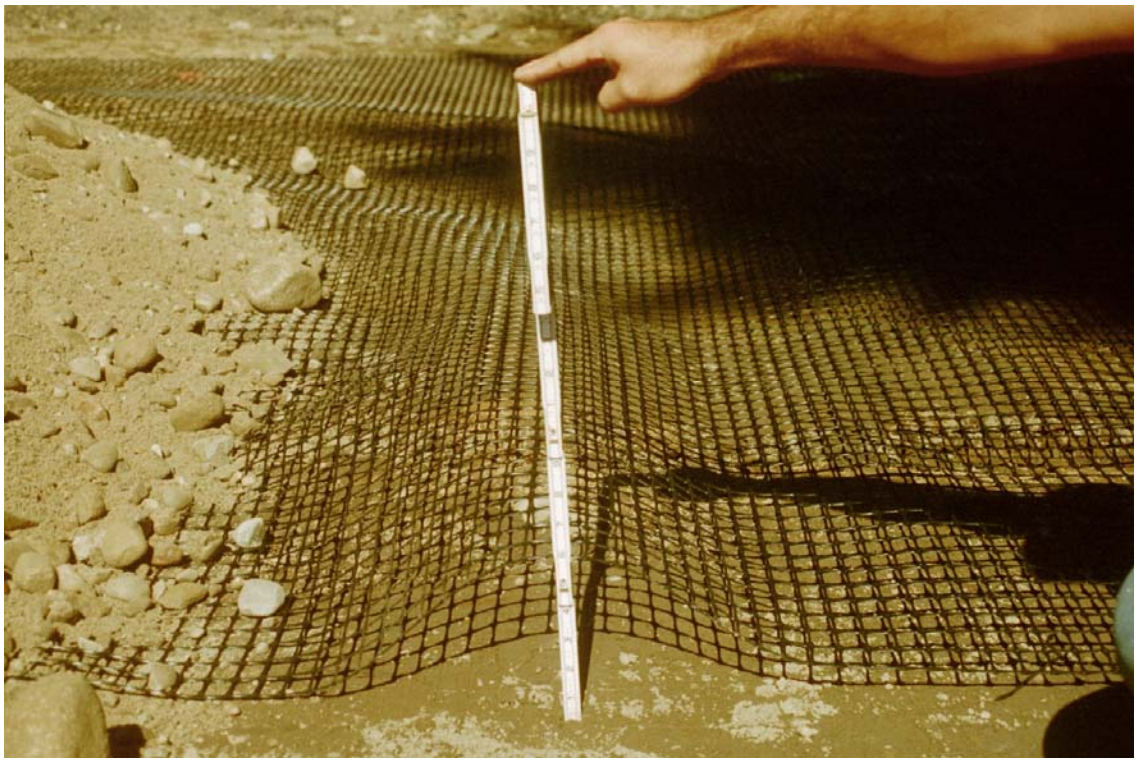

Figure 3.11 Wave of geogrid ahead of subbase placement.

To attempt to control this, laborers stood on the geogrid in front of the wave as subbase material was bladed forward by the dozer. This caused the wave of geogrid to fold over onto itself and the wave was eliminated. The geogrid was not anchored to the material it was placed on. As a result, even when waves were eliminated by the procedure described, the advance of subbase material quickly generated another. An effort was made to terminate waves just before instrumented sections of geogrid in order to keep the entire instrumented section in contact with the material it was placed on.

Upon excavation of the test sections large areas of soft and moist subgrade soils were observed. Ruts as deep as 75 mm (3 in.) developed in test section 3 when the reinforced subbase was opened to traffic. The addition of new material to the ruts helped to reduce their size and occurrence.

Despite the 150-mm (6-in.) maximum size specification on the subbase material, particles as large as 300 mm (12 in.) were observed. This included both boulders and pieces of discarded ceramic pipe.

3.5.2. Drainage Geocomposite Installation

The following procedures for the placement of the drainage geocomposite were developed by MaineDOT with the assistance of Dr. Barry Christopher. These procedures were well adhered to by the contractors.

The drainage geocomposite was unfolded and placed at the proper elevation and alignment as shown on MaineDOT construction plans.

The drainage geocomposite was oriented such that it could be unfolded parallel to the roadway centerline.

Subbase course aggregate was dumped from trucks traveling on previously placed fill and bladed onto the drainage geocomposite with a dozer, keeping the fill ahead of the dozer by gradually raising the blade while moving forward.

No construction equipment was allowed to travel on the drainage geocomposite without a minimum of 150 mm (6 in.) of subbase course aggregate cover.

Ruts that formed during construction were filled with additional material rather than blading down material from the high areas between the ruts. This procedure is necessary to prevent damage to the drainage geocomposite at the high areas between the ruts.

Initial compaction of the subbase course aggregate was done with a dozer and then with a smooth drum vibratory roller.

Adjacent panels were butt jointed flush at the core with the overlapping flap shingled in the direction of fill placement as shown in Figure 3.12

The centerline joint was overlapped a minimum of 75 mm (3 in.) with a 610 mm (24 in.) strip of non-woven, needle punched, polypropylene evenly spaced on the top and bottom of the joint as shown in Figure 3.13

The drainage geocomposite was wrapped around a slotted collector pipe running parallel to the centerline as shown in Figure 3.14. A photo of this installation is shown in Figure 3.15.

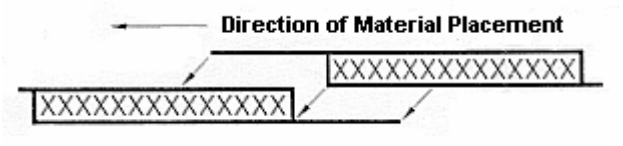

Figure 3.12 Butt joint detail.

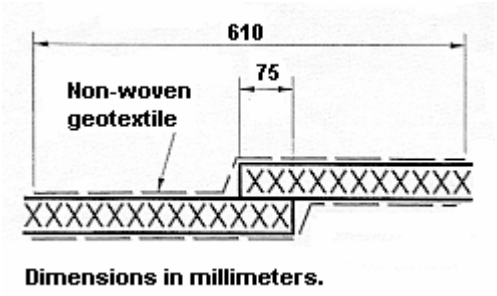

Figure 3.13 Centerline overlap joint detail.

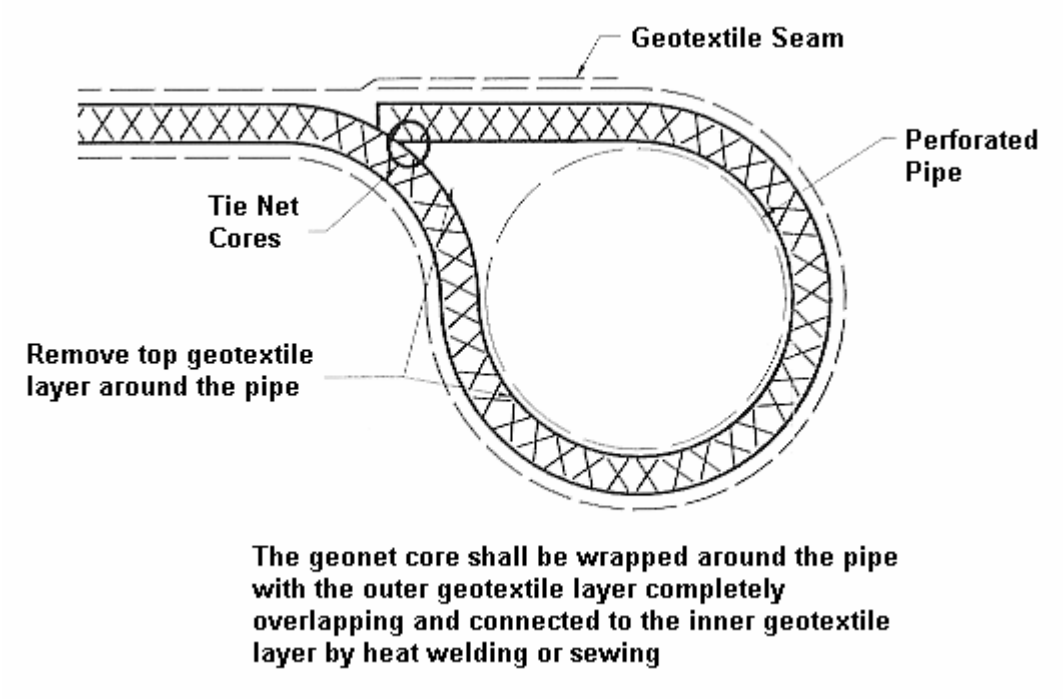

Figure 3.14 Collector pipe detail.

Figure 3.15 Drainage geocomposite and collector pipe.

It was relatively easy for the contractors to place the drainage geocomposite on subgrade. However, the installation of the collector pipe was very problematic. The internal drainage structure is stiff and did not fold around the pipe easily. Up to three laborers were required to hold the drainage geocomposite around the pipe while another attached a plastic tie to the internal drainage structure.

3.6. Summary

The reconstruction of Route 9 in Litchfield presented an opportunity to evaluate the performance of two types of geosynthetics on soft subgrade soils. Prior to reconstruction the road was in poor condition with several local bearing capacity failures that had resulted in substantial pavement rutting and cracking. The subgrade soils are generally classified as AASHTO A-4 with standard penetration blow counts as low as 10.

Reinforcement geogrid and drainage geocomposite were used to evaluate their performance on soft subgrade soils in a cold region. This was done by comparing data from test sections that used the geosynthetics with control sections that did not. In addition, comparisons with previous field studies were made.

A total of twelve test sections were constructed over the course of two work seasons. The performance of Tensar BX1200 geogrid and Tenax Tendrain 100-2 drainage geocomposite was investigated. Test sections 1 through 5 were constructed during the summer of 2002 and use a 300 mm (12 in.) subbase. Test sections 6 through 10 were constructed in the fall of 2001 and use a 600 mm (24 in.) subbase. Test sections 11 and 12, also constructed in the fall of 2001, have a 75 to 150 mm (3 to 6 in.) subbase of pavement grindings.

The test sections vary the type and location of the geosynthetics used. Geogrid on subgrade and at the center of the subbase was investigated using both a 300 mm (12 in.) and 600 mm (24 in.) subbase. Drainage geocomposite on subgrade was investigated using both a 300 mm (12 in.) and 600 mm (24 in.) subbase. Drainage geocomposite on subgrade and reinforcement geogrid at the center of the subbase was investigated for both a 300 mm (12 in.) and 600 mm (24 in.) subbase. Drainage geocomposite on subgrade overlain by 75 to 150 mm (3 to 6 in.) of pavement grindings was investigated.

Procedures for the placement of the geosynthetics were developed by MaineDOT with the help of Dr. Barry Christopher, a geotechnical consultant in the geosynthetics industry. The geosynthetics were oriented such that they could be unrolled or unfolded parallel to the roadway centerline. The reinforcement geogrid was overlapped and tied with plastic ties and the drainage geocomposite was butt jointed. Subbase course aggregate was dumped from trucks traveling on previously placed fill and bladed onto the geosynthetics using a dozer, keeping the fill ahead of the dozer by gradually raising the blade while moving forward. No construction traffic was allowed on the geosynthetics without a minimum of 300 mm (6 in.) of subbase aggregate cover. Initial compaction of the subbase course aggregate was done with a dozer and loaded truck traffic, followed by a smooth drum vibratory roller.

The subbase course aggregate was well-graded sandy gravel. It was classified as AASHTO A-1-a.

CHAPTER 4
INSTRUMENTATION AND FIELD MEASUREMENTS

4.1. Introduction

Instrumentation was installed to monitor the performance of the test sections. The reinforcement geogrid was equipped with strain gages to deduce tensile loads. Test sections using drainage geocomposite had vibrating wire piezometers to monitor porewater pressures in the subgrade and subbase course. Drainage sections also used flow meters to measure the amount of water captured by the drainage geocomposite collector pipe. Each test section had a thermocouple string to measure frost penetration.

The majority of the instruments were read hourly by a data acquisition system. However, the strain gages and thermocouples in test sections 1, 4, 6, and 10 were read manually. Piezometers and thermocouples were read manually in test sections 11 and 12. Manual strain gages were read monthly except from mid-February to late April when they were read weekly to capture the effects of the spring thaw. Manual thermocouples were read monthly from November to mid-February. Then, weekly until the end of the freezing season to ensure that the maximum frost penetration was recorded. Manual piezometers were read weekly from mid-February to late April to monitor porewater pressures during the spring thaw. Once the thawing season was over manual piezometer readings were taken monthly. Manual piezometers were not read during the freezing season since the porewater was frozen and the readings have no meaning.

The purpose of the instrumentation was to collect data that allowed for the performance of test sections using geosynthetics to be both quantified, and compared to the performance of the control sections. Strain gage data was used to verify that the

geogrid was supporting load and providing reinforcement to the pavement structure. Piezometer data indicates whether the subbase and subgrade were more readily drained when drainage geocomposite was installed. Thermocouple data provided a measurement of the maximum frost penetration and more importantly the timeline of the spring thaw.

4.2. Strain Gages on Geogrids

Each test section with geogrid was instrumented at two stations. Each instrumented station had strain gage pairs on five ribs located in the outside wheel path of the right (eastbound) lane. Four pairs were on ribs perpendicular to the roadway centerline, one pair was on a rib parallel to the centerline. The strain gages were installed in pairs, one on top and one on bottom, such that the values can be averaged to eliminate the effects of bending. In addition, each instrumented station had an instrumented rib that had been cut from geogrid. This rib was placed in a 100 mm (4 in.) PVC electrical junction box attached to the geogrid. The isolated rib only measures strains associated with thermal expansion and contraction.

4.2.1. Strain Gage Characteristics

The strain gages were Texas Measurements model FLA-5-23. They have a gage factor of 2.16 and are capable of measuring strains up to 3%. The gages use a copper-nickel alloy foil element 0.003 to 0.007 mm (0.00012 to 0.00027 in.) thick on a very thin epoxy backing measuring 10 mm by 3 mm (0.39 in. by 0.12 in.). The backing was attached to the instrumented ribs using a two-part epoxy. The gages had presoldered lead wires 5 m (16.4 ft) in length.

Readings were taken by attaching the lead wires to either a Micro Measurements P3500 Strain Indicator or a Campbell Scientific data acquisition system, which provided a known excitation voltage of approximately 2500 mV. Measurements were taken using the Wheatstone bridge, as shown in Figure 4.1.

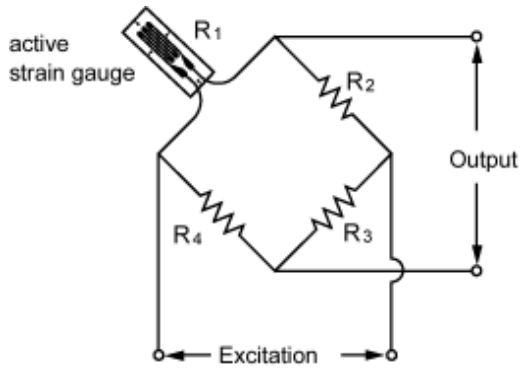

Figure 4.1 Wheatstone bridge configuration (Texas Measurements, 2001).

The strain gages used a quarter bridge configuration. The output voltage varies with the resistance of the gage, which is a function of the strain on the instrumented rib. Changes in the gage resistance over time using the Wheatstone bridge measurement with constant excitation voltage are directly proportional to changes in strain in the gage. Assuming that $R=R_1=R_2=R_3=R_4$ and that the strain gage resistance varies from R to $R+\Delta R$, then the output voltage can be calculated with Equation 4.1. When ΔR is << then R, Δe can be expressed as in Equation 4.2.

$$e = \frac{R_1 R_3 - R_2 R_4}{(R_1 + R_2)(R_3 + R_4)} E \qquad \text{Equation 4.1}$$

$$\Delta e = \frac{\Delta R}{4R} E = \frac{E}{4} K\varepsilon \qquad \text{Equation 4.2}$$

where:

e = output voltage

E = excitation voltage

R_1 = gage resistance

R_2-R_4 = resistance of fixed resistors

$R = R_1 – R_4$

K = gage factor

ε = strain

4.2.2. Strain Gage Attachment to Geogrid

The strain gages were attached to 15-m (49-ft) long sections of geogrid in the laboratory. Ribs to be instrumented were first burnished with emery cloth and then treated with Texas Measurements poly-primer. Roughing the surface of the rib and treating it with poly-primer helps to achieve a good bond. A piece of Scotch tape was applied to the gage backing and Cyanoacrylate CN adhesive was applied to the gages. The gages were centered on the prepared ribs and held in place with the scotch tape while the adhesive cured. Direct pressure was applied to the gage for at least one minute and the adhesive was allowed to cure for approximately five minutes before the tape was peeled off the backing. All of the gages on the top of the grid were applied first. Then the geogrid was flipped over and the bottom was instrumented.

Two protective coatings were then applied to the instrumented ribs. The first was a thinned neoprene rubber (Texas Measurements coating N-1). This was brushed over the gage and uninsulated portion of the leads and allowed to cure for a minimum of eight hours. The final protective coating was a two-part epoxy comprised of Araldite A-Epoxy Resin AW 106 and Araldite A-Hardener HV953U. This was applied over the entire instrumented rib and uninsulated portion of the gage leads creating a shell approximately 6 mm (0.25 in.) thick. The epoxy was allowed to cure for a minimum of 24 hours. A photo of two instrumented ribs with cured epoxy coating is shown in Figure 4.2.

Figure 4.2 Photo of epoxy coated strain gages.

Pairs of lead wires from each of the instrumented ribs were snaked through 10-mm (0.39-in.) Teflon tubing extending from the instrumented ribs to a central 100-mm (4-in.) PVC electrical junction box. Silicon caulk was injected into the tubing where the lead wires entered it for extra protection against the subbase course aggregate. The tubing was attached to the geogrid with plastic ties. The gage layout is shown in Figures 4.3 and 4.4. Gage orientations and offsets are summarized in Table 4.1. In addition, gages 11 and 12 were attached to a single rib housed in the 100-mm (4-in.) PVC electrical junction box to measure thermal effects on strain readings.

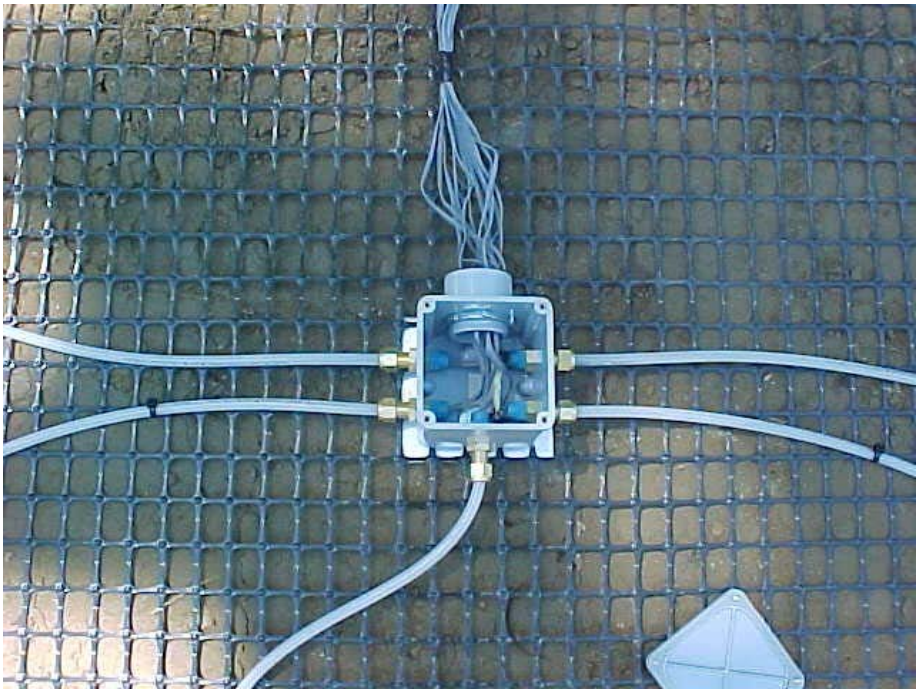

Figure 4.3 Photo of 4-in. PVC electrical junction box.

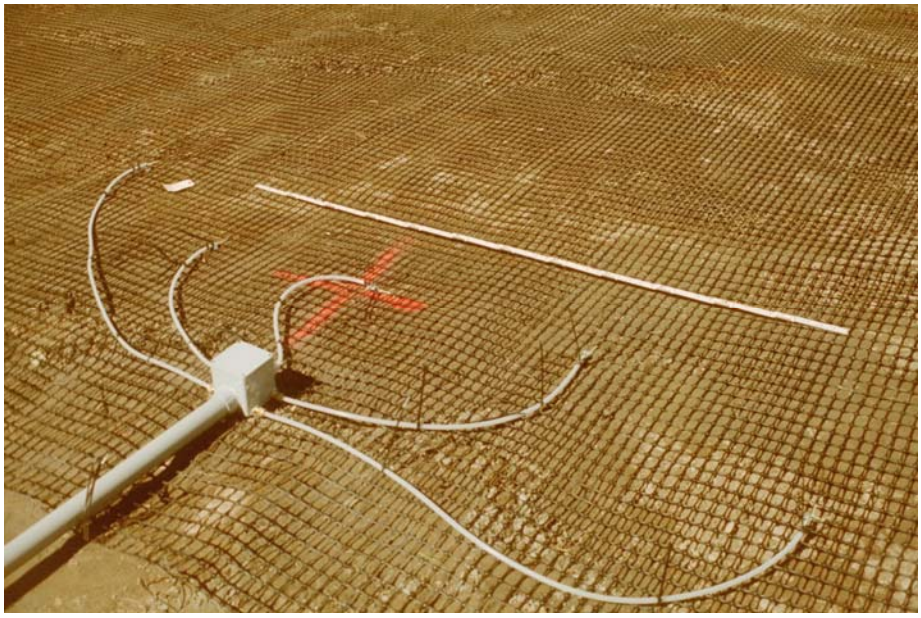

Figure 4.4 Photo of strain gages.

Table 4.1 Summary of gage offsets and orientations.

Gage Pair	Gage No.	Orientation Relative to Roadway Centerline	Offset From Roadway Centerline (m)
1	1	Perpendicular	2.6
	2	Perpendicular	2.6
2	3	Perpendicular	2.9
	4	Perpendicular	2.9
3	5	Parallel	2.9
	6	Parallel	2.9
4	7	Perpendicular	2.9
	8	Perpendicular	2.9
5	9	Perpendicular	3.2
	10	Perpendicular	3.2

4.2.3. Strain Gage Locations

Each test section with geogrid was instrumented with five pairs of strain gages at two stations. The location of each group of strain gages is summarized in Table 4.2.

Table 4.2 Strain gage locations.

Test Section	Station (m)	Offset of Rib Parallel to centerline (m)	Manual or Automated Readings
Test Section 1	1+540	2.9 RT	Manual
	1+560	2.9 RT	Automated
Test Section 2	1+600	2.9 RT	Automated
	1+620	2.9 RT	Automated
Test Section 4	1+720	2.9 RT	Automated
	1+740	2.9 RT	Manual
Test Section 6	3+950	2.9 RT	Manual
	3+970	2.9 RT	Automated
Test Section 7	3+990	2.9 RT	Automated
	4+010	2.9 RT	Automated
Test Section 10	4+110	2.9 RT	Automated
	4+130	2.9 RT	Manual

4.2.4. Field Installation

The instrumented sections were unrolled and aligned such that the center instrumented rib parallel to the centerline was at the desired station at an offset of 2.9 m (9.5 ft) right (see Figure 4.4). Approximately 75 mm (3 in.) of sand was shoveled over the instrumented ribs and the strain gage lead wires to protect them from direct contact with gravel-sized particles in the subbase aggregate that could cause damage during compaction. The leads were collected at the 100 mm (4 in.) electrical junction box. A 38 mm (1.5 in) PVC conduit extending from the 100 mm (4 in.) box to the top of the right backslope was installed. The conduit lay on subgrade from the 100 mm (4 in.) PVC box to the edge of the right travel lane. A trench was dug from there to the manual readout

station at the top of the right backslope to keep the conduit a minimum of 150 mm (6 in.) below the finish grade of the ditch as shown in Figure 4.5.

Figure 4.5 Photo of manual readout station and PVC conduit in the backslope.

Prior to snaking the leads through the 38-mm (1.5-in.) conduit to the manual readout station at the top of the backslope, critical initial strain readings were taken from the edge of the travel lane using a Micro Measurements P3500 Digital Strain Indicator. Two sets of initial readings were taken before any subbase course material was bladed onto the geogrid. Subsequent readings were taken following the placement of the first lift of subbase prior to compaction, following compaction of the first lift, after placement of the second lift prior to compaction, and following compaction of the second lift.

In test sections 6, 7, and 10 the factory leads were snaked from the 100 mm (4 in.) PVC box through the 38 mm (1.5 in.) conduit to a type C conduit body at the edge of the travel lane. There, Belden 18-AWG insulated extension leads were field soldered to the

factory strain gage leads to provide adequate length to reach the top of the backslope and eventually the data acquisition system. Individual soldered connections were protected with small diameter heat shrink tubing. Groups of three connections corresponding to a single strain gage were coated in silicon caulk and encased in a larger diameter heat shrink tube for a watertight connection. Following field soldering the extensions in test sections 6, 7, and 10 were snaked to the manual readout station at the top of the backslope. In test sections 1, 2, and 4 the extensions were soldered in the laboratory.

To speed the process of taking manual readings, a system of RJ11 four wire phone clips was devised. Lead wires coming from the strain gages are equipped with a male phone clip at the manual readout stations. Lead extensions that connect to the data acquisition system as well as those that connect to the P3500 Readout Unit have a female phone clip. This allows for each gage to easily be disconnected and reconnected to either the P3500 or the data acquisition system. A manual readout station with phone clip setup is shown in Figure 4.6.

Figure 4.6 Manual readout station.

Ten of the twelve instrumented stations have strain gages that are read hourly by a data acquisition system. These gages have lead extensions that travel from the manual readout stations to the data acquisition system through 38-mm (1.5-in.) PVC conduit along the top of the right backslope. The gages are wired to one of three Campbell Scientific AM416 multiplexers that relay the readings to a CR10X datalogger. The data acquisition system will be discussed in more detail in section 4.6.

4.2.5. Strain Gage Calibration

A series of wide-width tensile tests (ASTM D4595) were performed in the laboratory to determine the relationship between the strain gage readings and the load per unit width carried by the geogrid. Pieces of geogrid measuring 914 mm by 1524 mm (36 in. by 60 in.) were bolted into channel section grips measuring 1.5 m (5 ft) in length and spaced 0.30 m (1 ft) to maintain a width ratio 1:5. Epoxy was poured between the channel sections to secure the grid. West System 105 epoxy resin was combined with 206 hardener and 404 high-density filler in a 5:1:5 ratio, respectively.

Three test pieces of geogrid were instrumented with strain gages. Each test piece had at least two instrumented ribs each with a pair of strain gages oriented parallel to the direction of loading. The gages were attached and protective coating was applied using the same procedure as those installed in the field.

Each geogrid was loaded into an Instron Model 4400R and subjected to three load cycles at a rate of 1.02 mm/min (0.04 in./min). A photo of a test specimen secured in the grips and loaded into the testing machine is shown in Figure 4.7. Delta strain readings from three of the four strain gages were taken once per minute during each load cycle

using a Campbell Scientific CR10X datalogger. The remaining gage was read once per minute manually using a Micro Measurements P3500 Digital Strain Indicator. The applied load was read manually from the Instron once per minute. Loads were applied to achieve 100 to 150% of the maximum strain measured in the field. The data collected was plotted and it was determined that there was a nearly linear relationship between the delta microstrain recorded by the strain gages and the applied load per unit width. An average slope was calculated and applied to the field delta microstrain to determine the load per unit width in the field. A sample calibration plot is shown in Figure 4.8. The loading portion of the curve begins at zero delta microstrain and ends at the maximum value recorded. The best-fit slopes from all of the tensile tests are summarized in Table 4.3. The first test geogrid was not fully loaded and generated slightly higher slopes. The slopes from test grid one were not used in the average slope applied to the field delta microstrains. Complete test results and fit equations can be found in Appendix A.

Figure 4.7 Wide-width tensile test specimen.

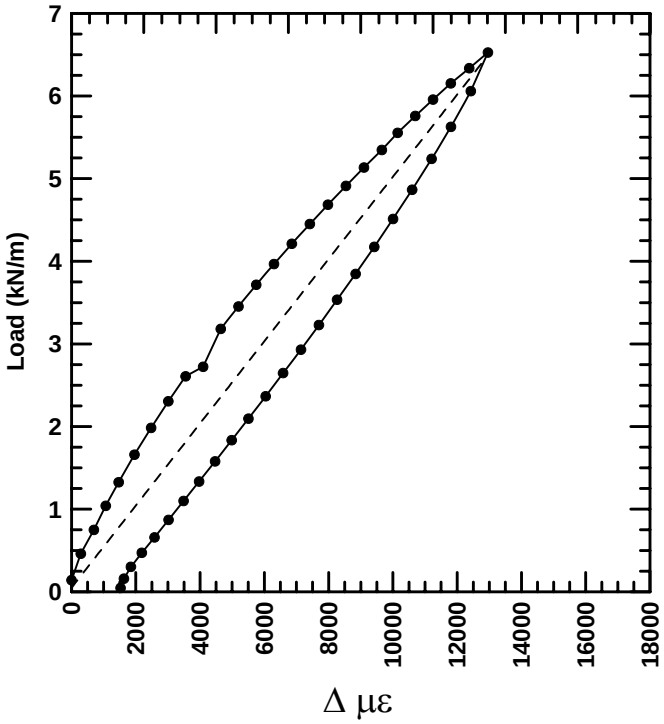

Figure 4.8 Sample wide-width tensile test calibration plot.

4.3. Vibrating Wire Piezometers

Vibrating wire piezometers were used to monitor porewater pressures in the subgrade and subbase course in test sections 3, 4, 5, 8, 9, 10, 11, and 12. These readings were used to evaluate the effectiveness of the drainage geocomposite in reducing the subgrade and subbase course porewater pressures, particularly during the spring thaw. All the piezometers were installed in the outside wheel path of the right eastbound lane.

4.3.1. Vibrating Wire Piezometer Characteristics

The vibrating wire piezometers were Roctest Model PW, capable of measuring porewater pressures ranging from –34 kN/m^2 to 34 kN/m^2 (-5 psi to 5 psi) with an accuracy of ± 0.5% full scale. A low air-entry porous stone was chosen because the adjacent soil would be partially saturated for a portion of the year. The low air entry stone helps to maintain saturation of interior cavity of the piezometer body. To increase

Table 4.3 Summary of best fit slopes from geogrid calibration tests.

Specimen	Load Cycle	Max Load (kN/m)	Gage	Slope
Specimen 1	Test 1	0.76	1	0.000642
			2	0.000850
			3	0.000878
			4	0.000710
	Test 2	0.89	1	0.000754
			2	0.000660
			3	0.000843
			4	0.000873
Specimen 2	Test 1	3.69	1	0.000570
			2	0.000482
			3	0.000570
			4	0.000383
	Test 2	5.16	1	0.000508
			2	0.000466
			3	0.000538
			4	0.000363
	Test 3	6.53	1	0.000497
			2	0.000484
			3	0.000547
			4	0.000371
	Test 4	4.40	1	0.000570
			2	0.000525
			3	0.000604
			4	0.000410
Specimen 3	Test 1	4.10	1	0.000617
			2	0.000513
			3	0.000528
			4	0.000557
	Test 2	5.26	1	0.000561
			2	0.000451
			3	0.000508
			4	0.000523

the service life of the piezometers under freezing conditions, the porous stone and the interior cavity of the piezometer body were saturated with 95% ethanol using the following procedure. First, the porous stones were removed from the piezometer body and saturated in 95% ethanol. Then, the piezometer bodies were submerged in 95% ethanol with the interior cavity facing up to insure that no air bubbles were trapped. With the piezometer bodies submerged in this position the porous stones were replaced. The piezometers remained submerged in ethanol until installation.

4.3.2. Vibrating Wire Piezometer Locations

Vibrating wire piezometers were installed in pairs in each of the test sections with drainage geocomposite as well as the control sections. At each instrumented station a piezometer was installed in the subgrade and the subbase course. The piezometer locations are summarized in Table 4.4.

Table 4.4 Piezometer locations.

Test Section	Station (m)	Subbase or Subgrade	Approximate Depth From Finish Grade (mm)	Connected to Data Acquisition System
Test Section 3 - Control	1+673	Subbase	405	YES
	1+673	Subgrade	660	YES
Test Section 4 - Drainage	1+732	Subbase	405	YES
	1+732	Subgrade	660	YES
Test Section 5 - Drainage	1+793	Subbase	405	YES
	1+793	Subgrade	660	YES
Test Section 8 – Control	4+042	Subbase	710	YES
	4+042	Subgrade	965	YES
Test Section 9 - Drainage	4+082	Subbase	710	YES
	4+082	Subgrade	965	YES
Test Section 10 – Drainage	4+122	Subbase	710	YES
	4+122	Subgrade	965	YES
Test Section 11 – Drainage	4+692	Subbase	255	NO
	4+692	Subgrade	510	NO
Test Section 12 - Control	4+712	Subbase	255	NO
	4+712	Subgrade	510	NO

4.3.3. Field Installation

The piezometers were transported to the field submerged in a bucket of 95% ethanol. In each instrumented test section piezometers were first installed in the subgrade. A hole approximately 203 mm (8 in.) deep was hand-augered in the subgrade soil. The porous stone was covered with moistened subgrade soil to insure good continuity with the soil at the bottom of the hole. The piezometer was inserted into the

hole, porestone end first. The annular space between the instrument body and the edge of the hole was sealed with bentonite.

After the subgrade installation was complete construction crews placed the subbase course material. Following compaction of the subbase course, a hole approximately 203 mm (8 in.) was hand augered. Piezometers were installed in the augered holes porestone end first. Given the permeable nature of the subbase there was no need to use a bentonite seal.

In test sections 3, 4, 5, 8, 9, and 10 the piezometer cables ran perpendicular to centerline to the edge of the travel lane. They were buried in a trench approximately 150 mm (6 in.) deep extending from the edge of the travel lane to the top of the right backslope. There, cables were then inserted into 38-mm (1.5-in.) PVC conduit and snaked to the data acquisition system.

In test sections 11 and 12 the subgrade piezometers were installed following grinding and removal of the existing pavement. A trench approximately 300 mm (12 in.) long and 75 mm (3 in.) deep was hand dug. The piezometers were placed horizontally in the trench with the porestone facing the roadway centerline. The porestone was covered with base material by hand and the trench was backfilled.

Construction crews placed 75 to 150 mm (3 to 6 in.) of pavement grindings over test sections 11 and 12. Following compaction of the grindings the subbase piezometers were installed. A trench approximately 300 mm (12 in.) long and 75 mm (3 in.) deep was hand dug. Piezometers were placed horizontally in the trench with the porestone facing the roadway centerline and the trench was backfilled.

Piezometer cables in test sections 11 and 12 ran perpendicular to centerline to the edge of the travel lane. They were buried in a trench approximately 150 mm (6 in.) deep extending from the edge of the travel lane to the top of the right backslope. There the cables entered a vertical 100-mm (4-in.) PVC pipe through the bottom and the excess cable was stored within the pipe. The piezometers in test sections 11 and 12 were not connected to a data acquisition system. The readings were taken manually at the locations of the 100-mm (4-in.) vertical pipes.

All of the initial piezometer readings as well as the manual readings in sections 11 and 12 were taken with a Roctest MB6T Vibrating Wire Readout Unit. Piezometer lead wires are connected to the unit and the frequency of the vibrating wire as well as the internal temperature of the instrument were recorded. Initial readings for each piezometer were taken with the instrument submerged in a bucket of 95% ethanol, just prior to installation.

The subbase piezometers in test sections eight, nine, and ten stopped functioning shortly after installation. Replacement piezometers were installed following paving of test sections 8 through 10. At each station, MaineDOT cut 100-mm (4-in.) circular holes in the pavement exposing the subbase material. Each pavement hole was located approximately 1 m (3.2 ft) east of the locations of the failed instruments. Holes approximately 203 mm (8 in.) were hand augered in the subbase course and replacement piezometers were inserted porestone end first. Sand was placed around the cable end of the instrument to protect it when the hole was filled with cold patch. A narrow slot approximately 38 mm (1.5 in.) deep was cut in the pavement extending from the location of the replacement piezometer to the edge of the pavement. The cable was placed in the

slot and the slot was filled to finish grade with asphalt crack sealer. The cables were buried in trenches approximately 150 mm (6 in.) deep from the edge of the pavement to the top of the backslope. There they entered 38-mm (1.5-in.) PVC conduit and were snaked to the data acquisition system.

4.4. Flow Meters

Flow meters were installed in test sections 4, 5, 9, 10, 11, and 12 to measure the amount of water captured by the drainage geocomposite collector pipe. They are attached to the outlet of the 100 mm (4 in.) slotted collector pipe that the drainage geocomposite is wrapped around. The collector pipe system is described in detail in Section 3.5.2.

4.4.1. Flow Meter Characteristics

Flow meters purchased from Omega Engineering were installed to measure the amount of water captured by the drainage geocomposite collector pipe. Two types of flow meters were installed. At stations where it was feasible to connect the flow meter to the data acquisition system automated units (Omega Engineering FTB2001) were installed. However, at stations on the left side of the road in test sections 9 and 10 as well as both the left and right stations in test section 11, manual units (Omega Engineering FTB 6105-A), similar to water meters for household connections to municipal water systems, proved more convenient to install.

The automated units measure flow by means of a pulse count. The meter generates 26,100 electrical pulses per gallon of water that travels though it. The data acquisition system counts the number of pulses over the course of each minute and

converts the number of pulses to a flow in gal/min for each one minute increment. The flows are reported as an average over each hour.

The manual units measure flow by means of a mechanical paddlewheel. The paddlewheel is calibrated to turn a dial on the face of the device that reports total flow through the device in gallons. The device is read on regular basis and average flow is calculated based on the total flow recorded over a given time period.

The devices were chosen based on the results of a laboratory test used to determine the minimum amount of head required to operate the device at flows similar to those expected in the field. A constant head tank was constructed and the accuracy of the flows reported by the devices was examined at various levels of upstream head. The devices installed in the field were selected based on their ability to accurately measure flow at very low levels up upstream head. The characteristics of the two devices chosen are summarized in Table 4.5.

Table 4.5 Flow meter characteristics.

Model Number	Measurement Range	Maximum Head Loss Across Instrument	Data Collection Method
FTB 2001	0.5 – 5.0 L/min (0.13 – 1.3 gal/min)	10.3 kPa (1.5 psi)	Automated Readings
FTB 6105-A	0.95 – 75.0 L/min (0.25 – 25.0 gal/min)	42.7 kPa (6.2 psi)	Manual Readings

4.4.2. Flow Meter Locations

Flow meters were installed at the outlets of the 100-mm (4-in.) diameter collector pipes. The collector pipe system is described in Section 3.5.2. Flow meter locations are summarized in Table 4.6.

Table 4.6 Flow meter locations.

Test Section	Station (m)	Flow Meter Model No.	Automated or Manual Readings
Test Section 4	1+760 RT	FTB 2001	Automated
	1+760 LT	FTB 2001	Automated
Test Section 5	1+820 RT	FTB 2001	Automated
	1+820 RT	FTB 2001	Automated
Test Section 9	4+110 RT	FTB 2001	Automated
	4+110 LT	FTB 6105-A	Manual
Test Section 10	4+160 RT	FTB 2001	Automated
	4+160 LT	FTB 6105-A	Manual
Test Section 11	4+700 RT	FTB 6105-A	Manual
	4+700 LT	FTB 6105-A	Manual

4.4.3. Field Installation

The first step was to attach an adapter to the end of the collector pipe. A 600-mm (24-in.) long piece of 150-mm (6-in.) diameter PVC pipe was slipped over the 100-mm (4-in.) collector pipe. The annular space between the two pipes was filled with spray foam insulation (Great Stuff brand). A 150 mm (6 in.) female threaded adapter was glued to the 150 mm (6 in.) pipe and a threaded cap was screwed in.

4.4.3.1 Automated Flow Meter Installation. At stations 1+760 RT, 1+760 LT, 1+820 RT, 1+820 LT, 4+110 RT, and 4+160 RT, an Omega FTB 2001 was installed. A 25-mm (1-in.) hole was tapped in the 150-mm (6-in.) PVC cap and a 25-mm (1-in.) threaded PVC adapter was screwed in. A 25-mm (1-in.) long section of 25-mm (1-in.) diameter PVC was glued to the adapter. Attached to the end of the 25-mm (1-in.) PVC was a 25-mm (1-in.) union fitting to allow for convenient removal of the instrument during the freezing season. A U-shaped 13-mm (0.5-in.) PVC trap was installed with the

flow meter at the low point to insure the line was saturated as shown in the photo in Figure 4.9.

Figure 4.9 Photo of automated flow meter installation.

The 150 mm (6 in.) PVC pipe and 13 mm (0.5 in.) PVC trap were housed in a bottomless plywood box insulated with 25 mm (1 in.) of extruded polystyrene insulation (Figure 4.9). Belden three conductor 16 AWG jacketed lead wire extensions were crimp connected to the factory flow meter leads. Lead wires from flow meters on the right side of the road were snaked through 13-mm (0.5-in.) PVC that extended from the plywood boxes to a 38-mm (1.5 in.) PVC conduit oriented parallel to the top of the right backslope extending from the flow meter stations to a data acquisition system. Lead wires from flow meters on the left side of the road cross to the right side of the road through 19-mm (0.75-in.) diameter PVC conduit placed during construction and continue through 19-mm

(0.75-in.) PVC conduit oriented parallel to the roadway centerline extending from the flow meter stations to a data acquisition system.

4.4.3.2 Manual Flow Meter Installation. At stations 4+110 LT, 4+160 LT, 4+700 RT, and 4+700 LT, an Omega FTB 6105-A was installed. A garden hose spigot was installed at the 150 mm (6 in.) PVC cap. Approximately 15 m (50 ft) of garden house was attached to the spigot and ran down station parallel to the roadway centerline at the bottom of the ditch to provide enough head to operate the device. At the end of the hose the flow meters were attached with hose clamps. The outlet hose was situated below the elevation of the device to insure that the meter remained saturated. This condition must be satisfied for the manual devices to accurately measure flow.

4.5. Thermocouple Strings

Thermocouple strings were installed to measure frost penetration. With the exception of test section 5, there is one thermocouple string in each section. A thermocouple string was installed in what was intended to be test section 1 at station 1+465 m (4+806 ft) prior to MaineDOT's decision to move the test sections ahead 60 m (197 ft). Based on available cable lengths the decision was made to install the thermocouple string intended for test section 5 in the new location of test section 1.

4.5.1. Thermocouple Characteristics

The thermocouples were twelve-pair 20 AWG copper constantan wire (Type T) constructed of TX-212PC/PC041-20 cable from PMC. A bimetal reaction occurs where

the ends of a wire pair are connected resulting in an electrical potential. This potential is proportional to the temperature difference between the end in the ground and the end connected to the readout unit. Using a reference potential from either a handheld readout unit or a data acquisition system, the temperature at the point where the wires are joined in the ground can be calculated. The initial calibration tolerance of the thermocouples was +/- 1 °C (2 °F). This calibration check was performed by comparing the readings at three different temperatures from a thermocouple using the Omega Engineering Readout Unit with those from an ASTM certified mercury thermometer.

The thermocouple strings use a simple construction. Wooden dowels 25-mm (1-in.) in diameter were cut to 1.8-m (6-ft) lengths. Eleven 6-mm (0.25-in.) holes were drilled at 150-mm (6-in.) intervals starting at one end of the rod. The twelfth 6-mm (0.25-in.) hole was spaced 300-mm (12-in.) from the eleventh hole. The outer jacket of the 12-pair cable was removed and the ends of the twelve pairs were joined using a crimped connection. The crimped connections were threaded through the 6-mm (0.25-in.) holes and secured with plastic wire ties. The crimped connections were protected with silicon caulk and covered with rubber heat shrink caps.

All of the wires were gathered at the second thermocouple from the top on thermocouple strings installed in test sections 2 through 4 such that the cable is connected perpendicular to the dowel at that location. This allows the cable to rest on subgrade and hold the dowel in place with the top thermocouple in the center of the 300-mm (12-in.) subbase. Wires were gathered at the third thermocouple from the top of the dowel rod installed in test sections 6 through 10. The cable rests on subgrade and holds the dowel in place with the top thermocouple in the center of the 600-mm (24-in.) subbase.

Thermocouple strings in test sections 11 and 12 were constructed with the cables gathered at the third thermocouple from the top. The cable rests on the existing base and holds the top thermocouple in place in the pavement grindings. All of the thermocouples are spaced 150 mm (6 in.) apart except for the two at the bottom of the string which are spaced 300 mm (12 in.) apart. A diagram of the thermocouple string used in test section six is shown in Figure 4.10.

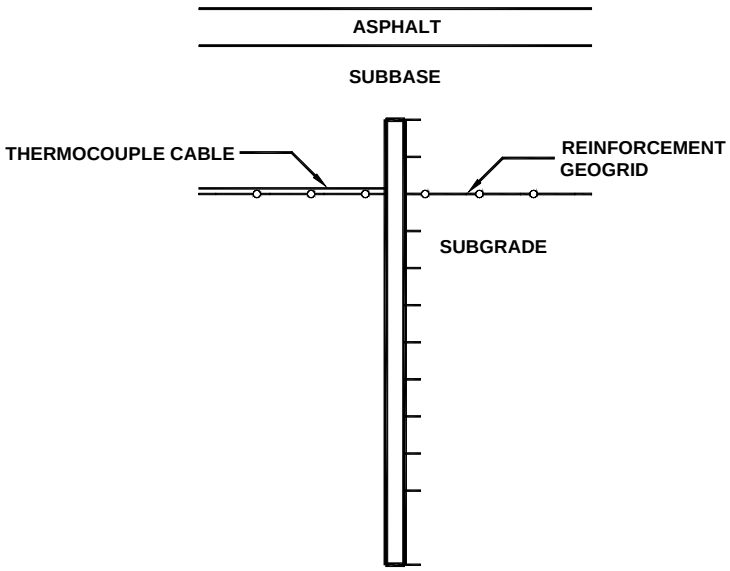

Figure 4.10 Test section six thermocouple diagram.

4.5.2. Thermocouple String Locations

One thermocouple string was installed in each test section, except for in test section five. The depth of the top sensor from finish grade was measured during installation. Given the uniform spacing of the probes this measurement allows for the

depth of each probe to be determined and the depth of frost penetration to be interpolated. The thermocouple string locations are summarized in Table 4.7.

Table 4.7 Thermocouple string locations.

Test Section	Station (m)	Offset (m)	Depth of Top Sensor From Finish Grade (mm)	Automated or Manual Readings
	1+490	2.9 RT	300	Manual
Test Section 1	1+550	2.9 RT	300	Automated
Test Section 2	1+612	2.9 RT	460	Automated
Test Section 3	1+670	2.9 RT	300	Automated
Test Section 4	1+730	2.9 RT	300	Automated
Test Section 5	NI	--	--	--
Test Section 6	3+965	2.9 RT	550	Manual
Test Section 7	4+000	2.9 RT	460	Automated
Test Section 8	4+040	2.9 RT	460	Automated
Test Section 9	4+080	2.9 RT	460	Automated
Test Section 10	4+120	2.9 RT	460	Manual
Test Section 11	4+690	2.9 RT	150	Manual
Test Section 12	4+710	2.9 RT	150	Manual

*NI = Not Instrumented

4.5.3. Field Installation

Prior to the start of construction, MaineDOT augered 100 mm (4 in.) holes in each test section. The holes were held open with a 75 mm (3 in.) steel casing until the thermocouples were installed. The casings were pulled using a chain hooked to the bucket of an excavator and the dowel rods were inserted into the hole. The annular space between the dowel and the edge of the hole was filled with native subgrade material compacted with a wooden dowel.

The lead wires were gathered at sensor two or three (see Figure 4.10). The twelve-pair cable ran on subgrade perpendicular to centerline to the edge of the travel

lane. The cable was directly buried a minimum of 150 mm (6 in.) in a trench running from the edge of the travel lane to the top of the right backslope. At the manual readout stations the cable was coiled there and hung from a 100 mm (4 in.) square post. The cables from automated stations were snaked through 38 mm (1.5 in.) PVC conduit oriented parallel to the roadway centerline located at the top of the backslope to one of the data acquisition systems.

4.6. Data Acquisition Systems

Two identical data acquisition systems were installed on this project. The first system is located at station 4+040 m (13+255 ft) and reads instruments in test sections 6 through 10. The second system is located at 1+610 m (5+282 ft) and reads instruments in test sections 1 through 5.

Each of the data acquisition systems consists of data acquisition equipment from Campbell Scientific housed in a weather tight steel NEMA Type 12 enclosure. A CR10X control and storage module is connected to a series of multiplexers that relay hourly readings from each connected instrument. Three 12 thermocouple strings as well as an air temperature thermocouple inside the enclosure and another outside the enclosure are connected to one of two AM25T multiplexers. The AM25T provides a reference temperature for the thermocouples and allows the CR10X to store data from the thermocouples using one input channel per multiplexer. A total of 48 strain gages are connected to one of three AM416 multiplexers. The AM416 transmits an excitation voltage from the CR10X and allows output voltages from the stain gages to be stored on the CR10X using one input channel per multiplexer. Six vibrating wire piezometers are

connected to a fourth AM416. The signal from the CR10X is conditioned by an AVW4 vibrating wire interface which conditions a signal from the CR10X used to excite the vibrating wire in the instruments. The AM416 allows the return signal from the piezometers to be stored on the CR10X using one input channel.

Hourly readings from all of the instruments are stored in comma delineated format on the datalogger and are downloaded from the datalogger on a monthly basis. A phone line and modem were installed which allows data to be downloaded from the University of Maine. Data can also be downloaded directly from the data acquisition systems using a laptop computer.

The steel enclosures are mounted on two 100 mm (4 in.) square wooden posts. Lead wires from the instruments travel through 38 mm (1.5 in.) PVC along the top of the backslope oriented parallel to the roadway centerline to the enclosures. The conduit enters the enclosures through the bottom as shown in the photo in Figure 4.11.

The systems are powered by 120-volt AC circuits from Central Maine Power. A duplex outlet was installed inside each of the two enclosures. Each system has a 12 volt battery backup system. A telephone line was installed by Verizon to accommodate data downloads from the University of Maine via modem.

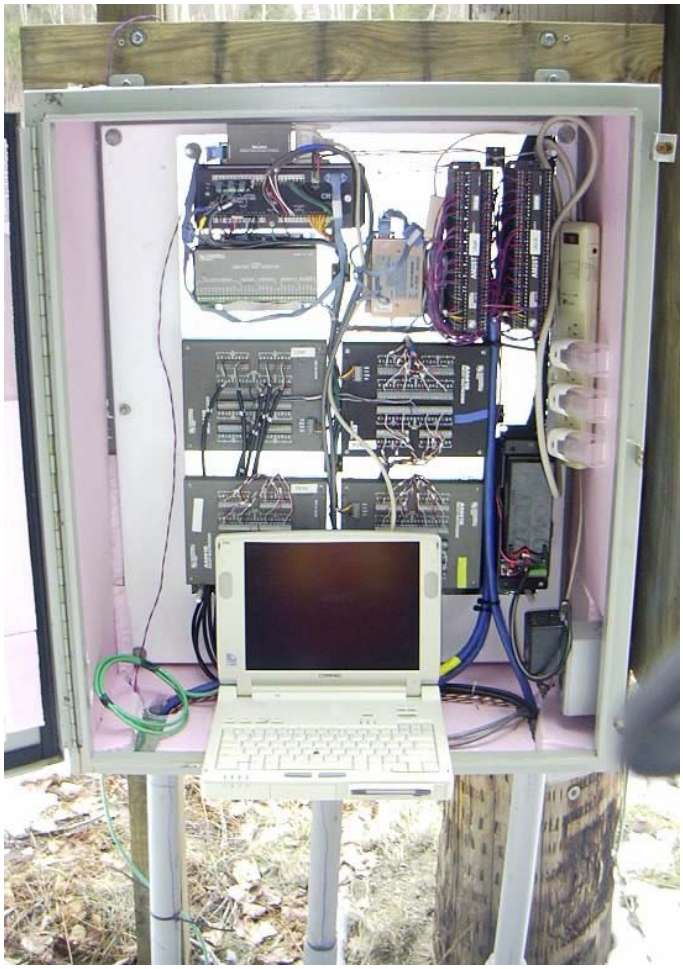

Figure 4.11 Photo of data acquisition system enclosure.

4.7. Summary

Field instrumentation was installed on this project to evaluate the performance of test sections constructed using geosynthetics. Strain gages attached to the reinforcement geogrid were used to deduce the tensile loads during both during and after construction. Vibrating wire piezometers were installed to monitor the porewater pressures in the subbase and subgrade in sections using drainage geocomposite and in the adjacent control sections. Flow meters were installed to measure the amount of water captured by the

drainage geocomposite collector pipes. Thermocouple strings were installed to measure frost penetration.

A total of 144 strain gages were installed to deduce tensile loads on sections of geogrid. In addition, a series of wide width tensile tests (ASTM D4595) were performed on pieces of geogrid in the laboratory. It was determined that a nearly linear relationship exists between measured strain in the lab and load per unit width on the grid. Linear fits were applied to the laboratory test results and averaged. The average slope was multiplied by delta strain values from the strain gages to infer tensile loads in the field.

A total of 14 vibrating wire piezometers were installed to monitor porewater pressures in the subbase and subgrade in the control sections as well as sections constructed with drainage geocomposite on subgrade. Piezometer data from the control sections was compared with that from drainage sections to evaluate the effectiveness of the drainage geocomposite in reducing subbase and subgrade porewater pressures.

A total of ten flow meters were installed to measure the amount of water captured by the drainage geocomposite collector pipe. Data from the flow meters was used in conjunction with the piezometer data to evaluate the performance of the drainage geocomposite.

Thermocouple strings were installed to measure the frost penetration in the test sections. Temperature data was used to determine the maximum depth frost penetration and more importantly the timeline for the spring thaw. This information was used in conjunction with stain gage data to determine the effects of frost on the performance of the geogrid.

(BLANK PAGE)

CHAPTER 5
RESULTS

5.1. Introduction

Route 9 in Litchfield, Maine was reconstructed over the course of two work seasons in the fall of 2001 and summer of 2002. Test sections were constructed using reinforcement geogrid and drainage geocomposite. The University of Maine installed instrumentation to monitor the performance of the geosynthetics. Strain gages were attached to the geogrid to determine tensile loads. Vibrating wire piezometers were installed to evaluate the effectiveness of the drainage geocomposite in reducing subbase and subgrade porewater pressures. Flow meters were installed to measure the amount of water captured by the drainage geocomposite collector pipe. Thermocouple strings were installed to measure frost penetration in the test sections. The details of the instrumentation and installation procedures are described in Chapter 4. Test sections 6 through 12 were constructed in the fall of 2001. Test sections 1 through 5 were constructed in the summer of 2002. Instrument readings from installation through May 2005 are included in this report. The results from these measurements are presented in this chapter.

5.2. Strain Gage Results

Ten strain gages were attached to the geogrid at each instrumented station. Test sections 1, 2, 4, 6, 7, and 10 are instrumented at two stations each. The gages were installed in pairs with one gage on top and one on the bottom of the instrumented ribs.

Pairs 1-2, 3-4, 7-8, and 9-10 are attached to ribs oriented perpendicular to the roadway centerline. Pair 5-6 is attached to a rib oriented parallel to the roadway centerline.

Strain gage survivability is summarized in Table 5.1. The average survival rate of strain gage pairs was 93% at the end of construction but this had decreased to 35% by May 2005. Failure was defined as malfunction of one strain gage in a pair. Possible causes of these failures include impact from subbase aggregate particles, severe bending of instrumented ribs, and excessive elongation of the strain gages. Post construction failures could be due to water penetrating the protective coverings causing electrical malfunctions. Lead wires from two of the instrumented stations (Stations 1+620 m and 1+720 m) were seriously damaged by construction equipment. As will be discussed below, as technique was developed to obtain useable data for the situation where only one gage in a pair was still working.

Table 5.1 Geogrid strain gage pair survivability

Test Section	Station (m)	Pair 1-2	Pair 3-4	Pair 5-6	Pair 7-8	Pair 9-10	Survival at End of Construction	Long Term Survival
1	1+540	FA	FA	FA	W	FA	100%	20%
	1+560	W	W	FA	W	W	100%	80%
2	1+600	W	W	FA	W	W	100%	80%
	1+620	FA	W	LD	FA	LD	60%	20%
4	1+720	FC	W	LD	W	W	60%	60%
	1+740	W	FA	FC	FA	FA	80%	20%
6	3+950	W	FA	FA	W	FA	100%	40%
	3+970	FA	FA	FA	FC	FA	80%	0%
7	3+990	FA	FA	FA	FA	FA	100%	0%
	4+010	FA	FA	W	FA	FA	100%	20%
10	4+110	FA	FA	W	FA	FA	100%	20%
	4+130	FA	W	W	W	FA	100%	60%

W = Working
FC = Failed During Construction
FA = Failed After Construction
LD = Leads Permanently Damaged by Construction Equipment

5.2.1. Strain Gages Perpendicular to Centerline

The instrumented sections of reinforcement geogrid have four strain gage pairs oriented perpendicular to the roadway centerline. These gages were placed at offsets of 2.6 m (8.5 ft), 2.9 m (9.5 ft), and 3.2 m (10.5 ft) from the centerline to measure the force in the geogrid perpendicular to centerline in the outside wheel path of the right (eastbound) lane.

Strain gage pair averages were plotted to remove the effects of bending. However, in some cases one gage in a pair failed during the monitoring period. A technique was developed to make use of the valuable data provided by the remaining functioning gage. For the period when both gages were functioning, data from each individual gage was plotted versus time. The lines were parallel after the initial construction period. This indicates that there was negligible bending after construction and that the data from a single gage could be used to indicate subsequent changes in tensile force in the geogrid. Thus, strain gage pair averages were used if both gages were functioning, then, if one gage failed, the subsequent change in force was determined from the surviving gage. These are termed "adjusted forces" in the following sections.

The results are organized by instrumented station. Figures 5.1 through 5.6 show forces in the geogrid perpendicular to centerline in test sections 1, 2, and 4 over the 35-month period from installation through May 2005. Figures 5.7 through 5.12 show forces in the geogrid perpendicular to centerline in test sections 6, 7, and 10 over the 45-month period from installation through May 2005. Manual readout stations have a data point symbol at every data point whereas automated readout stations have a data point symbol every 50 data points, however, all the data points are plotted.

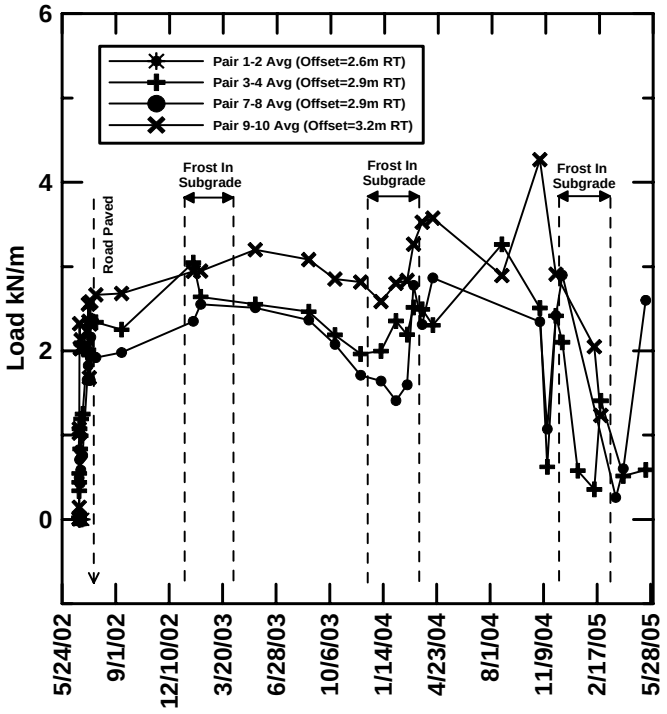

Figure 5.1 Force perpendicular to centerline in geogrid located on subgrade with 300-mm (12-in.) subbase in test section 1 station 1+540 m.

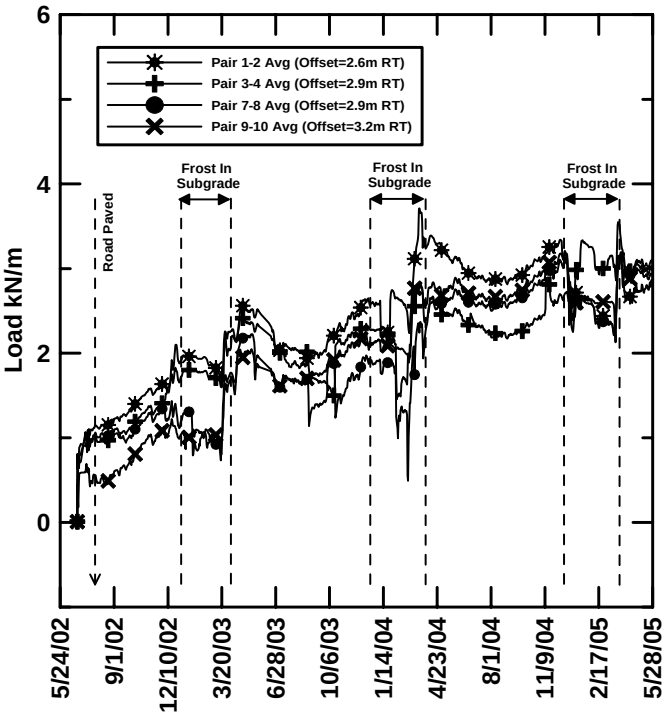

Figure 5.2 Force perpendicular to centerline in geogrid located on subgrade with 300-mm (12-in.) subbase in test section 1 station 1+560 m.

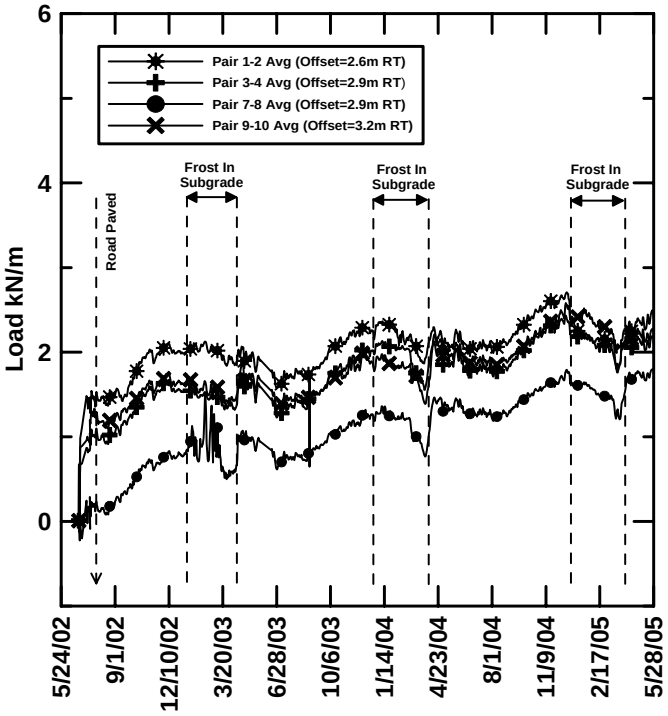

Figure 5.3 Force perpendicular to centerline in geogrid located in 300-mm (12-in.) subbase in test section 2 station 1+600 m.

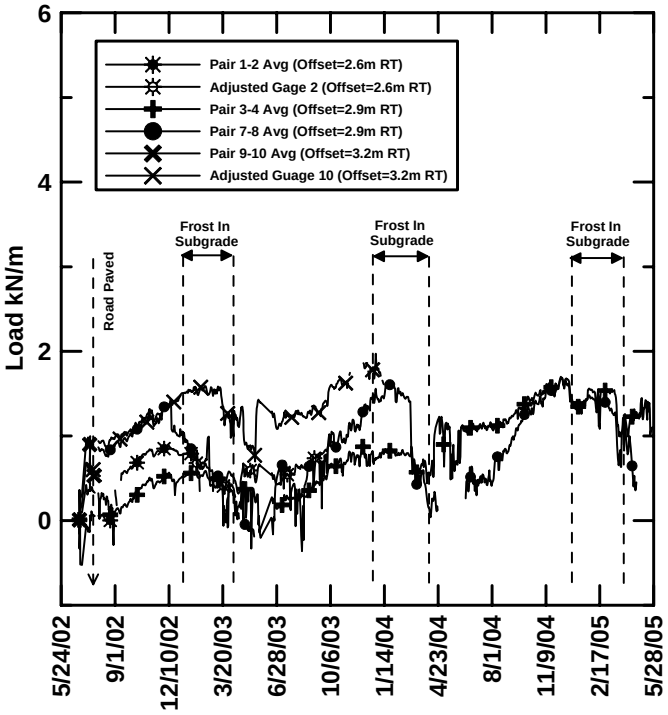

Figure 5.4 Force perpendicular to centerline in geogrid located in 300-mm (12-in.) subbase in test section 2 station 1+620 m.

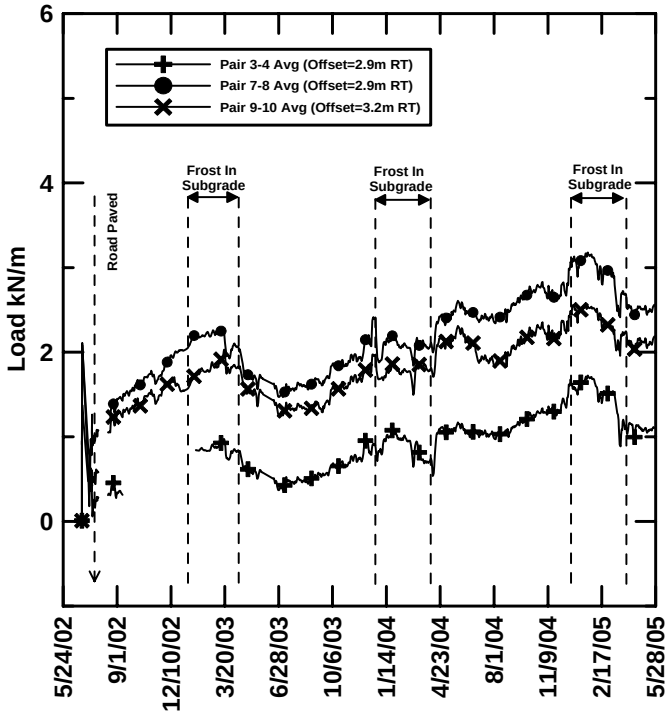

Figure 5.5 Force perpendicular to centerline in geogrid located in 300-mm (12-in.) subbase in test section 4 station 1+720 m.

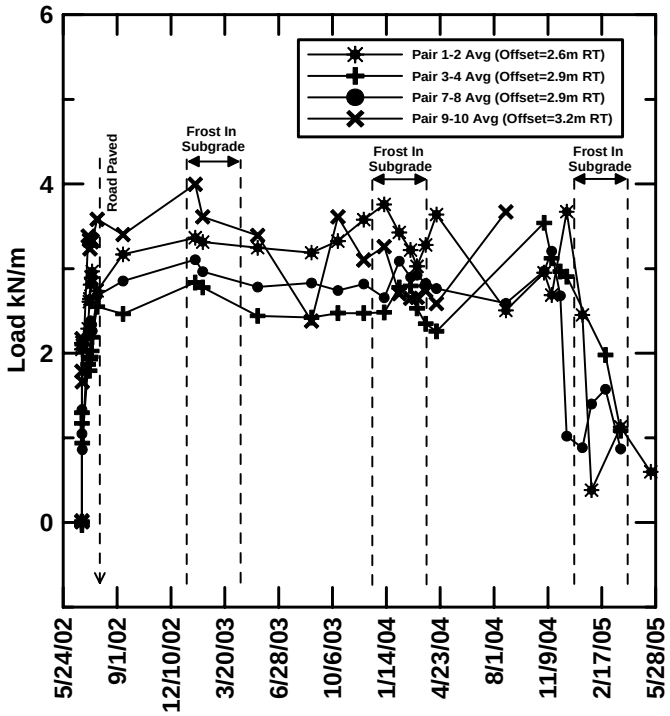

Figure 5.6 Force perpendicular to centerline in geogrid located in 300-mm (12-in.) subbase in test section 4 station 1+740 m.

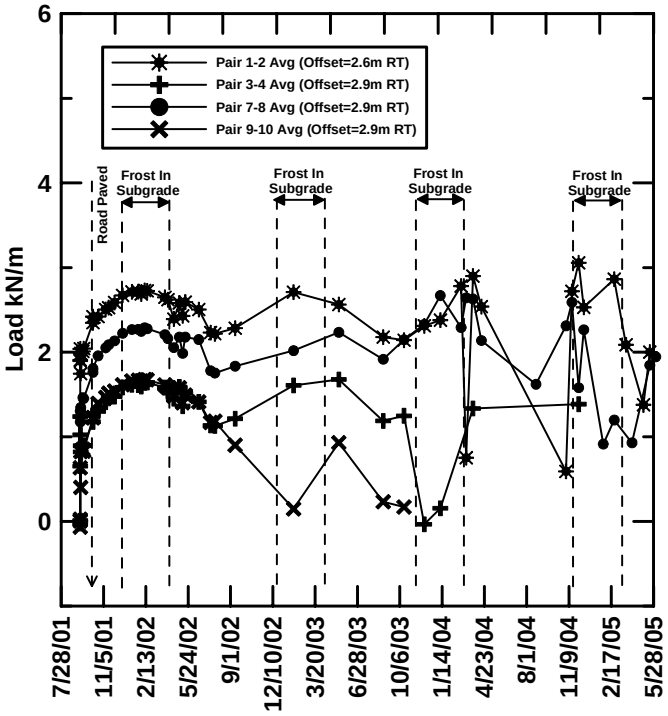

Figure 5.7 Force perpendicular to centerline in geogrid located on subgrade with 600-mm (24-in.) subbase in test section 6 station 3+950 m.

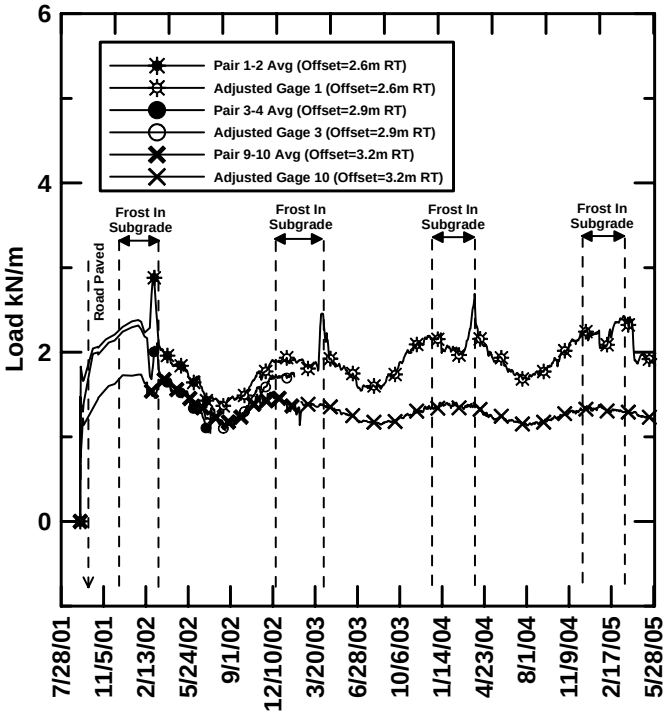

Figure 5.8 Force perpendicular to centerline in geogrid located on subgrade with 600-mm (24-in.) subbase in test section 6 station 3+970 m.

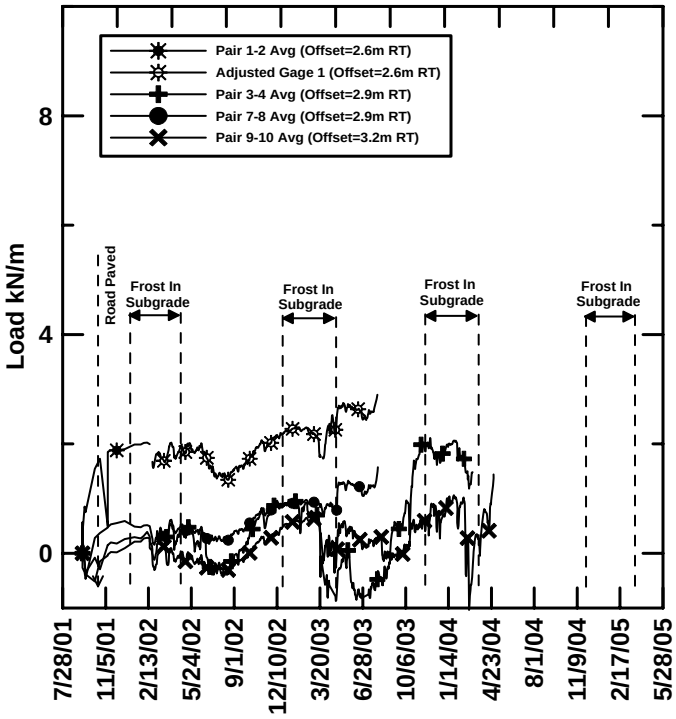

Figure 5.9 Force perpendicular to centerline in geogrid located in 600-mm (24-in.) subbase in test section 7 station 3+990 m.

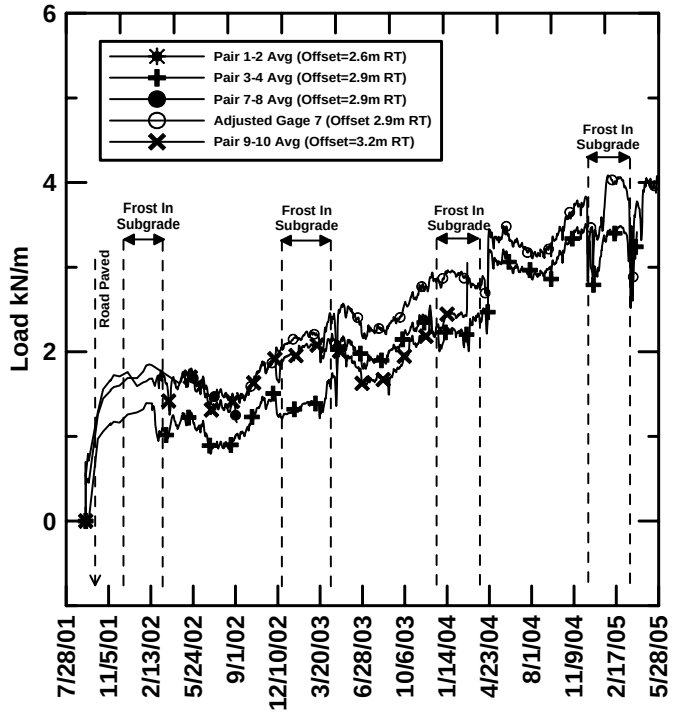

Figure 5.10 Force perpendicular to centerline in geogrid located in 600-mm (24-in.) subbase in test section 7 station 4+010 m.

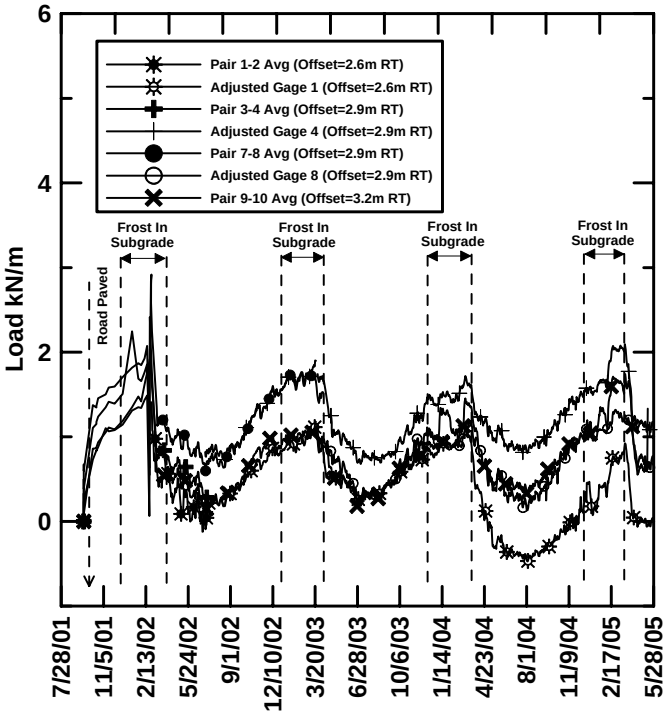

Figure 5.11 Force perpendicular to centerline in geogrid located in 600-mm (24-in.) subbase in test section 10 station 4+110 m.

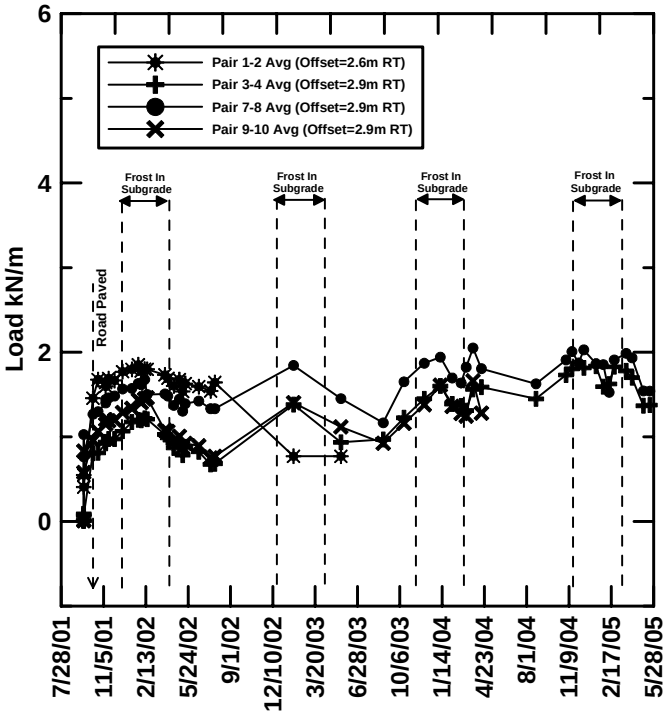

Figure 5.12 Force perpendicular to centerline in geogrid located in 600-mm (24-in.) subbase in test section 10 station 4+130 m.

The forces in Figures 5.1 through 5.12 were tabulated and examined at various intervals following installation. The geogrid forces measured between installation and paving of the test sections were termed construction forces. Geogrid forces measured after paving of the test section were termed long-term forces. To simplify comparisons, the average and standard deviation of the forces at each station was computed. The average and standard deviation of the forces in sections with similar geogrid placement were also computed. Thus, test sections 2 and 4 were combined as they both have geogrid in the center of a 300-mm (12-in.) subbase. Test sections 7 and 10 were also combined as both have geogrid in the center of a 600-mm (24-in.) subbase.

5.2.1.1. Construction Forces. Forces in the geogrid during construction were examined after the first lift of overlying subbase aggregate was placed and compacted, and immediately after paving. Data for the sections with 300 mm (12 in.) and 600 mm (24 in.) of subbase aggregate are examined in the following sections.

5.2.1.1.1. 300-mm Subbase Sections. Test sections 1, 2, and 4 were constructed using a reduced subbase section. In test section 1 geogrid was placed on subgrade and overlain by a 300-mm (12-in.) subbase course. Test sections 2 and 4 have geogrid in the center of the 300-mm (12-in.) subbase. Section 4 also has drainage geocomposite at the subgrade-subbase interface. Tensile forces following compaction and immediately after paving are summarized in Tables 5.2 and 5.3, respectively.

Negative values in Table 5.2 and 5.3 indicate that average strain in an instrumented rib was compressive. These apparent compressive forces may be the result of difficulties encountered during the placement of the geogrid. A wave in the geogrid

typically advanced ahead of the subbase placement. Entrapment of the wave beneath the advancing lift of subbase could generate localized areas of compression in the geogrid.

The geogrid forces in test section 4 were significantly larger than those in test section 2 after subbase compaction (Table 5.2). This could be the result of subbase particles slipping on the top geotextile surface of the underlying drainage geocomposite, creating more lateral displacement of the aggregate and thus more strain and resulting force in the geogrid.

Table 5.2 Actual force in geogrid after subbase compaction in test sections constructed with 300-mm (12-in.) subbase.

300 mm Subbase – Actual Force in Geogrid After Subbase Compaction kN/m (lb/ft)								
Test Section	Station	Pair 1-2 2.6m Offset	Pair 3-4 2.9m Offset	Pair 7-8 2.9m Offset	Pair 9-10 3.2m Offset	Station Average & *Standard Deviation*	Section Average & *Standard Deviation*	Section Range
Section 1	1+540 Geogrid on Subgrade	0.28 (19)	0.44 (30)	0.44 (30)	1.02 (70)	0.55 (37) *0.33 (22)*	0.53 (36) *0.22 (15)*	0.28 – 1.02 (19 – 70)
	1+560 Geogrid on Subgrade	0.53 (36)	0.51 (35)	0.53 (36)	0.46 (32)	0.51 (35) *0.03 (2)*		
Section 2	1+600 Geogrid at Center of Subbase	0.56 (38)	0.26 (18)	-0.12 (-8)	0.38 (26)	0.27 (19) *0.29 (20)*	0.81 (55) *0.75 (52)*	-0.12 – 2.38 (-8 – 163)
	1+620 Geogrid at Center of Subbase	-0.10 (-7)	0.01 (1)	0.35 (24)	0.33 (23)	0.15 (10) *0.23 (16)*		
Section 4	1+720 Geogrid at Center of Subbase	2.38 (163)	0.98 (67)	0.92 (63)	0.92 (63)	1.30 (89) *0.72 (49)*		
	1+740 Geogrid at Center of Subbase	2.05 (140)	1.17 (80)	1.05 (72)	1.79 (123)	1.52 (104) *0.48 (33)*		

Table 5.3 Actual force in geogrid immediately following paving in test sections constructed with 300-mm (12-in.) subbase.

300 mm Subbase – Actual Force in Geogrid After Paving of Test Sections kN/m (lb/ft)								
Test Section	Station	Pair 1-2 2.6m Offset	Pair 3-4 2.9m Offset	Pair 7-8 2.9m Offset	Pair 9-10 3.2m Offset	Station Average & *Standard Deviation*	Section Average & *Standard Deviation*	Section Range
Section 1	1+540 Geogrid on Subgrade	2.44 (167)	2.36 (162)	2.16 (148)	2.58 (177)	2.39 (163) *0.18 (12)*	1.62 (111) *0.84 (58)*	0.51 – 2.58 (35 – 177)
	1+560 Geogrid on Subgrade	1.16 (79)	0.80 (55)	0.97 (66)	0.51 (35)	0.86 (59) *0.28 (19)*		
Section 2	1+600 Geogrid at Center of Subbase	1.29 (88)	0.89 (61)	0.06 (4)	1.15 (79)	0.85 (58) *0.55 (38)*	1.27 (87) *1.09 (75)*	0.06 – 3.33 (4 – 228)
	1+620 Geogrid at Center of Subbase	0.32 (22)	0.34 (23)	0.57 (39)	0.60 (41)	0.46 (31) *0.15 (10)*		
Section 4	1+720 Geogrid at Center of Subbase	2.85 (195)	0.17 (12)	0.91 (62)	0.47 (32)	1.10 (75) *1.21 (83)*		
	1+740 Geogrid at Center of Subbase	2.97 (204)	2.19 (150)	2.26 (155)	3.33 (228)	2.69 (184) *0.55 (38)*		

The average force computed using all the gages with the same geogrid position (i.e., on subgrade or centered in subbase) increased between compaction and paving, even though the forces in a few individual gages decreased. For the geogrid placed on subgrade the average force increased by more than 300%, while the force increased by more than 50% in the sections with geogrid in the subbase. The road was open to traffic

during this period and the resulting imposed stresses and deformations may be responsible for this increase. The change in geogrid forces between subbase compaction and paving for each gage pair in test sections 1, 2 and 4 is summarized in Table 5.4.

Table 5.4 Change in geogrid force between subbase compaction and paving in test sections constructed with 300-mm (12-in.) subbase.

300 mm Subbase – Change in Geogrid Force Between Subbase Compaction and Paving kN/m (lb/ft)								
Test Section	Station	Pair 1-2 2.6m Offset	Pair 3-4 2.9m Offset	Pair 7-8 2.9m Offset	Pair 9-10 3.2m Offset	Station Average & *Standard Deviation*	Section Average & *Standard Deviation*	Section Range
Section 1	1+540 Geogrid on Subgrade	2.16 (148)	1.92 (132)	1.72 (118)	1.56 (107)	1.84 (126) *0.26 (18)*	1.10 (75) *0.83 (57)*	0.05 – 2.16 (3 – 148)
	1+560 Geogrid on Subgrade	0.63 (43)	0.29 (20)	0.44 (30)	0.05 (3)	0.35 (24) *0.25 (17)*		
Section 2	1+600 Geogrid at Center of Subbase	0.73 (50)	0.63 (43)	0.18 (12)	0.77 (53)	0.58 (40) *0.27 (19)*	0.47 (32) *0.59 (41)*	-0.01 – 1.54 (-1 – 106)
	1+620 Geogrid at Center of Subbase	0.42 (29)	0.33 (23)	0.22 (15)	0.27 (19)	0.31 (21) *0.09 (6)*		
Section 4	1+720 Geogrid at Center of Subbase	0.47 (32)	-0.81 (-56)	-0.01 (-1)	-0.45 (-31)	-0.20 (-14) *0.55 (38)*		
	1+740 Geogrid at Center of Subbase	0.92 (63)	1.02 (70)	1.21 (83)	1.54 (106)	1.17 (80) *0.27 (19)*		

5.2.1.1.2. 600-mm Subbase Sections. Test sections 6, 7, and 10 were constructed using a full 600-mm (24-in.) subbase section. In test section 6, geogrid was placed directly on subgrade. Test sections 7 and 10 have geogrid in the center of the subbase course. Section 10 also had drainage geocomposite at the subbase-subgrade interface. The geogrid forces after subbase compaction in test section 6 were compiled after compaction of the first lift. The change in geogrid forces between compaction of the first and second subbase lift in test section 6 was small. Thus, only the geogrid forces after compaction of the first lift are discussed below.

Geogrid forces following compaction of the first subbase lift in test section 6 ranged from 0.49 to 1.90 kN/m (34 to 130 lb/ft). Geogrid forces in test sections 7 and 10 following subbase compaction ranged from -0.26 to 0.76 kN/m (-18 to 52 lb/ft). It appears that less force is developed when the geogrid is placed in the subbase course. This could be due to support provided by the underlying first lift of compacted aggregate which limited deformation and subsequent development of the force in the geogrid for sections 7 and 10. The geogrid forces in test sections 6, 7, and 10 following subbase compaction are summarized in Table 5.5.

The increase in geogrid forces between subbase compaction and paving in test section 6 ranged from 0.28 to 1.53 kN/m (19 to 105 lb/ft) with an average increase of 0.73 kN/m (50 lb/ft). The change in geogrid forces in test sections 7 and 10 ranged from a decrease of 0.45 to an increase of 1.37 kN/m (-31 to 94 lb/ft) with an average increase of 0.69 kN/m (47 lb/ft). The change in geogrid forces between subbase compaction and paving in test sections 6, 7, and 10 is summarized in Table 5.6.

Table5.5 Actual force in geogrid after subbase compaction in test sections constructed with 600-mm (24-in.) subbase.

600 mm Subbase – Actual Force in Geogrid After Subbase Compaction kN/m (lb/ft)								
Test Section	Station	Pair 1-2 2.6m Offset	Pair 3-4 2.9m Offset	Pair 7-8 2.9m Offset	Pair 9-10 3.2m Offset	Station Average & *Standard Deviation*	Section Average & *Standard Deviation*	Section Range
Section 6*	3+950 Geogrid on Subgrade	1.90 (130)	1.02 (70)	1.30 (89)	0.63 (43)	1.21 (83) *0.53 (37)*	1.08 (74) *0.46 (32)*	0.49 – 1.90 (34 – 130)
	3+970 Geogrid on Subgrade	1.09 (75)	0.49 (34)	NF	1.11 (76)	0.90 (61) *0.35 (24)*		
Section 7	3+990 Geogrid at Center of Subbase	0.38 (26)	-0.26 (-18)	0.16 (11)	0.29 (20)	0.14 (10) *0.28 (19)*	0.37 (25) *0.26 (18)*	-0.26 – 0.76 (-18 – 52)
	4+010 Geogrid at Center of Subbase	0.65 (45)	0.06 (4)	0.45 (31)	0.53 (36)	0.42 (29) *0.26 (17)*		
Section 10	4+110 Geogrid at Center of Subbase	0.60 (41)	0.48 (33)	0.52 (36)	0.24 (16)	0.46 (32) *0.15 (11)*		
	4+130 Geogrid at Center of Subbase	0.41 (28)	0.07 (5)	0.76 (52)	0.58 (40)	0.46 (31) *0.29 (20)*		

NF = Not Functioning

*For section 6 forces shown are after placement and compaction of the first 300-mm (12-in.) lift of subbase over the geogrid.

The actual force in the geogrid immediately following paving in test section 6 ranged from 1.30 to 2.42 kN/m (89 to 166 lb/ft). The actual force in the geogrid following paving in test sections 7 and 10 ranged from -0.27 to 1.75 kN/m (-19 to 120 lb/ft). Again, lower force was measured in the sections with geogrid in the subbase course. The actual forces in the geogrid immediately following paving in test sections 6, 7, and 10 are summarized in Table 5.7.

Table 5.6 Change in geogrid force between subbase compaction and paving in test sections constructed with 600-mm (24-in.) subbase.

600 mm Subbase – Change in Geogrid Force Between Subbase Compaction and Paving kN/m (lb/ft)								
Test Section	Station	Pair 1-2 2.6m Offset	Pair 3-4 2.9m Offset	Pair 7-8 2.9m Offset	Pair 9-10 3.2m Offset	Station Average & *Standard Deviation*	Section Average & *Standard Deviation*	Section Range
Section 6	3+950 Geogrid on Subgrade	0.52 (36)	0.28 (19)	0.66 (45)	0.77 (53)	0.56 (38) *0.21 (14)*	0.73 (50) *0.43 (30)*	0.28 – 1.53 (19 – 105)
	3+970 Geogrid on Subgrade	1.00 (69)	1.53 (105)	NF	0.34 (23)	0.96 (66) *0.60 (41)*		
Section 7	3+990 Geogrid at Center of Subbase	1.37 (94)	0.65 (45)	-0.43 (-29)	-0.45 (-31)	0.29 (20) *0.89 (61)*	0.69 (47) *0.51 (35)*	-0.45 – 1.37 (-31 – 94)
	4+010 Geogrid at Center of Subbase	0.49 (34)	1.00 (69)	1.03 (71)	1.05 (72)	0.89 (61) *0.27 (18)*		
Section 10	4+110 Geogrid at Center of Subbase	0.87 (60)	0.87 (60)	0.86 (59)	0.66 (45)	0.82 (56) *0.10 (7)*		
	4+130 Geogrid at Center of Subbase	1.27 (87)	0.74 (51)	0.54 (37)	0.48 (33)	0.76 (52) *0.36 (25)*		

NF = Not Functioning

Table 5.7 Actual force in geogrid immediately following paving in test sections constructed with 600-mm (24-in.) subbase.

600 mm Subbase – Actual Force in Geogrid After Paving of Test Sections kN/m (lb/ft)								
Test Section	Station	Pair 1-2 2.6m Offset	Pair 3-4 2.9m Offset	Pair 7-8 2.9m Offset	Pair 9-10 3.2m Offset	Station Average & *Standard Deviation*	Section Average & *Standard Deviation*	Section Range
Section 6	3+950 Geogrid on Subgrade	2.42 (166)	1.30 (89)	1.96 (134)	1.40 (96)	1.77 (121) *0.52 (36)*	1.81 (124) *0.42 (29)*	1.30 – 2.42 (89 – 166)
	3+970 Geogrid on Subgrade	2.09 (143)	2.02 (138)	NF	1.45 (99)	1.85 (127) *0.35 (24)*		
Section 7	3+990 Geogrid at Center of Subbase	1.75 (120)	0.39 (27)	-0.27 (-19)	-0.16 (-11)	0.43 (29) *0.93 (64)*	1.06 (72) *0.61 (42)*	-0.27 – 1.75 (-19 – 120)
	4+010 Geogrid at Center of Subbase	1.14 (78)	1.06 (73)	1.48 (101)	1.58 (108)	1.32 (90) *0.25 (17)*		
Section 10	4+110 Geogrid at Center of Subbase	1.47 (101)	1.35 (93)	1.38 (95)	0.90 (62)	1.28 (87) *0.26 (17)*		
	4+130 Geogrid at Center of Subbase	1.68 (115)	0.81 (56)	1.30 (89)	1.06 (73)	1.21 (83) 0.37 (25)		

NF = Not Functioning

5.2.1.2. Long Term Forces. The forces developed between paving of the test sections and May 2005, which is the end of the monitoring period for this project, are termed long term forces. Test sections 1 through 5, constructed in June 2002, were monitored for 35 months. Test sections 6 through 12, constructed in September 2001, were monitored for 45 months. The forces at 12, 24, and 35 months after paving are examined in the following sections. In addition, forces 45 months after paving are examined for sections 6, 7, and 10.

5.2.1.2.1. 300-mm Subbase Sections. The change in geogrid force between the end of construction (paving) and 12 months after installation in test section 1 ranged from an increase of 0.11 to 1.08 kN/m (7.5 to 74 lb/ft) with and average increase of 0.60 kN/m (41 lb/ft). The change in force in test sections 2 and 4 ranged from a decrease of 0.95 to an increase of 0.75 kN/m (-65 to 51 lb/ft) with an average increase of 0.24 kN/m (16 lb/ft). Since the geogrid forces where obtained by monitoring the strain of selected ribs, it is possible that an apparent increase in force could be due to creep of the geogrid. This will be discussed further in Section 5.2.5. Changes in geogrid force between paving and 12 months in test sections 1, 2, and 4 are summarized in Table 5.8. Actual forces in the geogrid 12 months after installation are summarized in Table 5.9.

The change in geogrid force between the end of 12 months and 24 months after installation in test section 1 ranged from a decrease of 0.19 to an increase of 0.99 kN/m (-13 to 68 lb/ft) with an average increase of 0.62 kN/m (43 lb/ft). The change in force in test sections 2 and 4 ranged from a decrease of 0.68 to an increase of 1.29 kN/m (-47 to 88 lb/ft) with an average increase of 0.43 kN/m (29 lb/ft). Since the geogrid forces where obtained by monitoring the strain of selected ribs, it is possible that an apparent increase in force could be due to creep of the geogrid. This will be discussed further in Section 5.2.5. Changes in geogrid force between 12 and 24 months in test sections 1, 2, and 4 are summarized in Table 5.10. The actual forces at 24 months are summarized in Table 5.11.

Table 5.8 Change in geogrid force between paving and 12 months after installation in test sections constructed with 300-mm (12-in.) subbase.

300 mm Subbase – Change in Geogrid Force From Paving To 12 Months After Installation kN/m (lb/ft)								
Test Section	Station	Pair 1-2 2.6m Offset	Pair 3-4 2.9m Offset	Pair 7-8 2.9m Offset	Pair 9-10 3.2m Offset	Station Average & *Standard Deviation*	Section Average & *Standard Deviation*	Section Range
Section 1	1+540 Geogrid on Subgrade	NF	0.11 (8)	0.20 (14)	0.50 (34)	0.27 (19) *0.17 (12)*	0.60 (41) *0.46 (32)*	0.11 – 1.08 (8 – 74)
	1+560 Geogrid on Subgrade	0.82 (56)	1.07 (73)	0.75 (51)	1.08 (74)	0.93 (64) *0.59 (40)*		
Section 2	1+600 Geogrid at Center of Subbase	0. 27 (19)	0.35 (24)	0.49 (34)	0.27 (19)	0.35 (24) *0.09 (6)*	0.24 (16) *0.32 (22)*	-0.95 – 0.75 (-65 – 51)
	1+620 Geogrid at Center of Subbase	0.09* (6)	0.20 (14)	-0.04 (-3)	0.51* (35)	0.19 (13) 0.20 (14)		
Section 4	1+720 Geogrid at Center of Subbase	NF	0.13 (9)	0.53 (36)	0.75 (51)	0.47 (32) *0.26 (18)*		
	1+740 Geogrid at Center of Subbase	0.22 (15)	0.23 (16)	0.57 (39)	-0.95 (-65)	0.02 (1) *0.53 (36)*		

NF = Not Functioning
NA = Not Applicable
* = Adjusted Data

Table 5.9 Actual force in geogrid 12 months after installation in test sections constructed with 300-mm (12-in.) subbase.

300 mm Subbase – Actual Force in Geogrid 12 Months After Installation kN/m (lb/ft)								
Test Section	Station	Pair 1-2 2.6m Offset	Pair 3-4 2.9m Offset	Pair 7-8 2.9m Offset	Pair 9-10 3.2m Offset	Station Average & *Standard Deviation*	Section Average & *Standard Deviation*	Section Range
Section 1	1+540 Geogrid on Subgrade	NF	2.46 (169)	2.36 (162)	3.08 (211)	2.63 (180) *0.32 (22)*	2.19 (150) *0.26 (18)*	1.71 – 3.08 (117 – 211)
	1+560 Geogrid on Subgrade	1.92 (132)	2.09 (143)	1.72 (118)	1.71 (117)	1.86 (127) *0.16 (11)*		
Section 2	1+600 Geogrid at Center of Subbase	1.73 (119)	1.39 (95)	0.78 (53)	1.47 (101)	1.34 (92) *0.35 (24)*	1.56 (107) *0.42 (29)*	0.27 – 3.19 (50 – 219)
	1+620 Geogrid at Center of Subbase	NF	0.27 (50)	0.60 (41)	1.23* (84)	0.70 (48) 0.40 (27)		
Section 4	1+720 Geogrid at Center of Subbase	NF	0.49 (34)	1.59 (109)	1.36 (93)	1.15 (79) *0.47 (32)*		
	1+740 Geogrid at Center of Subbase	3.19 (219)	2.42 (166)	2.83 (194)	2.38 (163)	2.71 (204) *0.33 (23)*		

NF = Not Functioning
NA = Not Applicable
* = Adjusted Data

Table 5.10 Change in geogrid force between 12 and 24 months after installation in test sections constructed with 300-mm (12-in.) subbase.

300 mm Subbase – Change in Geogrid Force From 12 To 24 Months After Installation kN/m (lb/ft)								
Test Section	Station	Pair 1-2 2.6m Offset	Pair 3-4 2.9m Offset	Pair 7-8 2.9m Offset	Pair 9-10 3.2m Offset	Station Average & *Standard Deviation*	Section Average & *Standard Deviation*	Section Range
Section 1	1+540 Geogrid on Subgrade	NF	0.80 (55)	NF	-0.19 (-13)	0.31 (21) *0.50 (34)*	0.62 (43) *0.39 (27)*	-0.19 – 0.99 (-13 – 68)
	1+560 Geogrid on Subgrade	0.99 (68)	0.23 (16)	0.88 (60)	0.99 (68)	0.77 (53) *0.32 (22)*		
Section 2	1+600 Geogrid at Center of Subbase	0.40 (27)	0.48 (33)	0.54 (37)	0.48 (33)	0.48 (33) *0.05 (3)*	0.43 (29) *0.46 (32)*	-0.68 – 1.29 (-47 – 88)
	1+620 Geogrid at Center of Subbase	NF	0.89 (61)	-0.07 (-5)	NF	0.41 (28) 0.42 (29)		
Section 4	1+720 Geogrid at Center of Subbase	NF	0.58 (38)	0.86 (59)	0.60 (41)	0.68 (47) *0.13 (9)*		
	1+740 Geogrid at Center of Subbase	-0.68 (-47)	NF	-0.24 (-16)	1.29 (88)	0.12 (8) *0.84 (58)*		

NF = Not Functioning
NA = Not Applicable

Table 5.11 Actual force in geogrid 24 months after installation in test sections constructed with 300-mm (12-in.) subbase.

300 mm Subbase – Actual Force in Geogrid 24 Months After Installation kN/m (lb/ft)								
Test Section	Station	Pair 1-2 2.6m Offset	Pair 3-4 2.9m Offset	Pair 7-8 2.9m Offset	Pair 9-10 3.2m Offset	Station Average & *Standard Deviation*	Section Average & *Standard Deviation*	Section Range
Section 1	1+540 Geogrid on Subgrade	NF	3.26 (223)	NG	2.89 (198)	3.1 (212) *0.19 (13)*	2.78 (191) *0.21 (14)*	2.32 – 3.26 (159 – 223)
	1+560 Geogrid on Subgrade	2.92 (200)	2.32 (159)	2.60 (178)	2.70 (185)	2.64 (181) *0.22 (15)*		
Section 2	1+600 Geogrid at Center of Subbase	2.13 (146)	1.86 (127)	1.32 (90)	1.94 (133)	1.81 (124) *0.30 (21)*	1.93 (132) *0.45 (31)*	0.53 – 3.67 (36 – 251)
	1+620 Geogrid at Center of Subbase	NF	1.16 (79)	0.53 (36)	NF	0.85 (58) 0.32 (22)		
Section 4	1+720 Geogrid at Center of Subbase	NF	1.06 (73)	2.45 (168)	1.96 (134)	1.82 (125) *0.58 (40)*		
	1+740 Geogrid at Center of Subbase	2.51 (172)	NF	2.59 (178)	3.67 (251)	2.92 (200) *0.53 (36)*		

NF = Not Functioning
NA = Not Applicable

The change in geogrid force between 24 months and 35 months after installation in test section 1 ranged from a decrease of 0.15 to and increase of 0.53 kN/m (-10 to 36 lb/ft) with and average increase of 0.26 kN/m (18 lb/ft). The change in force in test sections 2 and 4 ranged from a decrease of 0.19 to an increase of 0.42 kN/m (-13 to 29 lb/ft) with an average increase of 0.14 kN/m (10 lb/ft). Changes in geogrid force between 12 and 24 months in test sections 1, 2, and 4 are summarized in Table 5.12. The actual force at 24 months is summarized in Table 5.13.

Table 5.12 Change in geogrid force between 24 and 35 months after installation in test sections constructed with 300-mm (12-in.) subbase.

300 mm Subbase – Change in Geogrid Force From 24 To 35 Months After Installation kN/m (lb/ft)								
Test Section	Station	Pair 1-2 2.6m Offset	Pair 3-4 2.9m Offset	Pair 7-8 2.9m Offset	Pair 9-10 3.2m Offset	Station Average & *Standard Deviation*	Section Average & *Standard Deviation*	Section Range
Section 1	1+540 Geogrid on Subgrade	NF	NF	NF	NF	NA	0.29 (20) *0.25 (17)*	-0.15– 0.53 (-10 – 36)
	1+560 Geogrid on Subgrade	-0.15 (-10)	0.53 (36)	0.33 (23)	0.32 (22)	0.26 (18) *0.25 (17)*		
Section 2	1+600 Geogrid at Center of Subbase	0.26 (18)	0.23 (16)	0.42 (29)	0.24 (16)	0.29 (20) *0.08 (6)*	0.14 (10) *0.07 (3)*	-0.19 – 0.42 (-13 – 29)
	1+620 Geogrid at Center of Subbase	NF	-0.19 (-13)	NF	NF	-0.19 (13) NA		
Section 4	1+720 Geogrid at Center of Subbase	NF	0.10 (7)	0.05 (3)	0.18 (12)	0.11 (8) *0.05 (3)*		
	1+740 Geogrid at Center of Subbase	-0.06 (-4)	NF	NF	NF	-0.06 (-4) *NA*		

NF = Not Functioning
NA = Not Applicable

Table 5.13 Actual force in geogrid 35 months after installation in test sections constructed with 300-mm (12-in.) subbase.

300 mm Subbase – Actual Force in Geogrid 35 Months After Installation kN/m (lb/ft)								
Test Section	Station	Pair 1-2 2.6m Offset	Pair 3-4 2.9m Offset	Pair 7-8 2.9m Offset	Pair 9-10 3.2m Offset	Station Average & *Standard Deviation*	Section Average & *Standard Deviation*	Section Range
Section 1	1+540 Geogrid on Subgrade	NF	NF	NF	NF	NA	2.90 (199) *0.09 (6)*	2.77 – 3.02 (190 – 207)
	1+560 Geogrid on Subgrade	2.77 (190)	2.86 (196)	2.94 (201)	3.02 (207)	2.90 (199) *0.09 (6)*		
Section 2	1+600 Geogrid at Center of Subbase	2.38 (163)	2.09 (143)	1.74 (119)	2.19 (150)	2.1 (144) *0.23 (16)*	1.95 (134) *0.41 (28)*	0.97 – 2.45 (66 – 168)
	1+620 Geogrid at Center of Subbase	NF	0.97 (66)	NF	NF	0.97 (66) NA		
Section 4	1+720 Geogrid at Center of Subbase	NF	1.17 (80)	2.50 (171)	2.14 (147)	1.94 (133) *0.56 (38)*		
	1+740 Geogrid at Center of Subbase	2.45 (168)	NF	NF	NF	2.45 (168) *NA*		

NF = Not Functioning
NA = Not Applicable

5.2.1.2.2. 600-mm Subbase Sections. The change in geogrid force between paving and 12 months after installation was chosen for examination since this would allow direct comparison to the sections with 300-mm (12-in) subbase. For this period the change in force in test section 6 ranged from a decrease of 0.76 to a decrease of 0.07 kN/m (-52 to -5 lb/ft) with an average decrease of 0.27 kN/m (-19 lb/ft). The change in geogrid force in test sections 7 and 10 ranged from a decrease of 0.82 to an increase of 1.00 kN/m (-56 to 66 lb/ft) with an average increase of 0.08 kN/m (5 lb/ft). Changes in

geogrid force between paving and 12 months after installation in test sections 6, 7, and 10 are summarized in Table 5.14. The actual force at 12 months is summarized in Table 5.15.

Table 5.14 Change in geogrid force between paving and 12 months after installation in test sections constructed with 600-mm (24-in.) subbase.

600 mm Subbase – Change in Geogrid Force From Paving To 12 Months After Installation kN/m (lb/ft)								
Test Section	Station	Pair 1-2 2.6m Offset	Pair 3-4 2.9m Offset	Pair 7-8 2.9m Offset	Pair 9-10 3.2m Offset	Station Average & *Standard Deviation*	Section Average & *Standard Deviation*	Section Range
Section 6	3+950 Geogrid on Subgrade	-0.14 (-10)	-0.09 (-6)	-0.12 (-8)	-0.49 (-34)	-0.21 (-14) *0.16 (11)*	-0.27 (-19) *0.27 (19)*	-0.76 – -0.07 (-52 – -5)
	3+970 Geogrid on Subgrade	-0.25* (-17)	-0.76* (-52)	NF	-0.07 (-5)	-0.36 (-25) *0.31 (21)*		
Section 7	3+990 Geogrid at Center of Subbase	0.21* (14)	0.24 (16)	1.00 (66)	0.33 (23)	0.45 (31) 0.32 (22)	0.08 (5) *0.23 (16)*	-0.82 – 1.00 (-56 – 66)
	4+010 Geogrid at Center of Subbase	0.29 (20)	0.28 (19)	0.32* (22)	0.18 (12)	0.27 (19) *0.05 (3)*		
Section 10	4+110 Geogrid at Center of Subbase	-0.82* (-56)	-0.25* (-17)	0.00 (0)	-0.15 (-10)	-0.31 (-21) *0.31(21)*		
	4+130 Geogrid at Center of Subbase	-0.03 (-2)	-0.13 (-9)	0.03 (2)	-0.29 (-20)	-0.11 (-8) *0.12 (8)*		

NF = Not Functioning
* = Adjusted Data

Table 5.15 Actual force in geogrid 12 months after installation in test sections constructed with 600-mm (24-in.) subbase.

600 mm Subbase – Actual Force in Geogrid 12 Months After Installation kN/m (lb/ft)								
Test Section	Station	Pair 1-2 2.6m Offset	Pair 3-4 2.9m Offset	Pair 7-8 2.9m Offset	Pair 9-10 3.2m Offset	Station Average & *Standard Deviation*	Section Average & *Standard Deviation*	Section Range
Section 6	3+950 Geogrid on Subgrade	2.28 (156)	1.21 (77)	1.83 (120)	0.90 (81)	1.56 (108) *0.54 (37)*	1.54 (106) *0.41 (28)*	0.90 – 2.28 (81 – 156)
	3+970 Geogrid on Subgrade	1.66* (114)	1.48* (101)	NF	1.38 (95)	1.51 (103) *0.12 (8)*		
Section 7	3+990 Geogrid at Center of Subbase	1.94* (133)	0.61 (42)	0.70 (48)	0.19 (13)	0.86 (59) 0.65 (45)	1.09 (75) *0.41 (28)*	0.61 – 1.94 (42 – 133)
	4+010 Geogrid at Center of Subbase	1.40 (96)	1.34 (92)	1.77* (121)	1.74 (119)	1.56 (107) *0.19 (13)*		
Section 10	4+110 Geogrid at Center of Subbase	0.63* (43)	0.68* (47)	1.24 (84)	0.73 (85)	0.83 (57) *0.25 (17)*		
	4+130 Geogrid at Center of Subbase	1.64 (112)	0.68 (47)	1.33 (91)	0.77 (53)	1.11 (76) *0.40 (27)*		

NF = Not Functioning
NA = Not Applicable
* = Adjusted Data

The change in force between 12 and 24 months after installation in section 6 ranged from a decrease of 0.73 kN/m (-50 lb/ft) to an increase of 0.35 kN/m (24 lb/ft), with an average decrease of 0.14 kN/m (-10 lb/ft). The change in force in test sections 7 and 10 ranged from a decrease of 1.64 kN/m (-112 lb/ft) to an increase of 0.98 kN/m (67 lb/ft), with an average increase of 0.24 kN/m (16 lb/ft). The changes in force in sections

6, 7, and 10 between 12 and 24 months after installation are summarized in Table 5.16. The actual force at 24 months is summarized in Table 5.17.

Table 5.16 Change in geogrid force between 12 and 24 months after installation in test sections constructed with 600-mm (24-in.) subbase.

600 mm Subbase – Change In Geogrid Force From 12 Months To 24 Months After Installation kN/m (lb/ft)								
Test Section	Station	Pair 1-2 2.6m Offset	Pair 3-4 2.9m Offset	Pair 7-8 2.9m Offset	Pair 9-10 3.2m Offset	Station Average & *Standard Deviation*	Section Average & *Standard Deviation*	Section Range
Section 6	3+950 Geogrid on Subgrade	-0.14 (-10)	0.03 (2)	0.31 (21)	-0.73 (-50)	-0.13 (-9) *0.38 (28)*	-0.14 (-10) *0.18 (12)*	-0.73 – 0.35 (-17 – 24)
	3+970 Geogrid on Subgrade	0.35* (24)	NF	NF	-0.65 (-45)	-0.15 (-10) *0.5 (34)*		
Section 7	3+990 Geogrid at Center of Subbase	NF	0.89 (61)	0.89 (61)	0.40 (27)	0.73 (50) 0.23 (16)	0.30 (21) 0.53 (36)	-1.64 – 0.98 (-112 – 67)
	4+010 Geogrid at Center of Subbase	-0.01 (-1)	0.98 (67)	0.91* (62)	0.44 (30)	0.58 (40) *0.40 (27)*		
Section 10	4+110 Geogrid at Center of Subbase	0.04* (3)	-0.13* (-9)	0.02* (1)	0.02 (1)	-0.01 (-1) 0.07 (5)		
	4+130 Geogrid at Center of Subbase	-1.64 (-112)	0.54 (37)	0.32 (22)	0.39 (27)	-0.10 (-7) *0.89 (61)*		

NF = Not Functioning
NA = Not Applicable
* = Adjusted Data

Table 5.17 Actual force in geogrid 24 months after installation in test sections constructed with 600-mm (24-in.) subbase.

600 mm Subbase – Actual Force in Geogrid 24 Months After Installation kN/m (lb/ft)								
Test Section	Station	Pair 1-2 2.6m Offset	Pair 3-4 2.9m Offset	Pair 7-8 2.9m Offset	Pair 9-10 3.2m Offset	Station Average & *Standard Deviation*	Section Average & *Standard Deviation*	Section Range
Section 6	3+950 Geogrid on Subgrade	2.14 (147)	1.25 (86)	2.15 (147)	0.17 (12)	1.43 (98) *0.81 (56)*	1.41 (97) *0.76 (52)*	0.17 – 2.15 (12 – 147)
	3+970 Geogrid on Subgrade	2.01* (138)	NF	NF	0.73 (50)	1.37 (94) 0.64 (44)		
Section 7	3+990 Geogrid at Center of Subbase	NF	1.50 (103)	1.59* (109)	0.59 (40)	*1.23 (84)* 0.26 (18)	1.38 (95) *0.32 (22)*	0.59 – 2.68 (40 – 184)
	4+010 Geogrid at Center of Subbase	1.39 (95)	2.32 (159)	2.68* (184)	2.18 (149)	2.14 (147) *0.47 (32)*		
Section 10	4+110 Geogrid at Center of Subbase	0.67* (46)	0.55* (38)	1.26* (86)	0.75 (51)	0.81 (56) 0.27 (19)		
	4+130 Geogrid at Center of Subbase	NF	1.23 (84)	1.65 (113)	1.16 (79)	1.34 (92) *0.19 (13)*		

NF = Not Functioning
NA = Not Applicable
* = Adjusted Data

The change in geogrid force between 24 and 35 months after installation in test section 6 ranged between decreases of 1.55 kN/m (-106 lb/ft) and 0.02 kN/m (-1 lb/ft), with an average decrease of 0.61 kN/m (-42 lb/ft). The change in force in test sections 7 and 10 ranged from a decrease of 1.16 kN/m (-79 lb/ft) to an increase of 1.16 kN/m (79 lb/ft), with an average increase of 0.11 kN/m (8 lb/ft). The changes in force in sections 6,

7, and 10 between 24 and 35 months after installation are summarized in Table 5.18. The actual forces at 35 months are summarized in Table 5.19.

Table 5.18 Change in geogrid force between 24 and 35 months after installation in test sections constructed with 600-mm (24-in.) subbase.

600 mm Subbase – Change in Geogrid Force from 24 To 35 Months After Installation kN/m (lb/ft)								
Test Section	Station	Pair 1-2 2.6m Offset	Pair 3-4 2.9m Offset	Pair 7-8 2.9m Offset	Pair 9-10 3.2m Offset	Station Average & *Standard Deviation*	Section Average & *Standard Deviation*	Section Range
Section 6	3+950 Geogrid on Subgrade	-1.55 (106)	NF	-0.16 (-11)	NF	-0.86 (-59) *0.70 (48)*	-0.61 (-42) *0.53 (36)*	-1.55 – -0.02 (-106 – -1)
	3+970 Geogrid on Subgrade	-0.02* (-1)	NF	NF	-0.57 (-39)	-0.36 (-25) *0.28 (19)*		
Section 7	3+990 Geogrid at Center of Subbase	NF	NF	1.16* (79)	0.05* (3)	0.61(41) 0.56 (38)	0.11 (8) 0.52 (36)	-1.16 – 1.16 (-79 – 79)
	4+010 Geogrid at Center of Subbase	NF	0.95 (65)	0.89* (61)	NF	0.92 (63) *0.03 (2)*		
Section 10	4+110 Geogrid at Center of Subbase	-0.79* (54)	0.16* (11)	0.00* (0)	0.02 (1)	-0.15 (-10) *0.37 (25)*		
	4+130 Geogrid at Center of Subbase	NF	0.58 (40)	0.36 (25)	-1.16 (-79)	-0.07 (-5) *0.77 (53)*		

NF = Not Functioning
NA = Not Applicable
* = Adjusted Data

Table 5.19 Actual force in geogrid 35 months after installation in test sections constructed with 600-mm (24-in.) subbase.

600 mm Subbase – Actual Force in Geogrid 35 Months After Installation kN/m (lb/ft)								
Test Section	Station	Pair 1-2 2.6m Offset	Pair 3-4 2.9m Offset	Pair 7-8 2.9m Offset	Pair 9-10 3.2m Offset	Station Average & *Standard Deviation*	Section Average & *Standard Deviation*	Section Range
Section 6	3+950 Geogrid on Subgrade	0.59 (40)	NF	2.31 (158)	NF	1.45 (99) *0.86 (59)*	1.24 (85) *0.89(61)*	0.16 – 2.31 (11 – 158)
	3+970 Geogrid on Subgrade	1.99* (136)	NF	NF	0.16 (11)	1.03 (11) *0.92 (63)*		
Section 7	3+990 Geogrid at Center of Subbase	NF	NF	2.75* (188)	0.64* (44)	1.70 (116) 1.06 (73)	1.67 (114) *0.57 (39)*	-0.12 – 3.57 (-8 – 245)
	4+010 Geogrid at Center of Subbase	NF	3.27 (224)	3.57* (245)	NF	3.42 (234) *0.15 (10)*		
Section 10	4+110 Geogrid at Center of Subbase	-0.12* (8)	0.71* (49)	1.26* (86)	0.79 (54)	0.66 (45) *0.50 (34)*		
	4+130 Geogrid at Center of Subbase	NF	1.80 (123)	2.01 (138)	NF	1.91 (131) *0.11 (8)*		

NF = Not Functioning
NA = Not Applicable
* = Adjusted Data

The change in force between 35 and 45 months after installation in test section 6 ranged from a decrease of 0.37 kN/m (-25 lb/ft) to an increase of 1.55 kN/m (106 lb/ft), with an average increase of 0.26 kN/m (18 lb/ft). The change in force in sections 7 and 10 ranged from a decrease of 0.32 kN/m (-37 lb/ft) to an increase of 0.40 kN/m (27 lb/ft), with an average decrease of 0.09 kN/m (-6 lb/ft). The changes in force in sections 6, 7,

and 10 between 35 and 45 months after installation are summarized in Table 5.20. The actual force at 45 months is summarized in Table 5.21.

Table 5.20 Change in geogrid force between 35 and 45 months after installation in test sections constructed with 600-mm (24-in.) subbase.

600 mm Subbase – Change In Geogrid Force From 35 Months To 45 Months After Installation kN/m (lb/ft)								
Test Section	Station	Pair 1-2 2.6m Offset	Pair 3-4 2.9m Offset	Pair 7-8 2.9m Offset	Pair 9-10 3.2m Offset	Station Average & *Standard Deviation*	Section Average & *Standard Deviation*	Section Range
Section 6	3+950 Geogrid on Subgrade	1.55 (106)	NF	-0.37 (-25)	NF	0.59 (40) *0.96 (66)*	0.26 (18) *0.68 (47)*	-0.37 – 1.55 (-25 – 106)
	3+970 Geogrid on Subgrade	-0.10*	NF	NF	-0.04* (-45)	-0.07 (-5) *0.03 (2)*		
Section 7	3+990 Geogrid at Center of Subbase	NF	NF	0.38* (26)	-0.10* (-7)	0.14 (10) *0.24 (16)*	-0.09 (-6) *0.15 (10)*	-0.32 – 0.40 (-37 – 27)
	4+010 Geogrid at Center of Subbase	NF	NF	0.40* (27)	NF	0.40 (27) *NA*		
Section 10	4+110 Geogrid at Center of Subbase	0.06* (4)	-0.22* (-15)	-0.17* (-12)	-0.23* (16)	-0.14 (-10) 0.12 (8)		
	4+130 Geogrid at Center of Subbase	NF	-0.32 (-37)	-0.29 (-22)	NF	-0.31 (-21) *0.02 (1)*		

NF = Not Functioning
NA = Not Applicable
* = Adjusted Data

Table 5.21 Actual force in geogrid 45 months after installation in test sections constructed with 600-mm (24-in.) subbase.

600 mm Subbase – Actual Force in Geogrid 45 Months After Installation kN/m (lb/ft)								
Test Section	Station	Pair 1-2 2.6m Offset	Pair 3-4 2.9m Offset	Pair 7-8 2.9m Offset	Pair 9-10 3.2m Offset	Station Average & *Standard Deviation*	Section Average & *Standard Deviation*	Section Range
Section 6	3+950 Geogrid on Subgrade	2.15 (147)	NF	1.95 (134)	NF	2.05 (140) *0.10 (7)*	1.30 (89) *0.25 (17)*	1.21 – 2.15 (83 – 147)
	3+970 Geogrid on Subgrade	1.89 (130)	NF	NF	1.21 (83)	1.55 (106) 0.34 (23)		
Section 7	3+990 Geogrid at Center of Subbase	NF	NF	3.13* (215)	0.53* (36)	*1.83 (125)* 1.3 (89)	1.41 (97) *0.67 (46)*	-0.07 – 3.13 (-5 – 215)
	4+010 Geogrid at Center of Subbase	NF	NF	3.96* (271)	NF	3.96 (271) *NA*		
Section 10	4+110 Geogrid at Center of Subbase	-0.07* (-5)	0.49* (34)	1.09* (75)	0.57* (39)	0.52 (36) 0.41 (28)		
	4+130 Geogrid at Center of Subbase	NF	1.49 (102)	1.72 (118)	NF	1.61 (110) *0.12 (8)*		

NF = Not Functioning
NA = Not Applicable
* = Adjusted Data

5.2.1.3. Summary of Forces. To achieve a clearer picture of the change in forces over the life of the project, the average geogrid forces are summarized for several periods in Table 5.22. Average geogrid forces were examined after compaction, immediately after paving, and at 12, 24, 35, and 45 months after paving.

In sections with a 300-mm subbase layer with geogrid on subgrade as well as geogrid in the middle of the subbase showed that the average force increased over time,

with greater increases occurring in the section with geogrid on subgrade. In the sections with a 600-mm (24-in.) subbase and geogrid located on subgrade, the largest force was recorded right after paving and then the average force decreased over time. For sections with geogrid in a 600-mm (24-in.) subbase, a slight increase in force with time can be seen. For 12, 24, and 35 months after paving, the sections with 300-mm (12-in.) subbase had a higher force than sections with 600-mm (24-in.) subbase. The data is summarized graphically in Figure 5.13.

Table 5.22 Summary of average actual force in geogrid, all test sections

300 mm Subbase –Actual Force in Geogrid kN/m (lb/ft)							
Test Section	Geogrid Placement	After Subbase Compaction	After Paving	At 12 Months	At 24 Months	At 35 Months	After 45 Months
Section 1	Geogrid on subgrade	0.53 (36)	1.62 (111)	2.19 (150)	2.78 (191)	2.90 (199)	NA
Sections 2 & 4	Geogrid in center of subbase	0.81 (55)	1.27 (87)	1.56 (107)	1.93 (132)	1.95 (134)	NA
600 mm Subbase – Actual Force in Geogrid kN/m (lb/ft)							
Section 6	Geogrid on subgrade	1.08 (74)	1.81 (124)	1.54 (106)	1.41 (97)	1.24 (85)	1.30 (89)
Sections 7 & 10	Geogrid in center of subbase	0.37 (25)	1.06 (72)	1.09 (75)	1.38 (95)	1.67 (114)	1.41 (97)

NA = Not Applicable

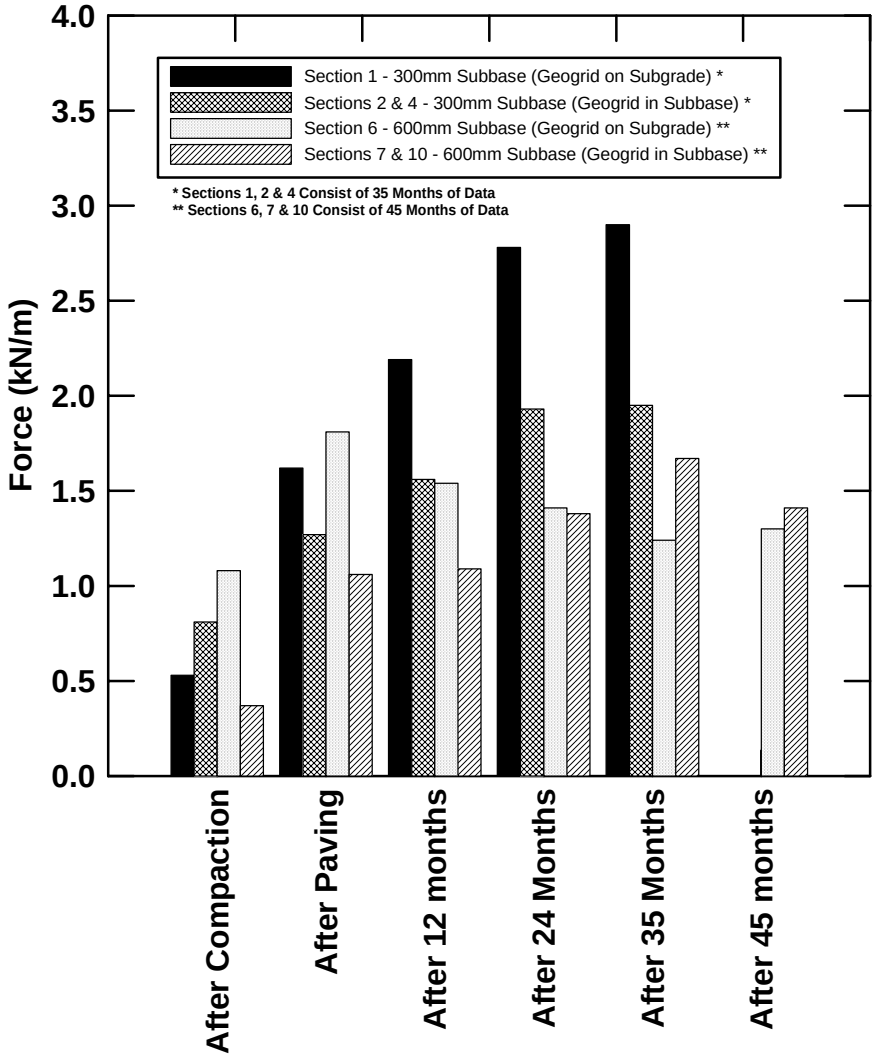

Figure 5.13 Summary of average force in geogrid.

5.2.1.4. Statistical Comparisons of Forces Perpendicular to Centerline. The geogrid forces in ribs oriented perpendicular to centerline were analyzed to evaluate the effects of elapsed time, subbase thickness, and geogrid location in the pavement system on the force in the geogrid. The statistical t-test and z-test were used.

5.2.1.4.1. Z-test Results. The z-test determines the difference between two sample means in terms of a confidence interval. The confidence interval is a function of the sample sizes and their standard deviations. The test assumes that the data is normally

distributed. The z-test was used to evaluate the effects of geogrid location and subbase thickness. The equations used in the analysis are described below (Neter, et al., 1982).

$$Y - X = \mu_1 - \mu_2 \qquad \text{Equation 5.1}$$

where: $Y - X$ = difference between sample means

μ_1 = mean of population 1

μ_2 = mean of population 2

$$s(Y - X) = ((s_1^2 / n_1) + (s_2^2 / n_2))^{0.5} \qquad \text{Equation 5.2}$$

where: $s(Y - X)$ = standard deviation of the sampling distribution

n_1 = number of values in sample 1

s_1 = standard deviation of sample 1

n_2 = number of values in sample 2

s_2 = standard deviation of sample 2

$$z^* = (Y - X) / s(Y - X) \qquad \text{Equation 5.3}$$

where: z^* = the z-score

$$\text{Confidence Limits} = (Y - X) \pm 1.96 * s(Y - X) \qquad \text{Equation 5.4}$$

If the z-score is less than or equal to 1.96 then the sample means are considered statistically equal with 95% confidence. If the z-score is greater than 1.96 then one of the sample means exceeds the other. In this case, the confidence interval can be calculated

using Equation 5.4 to express range by which the larger of the two means exceeds the other with 95% confidence. For example, if the z-score is 3.55, the lower limit of the confidence interval is 0.49, and the upper limit of the confidence interval is 1.69, then it can be concluded with 95% confidence that larger of the two means exceeds the other by between 0.49 and 1.69. The results of the statistical analyses on the effect of geogrid location and subbase thickness are shown in Tables 5.23 through 5.26.

Table 5.23 Effect of geogrid location for 300 mm subbase sections analyzed using statistical z-test.

Geogrid Location Effects – 300 mm (12 in.) Subbase Sections			
Forces Compared	**Difference in Average Force kN/m (lb/ft)**	**z***	**Conclusion**
geogrid on subgrade vs. geogrid in subbase after subbase compaction	0.28 (19)	1.38	geogrid on subgrade = geogrid in the subbase
geogrid on subgrade vs. geogrid in subbase after paving	0.35 (24)	0.87	geogrid on subgrade = geogrid in the subbase
geogrid on subgrade vs. geogrid in subbase 12 months after installation	0.63 (43)	4.22	geogrid on subgrade > geogrid in the subbase by between 0.34 and 0.92 kN/m (23 and 63 lb/ft).
geogrid on subgrade vs. geogrid in subbase 24 months after installation	0.85 (58)	5.46	geogrid on subgrade > geogrid in the subbase by between 0.54 and 1.16 kN/m (37 and 79 lb/ft).
geogrid on subgrade vs. geogrid in subbase 35 months after installation	0.95 (65)	6.60	geogrid on subgrade > geogrid in the subbase by between 0.67 and 1.23 kN/m (46 and 84 lb/ft).

Table 5.24 Effect of geogrid location for 600 mm subbase sections analyzed using statistical z-test.

Geogrid Location Effects – 600 mm (24 in.) Subbase Sections			
Forces Compared	**Difference in Average Force kN/m (lb/ft)**	**z***	**Conclusion**
geogrid on subgrade vs. geogrid in subbase after subbase compaction	0.71 (49)	3.83	geogrid on subgrade > geogrid in the subbase by between 0.35 and 1.07 kN/m (24 and 73 lb/ft).
geogrid on subgrade vs. geogrid in subbase after paving	0.75 (51)	3.41	geogrid on subgrade > geogrid in the subbase by between 0.32 and 1.18 kN/m (22 and 81 lb/ft).
geogrid on subgrade vs. geogrid in subbase 12 months after installation	0.45 (31)	2.54	geogrid on subgrade > geogrid in the subbase by between 0.10 and 0.80 kN/m (7 and 55 lb/ft).
geogrid on subgrade vs. geogrid in subbase 24 months after installation	0.03 (2)	0.09	geogrid on subgrade = geogrid in the subbase
geogrid on subgrade vs. geogrid in subbase 35 months after installation	-0.43 (-29)	0.9	geogrid on subgrade = geogrid in the subbase
geogrid on subgrade vs. geogrid in subbase 45 months after installation	-0.11 (-8)	0.43	geogrid on subgrade = geogrid in the subbase

Table 5.25 Effect of subbase thickness for sections with geogrid located on subgrade analyzed using statistical z-test.

Subbase Thickness Effects – Geogrid Located on Subgrade			
Forces Compared	**Difference in Average Force kN/m (lb/ft)**	**z***	**Conclusion**
600 mm (24 in.) subbase vs. 300 mm (12 in.) subbase immediately after subbase compaction	0.55 (38)	2.89	600 mm (24 in.) subbase > 300 mm (12 in.) subbase by between 0.18 and 0.92 kN/m (12 and 63 lb/ft)
600 mm (24 in.) subbase vs. 300 mm (12 in.) subbase immediately after paving	0.19 (13)	0.56	600 mm (24 in.) subbase = 300 mm (12 in.) subbase
600 mm (24 in.) subbase vs. 300 mm (12 in.) subbase 12 months after installation	0.65 (45)	3.75	300 mm (12 in.) subbase > 600 mm (24 in.) subbase by between 0.31 and 0.99 kN/m (21 and 68 lb/ft)
600 mm (24 in.) subbase vs. 300 mm (12 in.) subbase 24 months after installation	1.37 (94)	4.26	300 mm (12 in.) subbase > 600 mm (24 in.) subbase by between 0.74 and 2.00 kN/m (51 and 137 lb/ft)
600 mm (24 in.) subbase vs. 300 mm (12 in.) subbase 35 months after installation	1.66 (114)	3.71	300 mm (12 in.) subbase > 600 mm (24 in.) subbase by between 0.78 and 2.54 kN/m (53 and 174 lb/ft)

Table 5.26 Effect of subbase thickness for sections with geogrid located at center of subbase analyzed using statistical z-test.

Subbase Thickness Effects – Geogrid Located at Center of Subbase			
Forces Compared	**Difference in Average Force kN/m (lb/ft)**	**z***	**Conclusion**
600 mm (24 in.) subbase vs. 300 mm (12 in.) subbase immediately after subbase compaction	0.44 (30)	2.22	300 mm (12 in.) subbase > 600 mm (24 in.) subbase by between 0.05 and 0.83 kN/m (3 and 57 lb/ft)
600 mm (24 in.) subbase vs. 300 mm (12 in.) subbase immediately after paving	0.21 (14)	0.67	600 mm (12 in.) subbase = 300 mm (24 in.) subbase
600 mm (24 in.) subbase vs. 300 mm (12 in.) subbase 12 months after installation	0.47 (32)	3.09	300 mm (12 in.) subbase > 600 mm (24 in.) subbase by between 0.17 and 0.77 kN/m (12 and 53 lb/ft)
600 mm (24 in.) subbase vs. 300 mm (12 in.) subbase 24 months after installation	0.55 (38)	3.54	300 mm (12 in.) subbase > 600 mm (24 in.) subbase by between 0.25 and 0.85 kN/m (17 and 58 lb/ft)
600 mm (24 in.) subbase vs. 300 mm (12 in.) subbase 35 months after installation	0.28 (19)	1.24	600 mm (12 in.) subbase = 300 mm (24 in.) subbase

The force in the geogrid located on subgrade and in the middle of the subbase was statistically equal for 300-mm (12 in.) subbase sections immediately after subbase compaction and after paving. However, for 12, 24, and 35 months after paving, geogrid located on the subgrade produced a statistically higher force than when located in the subbase. In the 600-mm subbase sections, the opposite trends occurred. Up to 12 months after paving geogrid located on subgrade produced a statistically higher force, but for 24 months to the end of the project monitoring period the forces were statistically equal. Taken in total, these results suggest that geogrid located on subgrade develops a force that is equal to or greater than when the geogrid is located within the subbase for both subbase thicknesses in this study.

The force in the geogrid immediately after paving in 300-mm (12 in.) subbase sections was statistically equal to that in the 600-mm (24 in.) subbase sections for both geogrid on subgrade and in the subbase. However, after 12, 24, and 35 months, the force

in the geogrid in the 300-mm (12 in.) subbase sections was statistically greater that in the 600-mm (24 in.) subbase sections for geogrid on subgrade. The same was true for geogrid located in the subbase for 12 and 24 months after paving. This suggests that pavements with thinner pavement sections develop greater forces than thicker pavement sections.

5.2.1.4.2. T-test Results. The t-test determines if the average difference between matched samples is greater than zero, or less than or equal to zero in terms of a confidence interval. The confidence interval is a function of the sample size and the average and standard deviation of the differences between the matched samples. The test assumes that the data is normally distributed. The t-test was used to evaluate the effects of elapsed time on the geogrid. The matched samples were the force in the geogrid at two different times as indicated by a given strain gage pair. The equations used in the analysis are shown in Equations 5.5 through 5.7.

$$s(D) = (s_D^2 / n)^{0.5} \quad \text{Equation 5.5}$$

where: $s(D)$ = the standard deviation of the population difference

s_D = the standard deviation of the matched sample differences

n = the number of matched samples

$$t^* = D / s(D) \quad \text{Equation 5.6}$$

where: t^* = the t-score

D = the average difference between matched samples

Confidence Limits = D ± (t) * s(D) Equation 5.7

where: t is a statistical variable based on the confidence interval of 95% and the number of degrees of freedom

If the t-score is less than or equal to *t* then the difference between the matched samples is considered less than or equal to zero with 95% confidence. If the t-score is greater than *t* then the difference between the matched samples is considered greater than zero and the confidence limits can be computed. The results of the t-test analyses on the effect of elapsed time are summarized in Table 5.27 and 5.28.

The t-test indicated that the average force in the geogrid on subgrade and in the subbase in the 300-mm (12 in.) subbase sections increased between subbase compaction and paving, paving to 12 months, and 12 to 24 months after installation. However, the forces in the subgrade geogrid sections decreased or remained the same from 24 to 35 months, unlike the subbase geogrid sections which continued to increase. This could be an argument that reinforcement mechanisms were continuing to develop through the end of the monitoring period for the 300-mm (12 in.) subbase sections with geogrid on subgrade, but had ceased to develop in 300-mm (12 in.) sections with geogrid in the subbase. The geogrid on subgrade and in the subbase in the 600-mm (24 in.) subbase sections exhibited increases in force between subbase compaction and paving. However, these forces either decreased, or failed to exhibit appreciable increases from paving to 45 months. This could be an argument that reinforcement mechanisms did not continue to develop after paving in sections with 600-mm (24-in.) subbase sections.

Table 5.27 Elapsed time effects in 300-mm subbase sections, analyzed using the statistical t-test.

Elapsed Time Effects – 300 mm (12 in) Subbase Sections					
Test Section	**Forces Compared**	**Average Change in Force kN/m (lb/ft)**	**t**	**t***	**Conclusion**
Section 1 300 mm (12 in.) Subbase Geogrid on Subgrade	after subbase compaction vs. paving	1.10 (75)	2.37	3.74	average force increased by between 0.40 and 1.79 kN/m (27 and 122 lb/ft)
	paving vs. 12 months after installation	0.60 (41)	2.45	3.45	average force increased by between 0.17 and 1.03 kN/m (12 and 60 lb/ft)
	12 months vs. 24 months after installation	0.62 (43)	2.57	3.90	average force increased by between 0.21 and 1.03 kN/m (14 and 71 lb/ft)
	24 months vs. 35 months after installation	0.29 (20)	2.78	2.32	no statistically significant increase in force
Section 2 & 4 300 mm (12 in.) Subbase Geogrid in Subbase	after subbase compaction vs. paving	0.47 (32)	2.13	3.13	average force increased by between 0.15 and 0.78 kN/m (10 and 53 lb/ft)
	paving vs. 12 months after installation	0.24 (16)	2.15	2.90	average force increased by between 0.06 and 0.42 kN/m (4 and 28 lb/ft)
	12 months vs. 24 months after installation	0.43 (29)	2.20	3.24	average force increased by between 0.14 and 0.72 kN/m (10 and 49 lb/ft)
	24 months vs. 35 months after installation	0.14 (10)	2.31	6.00	average force increased by between 0.09 and 0.19 kN/m (6 and 13 lb/ft)

Table 5.28 Elapsed time effects in 600-mm subbase sections, analyzed using the statistical t-test.

Elapsed Time Effects – 600 mm (24 in) Subbase Sections					
Test Section	**Forces Compared**	**Average Change in Force kN/m (lb/ft)**	**t**	**t***	**Conclusion**
Section 6 600-mm (24 in.) Subbase Geogrid on Subgrade	after subbase compaction vs. paving	0.73 (50)	2.45	4.47	average force increased by between 0.33 and 1.13 kN/m (23 and 77 lb/ft)
	paving vs. 12 months after installation	-0.27 (-19)	2.45	-2.65	average force did not change or decreased
	12 months vs. 24 months after installation	-0.14 (-10)	2.57	-1.91	average force did not change or decreased
	24 months vs. 35 months after installation	-0.61 (-42)	3.18	-2.30	average force did not change or decreased
	35 months vs. 45 months after installation	0.26 (18)	3.18	0.89	no statistically significant increase in force
Section 7 & 10 600-mm (24 in.) Subbase Geogrid in Subbase	after subbase compaction vs. paving	0.69 (47)	2.13	5.39	average force increased by between 0.42 and 0.96 kN/m (29 and 66 lb/ft)
	paving vs. 12 months after installation	0.08 (5.5)	2.13	1.39	no statistically significant increase in force
	12 months vs. 24 months after installation	0.30 (21)	2.13	2.19	average force increased by between 0.01 and 0.59 kN/m (1 and 40 lb/ft)
	24 months vs. 35 months after installation	0.11 (8)	2.23	.70	no statistically significant increase in force
	35 months vs. 45 months after installation	-0.09 (-6)	2.31	-1.8	average force did not change or decreased

5.2.2. Strain Gages Parallel to Centerline

The instrumented sections of reinforcement geogrid have one strain gage pair oriented parallel to the roadway centerline. These gages were placed at offsets 2.9 m (9.5 ft) from the centerline to measure the force in the geogrid parallel to centerline in the outside wheel path of the right (eastbound) lane.

The average of each top and bottom strain gage pair was plotted to remove the effects of bending. The results are organized by instrumented station. Figures 5.14 and 5.15 show the forces in the geogrid parallel to centerline in test section 1. The parallel gages in Sections 2 and 4 failed soon after compaction of the subbase aggregate and are not plotted. Figures 5.16 through 5.20 show the forces in the geogrid parallel to centerline in test sections 6, 7, and 10. Manual readout stations have a data point symbol at every data point whereas automated readout stations have a data point symbol every 50 data points, however all the data points were plotted.

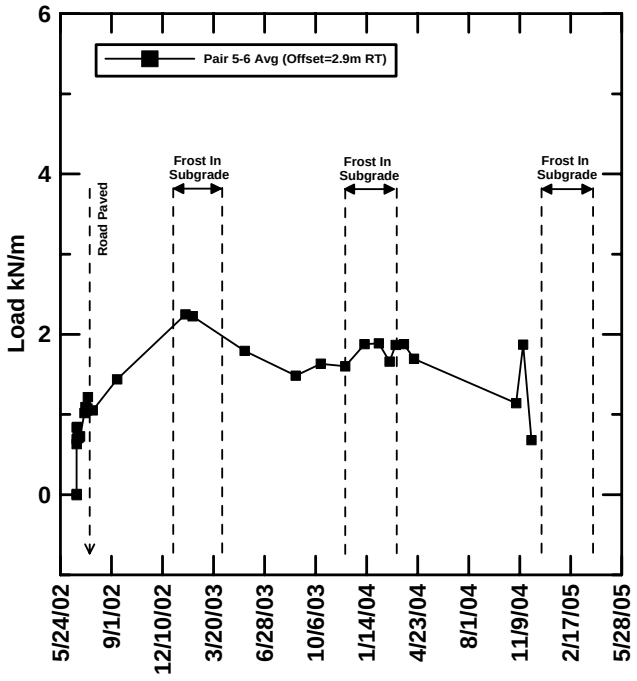

Figure 5.14 Force parallel to centerline in geogrid located on subgrade with 300-mm (12-in.) subbase in test section 1 station 1+540 m.

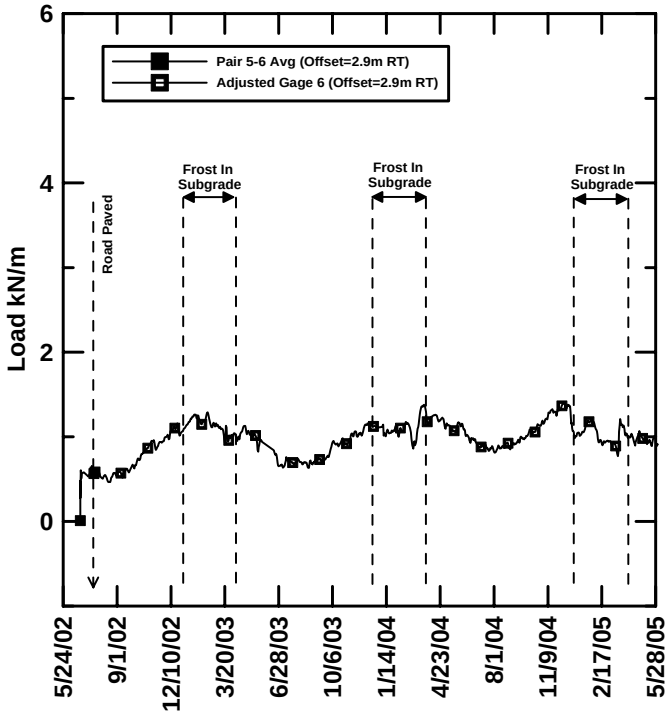

Figure 5.15 Force parallel to centerline in geogrid located on subgrade with 300-mm (12-in.) subbase in test section 1 station 1+560 m.

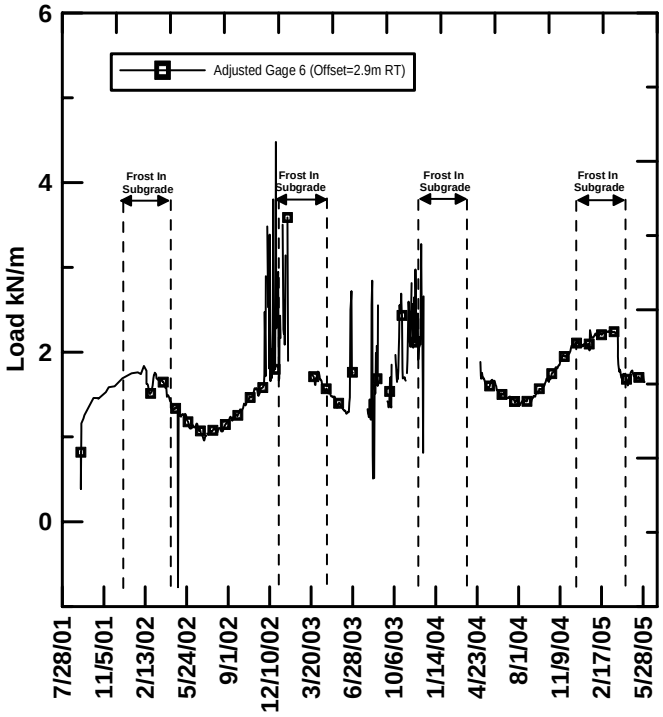

Figure 5.16 Force parallel to centerline in geogrid located on subgrade with 600-mm (24-in.) subbase in test section 6 station 3+970 m.

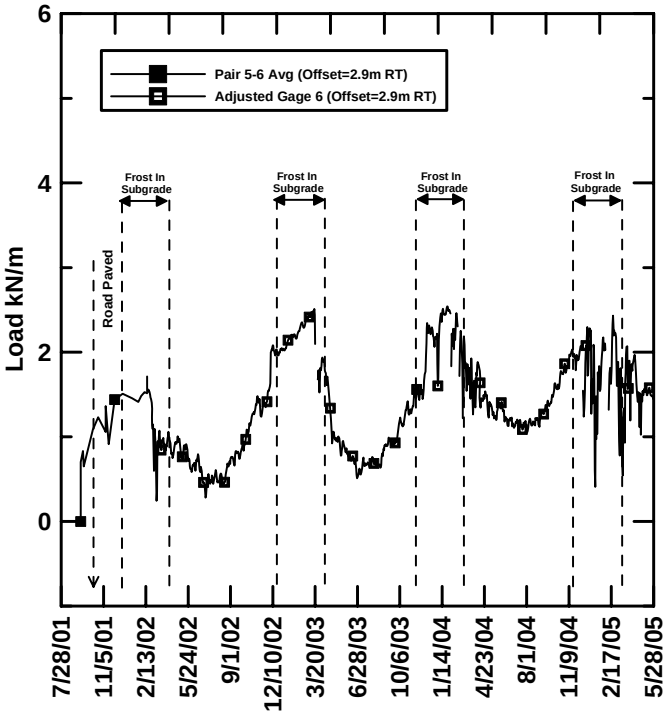

Figure 5.17 Force parallel to centerline in geogrid located in 600-mm (24-in) subbase in test section 7 station 3+990 m.

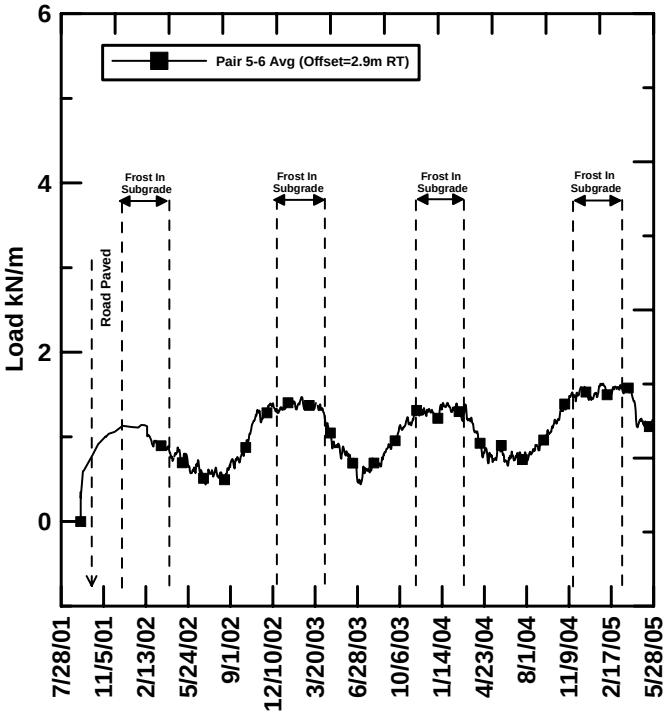

Figure 5.18 Force parallel to centerline in geogrid located in 600-mm (24-in.) subbase in test section 7 station 4+010 m.

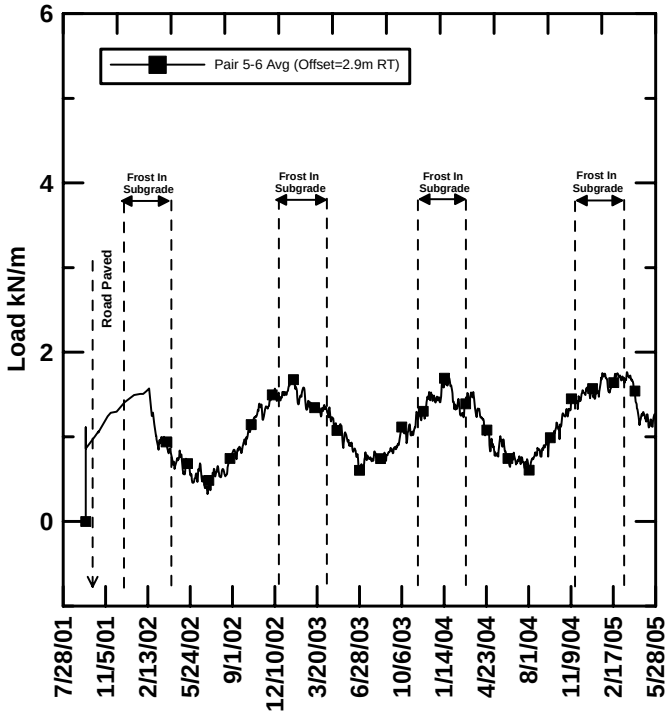

Figure 5.19 Force parallel to centerline in geogrid located in 600-mm (24-in.) subbase in test section 10 station 4+110 m.

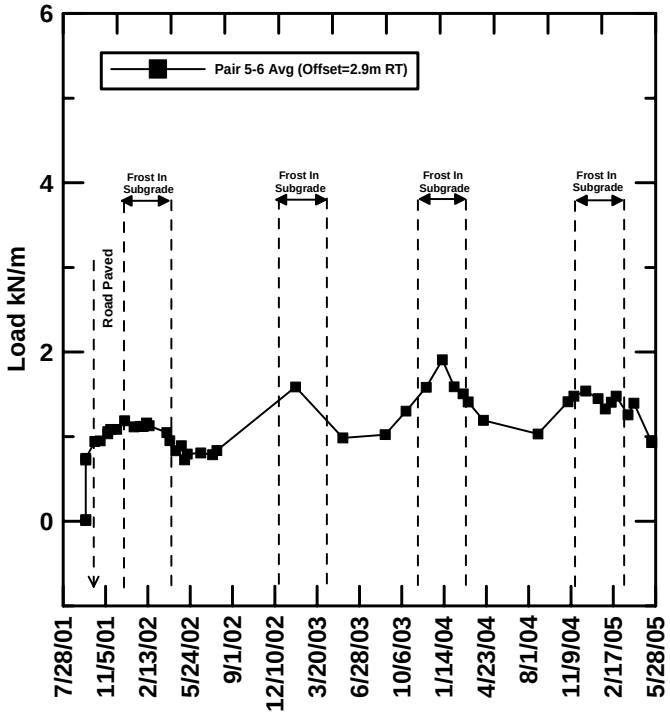

Figure 5.20 Force parallel to centerline in geogrid located in 600-mm (24-in.) subbase in test section 10 station 4+130 m.

5.2.2.1. 300-mm Subbase Sections. Test sections 1, 2, and 4 were constructed using a reduced subbase section. In test section 1 geogrid was placed on subgrade and overlain by a 300-mm (12-in.) subbase. Test sections 2 and 4 have geogrid in the center of the 300-mm (12-in.) subbase. The average construction and long term forces in the instrumented geogrid ribs oriented parallel to centerline are discussed in sections 5.2.2.1.1 and 5.2.2.1.2, and summarized in Table 5.29.

5.2.2.1.1. Construction Forces. The average tensile force in test section 1 following subbase compaction was 0.51 kN/m (35 lb/ft). This had increased to 0.92 kN/m (63 lb/ft) immediately after paving. Overall, the magnitudes of the forces are similar to those observed for the ribs oriented perpendicular to centerline (see Table 5.22)

5.2.2.1.2. Long Term Forces. Only the gages in section 1 survived long enough to establish long term trends. As seen in Table 5.30, the mean of the gages in the two stations in this section varied between 0.91 and 1.11 kN/m (62 to 76 lb/ft) for the period from paving through the end of monitoring. There was no clear trend of increasing or decreasing force over this time period. The long term forces are less than half of those observed for ribs oriented perpendicular to centerline (see Table 5.22).

Table 5.29 Force in geogrid ribs oriented parallel to centerline in test sections constructed with 300-mm (12-in.) subbase.

300 mm Subbase – Force in Geogrid Parallel to Centerline kN/m (lb/ft)							
Test Section	Station	Subbase Compacted	Road Paved	12 Month Force	24 Month Force	35 Month Force	45 Month Force
Section 1	1+540 Geogrid on Subgrade	0.69 (47)	1.22 (84)	1.48 (101)	1.14 (78)	NF	--
	1+560 Geogrid on Subgrade	0.33 (23)	0.61 (42)	0.73* (50)	0.91* (62)	0.91* (62)	--
Section Mean & Standard Deviation		0.51 (35) *0.26 (18)*	0.92 (63) *0.43 (29)*	1.11 (76) *0.14 (10)*	1.03 (71) *0.13 (9)*	0.91 (62) NA	--
Section 2	1+600 Geogrid at Center of Subbase	0.42 (29)	NF	NF	NF	NF	--
	1+620 Geogrid at Center of Subbase	0.72 (49)	NF	NF	NF	NF	--
Section 4	1+720 Geogrid at Center of Subbase	0.66 (45)	NF	NF	NF	NF	--
	1+740 Geogrid at Center of Subbase	2.00 (137)	NF	NF	NF	NF	--
Section Mean & *Standard Deviation*		0.95 (65) *0.71 (49)*	NA	NA	NA	NA	--

NF = Not Functioning
NA = Not Applicable
* = Adjusted Data

5.2.2.2. 600-mm Subbase Sections. Test sections 6, 7, and 10 were constructed using a full subbase section. In test section 6, geogrid was placed on subgrade and overlain by a 600-mm (24-in.) subbase. Test sections 7 and 10 have geogrid in the center of the 600-mm (24-in.) subbase. Construction of test section 6 required two 300-mm (12-in.) lifts of subbase material to cover the geogrid. The change in geogrid forces between compaction of the first and second subbase lift in test section 6 was small. Thus, only the

geogrid forces after compaction of the first lift are discussed below. The average construction and long term forces in the instrumented geogrid ribs oriented parallel to centerline are discussed in sections 5.2.2.2.1 and 5.2.2.2.2, and summarized in Table 5.30.

Table 5.30 Force in geogrid ribs oriented parallel to centerline in test sections constructed with 600-mm (24-in.) subbase.

600 mm Subbase – Parallel Force in Geogrid kN/m (lb/ft)							
Test Section	Station	Subbase Compacted	Road Paved	12 Month Force	24 Month Force	35 Month Force	45 Month Force
Section 6	3+950 Geogrid on Subgrade	NA	NA	NA	NA	NA	NA
	3+970 Geogrid on Subgrade	0.47 (32)	1.58 (108)	1.48* (101)	2.69* (184)	1.76* (121)	1.65* (113)
Section Mean & Standard Deviation		0.47 (32) *NA*	1.58 (108) *NA*	1.48 (101) *NA*	2.69 (184) *NA*	1.76 (121) *NA*	1.65 (113) *NA*
Section 7	3+990 Geogrid at Center of Subbase	0.71 (49)	1.23 (84)	1.27* (87)	1.38* (95)	1.75* (120)	1.41* (97)
	4+010 Geogrid at Center of Subbase	0.28 (19)	0.91 (62)	1.16 (79)	1.21 (83)	1.30 (89)	1.11 (76)
Section 10	4+110 Geogrid at Center of Subbase	0.96 (66)	1.09 (75)	1.23 (84)	1.12 (77)	1.25 (86)	1.12 (77)
	4+130 Geogrid at Center of Subbase	0.74 (51)	0.95 (65)	0.84 (57)	1.30 (89)	1.48 (101	1.06 (73)
Section Mean & *Standard Deviation*		0.67 (46) *0.28 (19)*	1.05 (72) *0.13 (9)*	1.13 (77) *0.17 (12)*	1.25 (86) *0.10 (7)*	1.45 (99) *0.20 (13)*	1.18 (81) *0.14 (9)*

NF = Not Functioning
NA = Not Applicable
* = Adjusted Data

5.2.2.2.1. Construction Forces. The force in the one station with functioning gages in section 6 was 0.47 kN/m (32 lb/ft). After paving the force was 1.58 kN/m (108 lb/ft), an increase of 236%. The mean force after compaction in sections 7 and 10 was 0.67 kN/m (46 lb/ft). After paving the force was 1.05 kN/m (72 lb/ft), an increase of 57%. Thus, the action of traffic and other factors seem to increase the force prior to paving. Overall, the magnitude of the forces are similar to those observed for the ribs oriented perpendicular to the centerline.

5.2.2.2.2. Long Term Forces. The long term force for the one station in section 6 with functioning gages ranged from 1.48 to 2.69 kN/m (101 to 184 lb/ft). The force observed immediately after paving falls within this range. For Sections 7 and 11 the mean force ranged from 1.13 to 1.45 kN/m (77 to 86 lb/ft) compared to a force of 1.05 kN/m (72 lb/ft) immediately after paving. Overall, the results suggest that there is little change in force after paving. In addition, as shown in Table 5.22, the long term force for ribs perpendicular to centerline ranged from 1.24 to 1.54 kN/m (85 to 106) in section 6, and 1.09 to 1.67 kN/m (75 to 114 lb/ft) in sections 7 and 10, so the force parallel and perpendicular to centerline appear to be similar. This is in contrast to the behavior observed for the sections with 300 mm (12 in.) subbase.

5.2.3. Thermal Strain Gages

Each station with instrumented geogrid has an instrumented rib that was cut from the material roll prior to construction. These isolated ribs are housed in 100-mm (4-in.) PVC electrical junction boxes and measure average strains associated with thermal

expansion and contraction. In addition, thermal strains were measured in the laboratory using several isolated instrumented ribs exposed to temperatures ranging from –15 to 25 ºC (5 to 77 ºF). In all cases, temperature change had negligible effect on the strain gage readings, so it was concluded that no correction for temperature change was needed.

5.2.4. Mobilization of geogrid strength

The highest force measured by any gage pair immediately after paving was approximately 4 kN/m (270 lb/ft). This is approximately 14% of the geogrid's ultimate tensile strength, which is 29 kN/m (1,985 lb/ft) in the direction perpendicular to centerline. The average forces summarized in Table 5.22 are less than or equal to 10% of the ultimate strength. Thus, only a fraction of the geogrid's strength was mobilized. Moreover, the tensile strains in the geogrid were small, with the maximum value after paving being 1.0% as computed using a modulus of 397 kN/m (27,200 lb/ft) reported by the manufacturer.

5.2.5. Creep Test Results

A laboratory creep test was performed to investigate strains in the geogrid under a sustained load. A wide-width tensile test specimen previously used for strain gage calibration tests was kept in the steel grips (described in Section 4.2.5). Steel plates were hung from the center of the bottom grip, subjecting the specimen to a constant tensile load of 1.66 kN/m (114 lb/ft) for a total of 9 weeks. Deflections were measured using a pair of dial gages accurate to 0.0025 mm (0.0001 in.) mounted to the steel grips. The results of the creep test are shown in Figures 5.21 and 5.22.

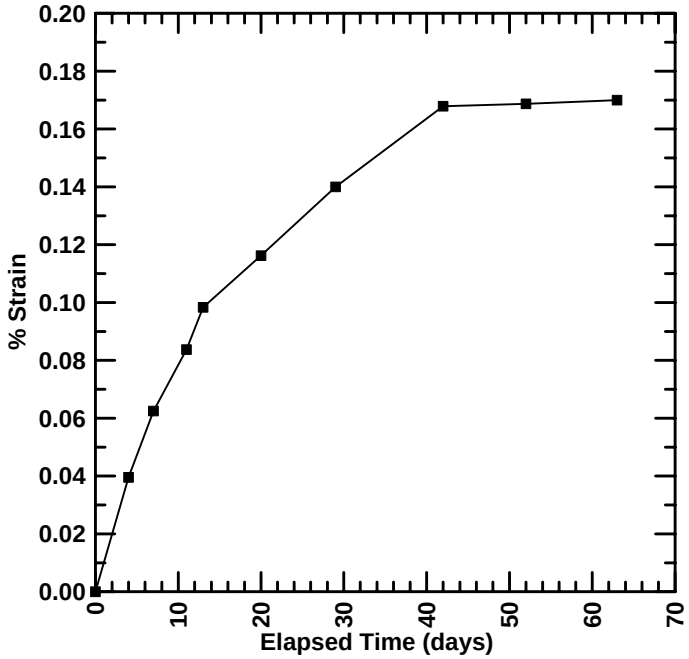

Figure 5.21 Creep test results plotted with linear time scale.

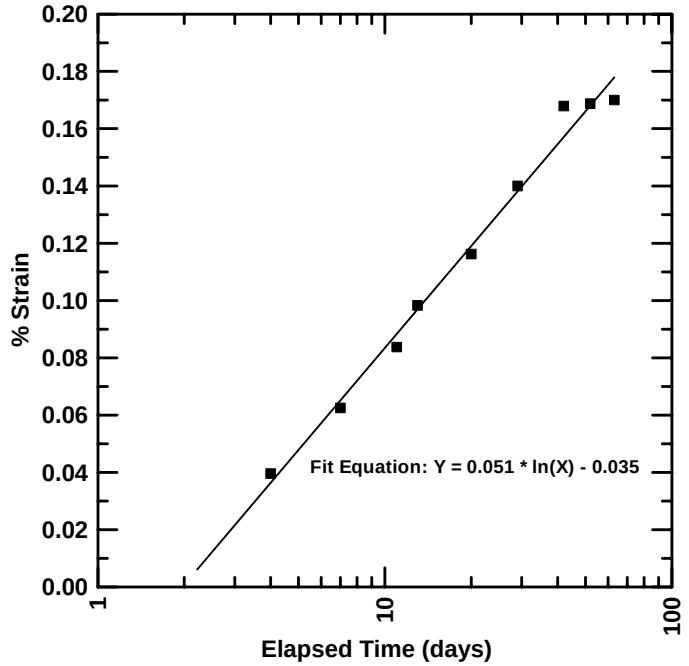

Figure 5.22 Creep test results plotted with logarithmic time scale.

The maximum strain, recorded at the end of the test, was approximately 0.17%. The geogrid developed strain quickly at the beginning of the test, reaching a strain of 0.10% in the first two weeks. Then, as shown in Figure 5.21, the strain rate slowed significantly. When plotted with a logarithmic time scale, as shown in Figure 5.22, the strain increases in a nearly linear fashion.

The creep behavior of geogrid confined in soil is different than that of geogrid tested in isolation. Nonetheless, the results shown in Figures 5.21 and 5.22 suggest that this geogrid may experience creep, as reflected by increases in strain, when subjected to a constant load. Considering that in this study the force per unit width in the geogrid was obtained from the change in strain in the instrumented ribs, strain due to creep would be interpreted as an increase in force per unit width. Thus, the increases in force per unit width with time reported in this study could be due to creep rather than an actual increase in force carried by the geogrid.

The possible role that creep could play was further investigated using field results. Four instrumented ribs with loads per unit width during the first 9 weeks similar to the 1.66 kN/m (114 lb/ft) applied during the laboratory creep were selected. Using the manufacturer's modulus the average % strain in these ribs during the first 9 weeks after installation was calculated. The results were plotted using linear and logarithmic time scales and are shown in Figures 5.23 through 5.30.

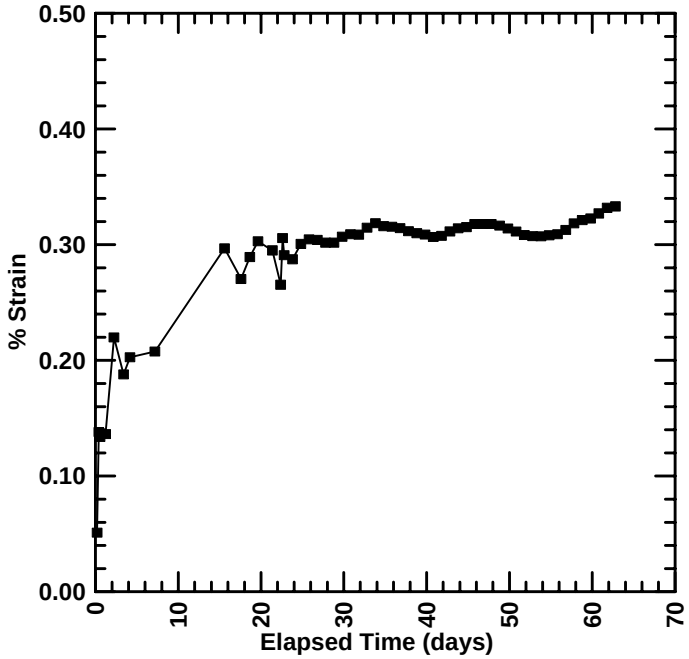

Figure 5.23 Average strain measured by strain gage pair 1-2 in test section 1 station 1+560 versus elapsed time.

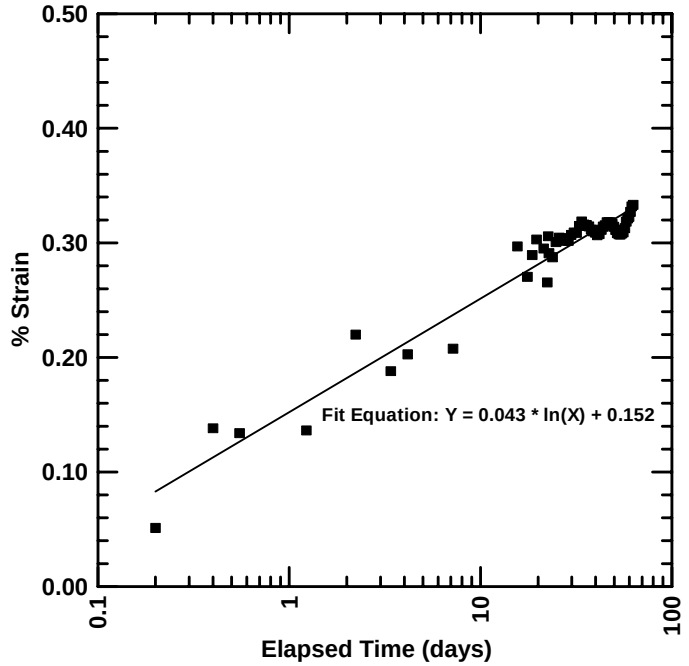

Figure 5.24 Average strain measured by strain gage pair 1-2 in test section 1 station 1+560 versus log elapsed time.

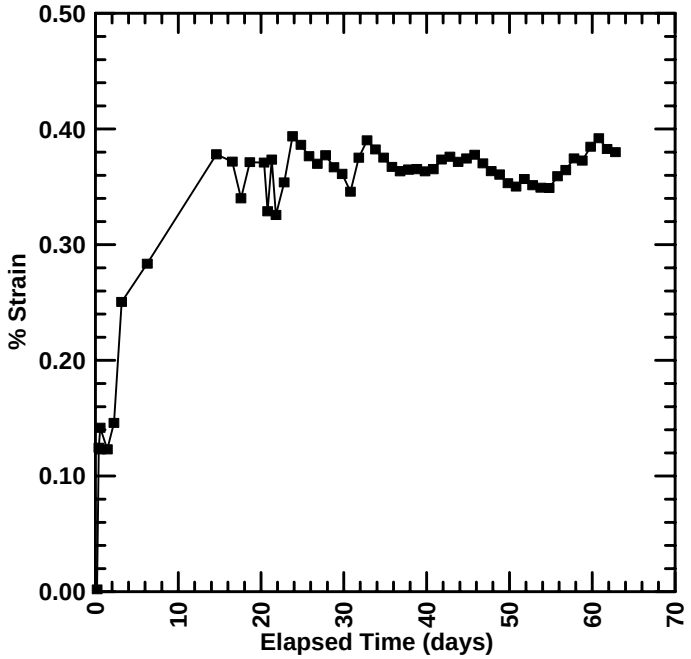

Figure 5.25 Average strain measured by strain gage pair 1-2 in test section 2 station 1+600 versus elapsed time.

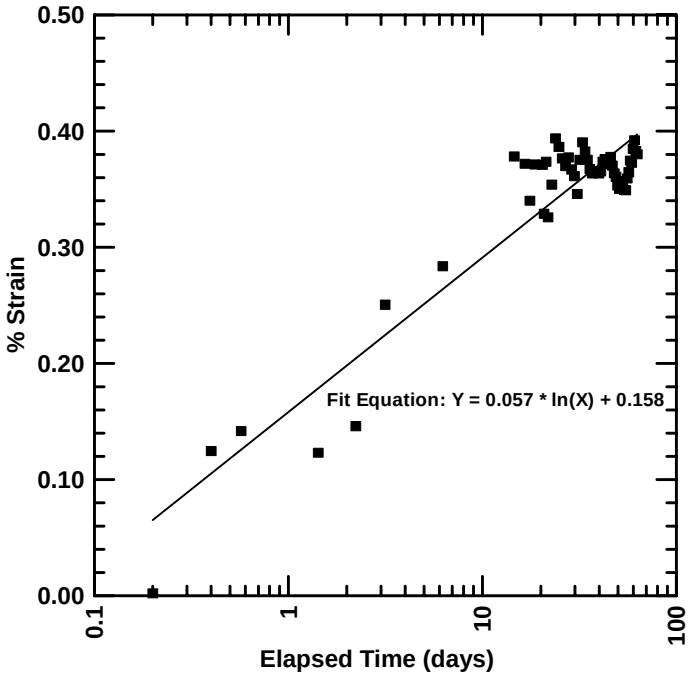

Figure 5.26 Average strain measured by strain gage pair 1-2 in test section 2 station 1+600 versus log elapsed time.

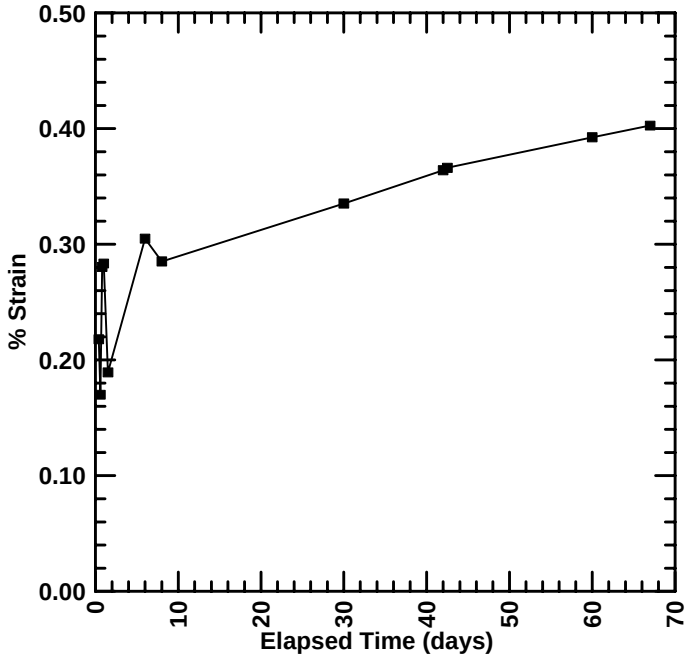

Figure 5.27 Average strain measured by strain gage pair 9-10 in test section 6 station 3+970 versus elapsed time.

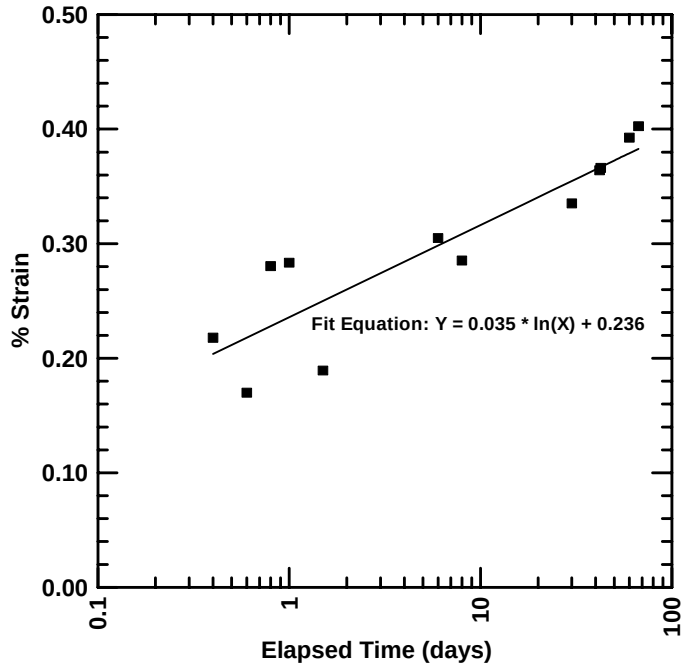

Figure 5.28 Average strain measured by strain gage pair 9-10 in test section 6 station 3+970 versus log elapsed time.

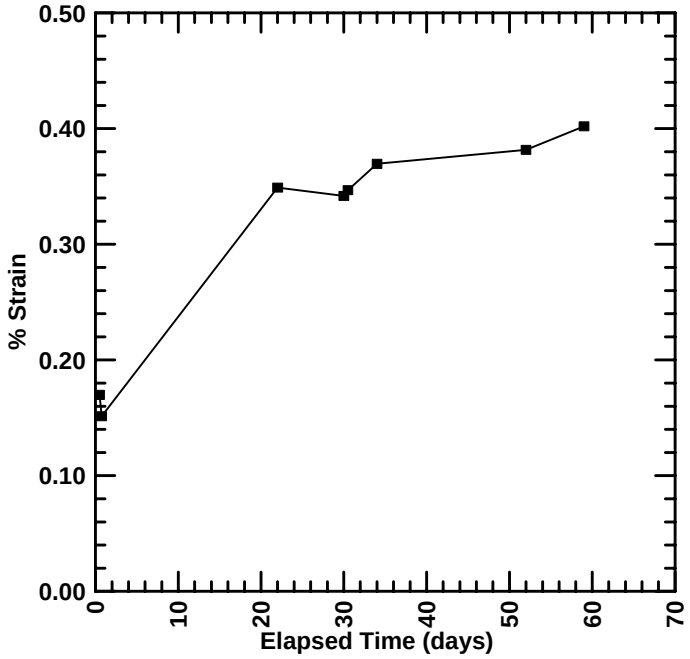

Figure 5.29 Average strain measured by strain gage pair 1-2 in test section 10 station 4+110 versus elapsed time.

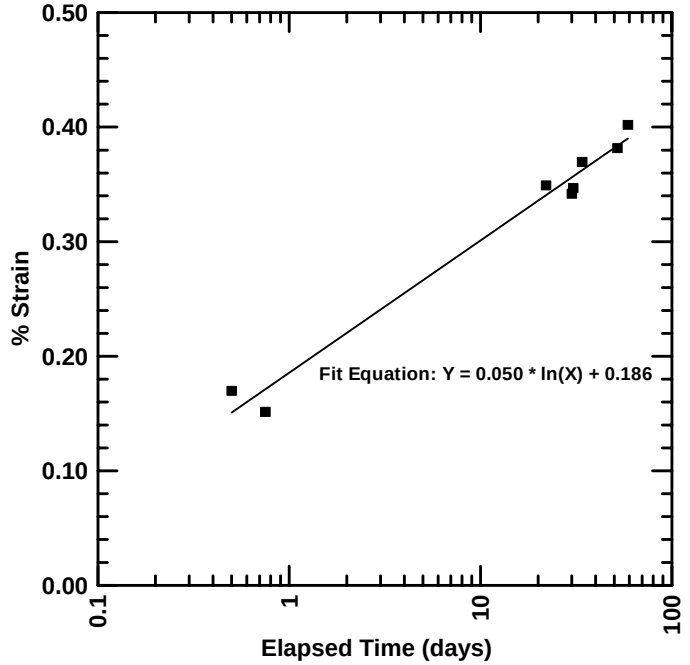

Figure 5.30 Average strain measured by strain gage pair 1-2 in test section 10 station 4+110 versus log elapsed time.

The results shown in Figures 5.23 through 5.30 suggest that the apparent increases in force per unit width determined from field strain measurements may be the result of creep strain rather than an actual increase in force carried by the geogrid. The shapes of the plots with a linear time scale are similar to the shape of the laboratory creep test curve plotted with a linear time scale. Furthermore, the slopes of the log fits in Figures 5.24, 5.26, 5.28, and 5.30 are similar to the slope of the log fit from the laboratory creep test. The field creep fit slopes vary from the laboratory creep fit slopes by between 2 and 31%, with an average variation of approximately 14%.

5.3. Vibrating Wire Piezometer Results

A pair of vibrating wire piezometers was installed in test sections 3, 4, 5, 8, 9, 10, 11, and 12 to evaluate the effectiveness of the drainage geocomposite in reducing subbase and subgrade porewater pressures. The instruments proved to be particularly vulnerable during construction. The cables leading to subbase piezometers in sections 8, 9, and 10 were severed during fine grading. These were replaced, however the subbase piezometers in sections 9 and 10 failed again. Both piezometers in test section 5 failed during construction and were not replaced. The overall long-term survivability of the vibrating wire piezometers was 67%.

5.3.1. Reconstructed Section Results

In test sections 3, 4, 5, 8, 9, and 10 the contractors used typical reconstruction techniques. The existing roadway was excavated to subgrade, and 300 mm (12 in.) or 600 mm (24 in.) of new subbase was placed and compacted prior to paving. Control

sections were constructed with no geosynthetics. Drainage sections were constructed with drainage geocomposite on subgrade. Results from these sections are shown in Figures 5.31 through 5.35. Pore pressures during freezing periods have no meaning and should be ignored.

During the non-freezing periods many of the piezometers had negative pore pressure. This would occur for partially saturated conditions and is an indication of good drainage. Well drained subbases would have zero porewater pressure, however the type of piezometer used for this study can exhibit readings with significant negative values for partially saturated conditions. This is due to the capillary menisci that form in the pores of the porestone at the interface with the well-drained subbase. Bouchedid and Humphrey (2004) investigated the behavior of a similar vibrating wire piezometer (GEOKON model 4500 ALX) in partially saturated subbase aggregate. They found the pore pressure readings were negative when the saturation was less than about 50%.

Results from all of the subbase piezometers are summarized in Figure 5.36. Careful examination of Figure 5.36 reveals that the sections with drainage geocomposite exhibited large periods of negative porewater pressure unlike the control sections, which exhibited mostly positive porewater pressures. This suggests that the drainage geocomposite assists with the removal of water from the subbase.

Results from all of the subgrade piezometers are summarized in Figure 5.37. These too exhibit negative porewater pressures indicating significant periods of partial saturation. However, for the subgrade piezometers, there is no clear difference in behavior between sections with and without drainage geocomposite. This suggests that the drainage geocomposite had little effect on subgrade porewater pressures.

Similar results were found during a previous study for MaineDOT by the University of Maine in the towns of Frankfort and Winterport. Test sections with drainage geocomposite on subgrade exhibited lower porewater pressures than the control sections, suggesting that the drainage geocomposite assisted in the removal of water from the overlying pavement system (Fetten and Humphrey,1998).

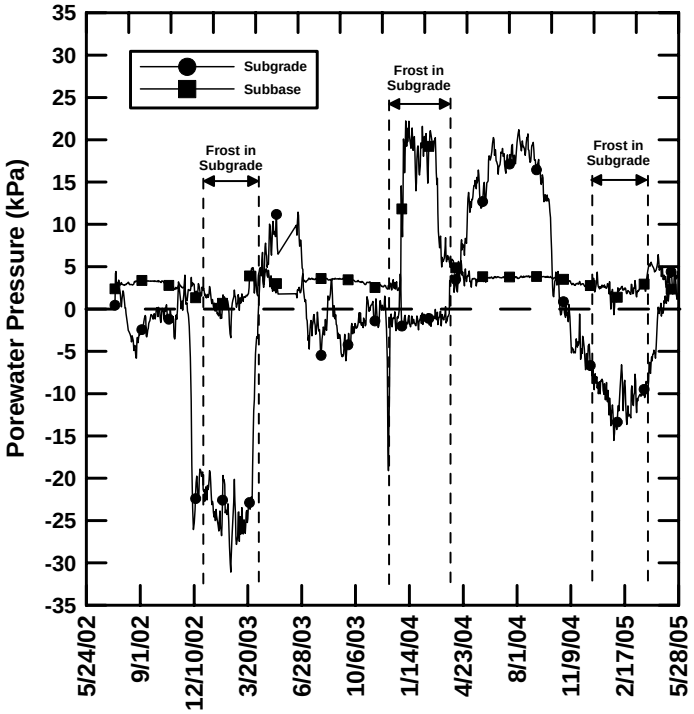

Figure 5.31 Porewater pressures in test section 3 (control).

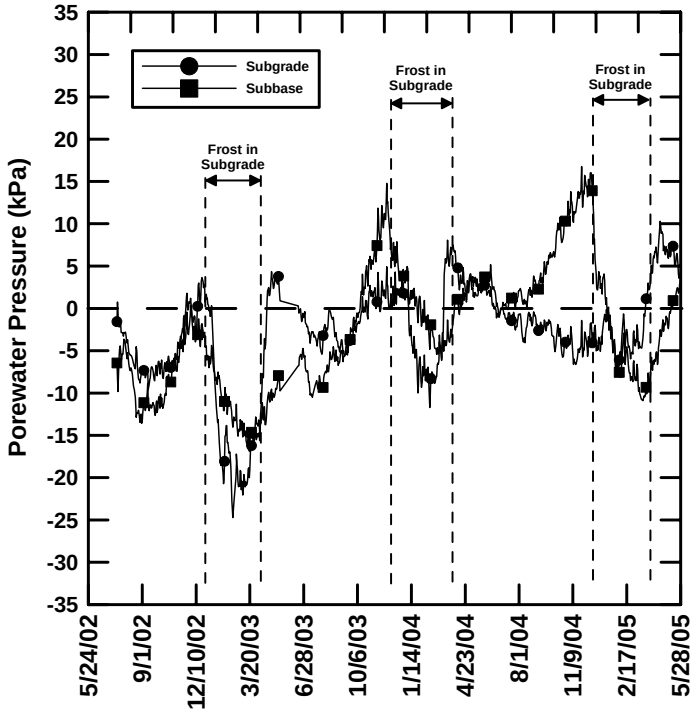

Figure 5.32 Porewater pressures in test section 4 (drainage).

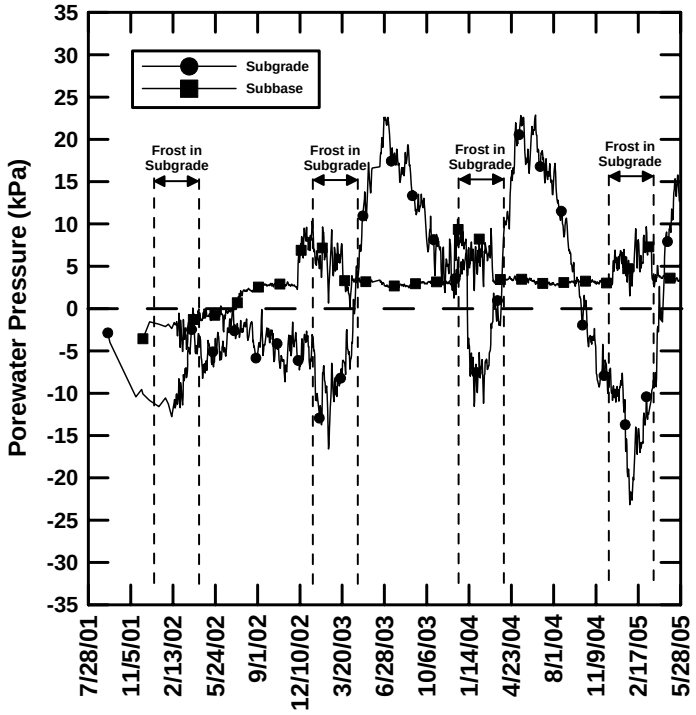

Figure 5.33 Porewater pressures in test section 8 (control).

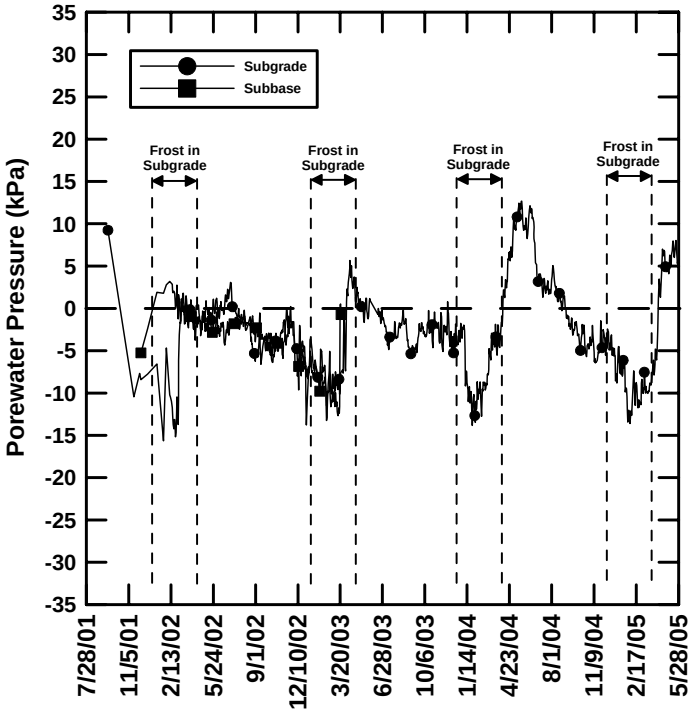

Figure 5.34 Porewater pressures in test section 9 (drainage).

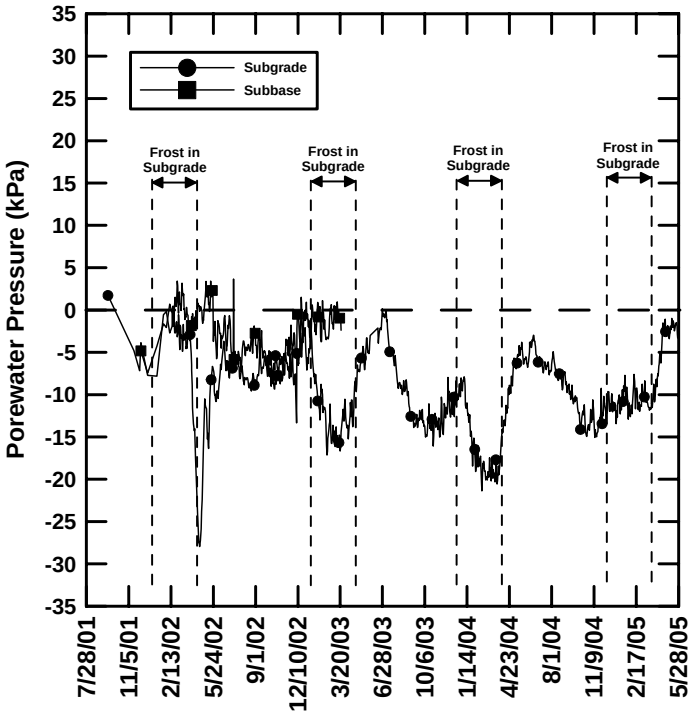

Figure 5.35 Porewater pressures in test section 10 (drainage).

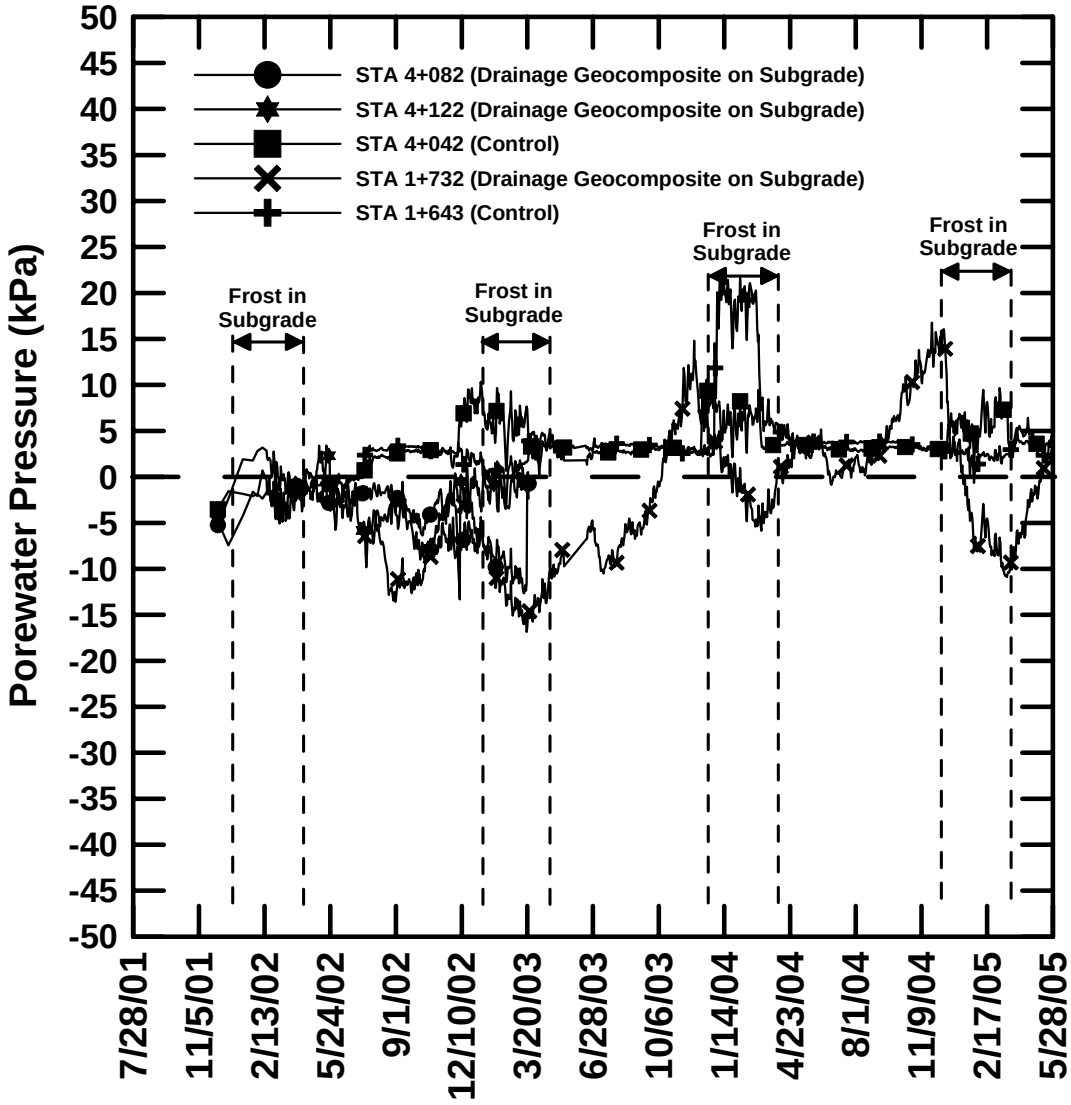

Figure 5.36 Subbase porewater pressures in test sections 3, 4, 8, 9, and 10.

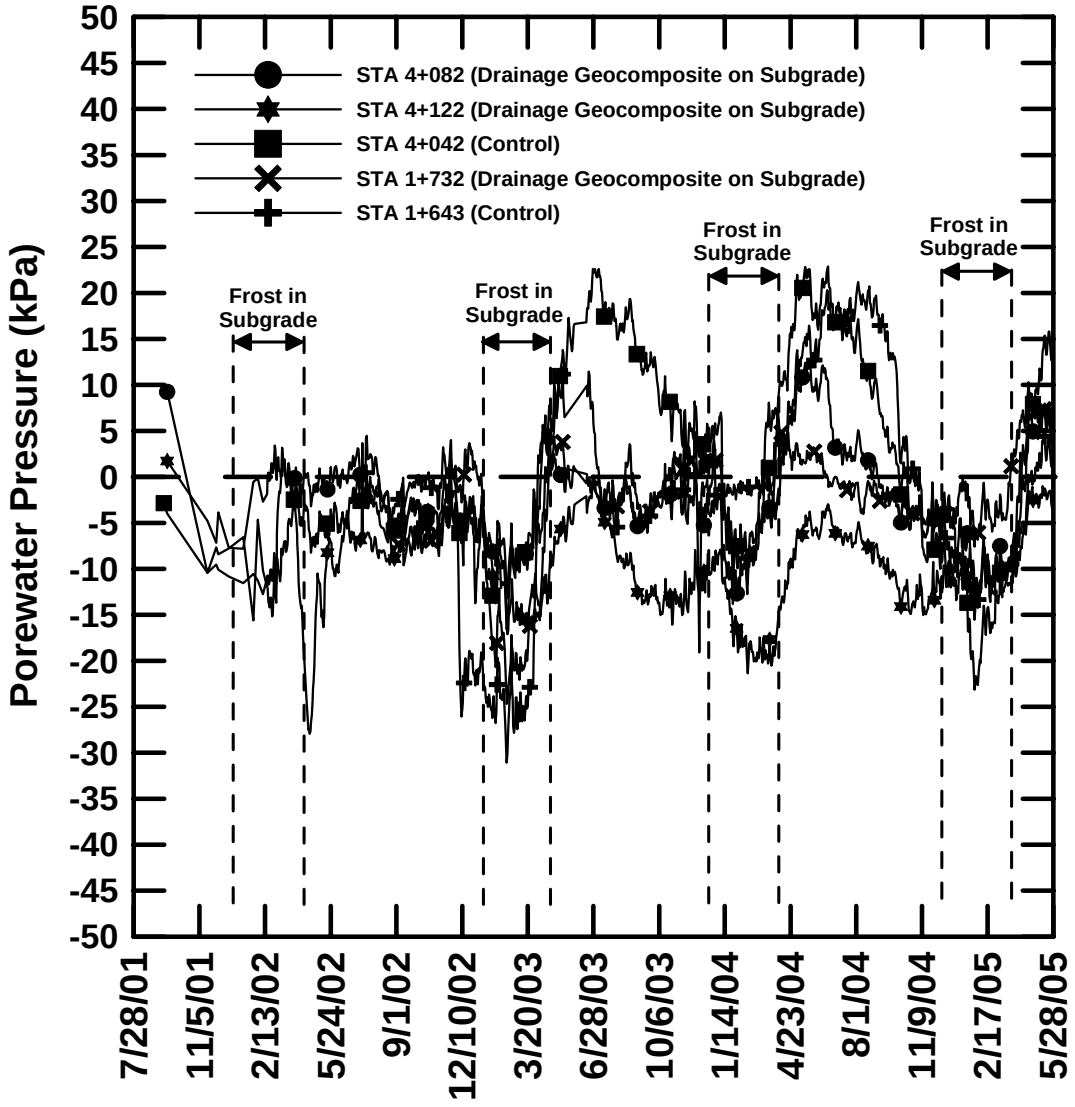

Figure 5.37 Subgrade porewater pressures in test sections 3, 4, 8, 9, and 10.

5.3.2. Reclaimed Section Results

In test sections 11 and 12 the existing pavement was reclaimed. A layer of grindings 75 to 150 mm (3 to 6 in.) thick was compacted over the existing subbase. Section 11 was constructed with drainage geocomposite beneath the pavement grindings. Section 12 is a control section constructed with no geosynthetics. Unlike the piezometers

in sections 3, 4, 8, 9, and 10 which were automatically read each hour by a data acquisition system, those in sections 11 and 12 were read periodically with a manual readout unit. The subbase and subgrade porewater pressures in sections 11 and 12 on each date manual readings were taken are shown in Figures 5.38 and 5.39. A comparison of the porewater pressure in the control section versus that in the drainage section is shown for the subbase and subgrade piezometers in Figures 5.40 and 5.41, respectively.

As shown in Figure 5.38, the piezometers in test section 11 had significant periods of positive porewater pressure indicating a high degree of saturation in both the subbase and subgrade throughout the monitoring period. The results from the piezometers in test section 12 shown in Figure 5.39 exhibit positive and negative porewater pressures indicating periods of high saturation and low saturation, respectively.

Figure 5.40 shows that throughout the monitoring period the subbase piezometer in the control section had a lower porewater pressure than in the drainage section. This suggests that the drainage geocomposite's ability to remove water from the subbase was limited in this section. Likewise, Figure 5.41 indicates significant periods where the subgrade piezometer in the control section had lower porewater pressure than that in the drainage section. This also indicated that the drainage geocomposite had limited effectiveness in this section.

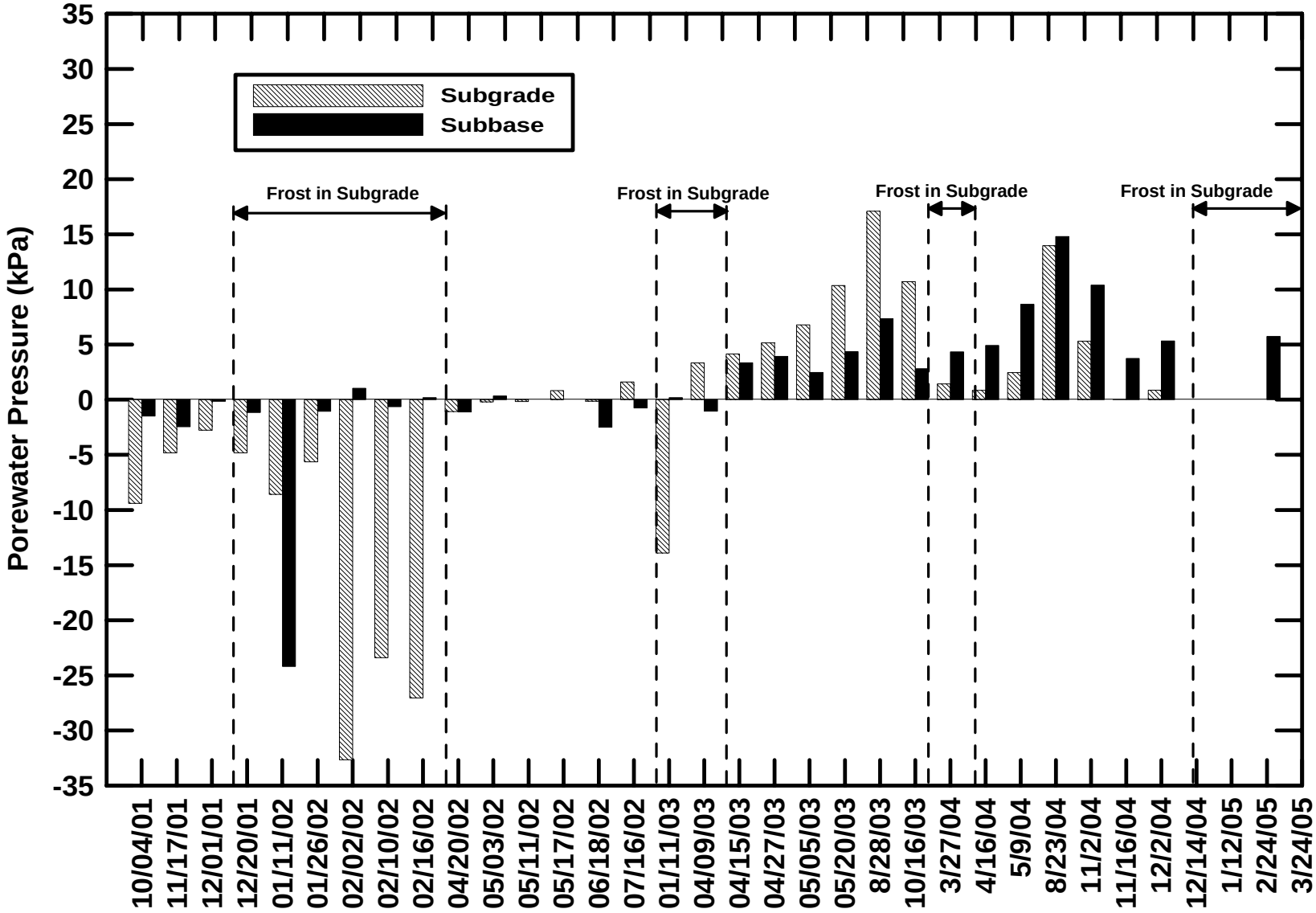

Figure 5.38 Porewater pressures in test section 11 (drainage).

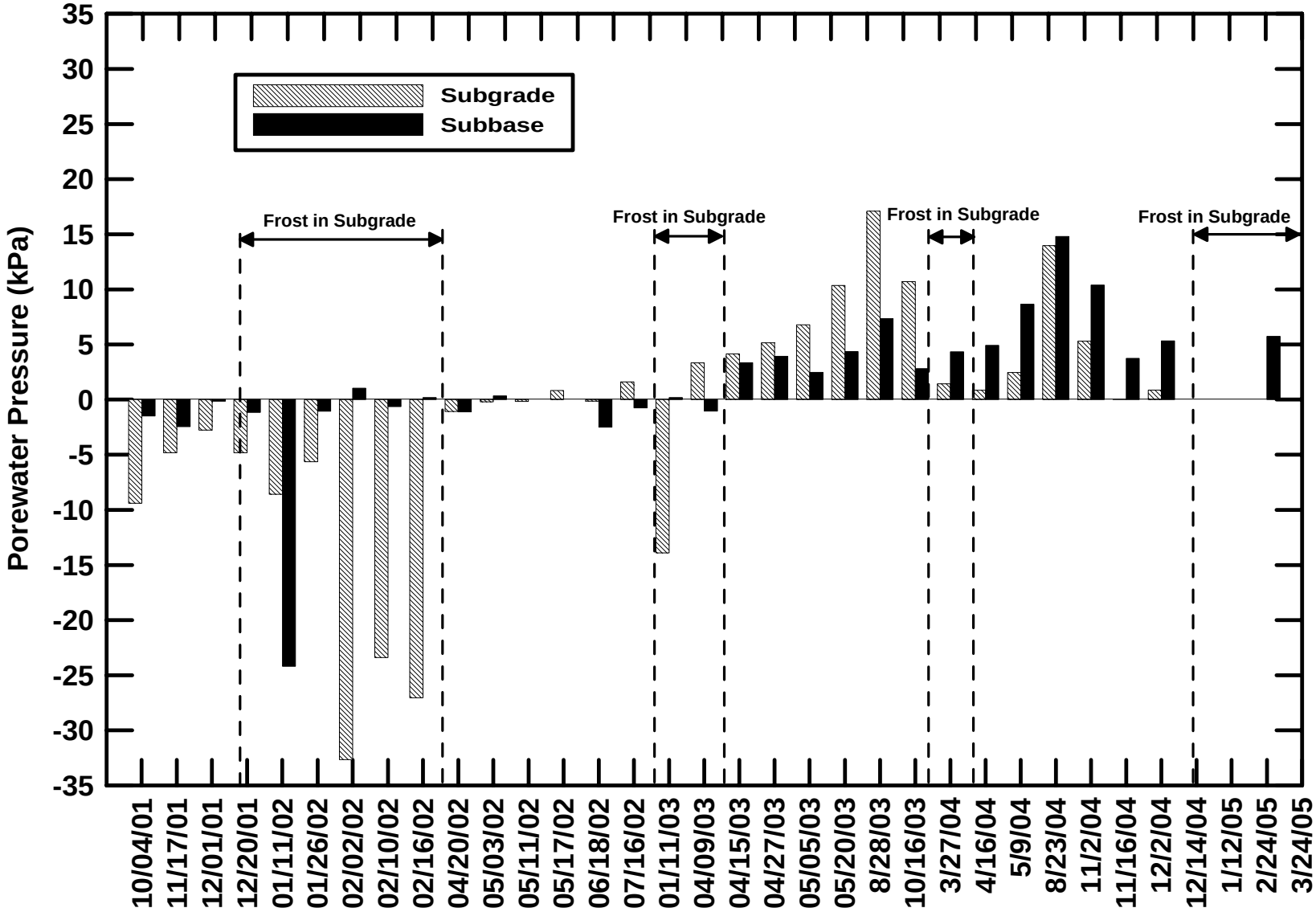

Figure 5.39 Porewater pressures in test section 12 (control).

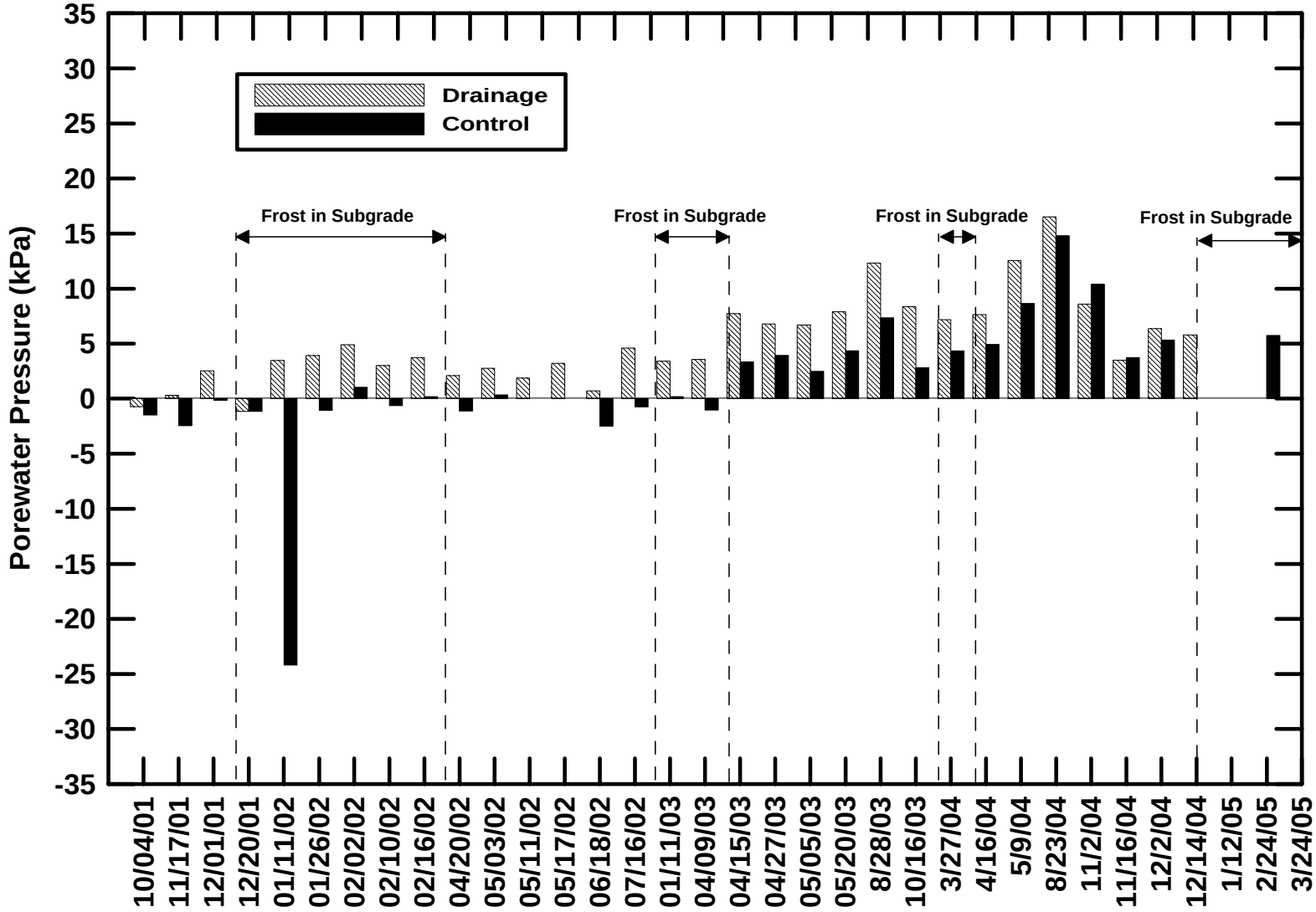

Figure 5.40 Subbase porewater pressures in reclaim sections.

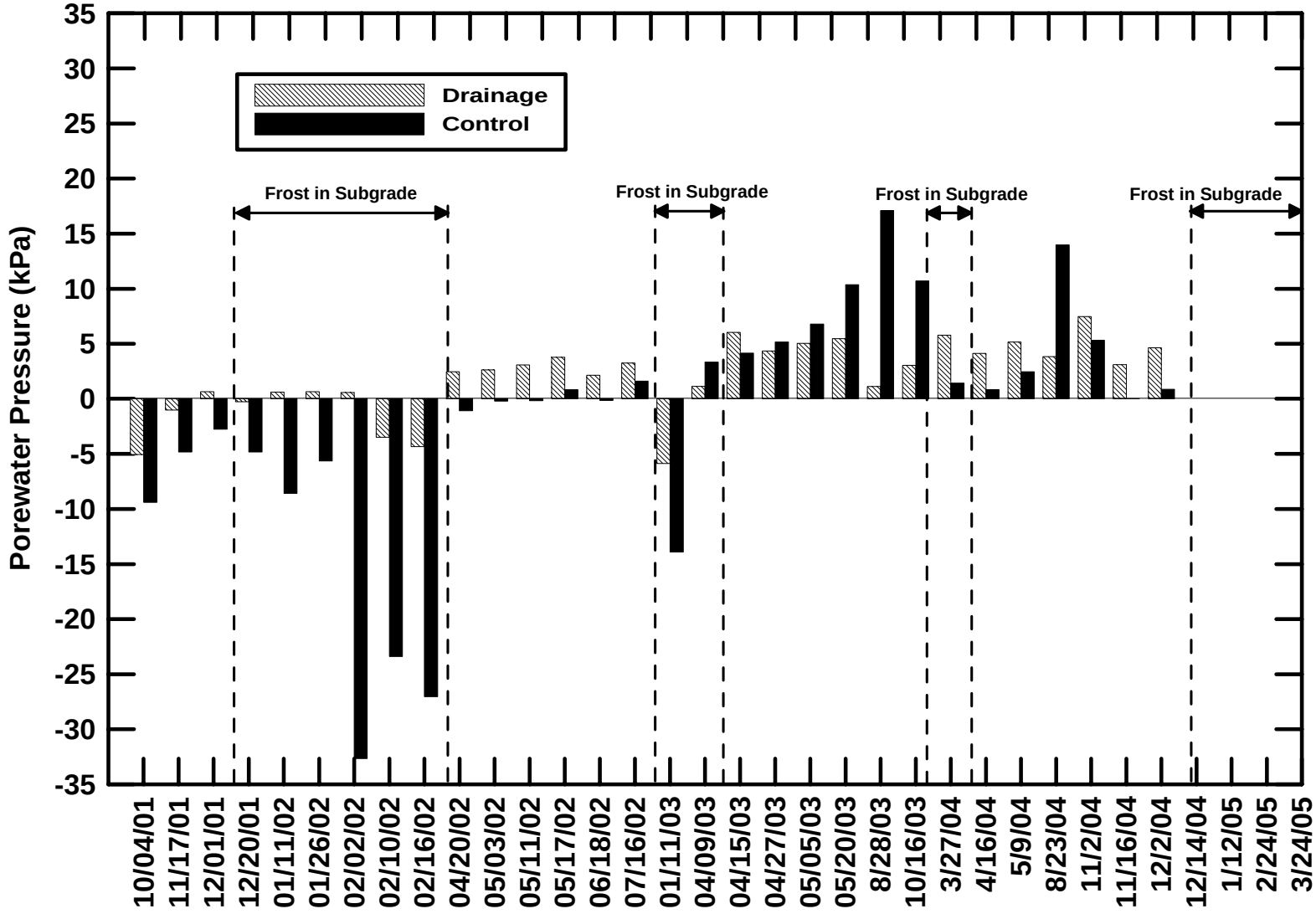

Figure 5.41 Subgrade porewater pressures in reclaim sections

5.4. Flow Meter Results

Flow meters were installed to measure the amount of water captured by the drainage geocomposite collector pipes. The length of the collector pipes varies between test sections. Approximate collector pipe lengths for each drainage test section are summarized in Table 5.31.

Table 5.31 Collector pipe lengths.

Test Sections	Collector Pipe Length (m)
4 and 5	60
9 and 10	40
11	20

Automated flow meters were used with the data acquisition systems to generate daily average flow rates, which were then normalized by dividing by the length of the collector pipes. Manual meters were installed at stations where lead wires from automated meters could not be connected to a data acquisition system. Average flow rates over the time increment between readings were calculated and then normalized to the length of the collector pipes. Flows are expressed in units of L/day/m.

5.4.1. Automated Flow Results

Collector pipes in test sections 4, 5, 9, and 10 were equipped with automated flow meters. The results are shown in Figures 5.42 through 5.47. Operation of the flow meters proved to be very problematic since iron dissolved in the water precipitated on the flow measuring impellers, preventing them from rotating. The limited available data is given below.

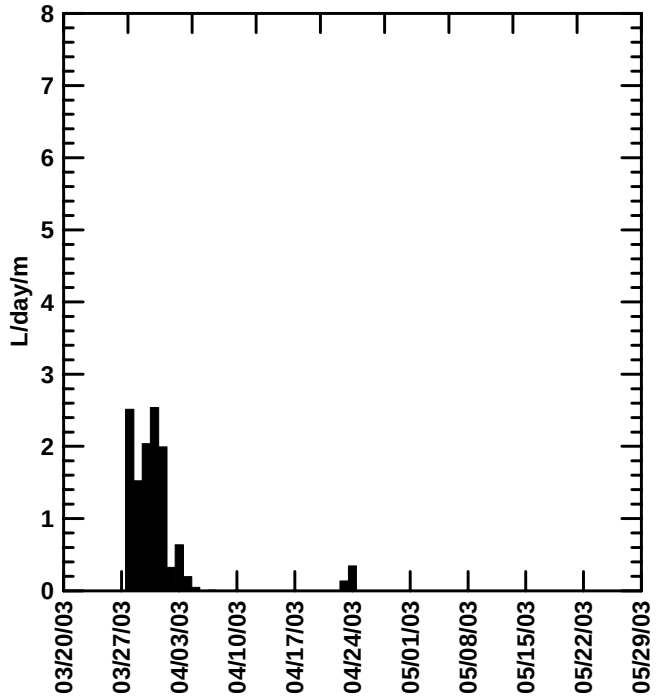

Figure 5.42 Flow from collector pipe in test section 4 station 1+760 RT.

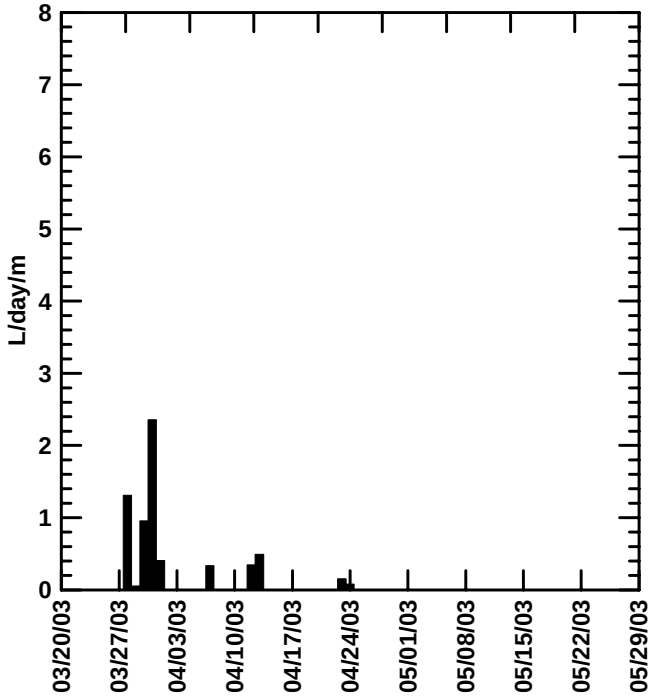

Figure 5.43 Flow from collector pipe in test section 4 station 1+760 LT.

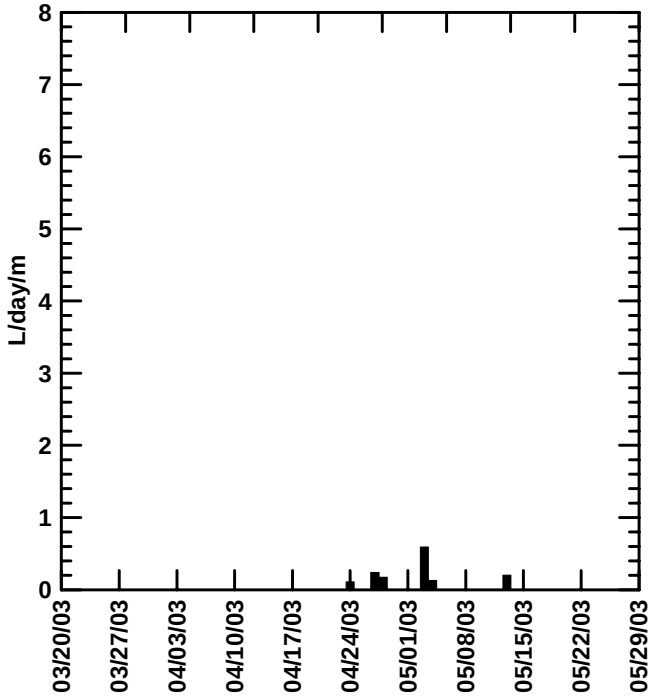

Figure 5.44 Flow from collector pipe in test section 5 station 1+820 RT.

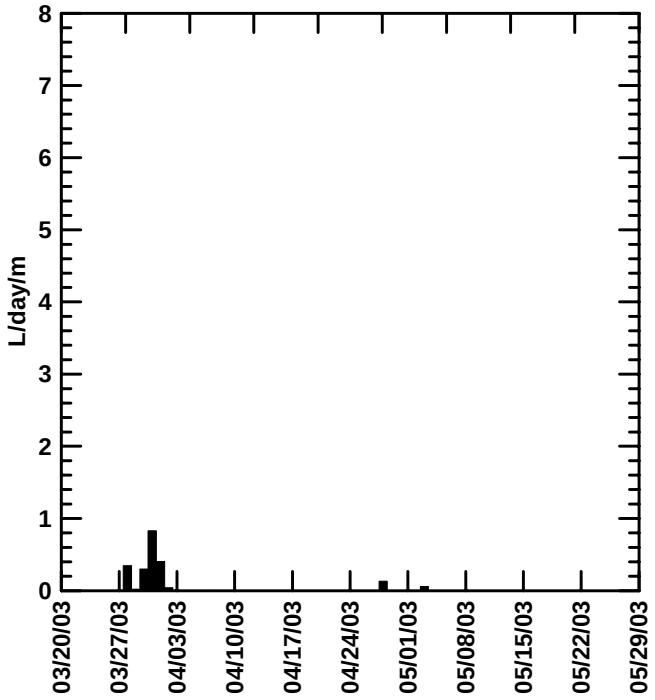

Figure 5.45 Flow from collector pipe in test section 5 station 1+820 LT

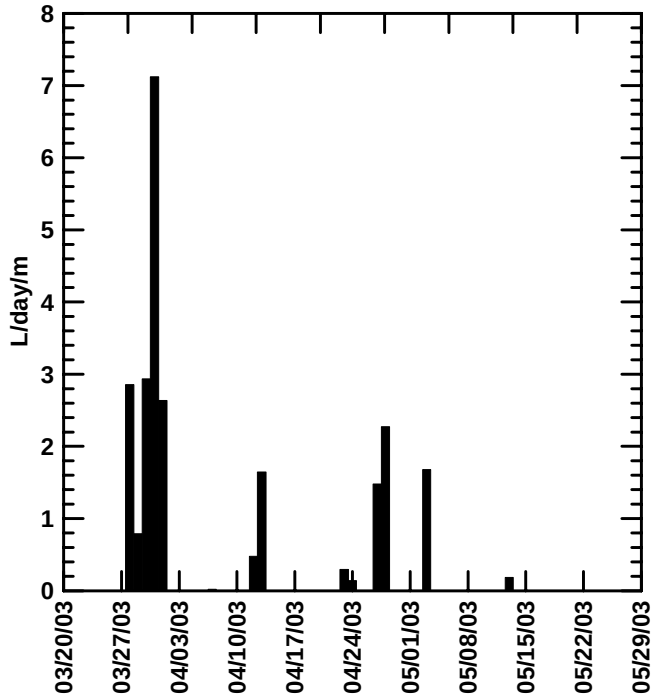

Figure 5.46 Flow from collector pipe in test section 9 station 4+100 RT.

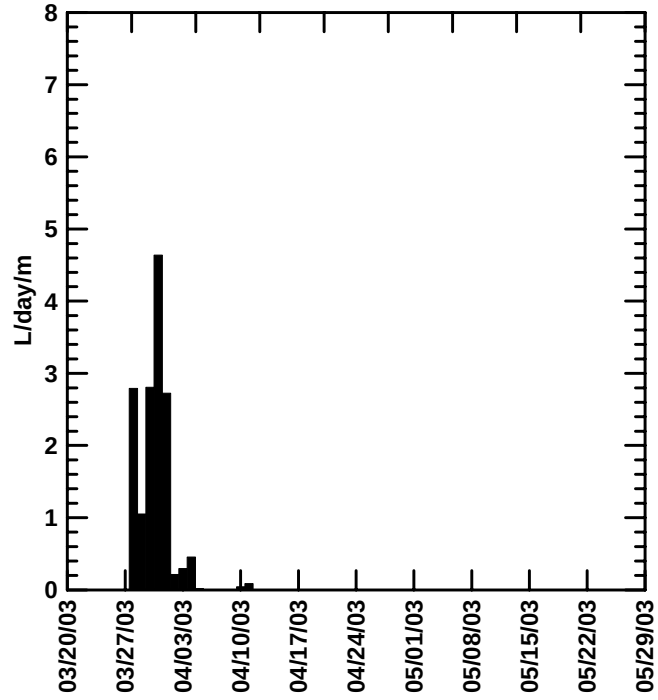

Figure 5.47 Flow from collector pipe in test section 10 station 4+140 RT.

5.4.2. Manual Flow Results

Collector pipes in test sections 9, 10, and 11 were equipped with manual flow meters. The results are summarized in Table 5.32.

Table 5.32 Manual flow meter results.

Period	Test Section 9 STA 4+100 LT Flow (L/day/m)	Test Section 10 STA 4+140 LT Flow (L/day/m)	Test Section 11 Reclaim RT Flow (L/day/m)	Test Section 11 Reclaim LT Flow (L/day/m)
3/23/03 to 3/26/03	No Flow	No Flow	No Flow	No Flow
3/26/03 to 4/9/03	No Flow	No Flow	0.297	0.033
4/9/03 to 4/15/03	No Flow	No Flow	4.320	No Flow
4/15/03 to 4/27/03	No Flow	No Flow	1.878	No Flow
4/27/03 to 5/5/03	No Flow	0.037	1.185	No Flow
5/5/03 to 5/20/03	No Flow	0.007	0.246	No Flow
5/20/03 to 7/2903	No Flow	0.041	No Flow	No Flow
7/29/03 to 8/28/03	No Flow	0.043	No Flow	No Flow
8/28/03 to 8/23/04	No Flow	No Flow	No Flow	No Flow
8/23/04 to 11/02/04	No Flow	No Flow	No Flow	No Flow
11/02/04 to 11/16/04	No Flow	No Flow	No Flow	No Flow
11/16/04 to 12/02/04	No Flow	No Flow	No Flow	No Flow
12/02/04 to 12/14/04	No Flow	No Flow	No Flow	No Flow
12/14/04 to 1/12/05	No Flow	No Flow	No Flow	No Flow
1/12/05 to 1/29/05	No Flow	No Flow	No Flow	No Flow
1/29/05 to 2/12/05	No Flow	No Flow	No Flow	No Flow
2/12/05 to 2/24/05	No Flow	No Flow	No Flow	No Flow
2/24/05 to 3/24/05	No Flow	No Flow	No Flow	No Flow
3/24/05 to 4/07/05	No Flow	No Flow	No Flow	No Flow
4/07/05 to 4/24/05	No Flow	No Flow	No Flow	No Flow
4/24/05 to 5/04/05	No Flow	No Flow	No Flow	No Flow
5/04/05 to 5/19/05	No Flow	No Flow	No Flow	No Flow

5.4.3. Discussion

As shown in Figures 5.42 through 5.47 as well as in Table 5.32, only isolated flow events were observed. With the exception of station 1+820, the computerized flow meters experienced their maximum flow at the onset of the spring thaw between 3/27/03 and 4/3/03. In test sections 4, 9, and 10 the peak flow observations coincide with

negative porewater pressure in the subbase, which suggests that the drainage geocomposite was helping to remove water from the subbase.

In general, the manual meters recorded very little flow. Possible explanations for this apparent lack of flow include loss of water at the interface of the drainage geocomposite and slotted collector pipe and loss of water from the slotted collector pipe upstream of the meter.

The maximum flow recorded by the manual flow meters occurred during the spring thaw in test section 11 between 4/9/03 and 4/15/03. This could be an indication that water was being removed from the pavement system by the drainage geocomposite, however, positive porewater pressure was measured in both the subbase and subgrade on 4/15/03.

Flow events following the spring thaw appear to correspond with rainfall events. This is shown in Figure 5.48 where flow from the collector pipe in section 9 at station 4+100 RT is plotted with daily rainfall for the period between 4/10/03 and 5/15/03 Rainfall data was obtained from a NOAA weather station in Waterville, Maine, approximately 30 miles north of the project.

A similar investigation of flow from drainage geocomposite collector pipes was performed in the Frankfort-Winterport study (Fetten and Humphrey, 1997). The magnitudes of flow normalized to the length of road being drained (length of the collector pipe) observed were similar to those observed in this study. In addition, the maximum flows observed in the Frankfort-Winterport study came during the spring thaw and subsequent discharges corresponded with rainfall events.

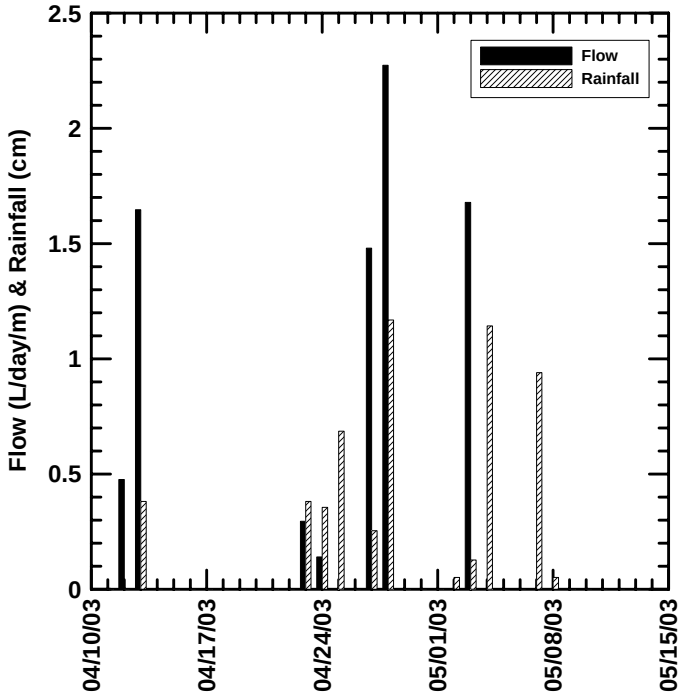

Figure 5.48 Flow and rainfall in test section 9 station 4+100 RT.

5.5. Frost Penetration Results

Test sections 6 through 12 were monitored over the course of the winters of 01-02, 02-03, 03-04, and 04-05. Test sections 1 through 5 were monitored during the winters of 02-03, 03-04, and 04-05. As explained in Chapter 4, a thermocouple string was not installed in test section 5. Thermocouples in test sections 1, 2, 3, 7, 8, and 9 were read hourly by a data acquisition system. The frost penetration results from these sections are plotted in Figures 5.49 through 5.65. Automated temperature readings in test sections 7 through 9 began in mid-February 2001. Since the entire frost penetration curve from the winter of 01-02 was not captured, only the maximum frost penetration is shown in Figures 5.58, 5.61, and 5.63. Thermocouples in test sections 4, 6, 10, 11, and 12 were read manually. The results from these sections are summarized in Table 5.33.

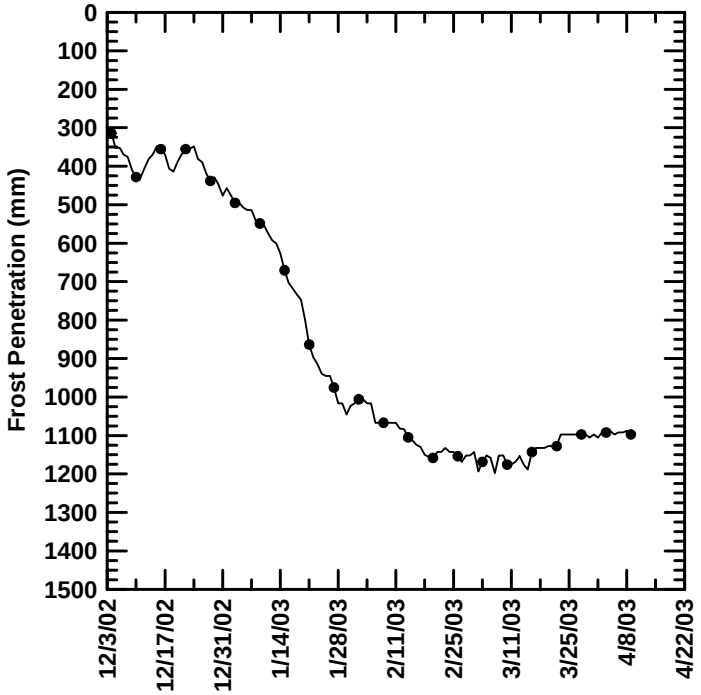

Figure 5.49 Frost penetration in test section 1 station 1+550 winter of 02-03.

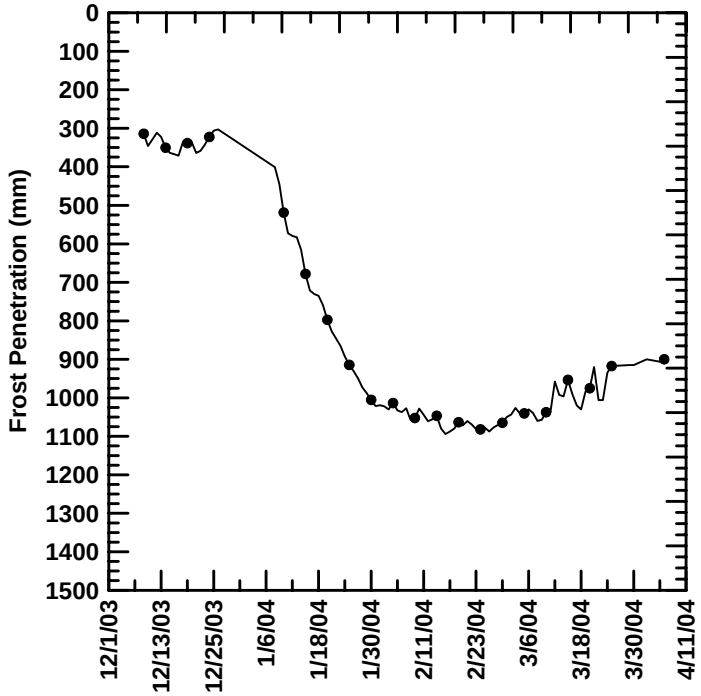

Figure 5.50 Frost penetration in test section 1 station 1+550 winter of 03-04.

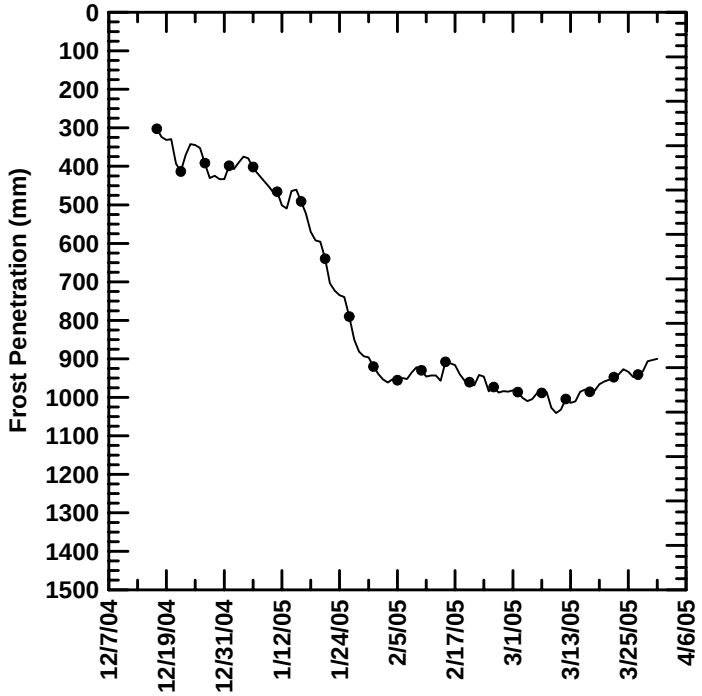

Figure 5.51 Frost penetration in test section 1 station 1+550 winter of 04-05.

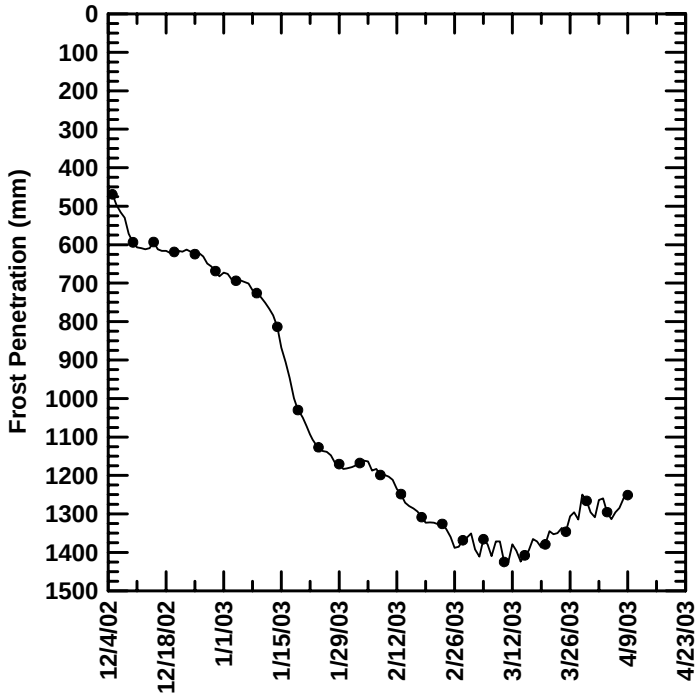

Figure 5.52 Frost penetration in test section 2 station 1+612 winter of 02-03.

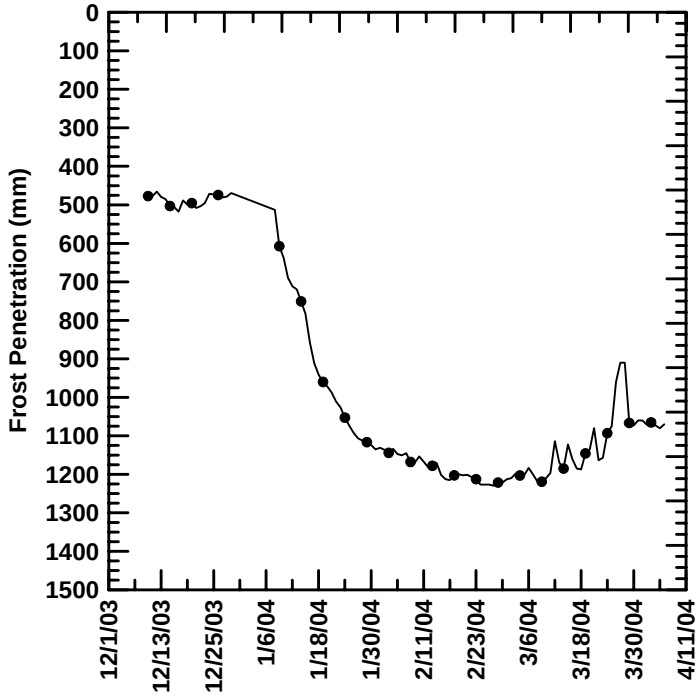

Figure 5.53 Frost penetration in test section 2 station 1+612 winter of 03-04.

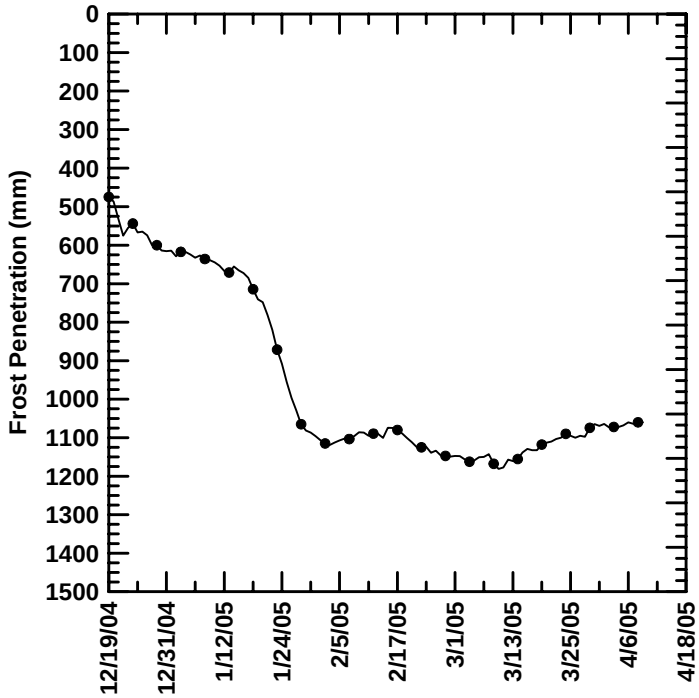

Figure 5.54 Frost penetration in test section 2 station 1+612 winter of 04-05.

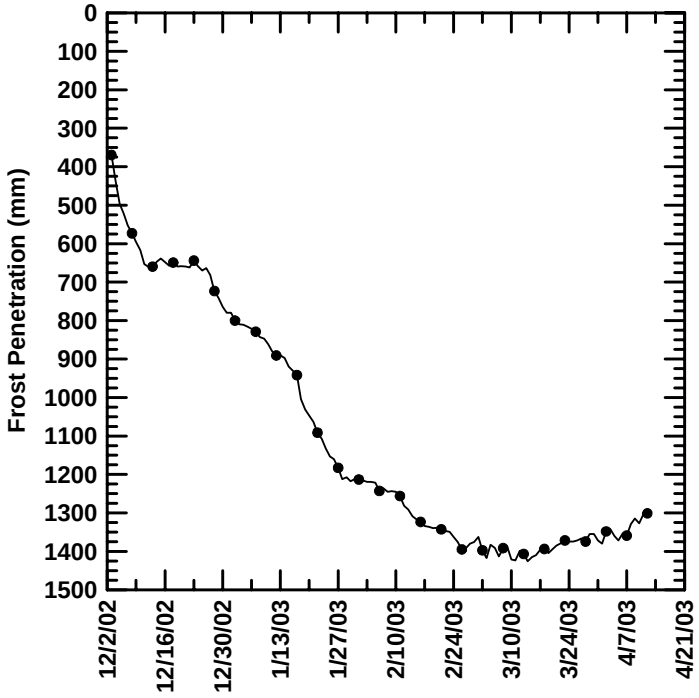

Figure 5.55 Frost penetration in test section 3 station 1+670 winter of 02-03.

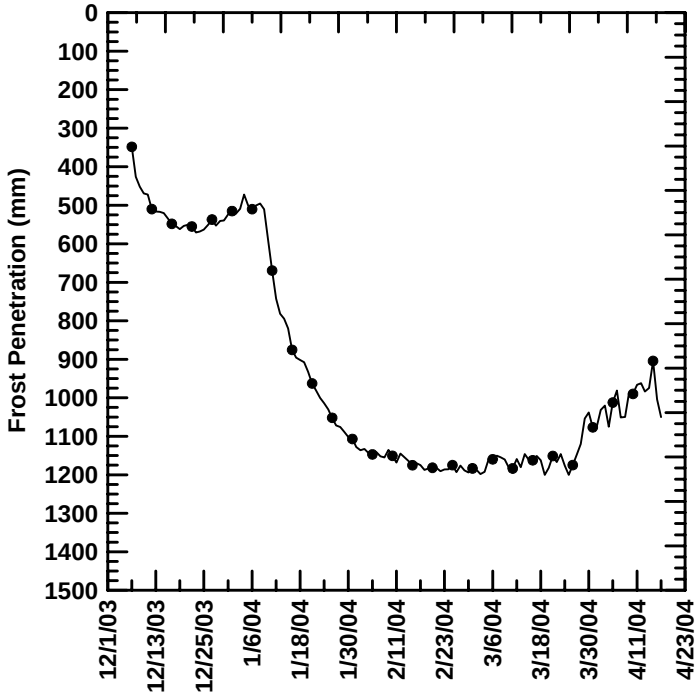

Figure 5.56 Frost penetration in test section 3 station 1+670 winter of 03-04.

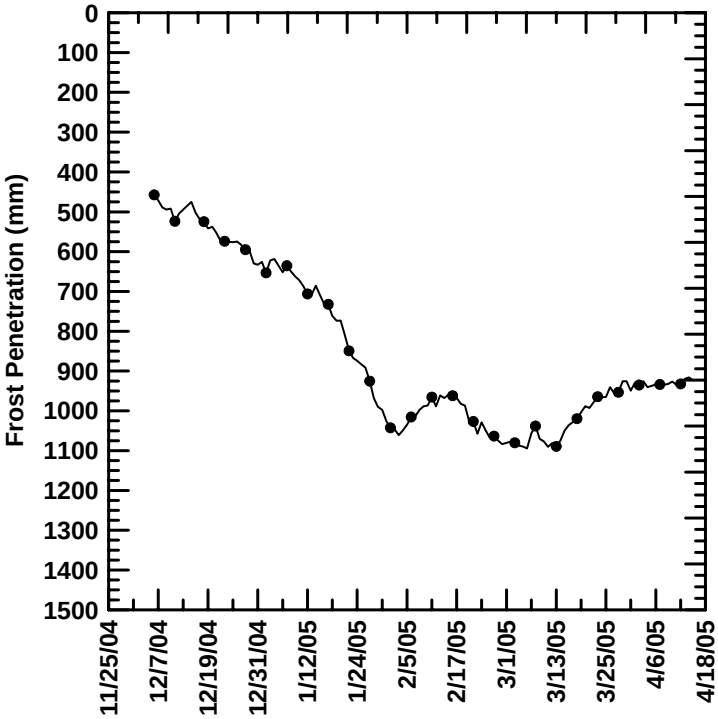

Figure 5.57 Frost penetration in test section 3 station 1+670 winter of 04-05.

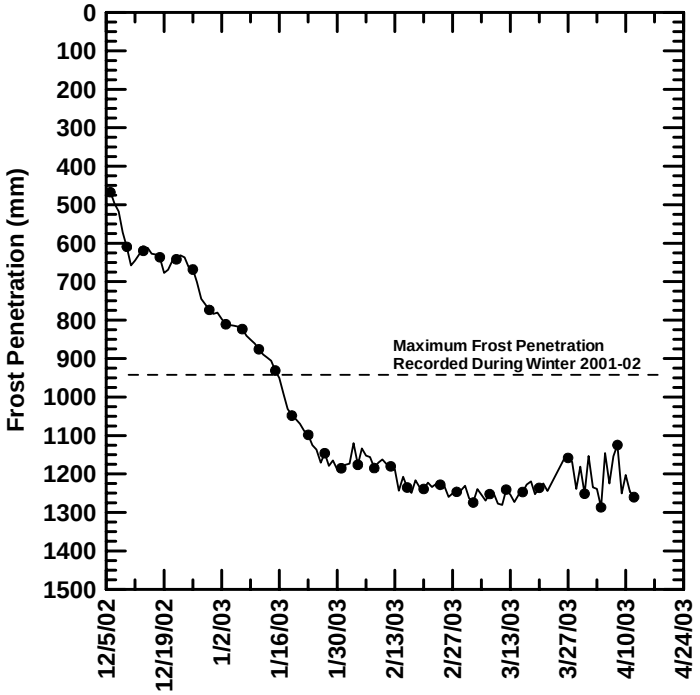

Figure 5.58 Frost penetration in test section 7 station 4+000 winter of 02-03.

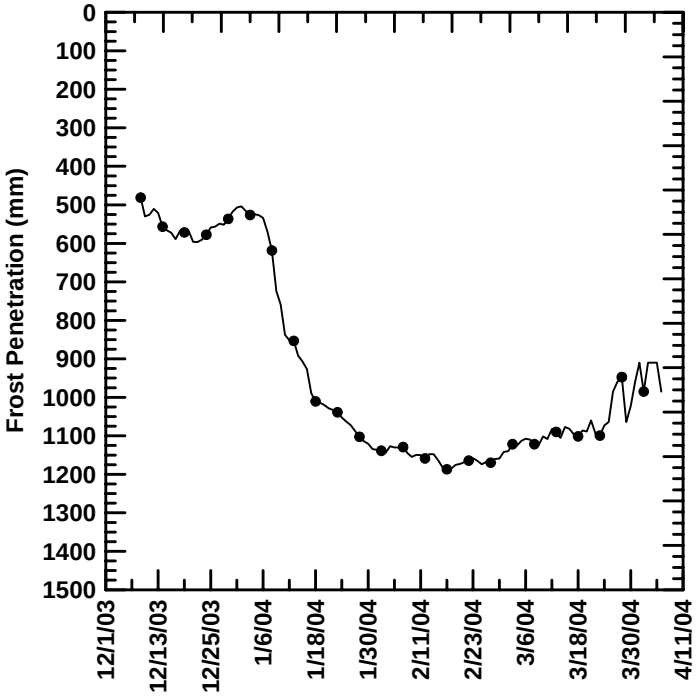

Figure 5.59 Frost penetration in test section 7 station 4+000 winter of 03-04.

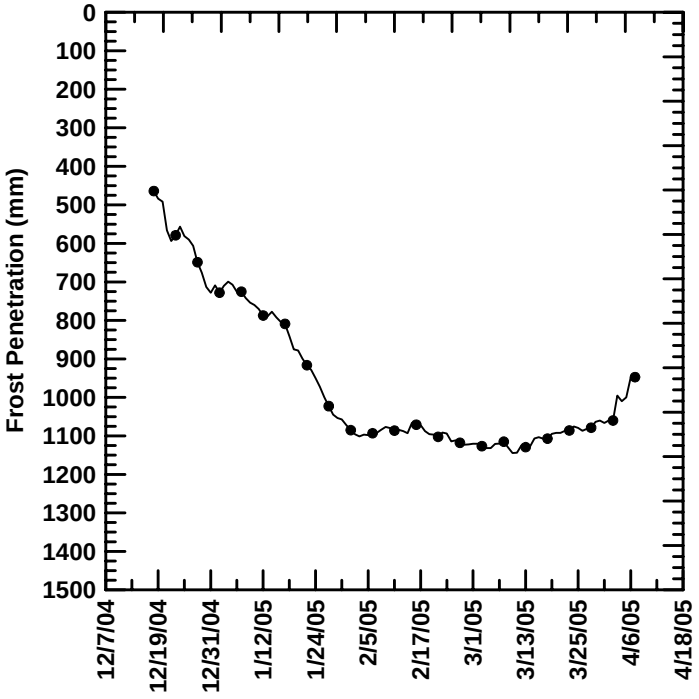

Figure 5.60 Frost penetration in test section 7 station 4+000 winter of 04-05.

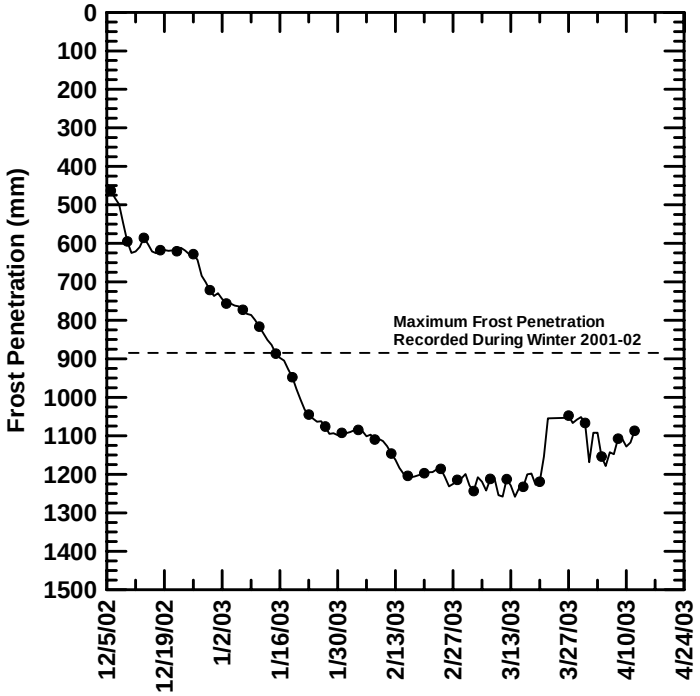

Figure 5.61 Frost penetration in test section 8 station 4+040 winter of 02-03.

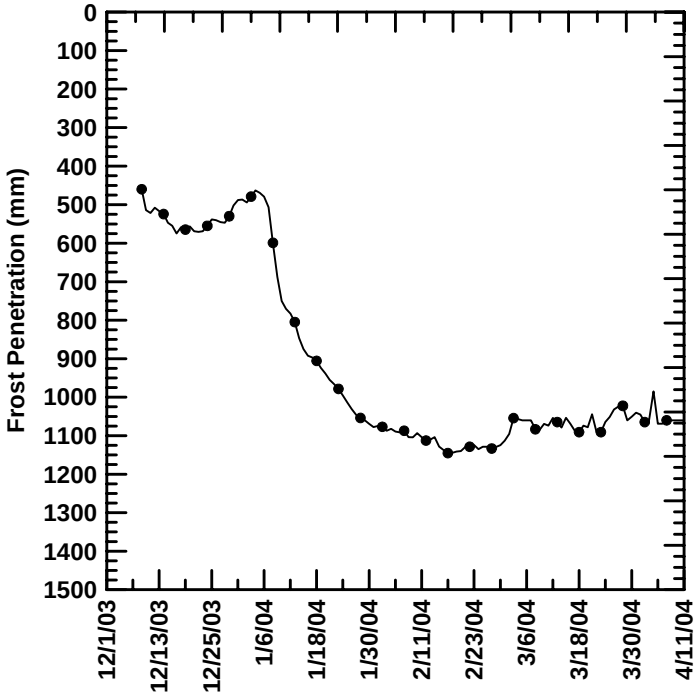

Figure 5.62 Frost penetration in test section 8 station 4+040 winter of 03-04.

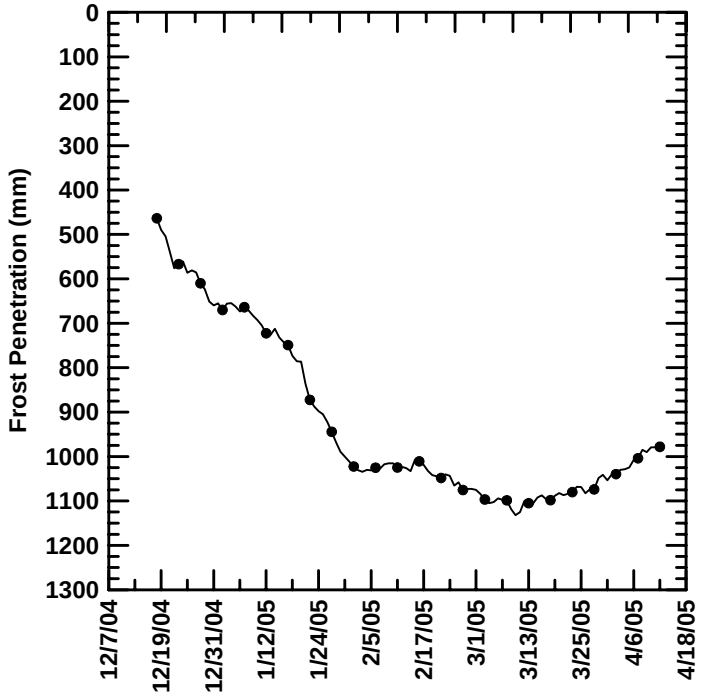

Figure 5.63 Frost penetration in test section 8 station 4+040 winter of 04-05.

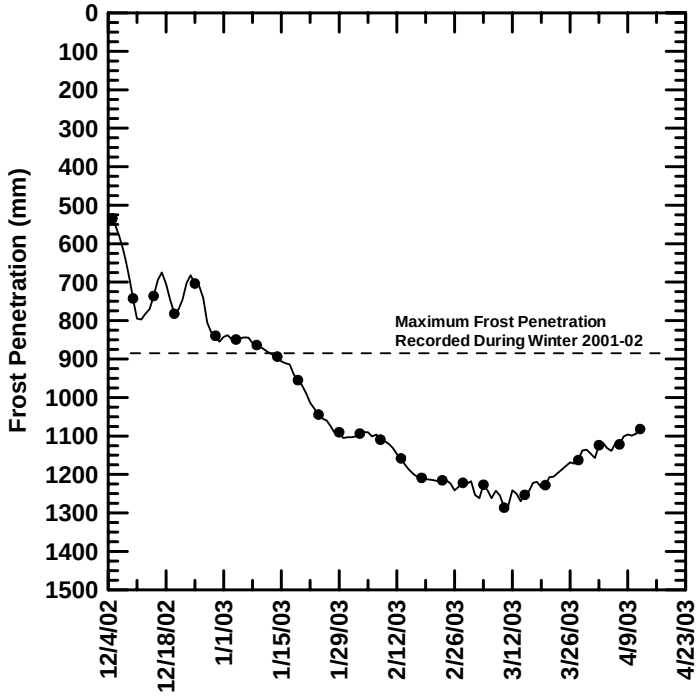

Figure 5.64 Frost penetration in test section 9 station 4+080 winter of 02-03.

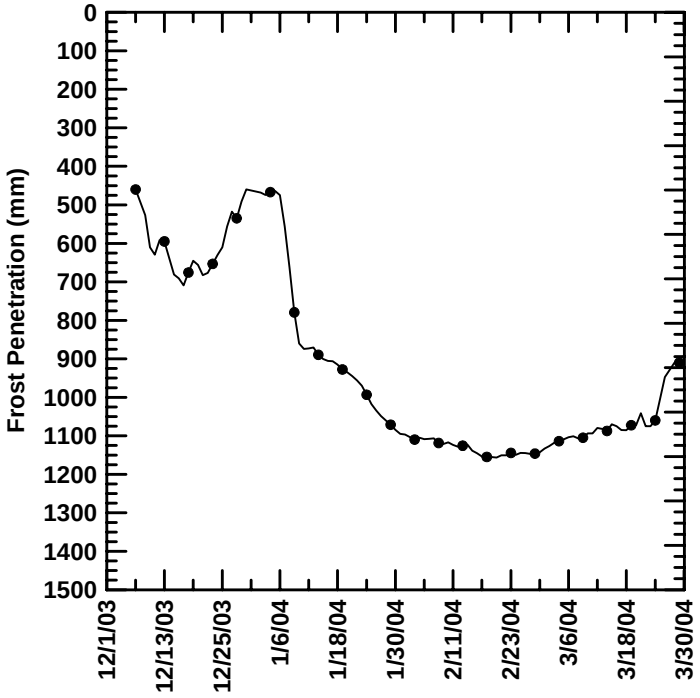

Figure 5.65 Frost penetration in test section 9 station 4+080 winter of 03-04.

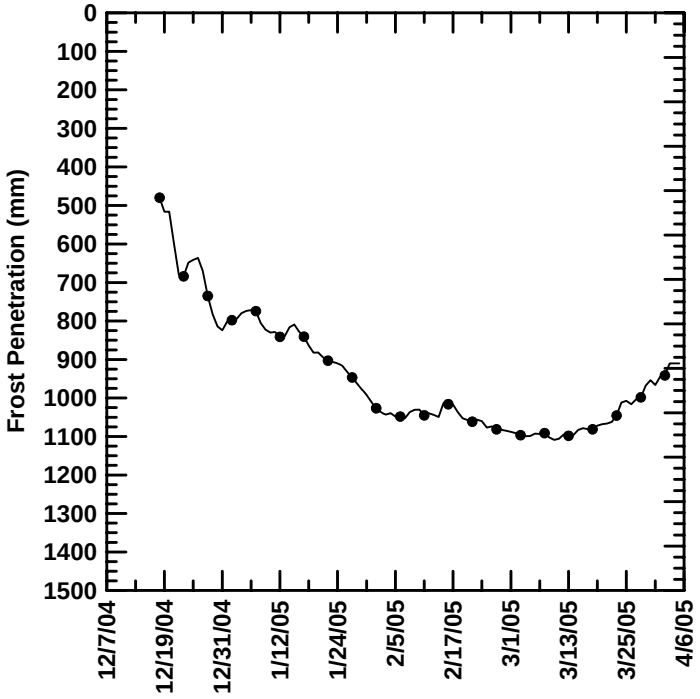

Figure 5.66 Frost penetration in test section 9 station 4+080 winter of 04-05.

Table 5.33 Frost penetration in test sections 4, 6, 10, 11, and 12.

Test Section	Date of Maximum Frost Penetration Measurement	Depth of Maximum Frost Penetration Measurement (mm)
Test Section 4	3/15/03	1371
	2/28/04	1313
	1/29/05	750
Test Section 6	2/16/02	823
	3/23/03	1341
	2/28/04	1720
	4/7/05	1225
Test Section 10	2/16/02	762
	3/15/03	1524
	2/28/04	1225
	4/7/05	1185
Test Section 11	2/16/02	609
	3/23/03	813
	2/28/04	713
	2/12/05	514
Test Section 12	2/16/02	611
	3/23/03	1067
	2/28/04	806
	2/24/05	450

The coldness of a winter is quantified using the freezing index. Daily average air temperature data obtained from a NOAA weather station in Augusta, Maine, was plotted cumulatively from fall to spring. The inflection points in the curve define the freezing season. The freezing index is the sum of cumulative freezing degree-days over the freezing season. Plots of cumulative degree-days for the freezing seasons of 2001-02 2002-03, 2003-04, and 2004-05, are shown in Figures 5.67, through 5.70.

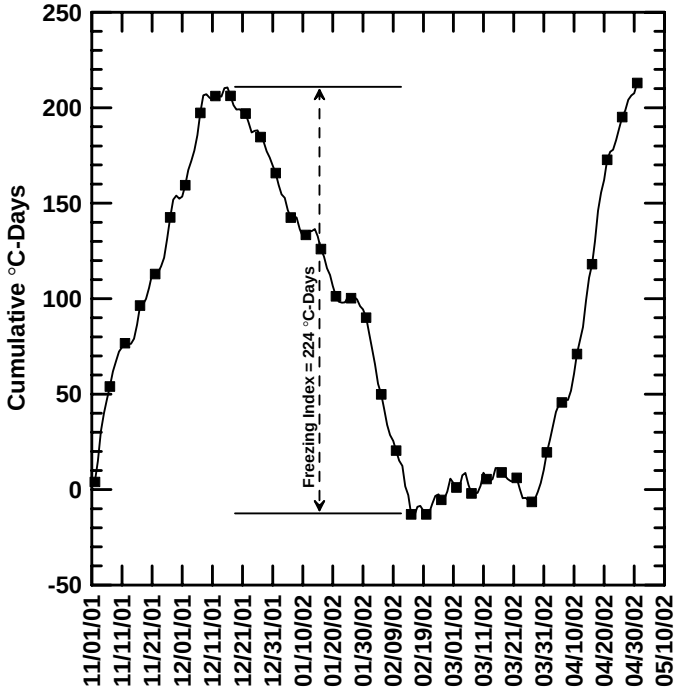

Figure 5.67 Cumulative degree-days for freezing season of 2001-02.

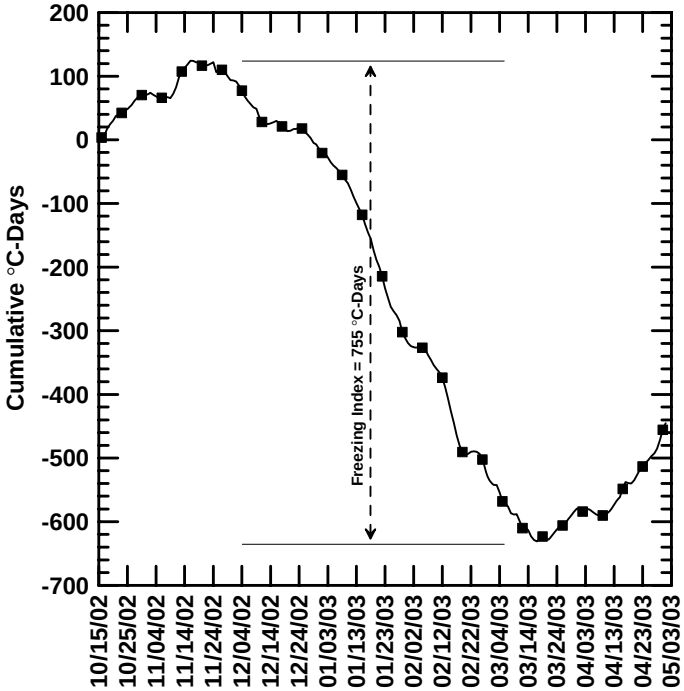

Figure 5.68 Cumulative degree-days for freezing season of 2002-03.

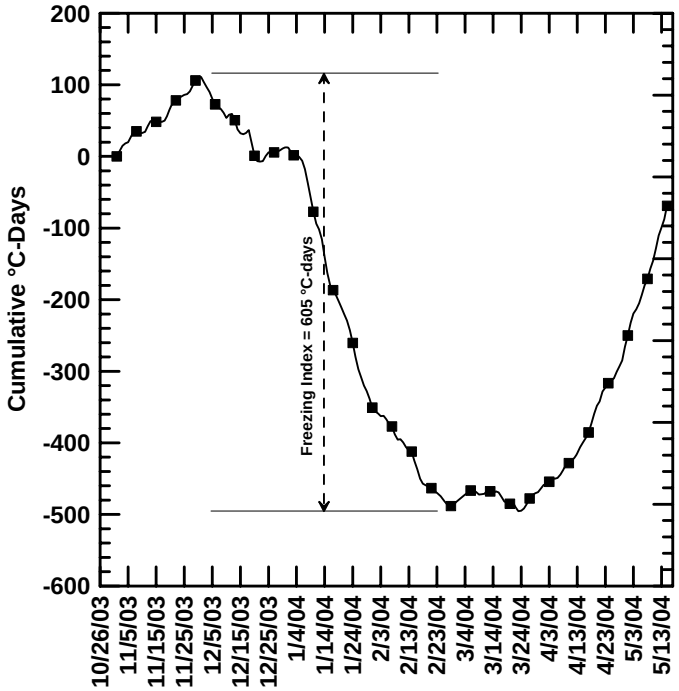

Figure 5.69 Cumulative degree-days for freezing season of 2003-04.

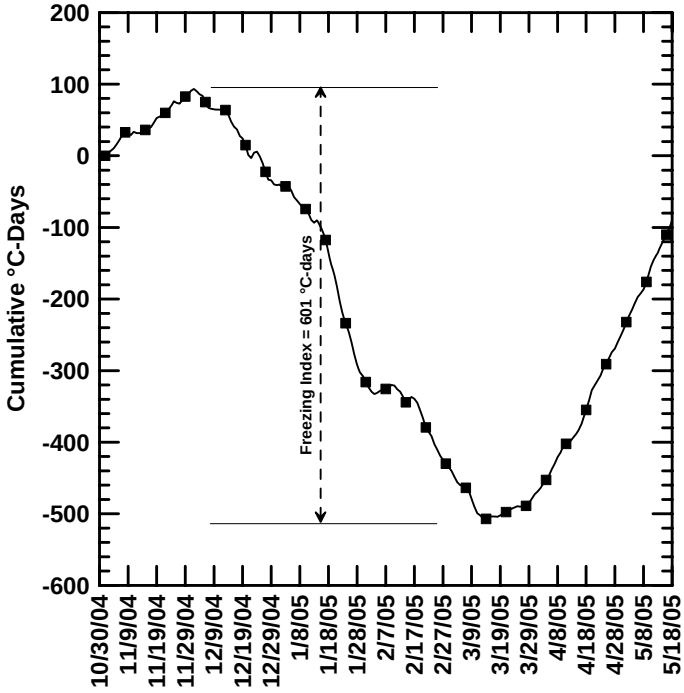

Figure 5.70 Cumulative degree-days for freezing season of 2004-05.

The mean freezing index for the project site is approximately 500 °C-days (900 °F-days) (Gilman, 1964). The winter of 2001-02 was fairly mild with a freezing index of 224 °C-days (403 °F-days), which is about half of the mean freezing index. The winters of 2002-03, 2003-4, and 2004-5 were all colder than the mean freezing index.

Minimum and maximum frost penetrations can be seen in Table 5.34. Minimum frost penetration over the monitoring period occurred during the winter of 2004-05 in test section 12, with a depth of 450 mm (18 in.). Maximum frost penetration over the monitoring period occurred during the winter of 2003-04 in test section 6, with a depth of 1720 mm (68 in.).

Table 5.34 Frost penetration in test sections 4, 6, 10, 11, and 12.

Minimum and Maximum Frost Penetration (mm) – Entire Project				
Freezing Season	Minimum Penetration		Maximum Penetration	
	Test Section	Depth (mm)	Test Section	Depth (mm)
2001-02	11	609	7	942
2002-03	1	1197	10	1524
2003-04	11	713	6	1720
2004-05	12	450	6	1225

5.6. Falling Weight Deflectometer Results

The site was evaluated using a falling weight deflectometer during the spring and early summer of 2004. The tests were performed using MaineDOT's JILS Model 20C Falling Weight Deflectometer manufactured by Foundation Mechanics, Inc. The unit has a drop weight of 340.2 kg (750 lb) and a loading plate diameter of 304.8 mm (12 in.). Deflection sensors are spaced at 0, 305, 457, 610, 914, 1219, and 1524 mm (0, 12, 18, 24, 36, 48, and 60 in.). One drop each at six different loads was performed. The loading sequence was as follows: 26.7, 40.0, 53.4, 71.2, 53.4, 40.0, and 26.7 kN (6, 9, 12, 16, 12,

9, and 6 kips). AASHTOWare DARWin V. 3.1.002 software was used by the MaineDOT to backcalculate the effective structural number for each drop location. Four locations in each section were tested on each of eight days with the first day being March 10, 2004 and the last day being June 29, 2004. For the first three test dates the subgrade was fully or partially frozen, which influenced the calculated effective structural number. The effective structural number for each drop location, on each date are given in Appendix B. The average and standard deviation of the four drops in each location are also given in Appendix B.

The average effective structural numbers for sections with 300 mm (12 in.) of subbase are plotted versus date in Figure 5.71. During the period when the subgrade was

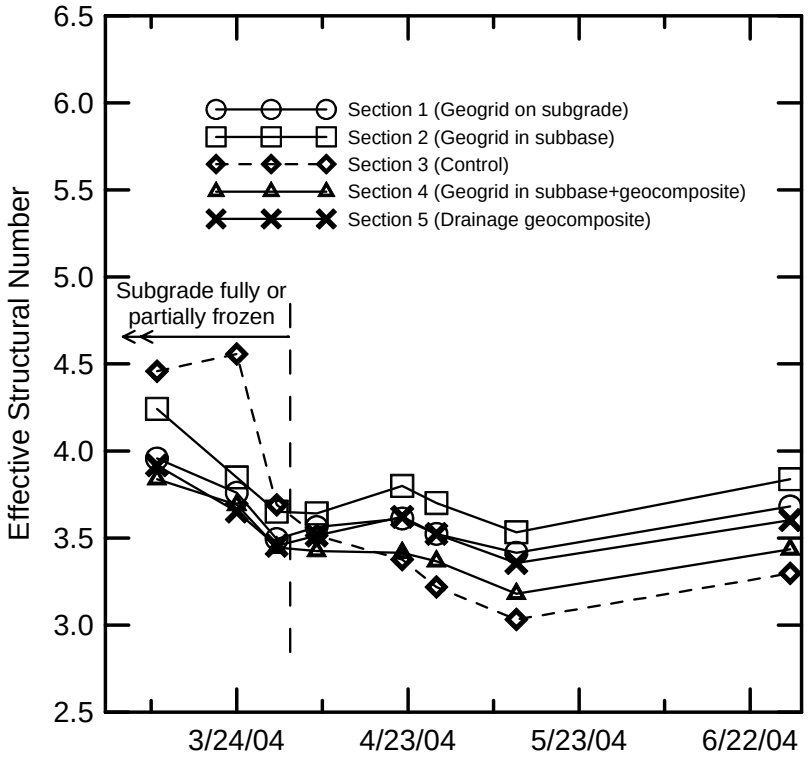

Figure 5.71 Effective structural number for sections with 300 mm (12 in.) subbase aggregate.

thawed, the sections with geogrid and drainage geocomposite had a higher effective structural number compared to the corresponding control section. Section 2 with geogrid in the subbase gave the highest structural number, whereas Section 4 with both geogrid in the subbase and drainage geocomposite gave a structural number that was only slightly higher than the control section. For data from May 12, 2004, a z-test with a confidence level of 95% showed that the structural number for sections 1, 2, and 5 were greater than the control section, but that section 4 and the control section were statistically equal. On this date, the difference between the effective structural number for section 2 and the control section was 0.5 or an increase of 17%. In section 4 the difference was 0.2 or an increase of 5%.

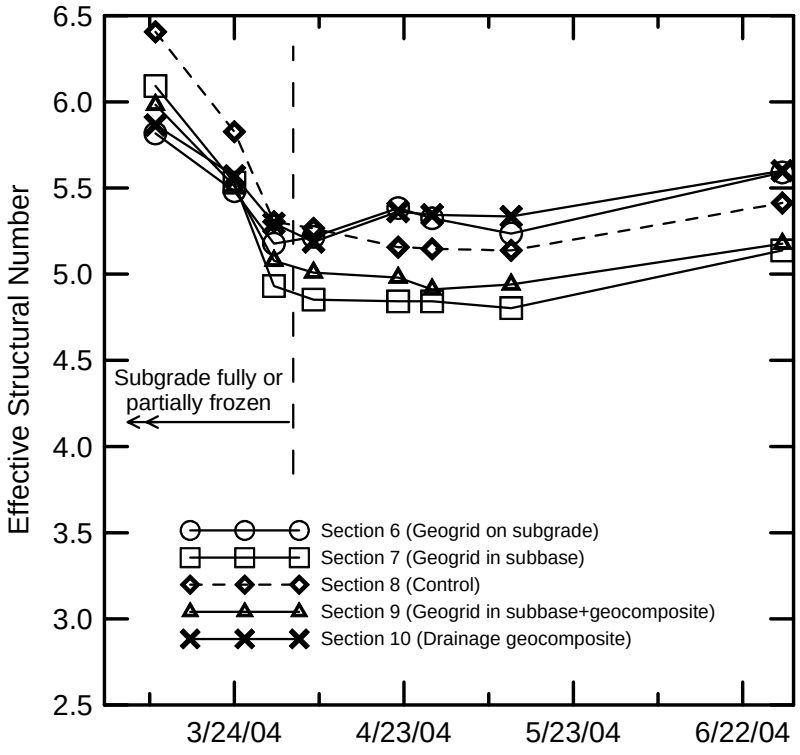

Figure 5.72 Effective structural number for sections with 600 mm (24 in.) subbase aggregate.

The average effective structural numbers for sections with 600 mm (24 in.) of subbase are plotted versus date in Figure 5.72. During the period when the subgrade was thawed, the effective structural number for the control section was midway between the values for the sections with geogrid and drainage geocomposite. This suggests that reinforcement geogrid and drainage geocomposite had little effect on structural number. For the data from May 12, 2004, a z-test with a confidence level of 95% confirmed that the effective structural numbers for sections 6, 7, and 9 were statistically equal to the value in the control section. However, the structural number in section 10 was statistically greater than the control section.

Comparing the sections for 300 mm (12 in.) and 600 (24 in.) of base show that the thicker base had a significantly higher structural number. On May 12, 2004, the difference in structural number for the two control sections was 2.1 which is equivalent to an increase of 70%. This suggests an increase in effective structural number of 0.18 for each 25 mm (1 in.) of subbase aggregate that is added. Thus, the increase in effective structural number that was produced by geogrid and/or drainage geocomposite in the 300-mm (12-in.) subbase sections could also be obtained by adding between 25 mm (1 in.) and 75 mm (3 in.) of subbase aggregate.

The average effective structural numbers for the reclaim sections are plotted versus date in Figure 5.73. During the period when the subgrade was thawed, the effective structural number for the control section was higher than that of the control section. For the data from May 12, 2004, a z-test with a confidence level of 95% showed that the structural number in the control was statically greater than in the section with

drainage geocomposite. This suggests that drainage geocomposite had little effect on structural number in this application.

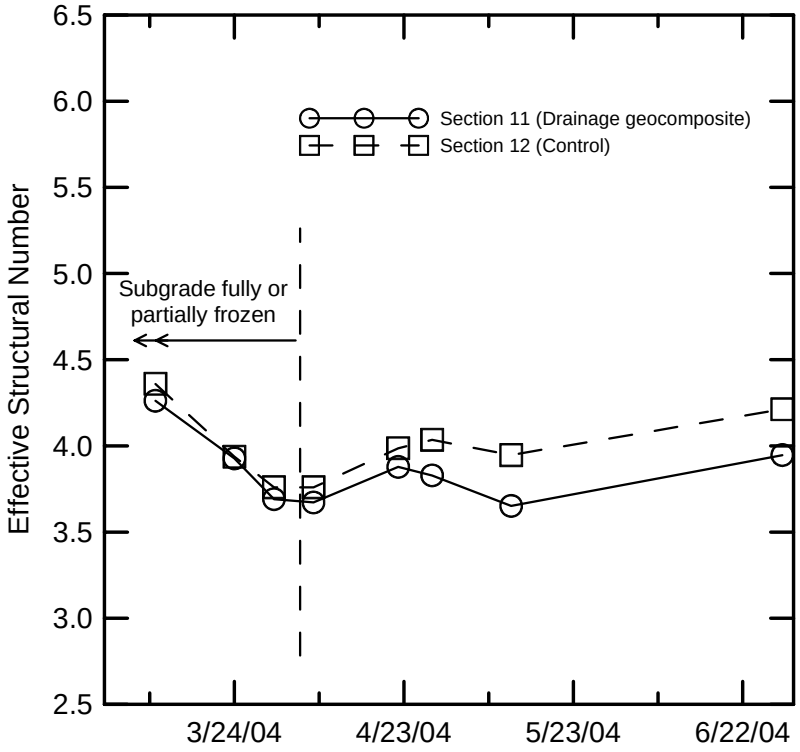

Figure 5.73 Effective structural number for reclaim sections.

5.7. Summary

Strain gages were used to determine the tensile force in the geogrid. The strain gages were installed in pairs with one gage on top and one on bottom of an instrumented rib. The data from each pair was averaged to remove the effects of bending. The survival rate of the strain gage pairs was 93% at the end of construction, but this had decreased to 35% by May 2005. Failure was defined as malfunction of one strain gage in a pair. After the initial construction period, examination of data from each gage in a pair showed that there was negligible bending. This allowed the data from a single functioning gage to be used to determine subsequent changes in force in the geogrid.

Examining the average geogrid force perpendicular to centerline for each subbase thickness and each geogrid position showed that 18 to 83% of the force measured at the end of the monitoring period was developed was developed by placement and compaction of the overlying aggregate. By the time the pavement was placed the force had increased to 56 to 139% of the final value. These results show that placement and compaction of the overlying aggregate, and subsequent loading by traffic prior to paving are both important in developing the force in the geogrid. In the sections with 300 mm (12-in.) subbase course, the geogrid forces tended to increase with time. However, this tend was less evident in sections with 600 mm (24 in.) subbase course and in some cases the force actually decreased with time.

The geogrid forces in ribs oriented perpendicular to centerline were analyzed statistically to evaluate the effects of elapsed time, subbase thickness, and geogrid location in the pavement system on the force in the geogrid.

The force in the geogrid located on subgrade and in the middle of the subbase was statistically equal for 300-mm (12 in.) subbase sections immediately after subbase compaction and after paving. However, for 12, 24, and 35 months after paving, geogrid located on the subgrade produced a statistically higher force than when located in the subbase. In the 600-mm subbase sections, the opposite trends occurred. Up to 12 months after paving geogrid located on subgrade produced a statistically higher force, but for 24 months to the end of the project monitoring period the forces were statistically equal. Taken in total, these results suggest that geogrid located on subgrade develops a force that is equal to or greater than when the geogrid is located within the subbase for both subbase thicknesses in this study.

The force in the geogrid immediately after paving in 300-mm (12 in.) subbase sections was statistically equal to that in the 600-mm (24 in.) subbase sections for both geogrid on subgrade and in the subbase. However, after 12, 24, and 35 months, the force in the geogrid in the 300-mm (12 in.) subbase sections was statistically greater that in the 600-mm (24 in.) subbase sections for geogrid on subgrade. The same was true for geogrid located in the subbase for 12 and 24 months after paving. This suggests that pavements with thinner pavement sections develop greater forces over time than thicker pavement sections.

The analysis indicated that the average force in the geogrid on subgrade and in the subbase in the 300-mm (12 in.) subbase sections increased between subbase compaction and paving, paving to 12 months, and 12 to 24 months after installation. However, the forces in the subgrade geogrid sections decreased or remained the same from 24 to 35 months, unlike the subbase geogrid sections which continued to increase. This suggests that reinforcement mechanisms continue to develop after paving in the sections with of 300 mm (12 in.) subbase. The geogrid on subgrade and in the subbase in the 600-mm (24 in.) subbase sections exhibited increases in force between subbase compaction and paving. However, these forces either decreased, or failed to exhibit appreciable increases from paving to 45 months. This could be an argument that reinforcement mechanisms did not continue to develop after paving in sections with 600-mm (24-in.) subbase sections.

The force in the geogrid parallel to centerline was also measured. Immediately after paving these forces were similar to that perpendicular to centerline for both the 300-mm (12-in.) and 600-mm (24-in.) subbase sections. At the end of the monitoring period

(May, 2005) they were also similar for the 600-mm (24-in.) subbase sections. However, for the 300-mm (12-in.) subbase sections the forces perpendicular to centerline in May 2005 were higher than parallel to centerline.

Laboratory tests showed that the geogrid may experience creep, as reflected by increases in strain, when subjected to a constant load similar to those measured in the field. Considering that in this study the force per unit width in the geogrid was obtained from the change in strain in the instrumented ribs, strain due to creep would be interpreted as an increase in force per unit width. Strain rates measured in the lab and long-term strain rates measured in the field were similar. Thus, the increases in force per unit width with time reported in this study could be due to creep rather than an actual increase in force carried by the geogrid.

Vibrating wire piezometers were used to measure porewater pressure in the subbase course and subgrade soils. Previous work showed that these types of piezometers indicate negative porewater pressures when the degree of saturation drops below about 50%. Low saturation indicates that the section is well drained.

Results from subbase piezometers showed that the sections with drainage geocomposite exhibited large periods of negative porewater pressure unlike the control sections, which exhibited mostly positive porewater pressures. This suggests that the drainage geocomposite assists with the removal of water from the subbase.

The subgrade piezometers also exhibit negative porewater pressures indicating significant periods of partial saturation. However, for the subgrade piezometers, there is no clear difference in behavior between sections with and without drainage

geocomposite. This suggests that the drainage geocomposite had little effect on subgrade porewater pressures.

The subbase and subgrade piezometers in the reclaimed control section had less porewater pressure than those in the drainage section. This suggests that the drainage geocomposite's ability to remove water from the subbase and subgrade may be inhibited in sections utilizing reclaim construction techniques.

The flowmeters used to measure the quantity of water discharging from the geocomposite collector pipes proved to be unreliable and were easilty clogged by iron that precipitated from the water. Thus, reliable data was obtained only for the spring of 2003. The majority of the collector pipes experienced their maximum flow at the onset of the spring thaw between 3/27/03 and 4/3/03. Flow events following the spring thaw appear to correspond with rainfall events. In test sections 4, 9, and 10 the peak flow observations coincide with negative porewater pressure in the subbase. This could be an indication that water was being removed from the pavement system by the drainage geocomposite.

Thermocouples were used to monitoring the depth of frost penetration. Minimum frost penetration over the monitoring period occurred during the winter of 2004-05 in test section 12, with a depth of 450 mm (18 in.). Maximum frost penetration over the monitoring period occurred during the winter of 2003-04 in test section 6, with a depth of 1720 mm (68 in.). The data obtained from the other instrumentation was evaluated in the context of the extent of frost penetration.

The results from falling weight deflectometer tests performed in spring and early summer of 2004 show that reinforcement geogrid and drainage geocomposite increase

the effective structural number by between 5% and 17% for sections with 300 mm (12 in.) of subbase aggregate. However, they had no apparent effect for sections with 600 mm (24 in.) of subbase aggregate or the reclaim sections. Comparing control sections with 300 mm (12 in.) and 600 mm (24 in.) of subbase aggregate showed that doubling the subbase thickness increased the effective structural number by 70%. The results suggest that the increase in effective structural number that was produced by geogrid and/or geocomposte in the 300-mm (12-in.) subbase sections could also be obtained by adding between 25 mm (1 in.) and 75 mm (3 in.) of subbase aggregate to an unreinforced section.

CHAPTER 6
SUMMARY, CONCLUSIONS, AND RECOMMENDATIONS

6.1. Summary

The New England Transportation Consortium sponsored a study to investigate the use of geosynthetics for reinforcement and drainage in two portions of Route 9 in the towns of Monmouth, Litchfield, and West Gardiner, Maine. Previous research on geosynthetic reinforcement in flexible pavement systems examined subbases 50 to 365 mm (2 to 14 in.) thick. An earlier study by the Maine Department of Transportation (Fetten and Humphrey, 1998) was the first known to investigate geosynthetic reinforcement with subbases as thick as 640 mm (25 in.). The use of drainage geocomposites was also investigated (Fetten and Humphrey, 1998). The present study continues to examine the use of thick subbases in reinforced flexible pavement systems with layers as thick as 600 mm (24 in.). The effectiveness of drainage geocomposites was also examined.

The objective of this study is to evaluate the reinforcement and drainage capabilities of geosynthetics in roadways in cold regions constructed on soft subgrade soils with the thick subbases typical of New England roads. The following tasks were completed during the evaluation:

1. A literature review of laboratory tests, field trials, computer analyses, and design methods for geosynthetic reinforcement in both unsurfaced and paved roads was conducted.

2. Over the course of two construction seasons, portions of Route 9 in the towns of Monmouth, Litchfield, and West Gardiner, Maine, were instrumented with strain gages, piezometers, flow meters, and thermocouples to evaluate the performance of the geosynthetics.

3. The instruments were monitored from September, 2001 until June, 2005. Force in the geogrid, porewater pressures in the drainage sections, flow from the drainage sections, and frost penetration were examined.

4. The performance of the test sections was evaluated by comparing results from sections constructed with geosynthetics with those from previous studies as well as control sections from this study.

6.1.1. Literature Review

The literature review included laboratory and field studies of geosynthetic applications in both unsurfaced and paved roads, design methods for geosynthetic reinforcement, and computer analysis of performance.

Geosynthetics have been in use since the mid-1970's. Early research focused on applications in temporary haul roads and unpaved roads. Their beneficial reinforcing effects in unsurfaced roads have since been documented. As wheel ruts develop the resulting movement of subbase particles allows for shear interaction with the geosynthetic. The tensile loads developed at the bottom of the subbase are transmitted to the geosynthetic, effectively providing the subbase with tensile strength (Bender and

Barenberg, 1978). Some authors believe that geogrid is superior to geotextile for lateral subbase restraint due to the interlock between the geogrid and subbase aggregate (Haas, et al., 1985; Barksdale, et al., 1989). Development of wheel ruts also deforms the subgrade and geosynthetic. The tensile forces in the deformed geosynthetic provide an upward resultant force just outside the wheel path that reduces the vertical stress applied to the subgrade. In addition, the tensile forces in the geosynthetic also provide a downward resultant force that helps to confine the subgrade on either side of the wheel path and increase its bearing capacity (Bender and Barenberg, 1978). The subgrade confinement and tensioned membrane subgrade improvement mechanisms originally investigated by Bender and Barenberg (1978) have also been shown to increase performance in unpaved roads where wheel ruts readily occur by Lai and Robnett (1982), and Leng and Gabr (2002). However, the effects of these mechanisms may be limited in roads paved with flexible pavements which cannot tolerate large permanent deflections.

Several full-scale laboratory experiments have been performed to investigate the reinforcement mechanisms of geosynthetics beneath flexible pavements. Studies by Kennepohl, et al. (1985), Penner, et al. (1985), Haas, et al. (1988), Barksdale, et al. (1989), Al-Qadi, et al. (1994), Cancelli, et al. (1996), Perkins, et al. (1996), and Montanelli, et al. (1997), showed some benefits of geosynthetic reinforcement beneath flexible pavements. However, the reinforcing benefit of geosynthetics in cold regions with subbase and pavement layers as thick as those used in New England was only previously investigated by Fetten and Humphrey (1997).

A computer analysis by Barksdale, et al. (1989) showed that roadway sections with pavement layers greater than 65 to 90 mm (2.5 to 3.5 in.) thick were not expected to

show improvement from geosynthetic reinforcement, even when constructed on weak subgrades. It was also shown that the beneficial effects of geosynthetic reinforcement in terms of stress, strain, and deflection were relatively small for reinforced sections designed to carry more than about 200,000 equivalent 80-kN (18-kip) single axle loads. The reconstructed section of Route 9 was designed to carry 500,000 equivalent 80-kN (18-kip) single axle loads.

There are a limited number of design procedures available for reinforcement beneath flexible pavements. Penner, et al. (1985) developed a method that used a layer coefficient ratio or equivalence factor applied to the reinforced layer to reflect the structural improvement to the subbase. Comparisons of this ratio to the behavior of test sections indicated that subbase thickness and performance improvement were inversely proportional. Although no test sections were constructed with a subbase thickness greater than 300 mm (12 in.), no improvement was expected for thicker subbase sections (Penner, et al., 1985).

The excess subgrade porewater pressure generated under cyclic traffic loads results in a pressure gradient between the subbase and subgrade. Geosynthetics intercept water flowing to the subbase and redirect it to pavement edge drains where it can be properly discharged, effectively increasing the rate of excess porewater pressure dissipation. Alobaidi and Hoare (1994, 1996) showed that geotextiles with high permeability provided greater rates of dissipation. Zhao and Banks (1997) concluded that a high compressive strength, high flow rate drainage geocomposite on subgrade can provide a means of escape for water in the pavement system. When placed below subgrade the geocomposite can act as capillary barrier, which helps mitigate frost

heaving (Henry, 1996). The performance of drainage geocomposite was previously investigated by MaineDOT in the towns of Frankfort and Winterport (Hayden, et al., 1999). It was concluded that the drainage geocomposite below subgrade could improve the structural characteristics of the road. In addition, the drainage geocomposite helped remove water from the pavement system and was most beneficial in cut sections when located as far below the pavement as possible (Hayden, et al., 1999).

6.1.2. Construction and Instrumentation of Test Sections

Route 9 in the towns of Monmouth, Litchfield, and West Gardiner, Maine, is underlain by very poor subgrade soils. These soils are classified as AASHTO A-2-4, A-4, and A-6 and are highly frost susceptible. Several of the subgrade soil samples taken for this study had standard penetration field blow counts as low as 7 and natural water contents approaching the liquid limit. Historically, Route 9 has been plagued with local bearing capacity failures resulting in substantial pavement cracking. The low shear strengths of the subgrade soils combined with the inadequacy of the existing drainage made this a suitable site for testing geosynthetics for reinforcement and drainage applications.

Two portions of Route 9 were used to study the performance of Tensar BX1200 geogrid and Tenax Tendrain 100-2 drainage geocomposite. A total of twelve test sections were constructed. Test sections 1 through 5 were constructed with a 300 mm (12 in.) subbase whereas test sections 6 through 10 were constructed with a 600 mm (24 in.) subbase. This allowed the effects of reducing subbase thickness to be evaluated. Test sections 11 and 12 were reclaimed and used 75 to 150 mm (3 to 6 in.) of pavement

grindings as the subbase. All of the test sections were surfaced with approximately 150 mm (6 in.) of bituminous pavement.

Four types of test sections were constructed: reinforcement, drainage, drainage with reinforcement, and control. Test sections using reinforcement geogrid have strain gages attached to the geogrid to measure induced forces. Some of the reinforcement sections have geogrid on subgrade whereas some have geogrid in the center of the subbase to evaluate the effects of geogrid location within the pavement structure. Drainage sections were constructed with drainage geocomposite on subgrade and have vibrating wire piezometers to monitor porewater pressure in the subgrade and subbase course. The drainage sections use a 100-mm (4-in.) diameter underdrain pipe to collect water from the drainage geocomposite. The outlet of each collector pipe is equipped with a flow meter to measure the amount of water coming from the drainage geocomposite. Each of the test sections has a thermocouple string that is used to measure frost penetration.

6.1.3. Results

6.1.3.1. Strain Gages. Each instrumented geogrid rib has a pair of strain gages. The data from each pair is averaged to remove the effects of bending from the results. The average survival rate of strain gage pairs was 93% at the end of construction but this had decreased to 35% by May 2005. Failure was defined as malfunction of one strain gage in a pair. A technique was developed to obtain useable data for the situation where only one gage in a pair was still working.

Average geogrid forces were examined after compaction, immediately after paving, and at 12, 24, 35, and 45 months after paving. In sections with a 300-mm (12-in.) subbase layer with geogrid on subgrade as well as geogrid in the middle of the subbase showed a general trend that the average force increased over time, with greater increases occurring in the section with geogrid on subgrade. In the sections with a 600-mm (24-in.) subbase and geogrid located on subgrade, the largest force was recorded right after paving and then the average force decreased over time. For sections with geogrid in the middle of a 600-mm (24-in.) subbase, a slight increase in force with time was observed. For 12, 24, and 35 months after paving, the sections with 300-mm (12-in.) subbase had a higher force than sections with 600-mm (24-in.) subbase.

The geogrid forces in ribs oriented perpendicular to centerline were analyzed statistically to further evaluate the effects of elapsed time, subbase thickness, and geogrid location in the pavement system on the force in the geogrid. The force in the geogrid located on subgrade and in the middle of the subbase was statistically equal for 300-mm (12 in.) subbase sections immediately after subbase compaction and after paving. However, for 12, 24, and 35 months after paving, geogrid located on the subgrade produced a statistically higher force than when located in the subbase. In the 600-mm subbase sections, the opposite trends occurred. Up to 12 months after paving geogrid located on subgrade produced a statistically higher force, but for 24 months to the end of the project monitoring period the forces were statistically equal. Taken in total, these results suggest that geogrid located on subgrade develops a force that is equal to or greater than when the geogrid is located within the subbase for both subbase thicknesses in this study.

The force in the geogrid immediately after paving in 300-mm (12 in.) subbase sections was statistically equal to that in the 600-mm (24 in.) subbase sections for both geogrid on subgrade and in the subbase. However, after 12, 24, and 35 months, the force in the geogrid in the 300-mm (12 in.) subbase sections was statistically greater that in the 600-mm (24 in.) subbase sections for geogrid on subgrade. The same was true for geogrid located in the subbase for 12 and 24 months after paving. This suggests that pavements with thinner pavement sections develop greater forces over time than thicker pavement sections.

The analysis indicated that the average force in the geogrid on subgrade and in the subbase in the 300-mm (12 in.) subbase sections increased between subbase compaction and paving, paving to 12 months, and 12 to 24 months after installation. However, the forces in the subgrade geogrid sections decreased or remained the same from 24 to 35 months, unlike the subbase geogrid sections which continued to increase. This suggests that reinforcement mechanisms continue to develop after paving in the sections with of 300 mm (12 in.) subbase. The geogrid on subgrade and in the subbase in the 600-mm (24 in.) subbase sections exhibited increases in force between subbase compaction and paving. However, these forces either decreased, or failed to exhibit appreciable increases from paving to 45 months. This indicates that reinforcement mechanisms did not continue to develop after paving in sections with 600-mm (24-in.) subbase sections.

The force in the geogrid parallel to centerline was also measured. Immediately after paving these forces were similar to that perpendicular to centerline for both the 300-mm (12-in.) and 600-mm (24-in.) subbase sections. At the end of the monitoring period (May, 2005) they were also similar for the 600-mm (24-in.) subbase sections. However,

for the 300-mm (12-in.) subbase sections the forces perpendicular to centerline in May 2005 were higher than parallel to centerline.

Laboratory tests showed that the geogrid may experience creep, as reflected by increases in strain, when subjected to a constant load similar to those measured in the field. Considering that in this study the force per unit width in the geogrid was obtained from the change in strain in the instrumented ribs, strain due to creep would be interpreted as an increase in force per unit width. Strain rates measured in the lab and long-term strain rates measured in the field were similar. Thus, the increases in force per unit width with time reported in this study could be due to creep rather than an actual increase in force carried by the geogrid.

6.1.3.2. Piezometers. Vibrating wire piezometers were used to measure porewater pressure in the subbase course and subgrade soils. Previous work showed that these types of piezometers indicate negative porewater pressures when the degree of saturation drops below about 50%. Low saturation indicates that the section is well drained.

Results from subbase piezometers showed that the sections with drainage geocomposite exhibited long periods of negative porewater pressure unlike the control sections, which exhibited mostly positive porewater pressures. This suggests that the drainage geocomposite assists with the removal of water from the subbase.

The subgrade piezometers also exhibit negative porewater pressures indicating significant periods of partial saturation. However, for the subgrade piezometers, there is no clear difference in behavior between sections with and without drainage

geocomposite. This suggests that the drainage geocomposite had little effect on subgrade porewater pressures.

The subbase and subgrade piezometers in the reclaimed control section had lower porewater pressure than those in the drainage section. This suggests that the drainage geocomposite's ability to remove water from the subbase and subgrade may be inhibited in sections utilizing reclaim construction techniques.

6.1.3.3. Flow Meters. The flowmeters used to measure the quantity of water discharging from the geocomposite collector pipes proved to be unreliable and were easily clogged by iron that precipitated from the water. Thus, reliable data was obtained only for the spring of 2003. The majority of the collector pipes experienced their maximum flow at the onset of the spring thaw between 3/27/03 and 4/3/03. Flow events following the spring thaw appear to correspond with rainfall events. In test sections 4, 9, and 10 the peak flow observations coincide with negative porewater pressure in the subbase. This could be an indication that water was being removed from the pavement system by the drainage geocomposite.

6.1.3.4. Thermocouples. Thermocouples were used to monitoring the depth of frost penetration. Minimum frost penetration over the monitoring period occurred during the winter of 2004-05 in test section 12, with a depth of 450 mm (18 in.). Maximum frost penetration over the monitoring period occurred during the winter of 2003-04 in test section 6, with a depth of 1720 mm (68 in.). The data obtained from the other instrumentation was evaluated in the context of the extent of frost penetration.

6.1.3.5. Falling Weight Deflectometer. The results from falling weight deflectometer tests performed in spring and early summer of 2004 show that reinforcement geogrid and drainage geocomposite increase the effective structural number by between 5% and 17% for sections with 300 mm (12 in.) of subbase aggregate. However, they had no apparent effect for sections with 600 mm (24 in.) of subbase aggregate or the reclaim sections. Comparing control sections with 300 mm (12 in.) and 600 mm (24 in.) of subbase aggregate showed that doubling the subbase thickness increased the effective structural number by 70%. The results suggest that the increase in effective structural number that was produced by geogrid and/or drainage geocomposite in the 300-mm (12-in.) subbase sections could also be obtained by adding between 25 mm (1 in.) and 75 mm (3 in.) of subbase aggregate to an unreinforced section.

6.2. Conclusions

1. The use of reinforcement geogrid in sections with a 300-mm (12-in.) thick base course increased the backcalculated effective structural number by between 5% and 17% compared to an unreinforced control section.
2. Inclusion of drainage geocomposite in sections with a 300-mm (12-in.) thick base course increased the backcalculated effective structural number by between 5% and 11% compared to a control section without geocomposite.
3. Inclusion of a combination of drainage geocomposite and reinforcement geogrid in sections with a 300-mm (12-in.) thick base course increased the backcalculated structural number by 5%.

4. Reinforcement geocomposite and drainage geocomposite had no significant effect on backcalculated structural number for sections with a 600-mm (24-in.) thick base course.
5. Doubling the thickness of the subbase course from 300 mm (12 in.) to 600 mm (24 in.) increased the backcalculated effective structural number by 70%.
6. For sections with a 300-mm (12-in.) thick base course, the increase in backcalculated effective structural number that was attributed to inclusion of reinforcement geogrid, drainage geocomposite, or a combination of reinforcement and drainage geocomposite could also be obtained by increasing the subbase thickness by between 25 mm (1 in.) and 75 mm (3 in.).
7. The results of this study are in general agreement with previous work which indicates that little improvement from geosynthetics reinforcement is expected in flexible pavement systems designed to carry more than 200,000 equivalent 80-kN (18-kip) single axle loads or constructed with subbases thicker than 300 mm (12 in.).
8. Placement and compaction of the subbase course developed between 18% and 83% of the long term force in the geogrid. This had increased to 65% to 139% of the long term force by the time the sections were paved. Thus, placement and compaction of the overlying subbase course, and the action of traffic and concomitant passage of time prior to paving, are both important to the development the force in the geogrid.
9. The force in the geogrid continued to increase after paving for sections with 300 mm (12 in.) subbase but the force remained the same or decreased for sections

with 600 mm (24 in.) subbase. Thus, for thinner sections, the passage of time and the action of traffic are needed to fully develop the geogrid force.

10. Geogrid located on subgrade develops a force that is equal to or greater than when the geogrid is located within the subbase for both subbase thicknesses in this study.
11. Pavements with thinner pavement sections tend to develop higher forces than thicker pavement sections.
12. The average geogrid strain was between 0.5% and 0.7% for sections with 300 mm (12 in.) base and 0.3% to 0.4% for sections with 600 mm (24 in.) base. For comparison, Perkins (1999) concluded that geogrid strains between 0.5 and 2.0% were adequate to mobilize the reinforcement and improve pavement performance. Thus, the sections with 300 mm (12 in.) base are at the lower bound of this range and the sections with 600 mm (24 in.) base below this range. Considered in conjunction with the backcalculated effective structural numbers, the results suggest a small improvement in pavement performance for the sections with 300-mm (12-in.) subbase and reinforcement geogrid but not improvement for sections with 600-mm (24-in.) subbase.
13. The drainage geocomposite appears to be assisting with the removal of water from the subbase in the reconstructed sections and lowering the porewater pressure in the subbase course. However, the effect on the backcalculated effective structural number was small with increases of 5 to 11% in sections with 300-mm (12-in.) subbase but no significant effect on sections with 600-mm (24-in.) subbase.

14. The drainage geocomposite had no effect on porewater pressure in the subgrade soils.
15. The drainage geocomposite had no significant effect on porewater pressures in the subbase and subgrade soils in the reclaim sections.

6.3. Recommendations For Future Research

The reinforcing effects of geogrid should be further investigated using numerical methods, such as a finite element analysis. The field measurements from the Route 9 field trial should be used to calibrate the model. The model should be used to more fully understand the reinforcing mechanisms, and the circumstances where the geogrid does and does not provide improved pavement performance.

The performance of the Route 9 field trial should be monitored visually for cracking and rutting, and with a FWD until the first rehabilitation.

REFERENCES

Al-Qadi, I., Brandon, T., Valentine, R., Lacina, B., and Smith, T. (1994), "Laboratory Evaluation of Geosynthetic-Reinforced Pavement Sections," Transportation Research Record No. 1439, Transportation Research Board, Washington, D.C., pp. 25-31.

Anderson, P., and Killeavy, M. (1989), "Geotextiles and Geogrids: Cost Effective Alternate Materials for Pavement Design and Construction", Proceedings of Geosynthetics '89, San Diego, CA, pp. 353-364.

Barksdale, R. D., and Brown, S. F. (1987), "Geosynthetic Reinforcement of Aggregate Bases of Surfaced Pavements." Paper presented at the 66th Annual TRB Meeting, Washington, D.C., pp. 1-32.

Barksdale, R. D., Brown, S. F., and Chan, F. (1989), "Potential Benefits of Geosynthetics in Flexible Pavement Systems" National Cooperative Highway Research Program Report 315, Transportation Research Board, Washington, D.C., pp. 1-28.

Bender, D. A., and Barenberg, E. J. (1978), "Design and Behavior of Soil-Fabric-Aggregate Systems" Transportation Research Record No. 671, Transportation Research Board, Washington, D.C., pp. 64-78.

Brandon, T. L., Al-Qadi, I., Lacina, B., and Bhutta, S. A. (1996), "Construction and Instrumentation of Geosynthetically Stabilized Secondary Road Test Sections" Transportation Research Record No. 1354, Transportation Research Board, Washington, D.C., pp. 50-57.

Cancelli, A., Montanelli, F., Rimoldi, P., and Zhao, A. (1996), "Full Scale Laboratory Testing on Geosythetic Reinforced Paved Roads" Proceedings of the International Symposium on Earth Reinforcement, Vol. I., pp. 573-578.

Holtz, R. D. (1991), "Geotextiles for Subgrade Stabilization in Permanent Roads and Highways," Proceedings of Geosynthetics '91, Atlanta, Georgia, pp. 701-713.

Das, B.M. (2000), "Shallow Foundations on Geogrid-Reinforced Soil," Transportation Research News No. 207, Transportation Research Board, Washington, D.C., pp. 19-20.

Gilman, G.D. (1964), "The freezing index in New England," Special Report 63, U.S. Army Cold Regions Research and Engineering Laboratory, Hanover, NH, 16 pp. + tables.

Giroud, J. P. (1985), "Design of Unpaved Roads and Trafficked Areas With Geogrids,"

PolymerGrid Reinforcement, Thomas Telford Limited, London, pp. 116-127.

Giroud, J.P., and Noiray, L. (1981), "Design of Geotextile-Reinforced Unpaved Roads, Journal of the Geotechnical Engineering Division, ASCE, Vol. 107, No. GT9, Sept., pp. 1233-1254.

Glynn, D. T., and Cochrane, S. R. (1987), "The Behavior of Geotextiles as Separating Membranes in Glacial Till Subgrade," Proceedings of Geosynthetics '87, New Orleans, LA, pp. 26-36.

Haas, R., Walls, J., and Carroll, R. G. (1988), "Geogrid Reinforcement of Granular Bases in Flexible Pavements," Transportation Research Record No. 1188, Transportation Research Board, Washington, D.C., pp. 19-27.

Halliday, A. R., and Potter, J. F. (1984), "The Performance of a Flexible Pavement Constructed on a Strong Fabric," Transport and Road Research Laboratory, Report LR1123, pp. 1-13.

Hayden, S. A., Christopher, B. R., Humphrey, D. N., Dunn, P. A., and Fetten, C. P. (1998), "Instrumentation of Reinforcement, Separation, and Drainage Geosynthetic Test Sections used in the Reconstruction of a Highway in Maine" Proceedings of the Conference on Cold Regions Impact on Civil Works, ASCE, New York, pp. 420-433.

Henry, K. S. (1996), "Geotextiles To Mitigate Frost Effects in Soils: A Critical Review," Transportation Research Record No. 1534, Transportation Research Board, Washington, D. C., pp. 5-11.

Henry, K. S. (1991), "Effect of Geotextiles on Water Migration in Freezing Soils and the Influence of Freezing on Performance," Proceedings of Geosynthetics '91, Atlanta, GA, pp. 469-483.

Jewell, R. A. (1985), "Interaction Between Soil and Geogrids," Polymer Grid Reinforcement, Thomas Telford Limited, London, pp. 18-30.

Kennepohl, G., Kamel, N., Walls, J., and Haas, R. C. (1985), "Geogrid Reinforcement of Flexible Pavements Design Basis and Field Trials," Asphalt Paving Technology, Association of Asphalt Paving Technologists, Vol. 54, San Antonio, TX, pp. 45-76.

Kinney, T., Abbott, J., and Schuler, J. (1998), "Benefits of Using Geogrids for Base Reinforcement with Regard to Rutting," Transportation Research Record No. 1611, Transportation Research Board, Washington, D. C., pp. 86-96.

Kinney, T., and Barenberg, E. (1982), "The Strengthening Effect of Geotextiles on Soil-Geotextile-Aggregate Systems," Proceedings of the Second International Conference on Geotextiles, Las Vegas, NV, pp. 347-352.

Kinney, T., and Savage, B. M. (1989), "Using Geosynthetics to Control Lateral Spreading of Pavements in Alaska – Preliminary Results," Proceedings of Geosynthetics '89, San Diego, CA, pp. 324-333.

Leng, J., and Gabr, M.A. (2002), "Characteristics of Geogrid-Reinforced Aggregate Under Cyclic Load," Transportation Research Record No. 1786, Transportation Research Board, Washington, D. C., pp. 29-35.

Ling, H. I., and Liu, Z. (2001), "Performance of Geosynthetic Reinforced Asphalt Pavements," Journal of Geotechnical and Geoenvironmental Engineering, Vol. 127, Issue 2, ASCE, Reston, VA, pp. 177-184.

Milligan, G. W., and Love, J. P. (1985), "Model Testing of Geogrids Under an Aggregate Layer on Soft Ground," Polymer Grid Reinforcement, Thomas Telford Limited, London. pp. 128-138.

Penner, R., Haas, R., and Walls, J. (1985), "Geogrid Reinforcement of Granular Bases," Presented to Roads and Transportation Association of Canada Annual Conference, Vancouver, pp. 263-292.

Perkins, S.W. (1999), "Geosynthetic Reinforcement of Flexible Pavements: Laboratory Based Pavement Test Sections," Montana Department of Transportation, Bozeman, MT, pp.32-95.

Perkins, S. W., Ismeik, M., Fogelson, M. L., Wang, Y., and Cuelho, E. V. (1998), "Geosynthetic-Reinforced Pavements: Overview and Preliminary Results," Proceedings of Sixth International Conference on Geosynthetics, Atlanta, GA, pp. 1-8.

Perkins, S. W., Ismeik, M., and Fogelson, M. L. (1998), "Mechanical Response of a Geosynthetic-Reinforced Pavement System to Cyclic Loading," Fifth International Conference on the Bearing Capacity of Roads and Airfields, Trondheim, Norway, Vol. 3, pp. 1503-1512.

Perkins, S. W., and Ismeik, M. (1997), "A Summary of Geosynthetic Reinforced Flexible Pavements," Proceedings of the 32nd Symposium on Engineering Geology and Geotechnical Engineering, March, Boise, ID, pp. 127-134.

Robnett, Q. L., and Lai, J. S. (1982), "Fabric-Reinforced Aggregate Roads – Overview," Transportation Research Record No. 875, Transportation Research Board, Washington, D. C., pp. 42-49.

Shrestha, S. C., and Bell, J. R. (1982), "Creep Behavior of Geotextiles Under Sustained Loads," Proceedings of the Second International Conference on Geotextiles, Las Vegas, NV, August, Vol. III, pp. 769-774 and Vol. IV, pp. 120-122.

Sowers, G. F., Collins, S. A., and Miller, D. G. (1982), "Mechanism of Geotextile-Aggregate Support in Low-Cost Roads," Proceedings of the Second International Conference on Geotextiles, Las Vegas, NV, Vol. II, pp. 341-346.

Thompson, M.R., and Raad, L. (1981), "Fabric Utilization in Low Deformation Transporation Support Systems," Transportation Research Record No. 810, Transportation Research Board, Washington, D. C., pp. 57-60.

Vischer, W. (2003), "Low-Volume Road Flexible Pavement Design with Geogrid-Reinforced Base," Transportation Research Record No. 1819, Transportation Research Board, Washington, D. C., pp. 247-254.

Webster, S. L. (1992), "Geogrid Reinforced Base Courses for Flexible Pavements for Light Aircraft, Test Section Construction, Behavior Under Traffic, Laboratory Results, and Design Criteria," Report No. 0156267, DOT/FAA/RD-92/95, U. S. Department of Transportation, Federal Aviation Administration, Washington, D.C., pp. 1-85.

White, D. W. (1991), "Literature Review on Geotextiles to Improve Pavements for General Aviation Airport," Report No. GL-91-3. U. S. Army Engineers Waterways Experiment Station, Vicksburg, MS, pp. 1-46.

Wu, T. H. (1989), "Behavior of Soil-Geotextile Composite and its Application to Finite Element Analysis," Proceeedings of Geosynthetics '89, San Diego, CA, pp. 365-372.

APPENDIX A -
LABORATORY CALIBRATION TESTS

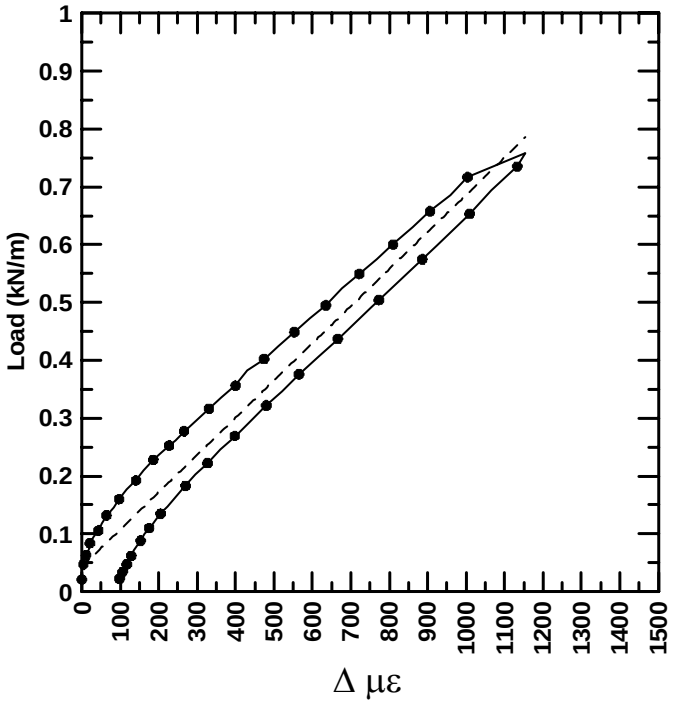

Figure A-1 Wide width tensile test calibration curve, specimen 1, test 1, gage 1.

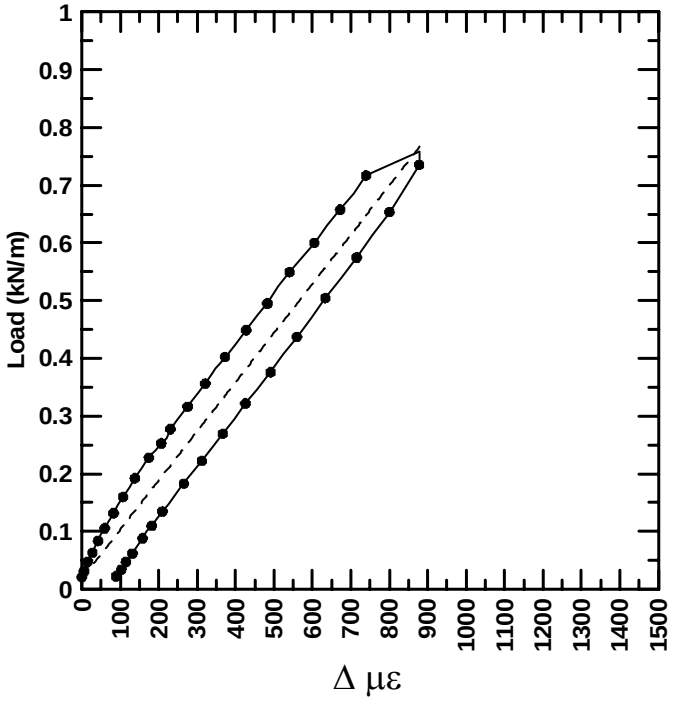

Figure A-2 Wide width tensile test calibration curve, specimen 1, test 1, gage 2.

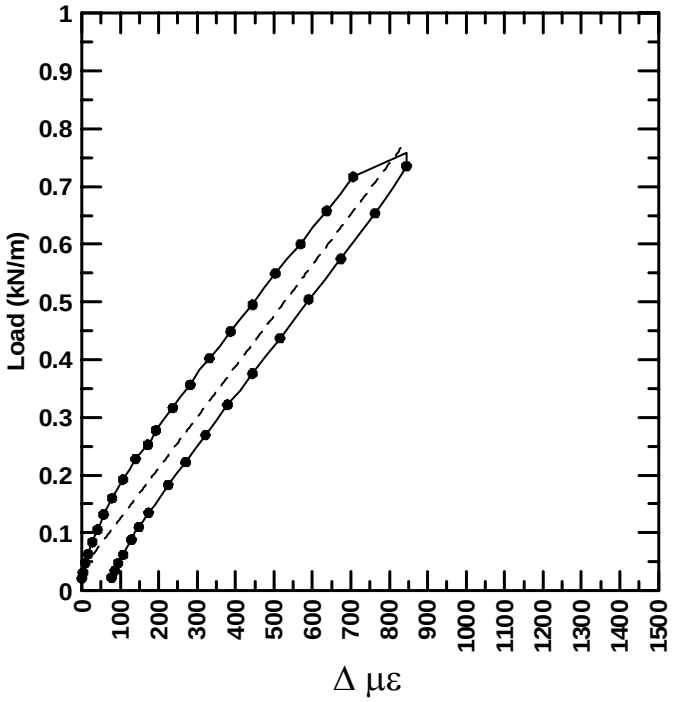

Figure A-3 Wide width tensile test calibration curve, specimen 1, test 1, gage 3.

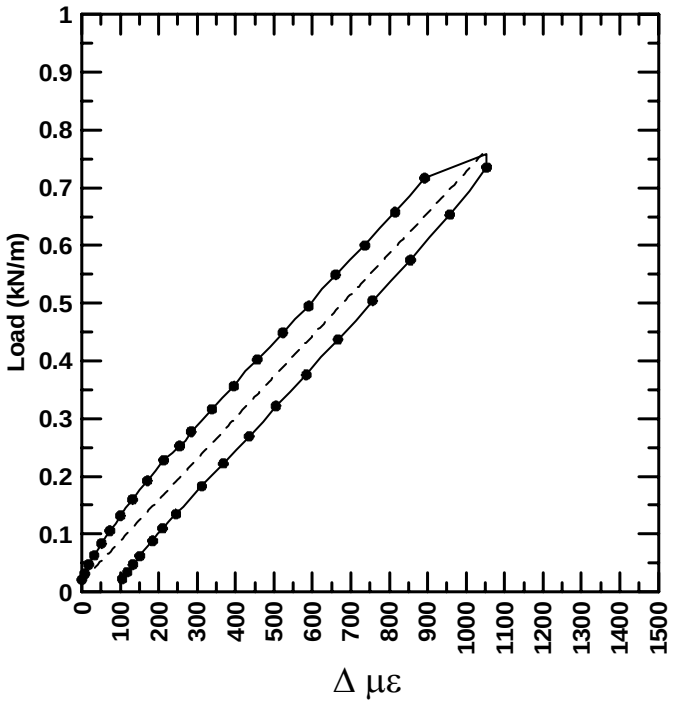

Figure A-4 Wide width tensile test calibration curve, specimen 1, test 1, gage 4.

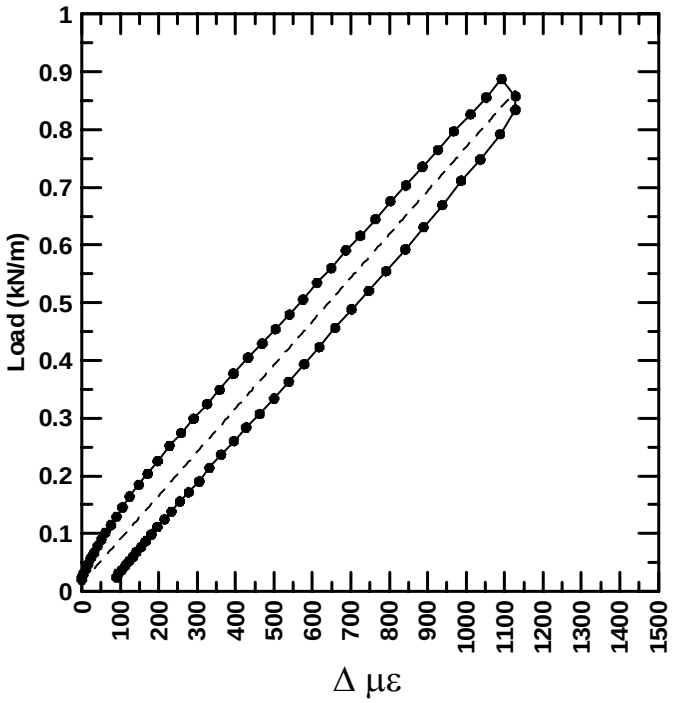

Figure A-5 Wide width tensile test calibration curve, specimen 1, test 2, gage 1.

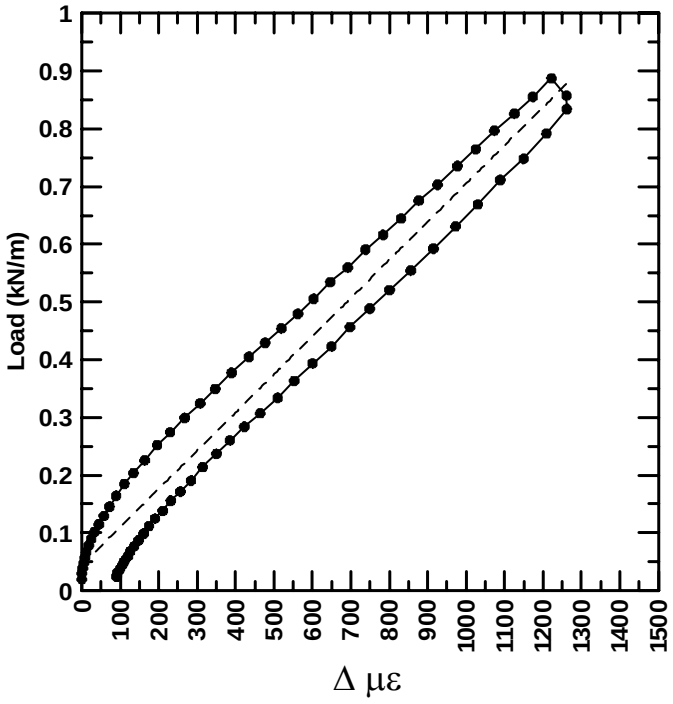

Figure A-6 Wide width tensile test calibration curve, specimen 1, test 2, gage 2.

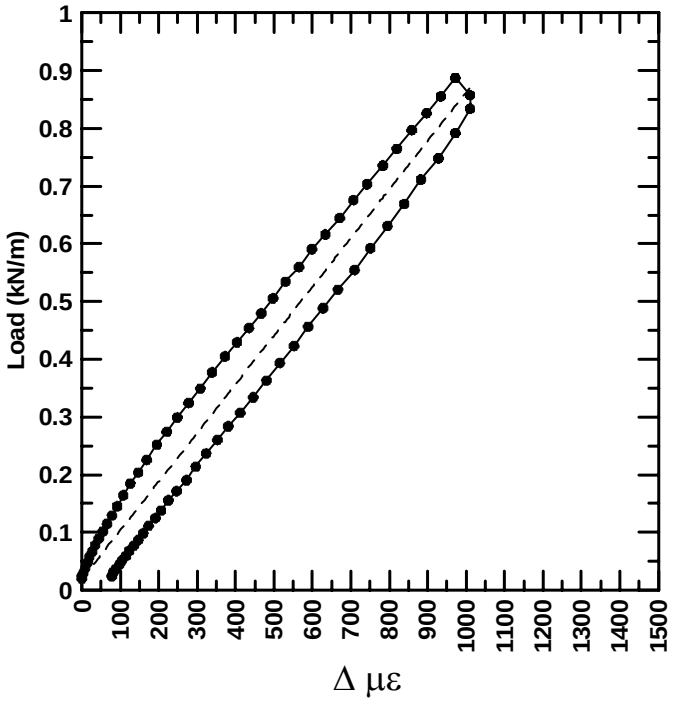

Figure A-7 Wide width tensile test calibration curve, specimen 1, test 2, gage 3.

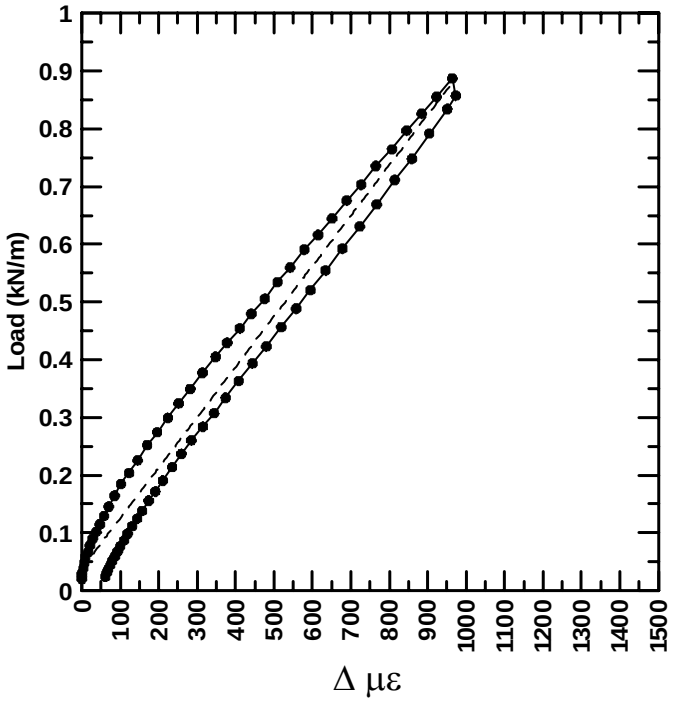

Figure A-8 Wide width tensile test calibration curve, specimen 1, test 2, gage 4.

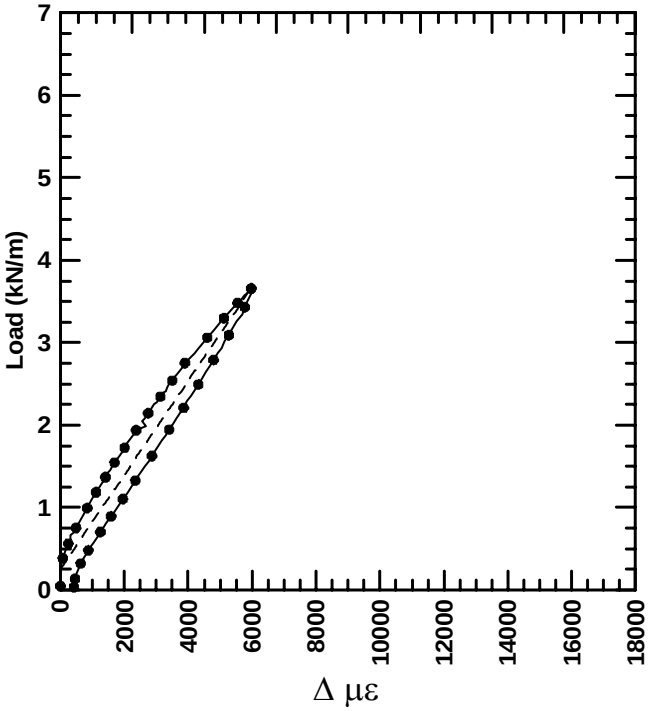

Figure A-9 Wide width tensile test calibration curve, specimen 2, test 1, gage 1.

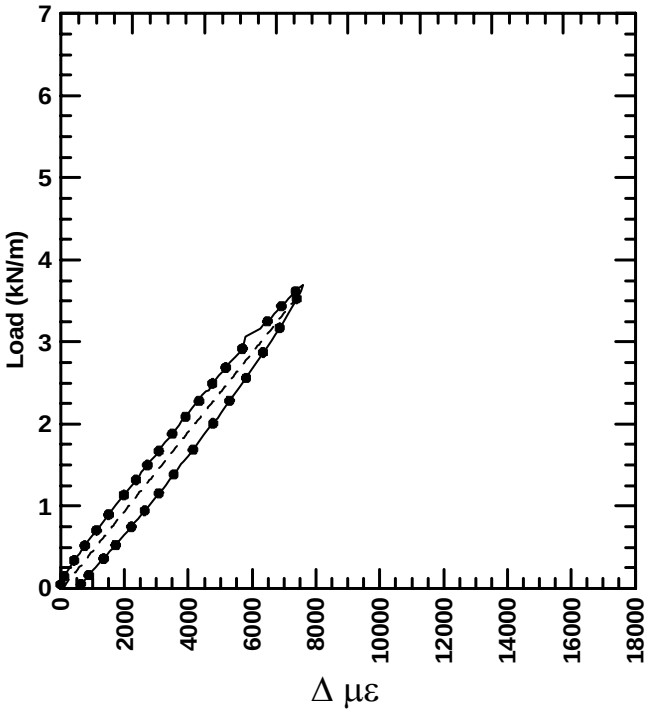

Figure A-10 Wide width tensile test calibration curve, specimen 2, test 1, gage 2.

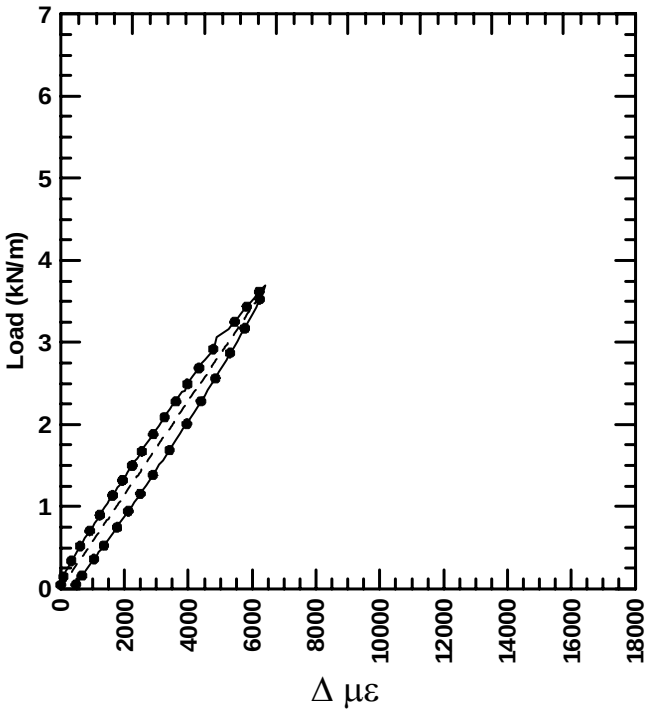

Figure A-11 Wide width tensile test calibration curve, specimen 2, test 1, gage 3.

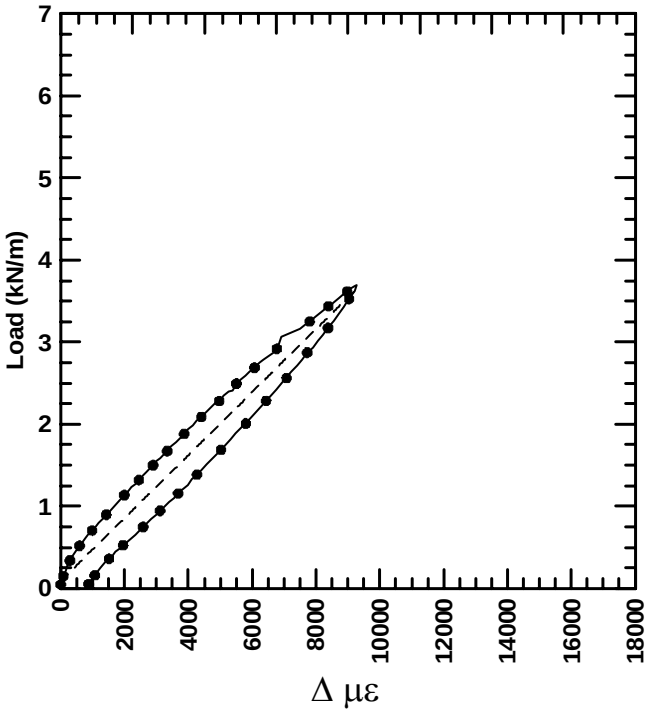

Figure A-12 Wide width tensile test calibration curve, specimen 2, test 1, gage 4.

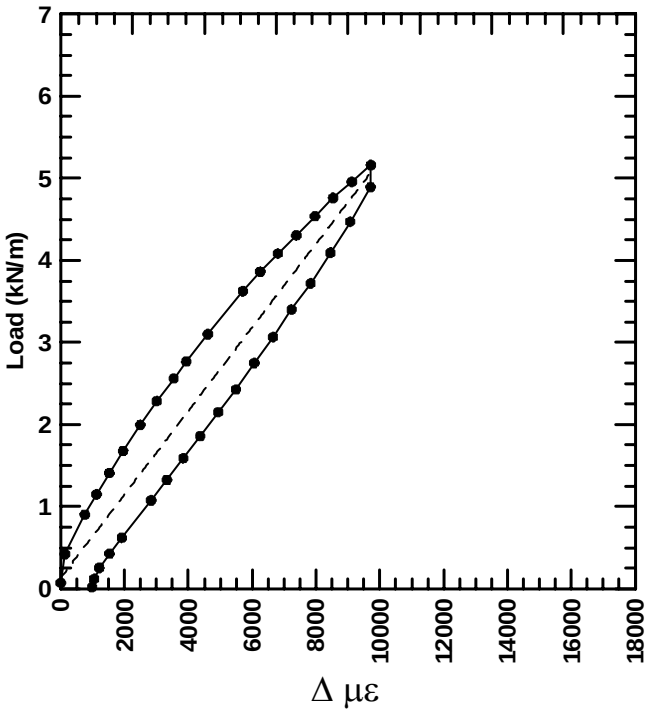

Figure A-13 Wide width tensile test calibration curve, specimen 2, test 2, gage 1.

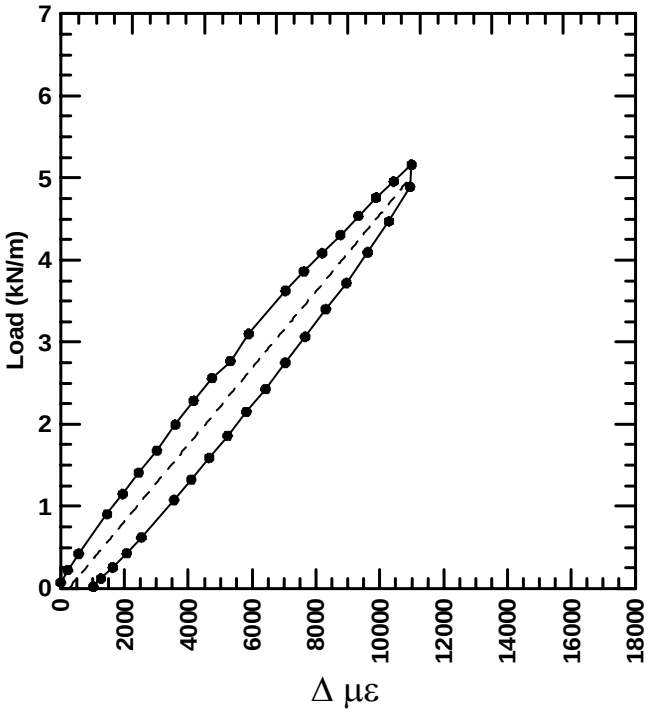

Figure A-14 Wide width tensile test calibration curve, specimen 2, test 2, gage 2.

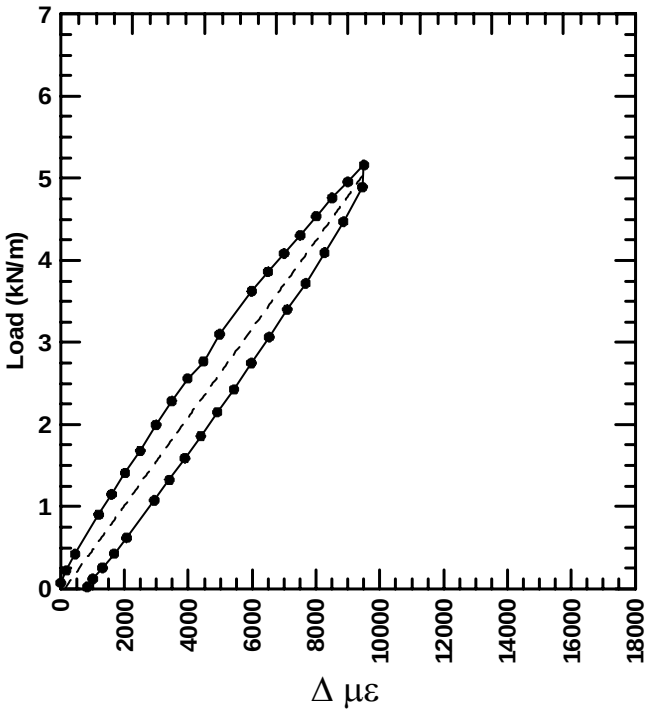

Figure A-15 Wide width tensile test calibration curve, specimen 2, test 2, gage 3.

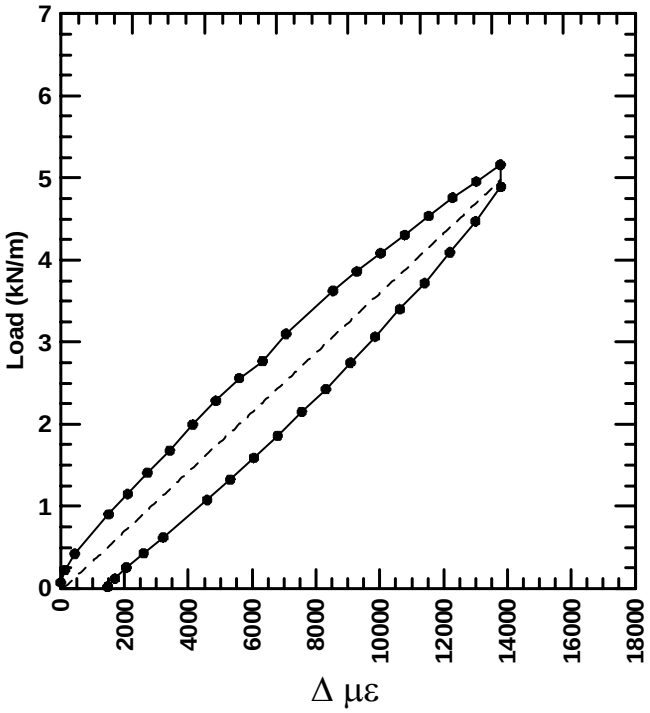

Figure A-16 Wide width tensile test calibration curve, specimen 2, test 2, gage 4.

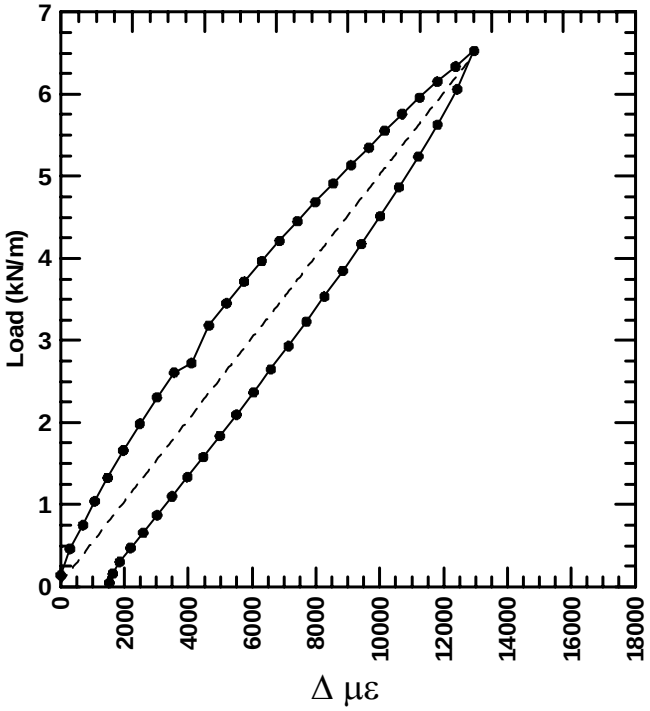

Figure A-17 Wide width tensile test calibration curve, specimen 2, test 3, gage 1.

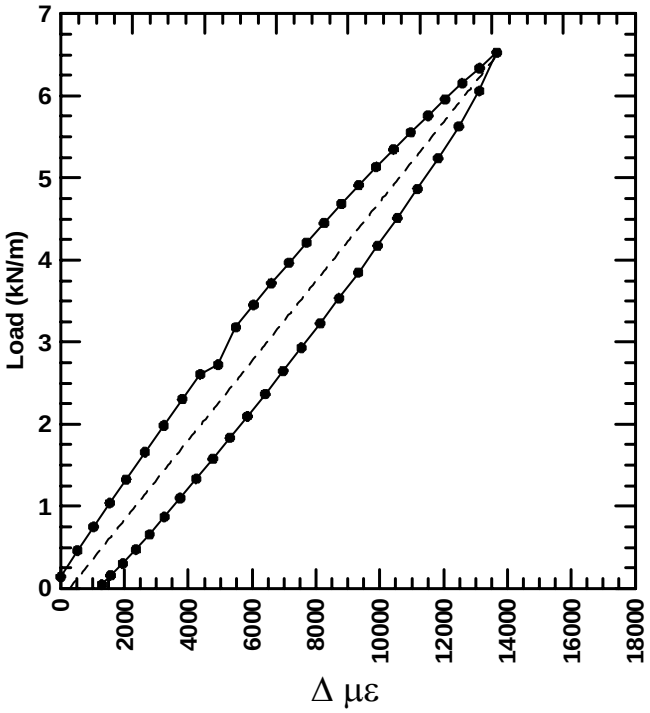

Figure A-18 Wide width tensile test calibration curve, specimen 2, test 3, gage 2.

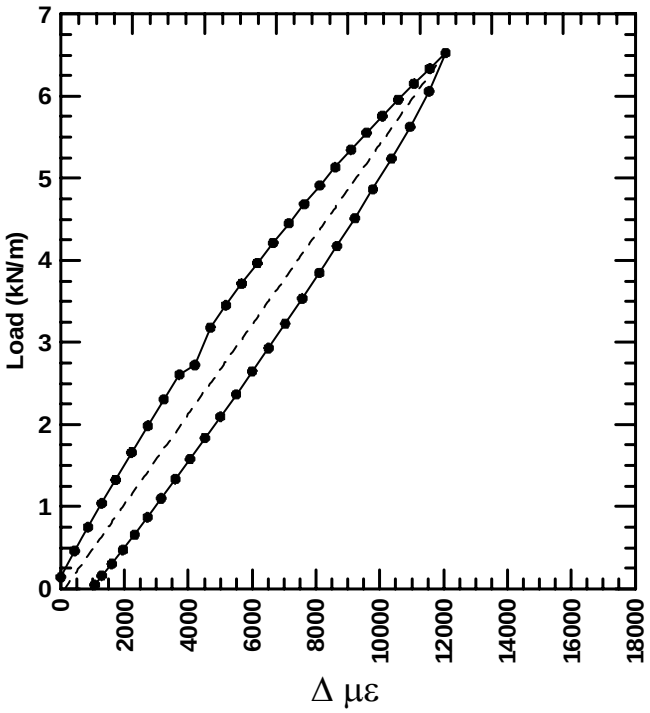

Figure A-19 Wide width tensile test calibration curve, specimen 2, test 3, gage 3.

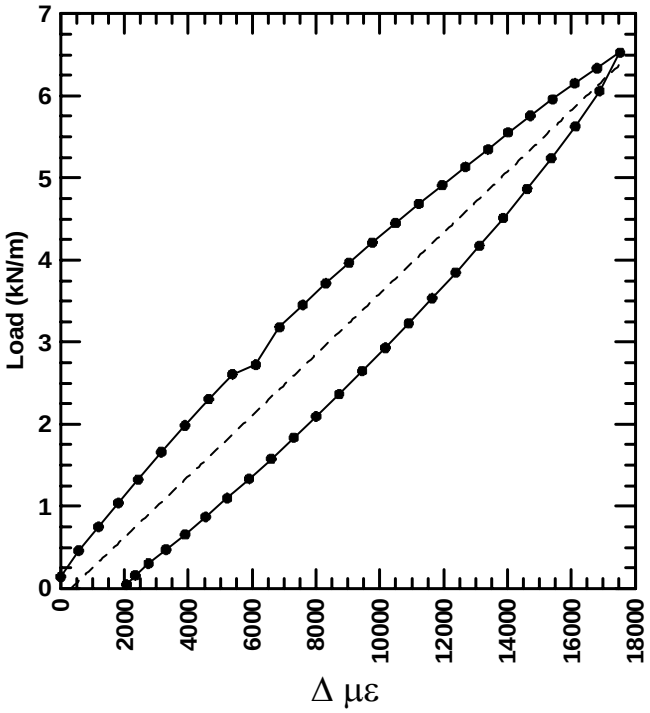

Figure A-20 Wide width tensile test calibration curve, specimen 2, test 3, gage 4.

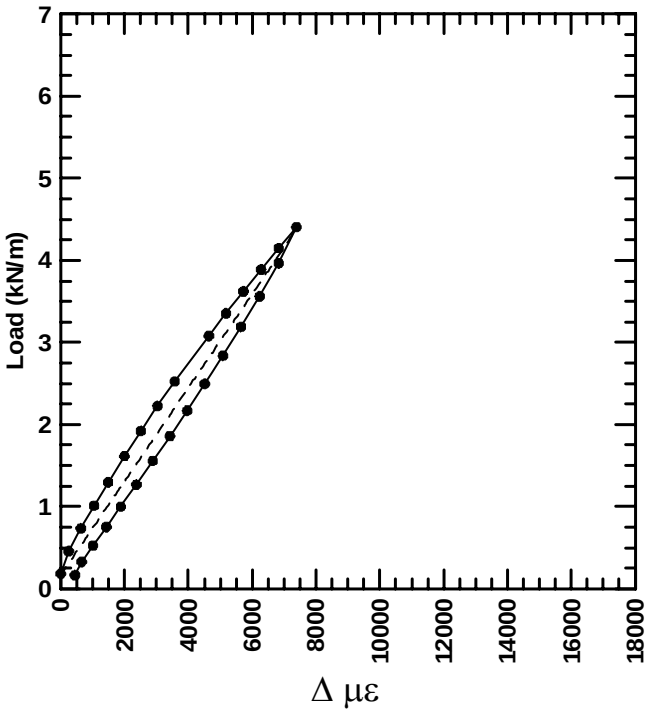

Figure A-21 Wide width tensile test calibration curve, specimen 2, test 4, gage 1.

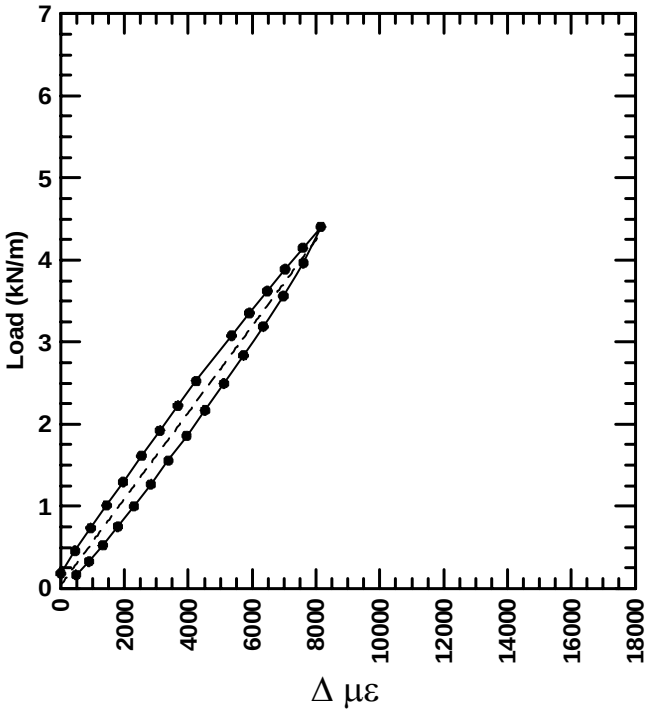

Figure A-22 Wide width tensile test calibration curve, specimen 2, test 4, gage 2.

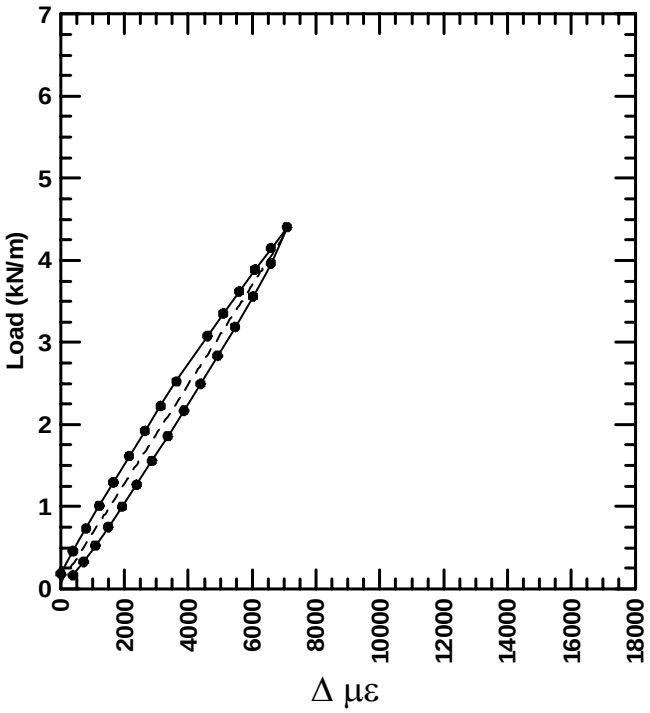

Figure A-23 Wide width tensile test calibration curve, specimen 2, test 4, gage 3.

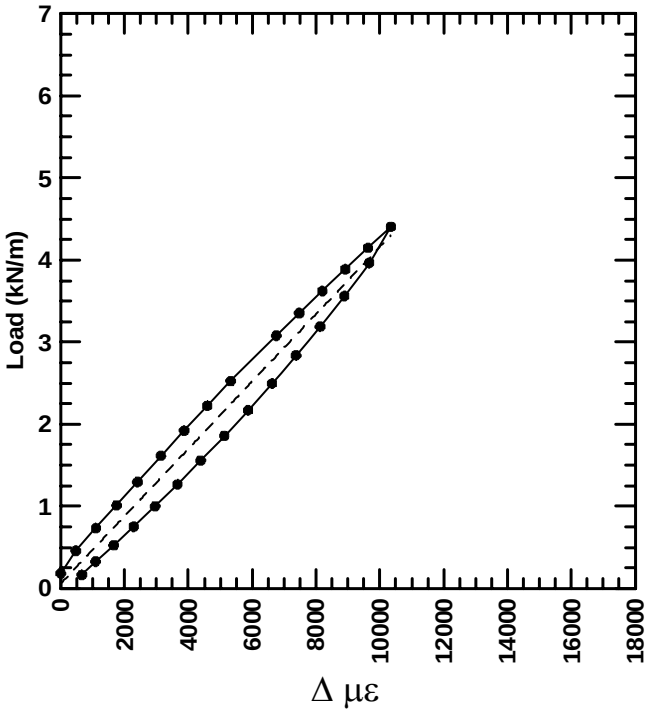

Figure A-24 Wide width tensile test calibration curve, specimen 2, test 4, gage 4.

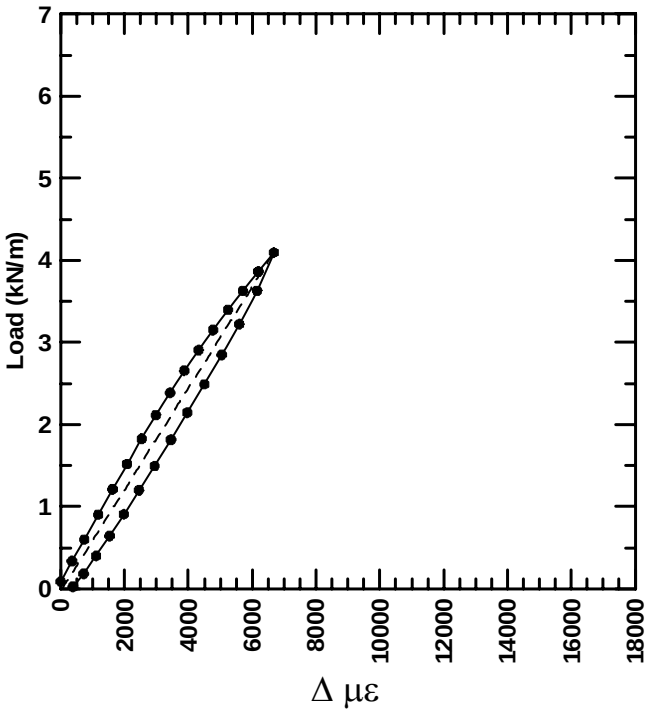

Figure A-25 Wide width tensile test calibration curve, specimen 3, test 1, gage 1.

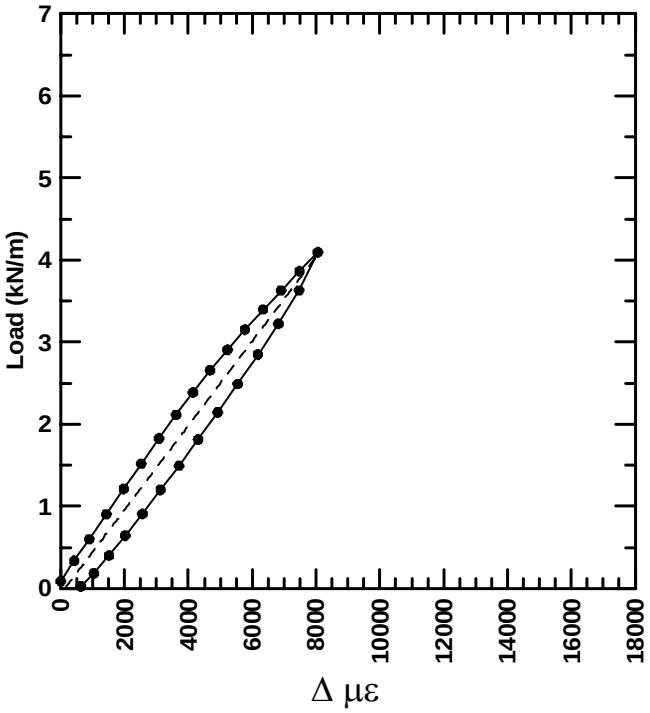

Figure A-26 Wide width tensile test calibration curve, specimen 3, test 1, gage 2.

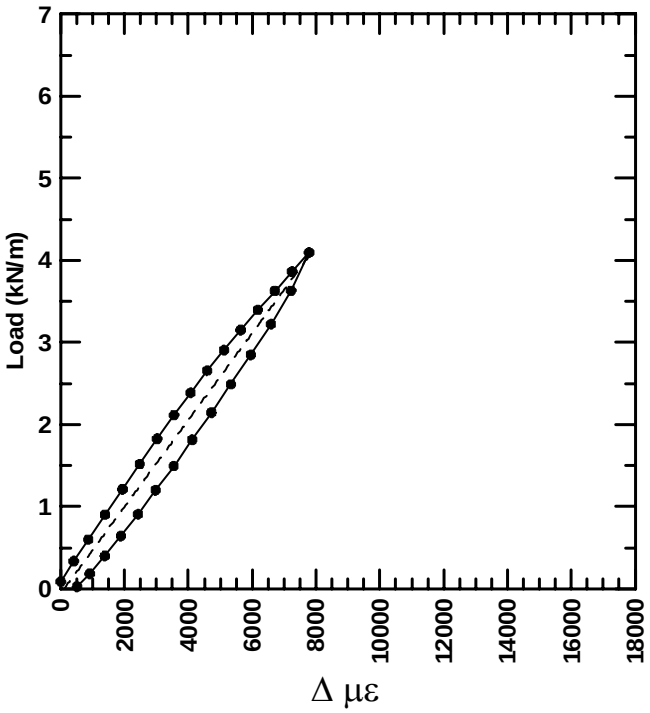

Figure A-27 Wide width tensile test calibration curve, specimen 3, test 1, gage 3.

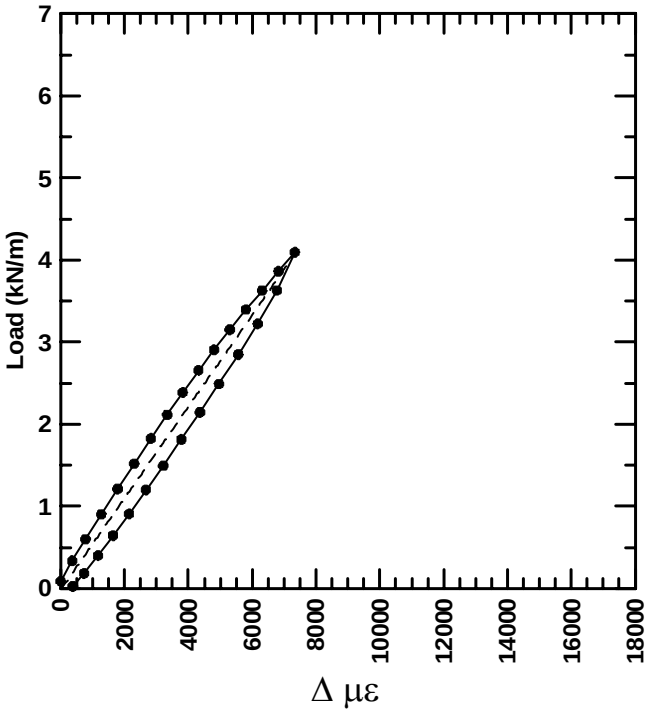

Figure A-28 Wide width tensile test calibration curve, specimen 3, test 1, gage 4.

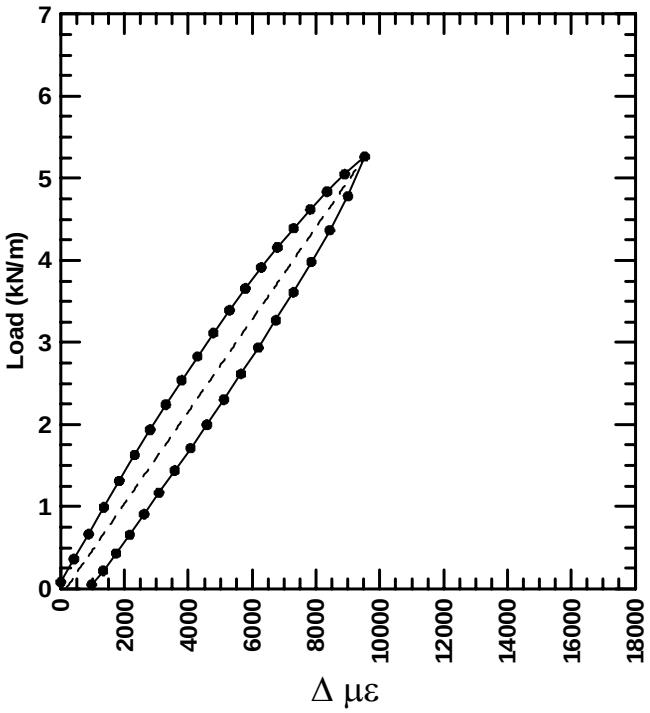

Figure A-29 Wide width tensile test calibration curve, specimen 3, test 2, gage 1.

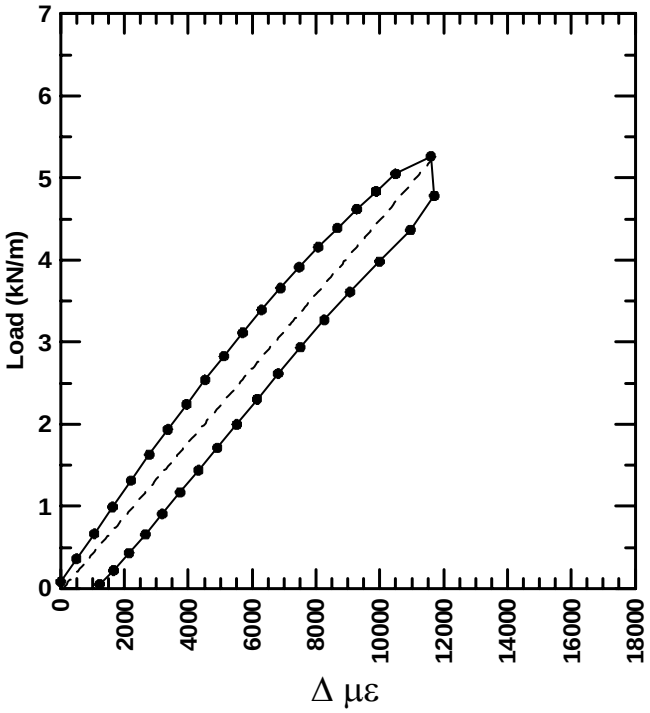

Figure A-30 Wide width tensile test calibration curve, specimen 3, test 2, gage 2.

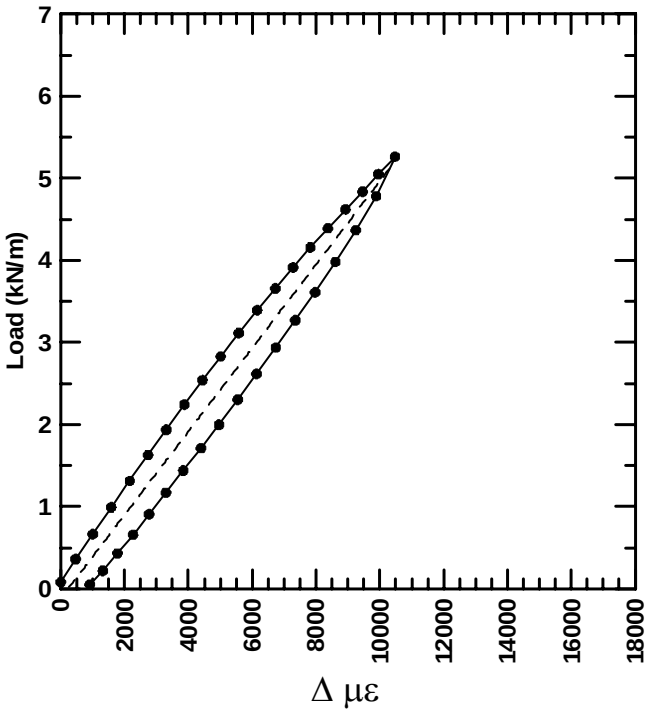

Figure A-31 Wide width tensile test calibration curve, specimen 3, test 2, gage 3.

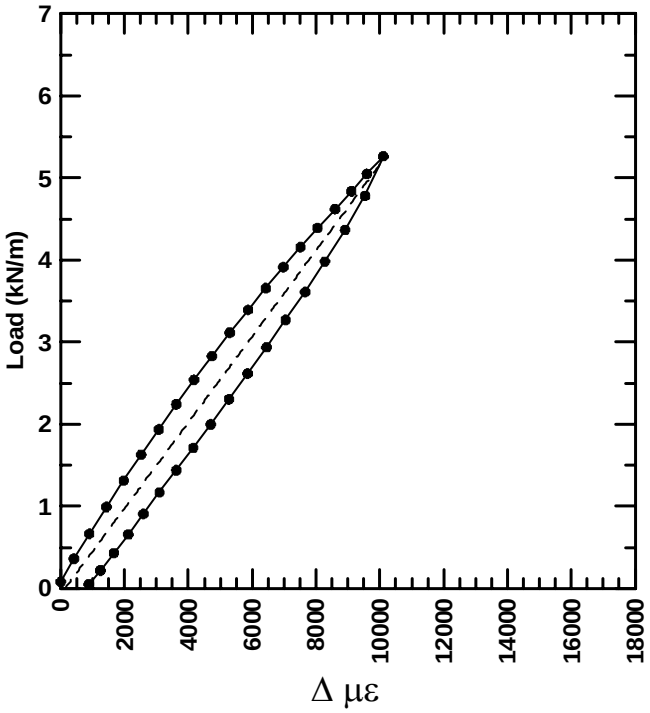

Figure A-32 Wide width tensile test calibration curve, specimen 3, test 2, gage 4.

(BLANK PAGE)

APPENDIX B -
FALLING WEIGHT DEFLECTOMETER RESULTS

Maine Department Of Transportation
Falling Weight Deflectometer (FWD)
Data Analysis Summary - Spring 2004

Monmouth - Litchfield Route # 126
Effective Structural Number
(based on English Units)

	Station	3/10	3/24	3/31	4/7	4/22	4/28	5/12	6/29
Section 1	1+532	3.9	3.9	3.4	3.4	3.5	3.4	3.3	3.7
	1+544	4.2	3.9	3.6	3.9	3.8	3.7	3.5	3.7
	1+556	4.0	3.7	3.5	3.5	3.5	3.4	3.3	3.6
	1+568	3.8	3.6	3.5	3.5	3.6	3.6	3.5	3.8
	Average	4.0	3.8	3.5	3.6	3.6	3.5	3.4	3.7
	Std Dev	0.17	0.15	0.10	0.20	0.12	0.17	0.11	0.10
Section 2	1+592	4.1	3.6	3.5	3.5	3.7	3.6	3.5	3.7
	1+604	4.1	3.9	3.8	3.8	3.9	3.9	3.7	3.9
	1+616	4.3	3.9	3.8	3.8	3.9	3.8	3.6	3.9
	1+628	4.4	3.9	3.5	3.5	3.7	3.6	3.4	3.9
	Average	4.2	3.8	3.7	3.6	3.8	3.7	3.5	3.8
	Std Dev	0.15	0.15	0.17	0.18	0.11	0.14	0.13	0.10
Section 3	1+652	4.4	4.1	3.7	3.5	3.5	3.3	3.2	3.4
	1+664	4.6	4.6	3.7	3.5	3.5	3.3	3.1	3.3
	1+676	4.6	5.2	3.8	3.6	3.4	3.2	3.0	3.3
	1+688	4.2	4.3	3.6	3.4	3.1	3.0	2.9	3.2
	Average	4.5	4.6	3.7	3.5	3.4	3.2	3.0	3.3
	Std Dev	0.18	0.48	0.07	0.09	0.19	0.13	0.12	0.09
Section 4	1+712	3.7	3.8	3.3	3.3	3.1	3.1	3.0	3.2
	1+724	4.0	3.8	3.5	3.5	3.4	3.3	3.1	3.1
	1+736	3.9	3.7	3.5	3.5	3.7	3.6	3.3	3.7
	1+748	3.7	3.5	3.4	3.4	3.5	3.4	3.3	3.6
	Average	3.8	3.7	3.4	3.4	3.4	3.4	3.2	3.4
	Std Dev	0.15	0.13	0.08	0.12	0.23	0.18	0.17	0.29
Section 5	1+772	3.9	3.5	3.5	3.5	3.7	3.6	3.4	3.6
	1+784	3.9	3.6	3.4	3.5	3.6	3.5	3.3	3.6
	1+796	3.9	3.8	3.4	3.5	3.6	3.5	3.3	3.6
	1+808	4.0	3.7	3.5	3.5	3.5	3.5	3.3	3.6
	Average	3.9	3.7	3.5	3.5	3.6	3.5	3.4	3.6
	Std Dev	0.07	0.13	0.04	0.04	0.06	0.04	0.05	0.02
Section 6	3+948	5.1	4.7	4.7	4.8	5.0	5.0	5.0	5.2
	3+956	5.9	5.6	5.2	5.4	5.5	5.4	5.3	5.7
	3+964	6.3	5.9	5.6	5.6	5.6	5.6	5.5	5.9
	3+972	5.9	5.6	5.2	5.1	5.4	5.4	5.2	5.6
	Average	5.8	5.5	5.2	5.2	5.4	5.3	5.2	5.6
	Std Dev	0.49	0.53	0.34	0.36	0.27	0.26	0.21	0.26

	Station	3/10	3/24	3/31	4/7	4/22	4/28	5/12	6/29
Section 7	3+988	6.4	5.7	5.2	5.0	5.1	5.1	5.1	5.4
	3+996	6.2	5.6	4.9	4.9	4.8	4.8	4.8	5.1
	4+004	5.8	5.4	4.8	4.6	4.6	4.6	4.6	4.9
	4+012	6.0	5.5	4.8	4.8	4.8	4.8	4.8	5.1
	Average	6.1	5.5	4.9	4.9	4.8	4.8	4.8	5.1
	Std Dev	0.24	0.13	0.15	0.16	0.21	0.21	0.23	0.19
Section 8	4+028	6.2	5.9	5.2	5.2	5.1	5.0	5.0	5.4
	4+036	6.4	5.7	5.2	5.1	5.0	5.0	5.0	5.3
	4+044	6.6	5.9	5.5	5.4	5.3	5.4	5.3	5.5
	4+052	6.4	5.9	5.4	5.4	5.2	5.2	5.2	5.5
	Average	6.4	5.8	5.3	5.3	5.2	5.1	5.1	5.4
	Std Dev	0.16	0.08	0.16	0.14	0.12	0.16	0.16	0.12
Section 9	4+068	6.5	6.4	5.5	5.5	5.3	5.2	5.1	5.3
	4+076	6.1	5.4	5.2	5.1	4.9	4.9	4.9	5.1
	4+084	5.6	5.0	4.6	4.4	4.6	4.5	4.6	4.9
	4+092	5.8	5.2	5.0	5.0	5.1	5.1	5.2	5.4
	Average	6.0	5.5	5.1	5.0	5.0	4.9	4.9	5.2
	Std Dev	0.40	0.60	0.37	0.42	0.29	0.28	0.24	0.22
Section 10	4+108	5.4	5.2	5.2	5.1	5.4	5.3	5.4	5.6
	4+116	5.6	5.4	5.2	5.1	5.2	5.2	5.3	5.5
	4+124	6.1	5.7	5.4	5.0	5.2	5.2	5.2	5.5
	4+132	6.4	6.1	5.5	5.6	5.7	5.6	5.6	5.8
	Average	5.9	5.6	5.3	5.2	5.4	5.3	5.3	5.6
	Std Dev	0.47	0.38	0.17	0.25	0.21	0.20	0.17	0.13
Section 11	4+684	4.0	3.8	3.6	3.6	3.9	3.7	3.5	3.8
	4+688	4.3	3.8	3.7	3.7	3.9	3.8	3.6	3.9
	4+692	4.3	4.1	3.7	3.7	3.8	3.8	3.7	4.0
	4+696	4.4	4.1	3.8	3.8	4.0	4.0	3.8	4.1
	Average	4.3	3.9	3.7	3.7	3.9	3.8	3.7	3.9
	Std Dev	0.18	0.17	0.10	0.08	0.07	0.13	0.13	0.15
Section 12	4+704	4.8	4.1	3.9	4.0	4.1	4.2	4.1	4.3
	4+708	4.3	3.9	3.8	3.8	4.0	4.1	4.0	4.3
	4+712	4.3	3.8	3.7	3.7	3.9	4.0	3.9	4.1
	4+716	4.1	3.9	3.6	3.6	3.9	3.9	3.8	4.1
	Average	4.4	3.9	3.8	3.8	4.0	4.0	3.9	4.2
	Std Dev	0.30	0.14	0.15	0.17	0.11	0.15	0.10	0.10

	Mid-depth Temp. C	12	12	13	16	13	18	24	29